Novel Mg-rich materials for hydrogen storage: bulk and nanoconfined $Mg_6Pd_{1-x}TM_x$ (TM = Ni, Ag, Cu) compounds and MgH_2-TiH_2 nanocomposites

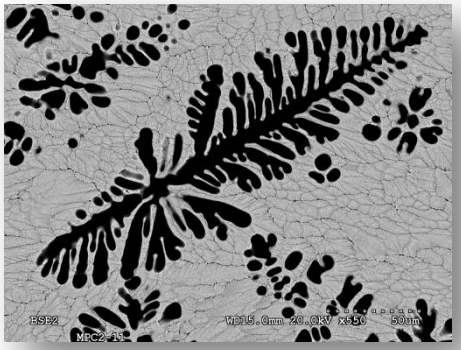

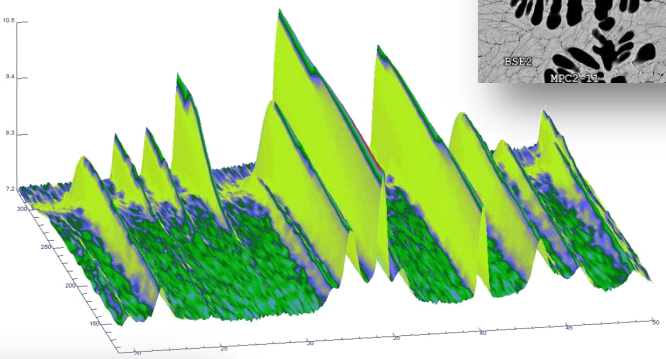

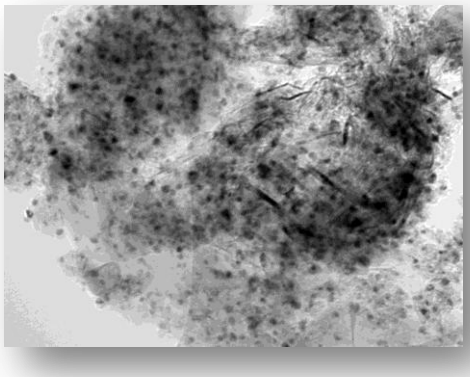

Marine Ponthieu

Ph.D. Thesis, 2013

Université Paris Est, France
École Doctorale Science, Ingénierie et Environnement
Laboratory:
Chimie Métallurgique des Terres Rares
Institut de Chimie de Matériaux de Paris-Est
CNRS UMR 7182

Universidad Autónoma de Madrid, Spain
Programa de Doctorado Energías y Combustibles para el Futuro
Laboratory:
Materials of Interest in Renewable Energies
Departamento de Física de Materiales

Thesis to obtain PhD degree:

From the University Paris Est, Speciality in Materials Science

From the University Autonoma of Madrid, Speciality in Energies and Fuels for the Future

Novel Mg-rich materials for hydrogen storage: bulk and nanoconfined $Mg_6Pd_{1-x}TM_x$ (TM = Ni, Ag, Cu) compounds and MgH_2-TiH_2 nanocomposites

Submitted by Marine PONTHIEU

Thesis defended on November, 29th 2013

Jury

Pr. Carlos SÁNCHEZ	University Autónoma of Madrid, Spain	Examiner
Dr. Patricia DE RANGO	Institut Néel, CNRS, France	Reviewer
Dr. Luca PASQUINI	University of Bologna, Italy	Reviewer
Dr. Martin DORNHEIM	Helmholtz-Zentrum Geesthacht, Germany	Reviewer
Dr. Jose Francisco FERNÁNDEZ	University Autónoma of Madrid, Spain	Thesis co-supervisor
Dr. Fermín CUEVAS	ICMPE, CNRS, France	Thesis co-supervisor

ACKNOWLEDGMENTS

While writing this manuscript, I have been thinking in all of you who helped me, collaborated and accompanied these three years of my life, between Paris and Madrid. Through these lines, I wish to thank this people in the warmest way.

First of all, I owe to my supervisors, Dr. Fermín Cuevas and Dr. Jose Francisco Fernández, the most sincere gratitude for their commitment along these three years. They have been receptive, reactive, dedicated, patient, full of valuable advices, trustful, friendly, *etc*. In some words, I could not have wish better supervisors.

I also wish to warmly thank the members of the jury: Dr. Patricia de Rango, Dr. Luca Pasquini and Dr. Martin Dornheim who kindly accepted to report my thesis; and Pr. Carlos Sánchez who accepted to be part of the jury. I am grateful to them for their interest and time devoted to examine this manuscript.

I want to thank Michel Latroche, director of the ICMPE, and Jean-Marc Joubert, team leader of the CMTR, for allowing me to work in their Institute and Laboratory in the best conditions. For this, I have to thank a second time Carlos Sánchez who leads the MIRE team and provided me a great working atmosphere. Of course, many other people also deserve a huge gratitude to make the laboratories running. I particularly think in Fabrice Couturas, Valérie Lalanne, Olivier Rouleau and Benjamin Villeroy, *l'équipe de choc*, always available and willing to help. I cannot say less of Fernando Moreno, *el alma del laboratorio*, its help is always precious and its good mood a present.

All along the elaboration of this PhD thesis, I was given the chance to collaborate with many people who provided me knowledge, fruitful discussions and support. I wish to express my gratitude to Yuen Au and Petra de Jongh who kindly received me in their laboratory at Utrecht University through the Van Gogh program. We carried out together a highly enriching scientific collaboration. Claudia Zlotea was also part of this adventure and I want to let her know my gratefulness for her assistance and perspicacity in numerous situations. I warmly thank Karine Provost who did not count her time spent in EXAFS analyses. I acknowledge as well the COST action MP1103 for financing my participation to two international conferences in Belgrade (First European Early Stage Researchers' Conference on Hydrogen Storage) and in Warsaw (E-MRS Fall Meeting).

I would like to share this PhD thesis with all the people who helped me in my experimental work: Paloma Adeva (CENIM) and Julio Bodega for alloy preparations, Eric Leroy and Julie Bourgon for TEM analyses, Laetitia Laversenne (ILL) and Florence Porcher (LLB) for neutron experiments, Sophie Nowak (ITODYS) for *in-situ* XRD measurements, and people from the SIDI in the UAM: Mario Ramírez and Noemi González (XRD), Enrique Rodríguez and Esperanza Salvador (SEM), María José de la Mata (thermal analysis). To all of them, I express my sincere gratitude for their availability and efficiency.

Besides the lab duty, I spent a lot of great moments with great people. I want them to know that their friendship has been precious all along these three years and I hope that it will last for some more.

A los de abajo (Xose, Julio, Mariam, Satoko, Fernando, Clama, Fabrice) y los de arriba (Paco, Isabel, Carlos), muchas gracias por hacerme sentir como en casa, por vuestra amistad y por vuestro apoyo incondicional. A mis compañeros del pasillo, con quienes he compartido tantas comidas y conversaciones animadas, Ricardo, Arturo, Emilie, Laura, ¡no cambiéis nada!

Je dois également beaucoup à toute l'équipe du CMTR, c'est une équipe en mouvement, pleine d'énergie et qu'on pourrait qualifier d'épicurienne ! La liste est trop longue pour en citer tous les membres, je les remercie pourtant tous chaleureusement. Je souhaiterai tout particulièrement m'adresser à Jean-Claude, Stéphane, Jean-Marc et Diane, apprentis jardiniers et cyclistes, grâce à qui Paris m'est apparue un peu plus verte ! À Dominique Alain, dont l'efficacité et la bonne humeur m'ont permis d'affronter les démarches administratives sous un nouveau jour. À mes compagnons doctorants, ex-doctorants et stagiaires, Delphine, Safa, Amaury, Claire, Véronique, JB, Hoda, Zineb, Aurore, Marco, Natacha, qui ont été sans aucun doute un soutien indispensable, surtout à l'heure de décompresser !

Finally, my strongest thoughts go to my friends and family.

À mes amis, éparpillés dans la France entière ou même dans le monde, ceux à qui je pense plus souvent qu'ils ne le croient, ceux avec qui on se retrouve après des mois ou des années comme si c'était hier, je sais que vous savez que je vous aime fort.

A mis amigos del Boalo-Mataelpino, os quiero un montón, gracias por ser tan buena gente. Le dedico a Diego un pensamiento muy especial, gracias por haberme animado y soportado en mi trabajo.

À mes parents (O & G), mes frères (François et Sylvain), mon neveu tout neuf Daniel, Mamé, mes oncles, cousines, cousins…, toujours présents, de près ou de loin, je vous en remercie du fond du cœur et vous dédie cet ouvrage.

ABSTRACT

Novel Mg-rich materials for hydrogen storage: bulk and nanoconfined $Mg_6Pd_{1-x}TM_x$ (TM = Ni, Ag, Cu) compounds and MgH_2-TiH_2 nanocomposites

This thesis is dedicated to the study of novel magnesium-rich compounds for solid state hydrogen storage. The aim is to destabilize Mg hydride and accelerate its sorption kinetics by alloying and nanostructuration. Three different kinds of materials have been studied.

The first family of materials concerns the $Mg_6Pd_{1-x}TM_x$ (TM = Ni, Ag, Cu) pseudo-binary compounds. Their structural properties and the effects of Pd substitution have been studied by X-ray diffraction, scanning electron microscopy and electron microprobe analyses. Their thermodynamics and kinetics of hydrogenation have been determined by solid-gas reaction. Different hydrogenation mechanisms take place depending on the substituting element. The stability of the metal-hydrogen system is altered by the nature of the phases formed during hydrogenation reaction. Thus, metal to hydride transformation is characterized by at least two absorption plateau pressures. The pressure of the first plateau is similar to that of Mg/MgH_2 while the second one occurs at higher pressure. The enthalpy and entropy of reaction are determined to quantify the destabilizing effect of Pd by TM substitution. Best desorption kinetics are found for the Ni containing alloy thanks to the catalytic effect of the Mg_2NiH_4 phase formed on hydrogenation.

The second approach aims to combine alloying with nanostructuration effects. Nanoparticles of Mg_6Pd as small as 3 nm are confined into nanoporous carbon matrix. By comparing their hydrogenation properties with those of the bulk alloy, we demonstrate that not only the (de)hydrogenation kinetics are much faster for the nanoparticles, but also that their hydrided state is destabilized.

Finally, MgH_2-TiH_2 nanocomposites were synthesized by mechanical milling under reactive atmosphere. The addition of a catalyst (TiH_2) and Mg nanostructuration allow strongly accelerating the sorption kinetics of hydrogen in Mg. To understand the role of the TiH_2 phase on the outstanding kinetics of these nanocomposites, their structural properties have been determined by X-ray and neutron diffraction. The existence of a coupled interface between Mg and TiH_2 phases is of major importance to facilitate H-mobility within the nanocomposite. Furthermore, it is shown that the TiH_2 inclusions inhibit the Mg/MgH_2 grain growth, thus maintaining the composites nanostructure during their cycling.

Keywords: *Metal hydrides, hydrogen storage, magnesium, intermetallic alloys, nanomaterials*

RÉSUMÉ

Nouveaux matériaux riches en Mg pour le stockage d'hydrogène : composés $Mg_6Pd_{1-x}MT_x$ (MT = Ni, Ag, Cu) massifs et nanoconfinés et nanocomposites MgH_2-TiH_2

Cette thèse est consacrée à l'étude de composés riches en magnésium innovants destinés au stockage solide de l'hydrogène. Le but est de déstabiliser l'hydrure de Mg et d'accélérer sa cinétique de sorption par des effets d'alliage et de nano-structuration. Trois différents types de matériaux ont été étudiés.

La première famille de matériaux concerne les composés pseudo-binaires $Mg_6Pd_{1-x}MT_x$ (MT = Ni, Ag, Cu). Leurs propriétés structurales et les effets de substitution du Pd ont été étudiés par diffraction des rayons X, microscopie électronique à balayage et microsonde de Castaing. Les propriétés thermodynamiques et cinétiques d'hydrogénation de ces matériaux ont ensuite été déterminées par réaction solide-gaz. Différents mécanismes d'hydrogénation sont mis en jeu en fonction de l'élément de substitution. La nature des phases formées lors de la réaction d'hydrogénation modifie la stabilité des systèmes métal-hydrogène. Ainsi, la transformation de métal à hydrure est caractérisée par au moins deux plateaux de pression. Le premier plateau a lieu à une pression proche de celle de Mg/MgH_2, alors que le second se produit à pression plus élevée. La détermination des valeurs d'enthalpie et d'entropie de réaction ont permis de quantifier la déstabilisation atteinte. Les meilleures cinétiques de désorption sont obtenues pour l'alliage au Ni, grâce à l'effet catalytique de la phase Mg_2NiH_4 formée lors de l'hydrogénation.

La seconde approche vise à combiner les effets d'alliage et de nano-structuration. Des nanoparticules de Mg_6Pd atteignant des tailles aussi petites que 3 nm sont confinées dans des matrices carbonées nano-poreuses. En comparant leurs propriétés d'hydrogénation à celles de l'alliage massif équivalent, on démontre non seulement que la cinétique de (dés)hydrogénation des nanoparticules est bien plus rapide, mais aussi que leur état hydrogéné est déstabilisé.

Enfin, des nano-composites MgH_2-TiH_2 ont été synthétisés par broyage mécanique sous atmosphère réactive. L'ajout d'un catalyseur (TiH_2) et la nano-structuration du Mg permettent de considérablement accélérer les cinétiques d'absorption et désorption d'hydrogène dans le Mg. Afin de comprendre le rôle de la phase TiH_2 sur les propriétés cinétiques remarquables de ces nano-composites, leurs propriétés structurales ont été déterminées par diffraction des rayons X et des neutrons. L'existence d'un couplage à l'interface entre les phases Mg et TiH_2 est d'importance majeure pour faciliter la mobilité de H au sein du nano-composite. De plus, il est démontré que les inclusions de TiH_2 freinent la croissance de grain de Mg/MgH_2, permettant ainsi de maintenir la nano-structuration des composés lors de leur cyclage.

Mots clés: *Hydrures métalliques, stockage d'hydrogène, magnésium, alliages intermétalliques, nanomatériaux.*

RESUMEN

Nuevos materiales ricos en Mg para el almacenamiento de hidrógeno: compuestos en volumen y nano-confinados $Mg_6Pd_{1-x}MT_x$ (MT = Ni, Ag, Cu) y nano-compuestos MgH_2-TiH_2

Esta tesis está dedicada al estudio de nuevos compuestos ricos en magnesio para el almacenamiento sólido de hidrógeno. El objetivo es desestabilizar el hidruro de Mg y acelerar su cinética de sorción mediante efectos de aleación y nano-estructuración. Tres distintos tipos de materiales se han estudiado.

La primera familia de materiales concierne los compuestos pseudo-binarios $Mg_6Pd_{1-x}MT_x$ (MT = Ni, Ag, Cu). Sus propiedades estructurales y los efectos de sustitución del Pd se han estudiado por difracción de rayos X, microscopía electrónica de barrido y microsonda electrónica. Las propiedades termodinámicas y cinéticas de hidrogenación de estos materiales se determinaron por reacción sólido-gas. Diferentes mecanismos de hidrogenación entran en juego dependiendo del elemento de sustitución. La naturaleza de las fases formadas durante la reacción de hidrogenación modifica la estabilidad de los sistemas metal-hidrógeno. A este respecto, la transformación de metal a hidruro se caracteriza por al menos dos plateaus de presión. El primer plateau ocurre a una presión cercana a la del Mg/MgH_2, mientras que el segundo se produce a mayor presión. La determinación de los valores de entalpía y entropía de reacción ha permitido cuantificar la desestabilización alcanzada. Las mejores cinéticas de desorción se obtienen para la aleación con Ni, gracias al efecto catalítico de la fase Mg_2NiH_4 formada durante la hidrogenación.

El segundo enfoque consiste en combinar los efectos de aleación y de nano-estructuración. Nano-partículas de Mg_6Pd con tamaños tan pequeños como 3 nm se han confinado en una matriz de carbono nano-poroso. Sus propiedades de hidrogenación se han comparado con las de la aleación en volumen equivalente, demostrando que no sólo la cinética de (de)hidrogenación de las nano-partículas es mucho más rápida, sino también que su estado hidrogenado se ha desestabilizado.

Por último, se han sintetizado nano-compuestos MgH_2-TiH_2 mediante molienda mecánica en atmósfera reactiva. La adición de un catalizador (TiH_2) y la nano-estructuración del Mg han permitido acelerar significativamente la cinética de absorción y desorción de hidrógeno por el Mg. Para entender el papel que juega la fase TiH_2 en las excelentes propiedades cinéticas de estos nano-compuestos, se han determinado sus propiedades estructurales mediante difracción de rayos X y de neutrones. La existencia de un acoplamiento a la interfase entre el Mg y el TiH_2 es clave para facilitar la movilidad de H en el nano-compuesto. Además, se demuestra que las inclusiones de TiH_2 ralentizan el crecimiento de grano de Mg/MgH_2, manteniendo la nano-estructura de los compuestos durante su ciclado.

Palabras claves: *Hidruros metálicos, almacenamiento de hidrogeno, magnesio, aleaciones intermetálicas, nanomateriales.*

TABLE OF CONTENTS

General introduction

One of the main issues of modern society concerns energy management at the global scale. On one hand, the fossil fuel reserves are reaching their limits and are source of many geopolitical conflicts. On the other hand, renewable energy sources are inexhaustible and a large variety of technologies are available to convert them into electricity or heat for industrial or individual utilisations. However, the production of renewable energies is intrinsically intermittent and, alone, is not able to supply on-time the energy needed to respond the consumer demand. Therefore, it is necessary to store the energy produced during over production of electricity to be able to return it during the consumption peaks. This process, also known as energy peak shaving, requires efficient and safe systems able to store large amount of energy during relatively long times.

One excellent candidate to fulfil this function is hydrogen, which can be used as an energy carrier, *i.e.* an intermediate between the energy production and consumption. Not only can this intermediate be consumed at any time but also at any place. That is why hydrogen is also very interesting for mobile applications. In a clean energy system, hydrogen can be produced from renewable sources, typically by water electrolysis powered by wind or solar energy. It can then be stored in a convenient way and finally used in a fuel cell to reject only water, thus closing the hydrogen cycle. Each of these steps requires efficient technologies, but hydrogen storage remains a key issue for industrial development of hydrogen utilisation as a clean energy carrier.

Conventionally, hydrogen is stored as a compressed gas. The containers commercially available, designated as type I, are made of steel and are designed for nominal pressure between 20 and 30 MPa. They offer good safety properties but relatively low gravimetric hydrogen density (~ 0.01 kgH_2/kg_{tank}). A second generation of high pressure tanks has been developed to store up to 0.05 kgH_2/kg_{tank} at pressure of 70 MPa for a container of type IV. They consist of composite structures made of a hydrogen-tight inner liner mechanically stabilized by carbon fibres. The main drawback

of such systems lies in their low volumetric hydrogen density (~ 23 gH_2/L_{tank} in the best case) [1].

This parameter can be considerably increased by cryogenic hydrogen liquefaction to reach 40 gH_2/L_{tank} (for a liquid hydrogen density of 71 gH_2/L). In these containers, hydrogen has to be maintained at temperature as low as 20 K through a sophisticated and expensive tank system that requires important energy input. In addition, about 1 % per day of hydrogen losses by evaporation cannot be avoided.

Alternatively, hydrogen can be reversibly stored in the solid form, either by physisorption in porous materials or by chemisorption in metal hydrides. The first method involves weak interaction between H_2 molecules and the atoms on the surface of a solid adsorbent. However, this mechanism is efficient only at low temperature (typically 77 K) where it can reach 7.5 wt.% H for the best materials, *i.e.* for the highest specific surface area (metal organic framework) [2]. Besides, the volumetric density achieved by physisorption process is limited to 34 $gH_2/L_{material}$.

In contrast, the strength of metal hydrides resides in their high volumetric hydrogen storage capacity that can reach 150 $gH_2/L_{material}$, *i.e.* more than twice the one of liquid hydrogen. Formation of metal hydrides involves the dissociation of hydrogen molecules into H-atoms which are then absorbed in the metal lattice. Hydrogen forms stable hydrides with many metallic species and alloys but only few of them are reversible at moderate temperature and pressure [3]. For example, we can mention $LaNi_5$ or FeTi compounds which are able to desorb hydrogen at ambient temperature and hydrogen pressure below 0.5 MPa. However, their reversible gravimetric storage capacity does not exceed 2 wt.% H (material basis) which is insufficient for most mobile applications. Hence, better gravimetric storage capacities are achieved using light elements. To this respect, Mg is an excellent candidate as it can store up to 7.6 wt.% H. Besides, this element possesses many advantages regarding the feasibility of a large scale utilisation as it is abundant on Earth, inexpensive and innocuous to human health and the environment. However, the Mg/MgH_2 system alone is not able to meet with the thermodynamic and kinetic requirements for hydrogen storage applications. It is yet possible to tailor these properties through the research of new phases and by tuning the materials at the nanoscale.

The objective of this PhD Thesis is to deeply develop these ideas to obtain new Mg-based materials with better properties than pure Mg. Kinetics and thermodynamics of (de)hydrogenation are extensively investigated to understand the mechanisms governing these reactions. The first chapter browses a state of the art of the relevant advancements in Mg-based materials for hydrogen storage. The experimental techniques used for this thesis are described in the second chapter. The subsequent investigation is organized according to three main axes, corresponding to three different types of materials. The first axis is developed in chapter 3 and focuses on Mg-rich alloys based on the Mg_6Pd intermetallic compound. Several transition metals (TM = Ag, Cu and Ni) are used to substitute Pd atoms and form $Mg_6Pd_{1-x}TM_x$ pseudo-binary phases which hydrogenation properties are deeply investigated. The fourth chapter is also centred on the Mg_6Pd phase but now nanoconfined in a porous carbon matrix. This hybrid material constitutes the second line of investigation of this thesis. The last type of materials is investigated in Chapter 5 through the structural and sorption properties of MgH_2-TiH_2 nanocomposites. Finally, the last chapter aims to evaluate and discuss the outcome of this Thesis in order to reach potential guidelines for future investigation.

References

1. Hirscher M. *Handbook of Hydrogen Storage*. John Wiley & Sons; 2010.
2. Thomas KM. Hydrogen adsorption and storage on porous materials. *Catal. Today* 2007; **120** (**3**–**4**): 389–398.
3. Sandrock G. A panoramic overview of hydrogen storage alloys from a gas reaction point of view. *J. Alloys Compd.* 1999; **293**–**295**: 877–888.

Chapter 1.

Overview of Mg-based materials for hydrogen storage

OUTLINE

This chapter aims to bring to the reader the state-of-the-art of hydrogen storage in Mg-based systems prior to the work undertaken in this Thesis study. General points on thermodynamic and kinetic characteristics of metal hydrides will be described and relevant results on Mg-based materials for hydrogen storage will be presented from bibliographic survey.

1 Hydrogen in Mg

1.1 Structural properties of the Magnesium-Hydrogen system

Magnesium and hydrogen form a simple system with a single hydride phase, MgH_2, which is stable below 553 K in atmospheric pressure condition [1]. During hydrogenation, H atoms can be absorbed into the hexagonal close-packed (*hcp*) metal lattice of Mg (S.G. $P6_3/mmc$) to form a solid solution phase at low hydrogen concentration, called α-Mg, with a very short range of solubility up to 9 at.% H at 833 K [2]. When H concentration increases, the β-MgH_2 phase is formed with a tetragonal crystal structure of rutile type (S.G. $P4_2/mnm$), as represented in Figure 1.1a.

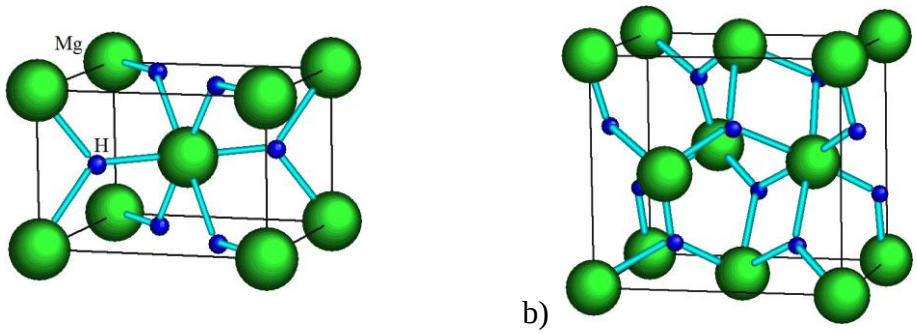

Figure 1.1. a) Rutile structure of β-MgH_2 and b) orthorhombic structure of γ-MgH_2.

The β-MgH_2 phase transforms into a metastable γ-MgH_2 phase at high pressure. The β to γ phase transition theoretically occurs at 0.39 GPa [3], but the coexistence of both phases is often observed during ball-milling preparations [4–11]. This high pressure modification has an orthorhombic structure (Figure 1.1b) with S.G. *Pbcn* [12] which is maintained as metastable at ambient conditions. Up to now, a complete β to γ conversion has never been achieved, making difficult to determine experimentally the

transition pressure. Crystallographic data of the different phases of the Mg-H system are summarized in Table 1.1.

Table 1.1. Crystal data of the Mg-H system

Phase	Space group	Cell parameters (Å)	Ref.
Mg	$P6_3/mmc$	a = 3.2125, c = 5.2132	[13]
β-MgH_2	$P4_2/mnm$	a = 4.5168, c = 3.0205	[14]
γ-MgH_2	*Pbcn*	a = 4.53, b = 5.44, c = 4.93	[15]

Under further compression, other pressure-induced phase transitions have been reported [3; 16] but they are out of the scope of this Thesis as pressures involved exceed several GPa.

Independently on its structual modification, MgH_2 possesses ionic bondings between Mg and H, with a charge distribution of $Mg^{1.91+}$ and $H^{0.26-}$ [17]. However, because of the weak ionisation of H, it is often considered as a transition hydride between ionic and covalent.

1.2 Sorption properties of Mg

Magnesium is able to reversibly absorb up to 7.6 wt.% H, according to the solid-gas reaction (1.1).

$$Mg(s) + H_2(g) \leftrightarrow MgH_2(s) \quad \textbf{(1.1)}$$

The formation of the hydride is exothermic and should thermodynamically occur at room temperature with a very low plateau pressure (0.05 Pa at 293 K). However this hardly happens because of important kinetic limitations. Mg surface easily passivates because of the formation of a thin layer of magnesium oxide impeding H absorption. Activation is usually achieved by applying high temperature and high hydrogen pressure [18].

Thermodynamic properties of Mg reflect the high stability of its hydride. The commonly accepted values for desorption enthalpy and entropy variations are 74.5 kJ/molH_2 and 135 J/KmolH_2 as determined by Stampfer *et al.* in 1960 [2] and latter confirmed by several authors [19; 20]. In consequence, a temperature of 553 K is required to desorb hydrogen at atmospheric pressure. This temperature is obviously too high for practical use of hydrogen storage.

Besides its high stability, MgH_2 also suffers from poor kinetics of hydriding and dehydriding reactions, which origin is generally attributed to the following barriers:

i) Passivation of Mg surface by formation of a MgO layer

ii) Limited dissociation rate of hydrogen molecules at Mg surface

iii) Slow diffusion coefficient of H atoms in MgH_2 ($D = 1.5 \times 10^{-16}$ m^2/s, almost constant within the temperature range 300 - 600 K [21]).

Owing to the first two barriers, hydrogen chemisorption on Mg surface is characterized by high activation energy. Atomic hydrogen penetrates then to the metal lattice where its mobility is hampered by the sluggish hydrogen diffusion through the magnesium hydride. The formation of MgH_2 is driven by nucleation and growth mechanism [22].

Magnesium hydride as a hydrogen store has been extensively investigated during the past fifty years. Significant improvements to previously described properties have been achieved by modification of Mg surface or by addition of other metals. The purpose of the next sections is, on one hand to describe how Mg sorption properties can be improved, and on the other hand to present a state-of-the-art of the most promising Mg-based materials for hydrogen storage.

2 Strategies to improve Mg sorption properties

The ability of any material to efficiently store hydrogen is defined according to two essential aspects: the thermodynamics and kinetics of its reaction of (de)hydrogenation. Besides its hydrogen storage capacity, these two aspects are commonly used to characterize the hydrogenation properties of a compound because they reflect its potential for practical applications. In this section we will consider a typical α to β phase transformation, where α is the hydrogen solid solution into a metal M and β is the metal hydride phase.

2.1 Thermodynamic approach

2.1.1 Basics of thermodynamics in metal hydrides

The equilibrium of a hydrogen-metal system is frequently described using the Van't Hoff equation (1.2):

$$ln\frac{P_p}{P_0} = \frac{\Delta H}{RT} - \frac{\Delta S}{R} \quad \textbf{(1.2)}$$

where P_p is the plateau pressure, T is the temperature, P_0 = 1.01325.10^5 Pa, R is the gas constant (R = 8.314 J/mol.K), ΔH and ΔS are the enthalpy and entropy changes occurring during the α → β transformation. The plateau pressure P_p corresponds to the coexistence of α and β phases and is experimentally determined by Pressure Composition Isotherms (PCI) measurements, as represented on the left of Figure 1.2. According to equation (1.2), if we plot the logarithm of P_p versus $1/T$ we obtain a straight line which slope is proportional to ΔH (Van't Hoff plot on the right of Figure 1.2). The intercept of this line with the vertical axis gives the value of ΔS.

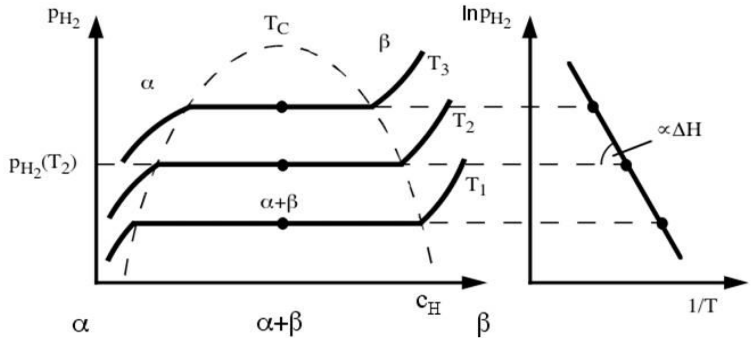

Figure 1.2. Schematic PCI diagram and corresponding Van't Hoff plot, taken from [23].

Therefore, the equilibrium conditions of pressure and temperature at which a hydride can be formed or decomposed are determined by its enthalpy and entropy changes. The entropy variation is mainly due to the transition of hydrogen gas molecules to atomic hydrogen absorbed in the metal lattice. Consequently, it will be very similar for most metal-hydrogen systems ($\Delta S_{absorption}$ ~ -130 J/K$molH_2$ [24]) and the stability of a hydrided compound will be mainly determined from its enthalpy of hydrogenation. Van't Hoff representation is then very convenient to visualize and compare thermodynamic characteristics of different hydrides. The Van't Hoff plots of various binary hydrides represented on Figure 1.3 show that most of them are out of the required thermodynamic window of 0.1 < P < 1 MPa and 273 < T < 373 K for most applications such as PEM fuel cells. Only VH_2 can be operated at room temperature, but

its reversible storage capacity remains limited (2.1 wt.% H_2 [25]) and pure vanadium is an expensive metal.

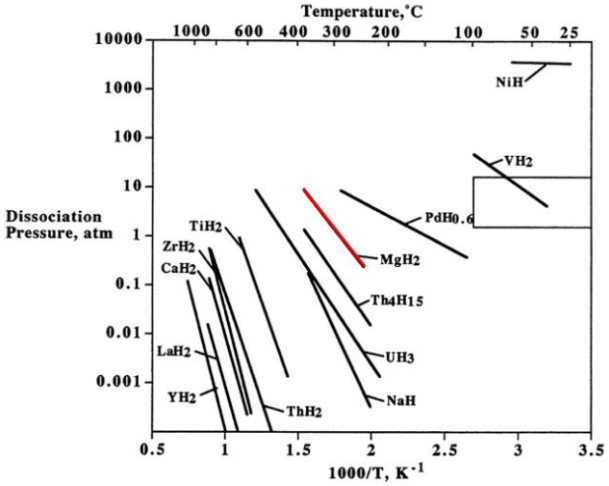

Figure 1.3. Van't Hoff lines (desorption) for binary hydrides. Box indicates 0.1-1 MPa and 273-373 K ranges. Taken from [26].

We saw in the previous section that one of the principal drawbacks of MgH_2 was its high thermodynamic stability, reflected by the too negative enthalpy of hydrogenation (ΔH = -74.5 kJ/molH_2). Therefore, one important objective in the quest for Mg-based material for hydrogen storage is to shift the absorption enthalpy to less negative values. The US Department of Energy (DOE) requires for on-board hydrogen storage system a dissociation pressure of 0.3 MPa at a maximum working temperature of 358 K. This leads to an ambitious target of ΔH = 43.3 kJ/molH_2.

2.1.2 Tailoring thermodynamics of Mg-H system

Traditionally, thermodynamic properties of metal hydrides can be tuned by building AB_n type intermetallic compounds where element *A* tends to form stable hydride (*e.g.* Mg) and element *B* does not form stable hydride. AB_n intermetallics are classified into several groups according to their stoichiometry, with n = 0.5, 1, 2 or 5.

Miedema *et al.* developed a semi-empirical model [27; 28] which allows predicting the enthalpy of formation of a ternary hydride from the heat of formation of elemental hydrides and of the alloy. The rule of Miedema, also known as the rule of reverse stability, can be written as:

$$\Delta H(AB_nH_{2x}) = \Delta H(AH_x) + \Delta H(B_nH_x) - \Delta H(AB_n) \quad \textbf{(1.3)}$$

This model implies that the more stable is the intermetallic compound, the less stable is the corresponding ternary hydride. Thus, MgH_2 can be destabilized by alloying Mg with other metals that have less affinity for hydrogen and that form stable intermetallic compounds with Mg.

Alternatively, MgH_2 destabilization can also be achieved by addition of suitable reactive components (A) to the hydride so that Mg does not return to its elemental structure but forms an intermediate compound (MgA_x) [29] according to the following reaction:

$$MgH_2 + xA \leftrightarrow MgA_x + H_2 \quad \textbf{(1.4)}$$

Figure 1.4 shows the corresponding destabilization mechanism. If the formation of the MgA_x compound is exothermic, it will offset the endothermic release of hydrogen from MgH_2 and consequently reduce the net enthalpy value of hydrogen desorption.

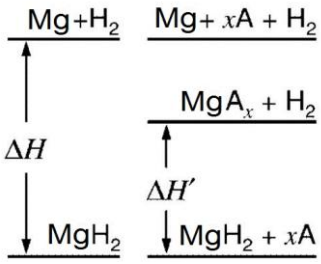

Figure 1.4. Schematic representation of enthalpy reduction by introduction of a reactive component A to the Mg-H system. Adapted from [30].

Finally, *ab intio* studies have demonstrated that MgH_2 stability can also be altered when particle size reaches the nanometric scale [30–32]. Indeed, the high surface to volume ratio, typical of nanomaterials, will add a non-negligible surface energy term to the molar free energy of reaction. The surface free energy γ represents the excess energy of surface atoms with respect to bulk atoms due to unsaturated electronic bonds. In the case of Mg/MgH_2, a sufficiently high surface area will result in a less exothermic hydriding reaction. Another contribution to the reduction of the absolute value of enthalpy, predicted for nanosized materials, comes from the high density of grain boundaries, which similarly leads to an excess energy. A combination of these

phenomena, specific of the nanometric scale, can result in a significant hydride destabilization. According to Wagemans *et al.*, if the size of MgH_2 crystallites is reduced to 0.9 nm, hydrogen desorption at atmospheric pressure can occur at temperature as low as 473 K [31]. Significant destabilization of MgH_2 was predicted for crystallite smaller than 1.3 nm while Bérubé *et al.* calculated a reduction by more than 30 % of enthalpy value for Mg crystals smaller than 5 nm [30]. Unfortunately, MgH_2 destabilization by size reduction is experimentally difficult to measure because of the rapid crystal growth of Mg phase when submitted to hydrogen absorption and desorption. However, this route remains a very promising field of investigation to achieve low temperature hydrogen storage in Mg.

2.2 Kinetic approach

2.2.1 Basics of kinetics in metal hydrides

Besides having suitable thermodynamic properties, a metal-hydrogen system is required to rapidly absorb and desorb hydrogen at moderate temperature. The time necessary to charge a storage tank must not exceed 5 minutes and hydrogen availability has to be sufficient to respond to a fuel cell supply. Kinetic performance of a system will be controlled by external thermodynamic variables such as pressure and temperature, but also by several intrinsic properties of the material. Thus, heat and mass transfer as well as surface interactions and phase transformations are important issues for (de)hydriding kinetics of a system. At the stage of laboratory work, it is considered that heat transport will not be a rate-limiting step and that this issue has to be addressed from an engineering point of view at the tank scale. The successive energy barriers that have to be overcome beforehand for absorption reaction concern the following steps:

i) Physisorption and dissociation (chemisorption) of hydrogen molecules on the metal surface
ii) Penetration of hydrogen atoms to the metal bulk and diffusion through the metal lattice
iii) Nucleation and growth of the β-hydride phase
iv) Diffusion of hydrogen atoms through the hydride phase

A simplified representation of the corresponding potential energy curve is given in Figure 1.5. Depending on the intrinsic properties of the storage media, any one of the energy barriers can be the rate-controlling step for the (de)hydriding reaction.

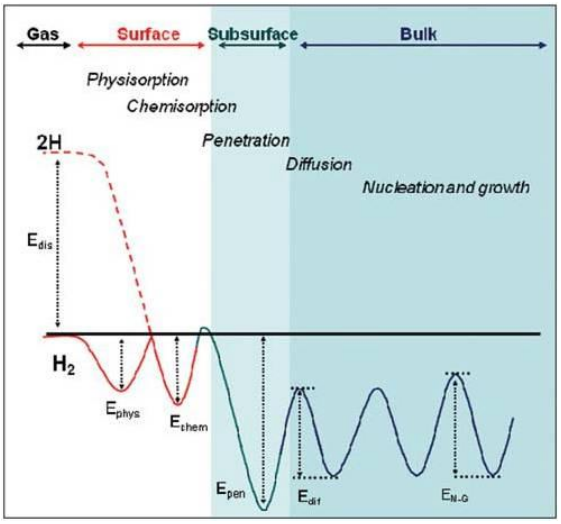

Figure 1.5. Potential diagram of a hydrogen molecule during absorption in a metal host, with E_{dis}: energy of dissociation, E_{phys}: energy of physisorption, E_{chem}: energy of chemisorption, E_{pen}: energy of penetration, E_{dif}: energy of diffusion and E_{N-G}: energy for the nucleation and growth. Taken from [33].

For metal hydrides, kinetic characterization is usually obtained from the transformed fraction (F) versus time. The sorption reaction highly depends on temperature, pressure and initial state of the sample, hence great attention has to be paid to experimental conditions and procedures. Afterwards, the rate-limiting step of hydrogen sorption can be identified by mathematical modelling of experimental kinetic curves. The existing models are generally based on three different types of mechanisms [34; 35]. The first one is the surface controlled process (SC), where chemisorption is the limiting step. The second one is the Johnson-Mehl-Avrami (JMA) mechanism, where nucleation and growth occurs randomly into the bulk and at the surface of a particle. The velocity of the metal/hydride interface growth becomes the controlling step, assuming that the nucleation rate is not limiting. Finally, the contracting volume (CV) model describes a nucleation at the surface of a particle and a growth from the surface into the bulk. Several equations result from the last two models, depending on the

material characteristics and external parameters, which can be fitted to experimental data.

Several investigations on kinetics of MgH_2 formation and decomposition seem to converge to a nucleation and growth mechanism both in absorption and desorption [9; 22; 36; 37]. The MgH_2 growth during absorption is limited by hydrogen diffusion into the MgH_2 phase [22; 37; 38] while desorption seems to be controlled by the MgH_2-Mg interface displacement [9; 37]. Therefore, to improve Mg (de)hydriding kinetics, one has to increase the number of nucleation sites and reduce the length of hydrogen diffusion. This can be achieved by adding suitable catalysts and by reducing the particle size of Mg [39].

2.2.2 Nanostructuration by ball milling

The particle and crystallite size of most hydrogen storage materials can be efficiently reduced by ball milling (BM) process. This method has been widely developed over the last twenty years to prepare Mg-based materials at low temperature and in relatively short times [40]. This technology offers a wide range of mills (vibratory mill, planetary mill, attritor mill), milling tools (made of different materials, with different ball diameters or vial volume) and process variables (milling time and speed, ball-to-powder weight ratio, temperature) that can be varied and combined for different milling output [41]. BM methods can be classified in three different types according to the targeted microstructure and composition of the final products [42].

The first type consists in nanostructuring a material without any change in its initial phase composition. The balls impacts can reduce the powder to micrometric particle size while the crystallites size reaches nanometer scale [41]. This technique can be used as well to incorporate catalyst additives during grinding. It presents the advantage to obtain a homogeneous distribution of the particles mixture at the nanometer scale.

Ball milling can also be employed to synthesize alloys from metallic elements. It is usually referred to as mechanical alloying. In this case, Mg powder is milled with another metal in the suitable composition. Nanostructured alloys are rapidly obtained at room temperature. Such materials exhibit better hydrogenation kinetics than equivalent alloy obtained by conventional metallurgy because of their high density of active

surface available for hydrogen absorption and due to the presence of defects introduced during plastic deformation.

Finally, milling of elemental mixtures or alloys can be performed under reactive atmosphere, *i.e.* hydrogen or deuterium gas, instead of an inert atmosphere. Reactive ball milling (RBM) allows synthesizing hydrided materials in a single step process by the formation of clean surface that is immediately available to react with hydrogen. Oxide formation, which is often an issue in nanoparticles handling, is then limited. Modern vials designed for this purpose are equipped with temperature and pressure sensors, allowing for *in situ* monitoring of hydrogen absorption.

In all cases, BM is an excellent method to obtain nanosized materials with improved kinetic properties through the generation of oxide-free surfaces and by reducing the length of hydrogen diffusion paths. In addition, the formation of multiple cracks and defects into the crystal lattice favours nucleation of the hydride phase.

2.2.3 Using catalysts

The use of catalyst additives, such as transition metals (TM) or metal oxides, is also known to improve Mg absorption kinetics by facilitating the electron transfer necessary for hydrogen dissociation. This mechanism is known as hydrogen spillover [43], which is described in Figure 1.6. The hydrogen molecule dissociates on the highly reactive catalyst located on the metal surface. Hydrogen atoms are then available to diffuse at the metal surface to finally penetrate in the metal bulk.

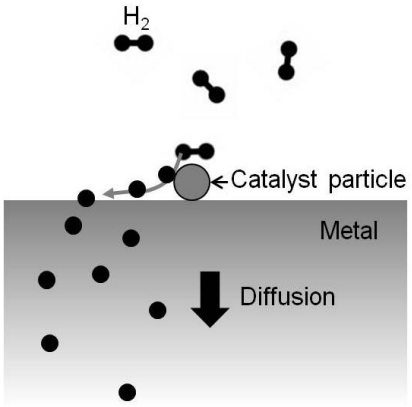

Figure 1.6. Hydrogen spillover mechanism: the hydrogen molecule dissociates on a catalyst particle. Atomic hydrogen then migrates to the metal surface and diffuses into the bulk of the material.

Catalysts are generally added to the storing material by BM which ensures a homogeneous distribution of doping particles. Usually, a small amount of catalyst is sufficient to significantly improve the sorption kinetics. Thus, the gravimetric absorption capacity loss can be minimized.

2.2.4 Nanoconfinement in porous materials

The use of nanoparticles as efficient media for hydrogen storage implies their stabilization against coalescence during heating or hydrogen cycling. To this purpose, nanoparticles are confined into nanoporous support with high surface area. Many additional advantages can be highlighted from the use of a suitable support. For example, the supporting material can provide additional storage capacity by hydrogen physisorption on its surface at low temperature. The interaction between the metal nanoparticles and its support can also result in a catalytic activity for the (de)hydrogenation process. From a large scale point of view, a support with high thermal conductivity allows for an efficient thermal management during refilling of a hydrogen tank [44]. The presence of a porous support also provides a better mechanical stability in a metal hydride tank. Indeed, absorption and desorption cycling causes volume variations of the material and induces mechanical stresses in the system.

The choice of the stabilizing matrix is guided by the following requirements [45]:

i) Light weight in order to preserve high gravimetric storage capacity
ii) High porosity and high surface area allowing high metal loading
iii) Chemically inert as respect to the active material
iv) Low cost

Hence, carbon materials are the more adapted to hydrogen storage applications, although metal-organic frameworks, mesoporous oxides or zeolites have been also considered. Different methods are used to deposit the nanoparticles into the pores, depending on the nature of the active material. If the active material can be dissolved in a suitable solvent, then it is possible to disperse the nanoparticles by solution impregnation of a porous matrix. After impregnation of the matrix with the precursor solution, the solvent is generally removed by heating. Another possibility is to infiltrate the active material as a molten phase. A mixture of powdered active material and the supporting matrix is heated up to the melting temperature of the phase, leading to the

infiltration of the liquid phase into the pores. This last method is recognized to be convenient for Mg based materials, as Mg melts at relatively low temperature (922 K). In addition, it can be combined with a prior precursor impregnation to obtain alloyed nanoparticles confined into the porous matrix.

The nanoconfinement technique is a relatively new approach to stabilize nanoparticles and several issues, such as high air sensitivity or poor gravimetric capacity, need to be solved. However, it is a promising way to improve hydrogen sorption kinetics.

3 Mg-based materials for hydrogen storage

In this section, the most relevant progresses on Mg-based materials for hydrogen storage will be reviewed, with a focus on the materials related to this Thesis.

3.1 Mg-based alloys

3.1.1 Mg-TM alloys

The first route considered to improve MgH_2 properties was to alloy Mg with other metals. The aim was to reduce desorption temperature within a realistic pressure window, while maintaining a high gravimetric capacity of hydrogen absorption.

Thus, in 1967, Reilly and Wiswall [46] initially characterized hydrogenation properties of Mg_2Cu and Mg_2Cu/Mg alloys. Upon hydrogenation, Mg_2Cu decomposes into MgH_2 and $MgCu_2$ with a higher plateau pressure than pure MgH_2 formation. The absorption enthalpy and entropy deduced from isothermal pressure-composition measurements were -73 ± 4 kJ/molH_2 and -142 ± 3 J/KmolH_2, respectively. More recently, Shao *et al.* [47] reported more negative values of -77.1 kJ/molH_2 and -146.4 J/KmolH_2 for the formation enthalpy and entropy, respectively, of hydrided Mg_2Cu. However, the storage capacity of Mg_2Cu is significantly reduced to 1 H/M (equivalent to 2.6 wt.% H) instead of 2 H/M for pure Mg. Reilly and Wiswall also suggested the catalytic property of Mg_2Cu during Mg hydrogenation reaction. This last point has been later deepen by Karty *et al.* [48] to reach the conclusion that Mg_2Cu was efficient to provide a clean surface for hydrogen dissociation but that hydrogen diffusion through the metal or the hydride was still the rate limiting step.

More interesting in terms of destabilization of the magnesium hydride is the alloying between Mg and Ni. Mg_2Ni intermetallic compound forms a ternary hydride, Mg_2NiH_4, with a hydrogenation enthalpy and entropy of -64 ± 4 kJ/molH_2 and -122 ± 6 J/KmolH_2, respectively [49], which is significantly lower than pure Mg. The catalytic properties of Ni for hydrogen dissociation also have a strong impact on sorption kinetics. For example, Mg_2NiH_4/MgH_2 mixtures obtained by BM presented lower desorption temperatures than both separated hydride [50]. The catalytic effect of Ni was also evidenced in BM Ni/MgH_2 mixtures, which desorption temperature was lowered by more than 200 K as compared to BM MgH_2 [51]. However, its storage capacity (3.6 wt.% H) is much lower than the one of Mg. Many researchers attempted to improve its properties by partial substitution of Ni by other transition metals (V, Cr, Fe, Co, Cu, Ag, Zn or Y) but efforts remained unsuccessful [52–55]. In all cases, the absorption capacity was reduced to even lower values and the thermodynamic gain was relevant only for Cu substitution [56].

It is noteworthy to mention here the difficulties to obtain reliable structural data on the Mg_2NiH_4 hydride due to its polymorphic properties. When formed at temperature higher than 508 K, it crystallizes in a cubic structure (called HT), with S.G. *Fm*-3*m* [57]. At temperature below 483 K, a monoclinic modification is formed (called LT1, S.G. *C*2/*c*) [58]. A third modification was reported when a HT polymorph was cooled down below the transition temperature, leading to the partial formation of an orthorhombic structure (called LT2) with S.G. *Pcc*2. This LT2 modification is the result of microtwinning in the LT1 lattice, favoured by the HT to LT transition [59]. In addition, several sub-stoichiometric Mg_2NiH_x phases have been reported. The solid solution $Mg_2NiH_{0.3}$ is isostructural to the Mg_2Ni phase [60] while the Mg_2NiH hydride has been identified with the same polymorphic properties as Mg_2NiH_4 phase [61].

Alloys of Mg with other transition metals have also been explored but only few elements exhibited relevant hydride properties. We can mention here the interesting properties of the Mg-Fe-H system. Although Mg and Fe are immiscible, they react with hydrogen to form a ternary hydride Mg_2FeH_6. Therefore, this hydride needs to be synthesised either by high pressure sintering [62] or by RBM processes [4; 63; 64]. The gravimetric capacity of such compound is relatively high with 5.5 wt.% H, and its volumetric hydrogen density is one of the highest with 150 kg_{H2}/m^3. Although a

catalytic effect due to the presence of Fe was reported for the decomposition reaction [64], this hydride remained too stable (ΔH = -77.4 kJ/molH_2 [65]) for possible hydrogen storage applications near room temperature.

Similarly, Mg-Co hydrides have to be prepared by direct synthesis methods (RBM or sintering techniques) as Mg_2Co alloy does not exist. Two different hydride phases belong to the Mg-Co-H system: $Mg_6Co_2H_{11}$ and Mg_2CoH_5, respectively storing 4.0 and 4.5 wt.% H. This material showed very good reversibility and cycling properties [66; 67] but the stability of the hydride remained too high (ΔH = -83.2 kJ/molH_2 [68]).

Mg also forms stable alloys with Pd. This system and its hydrogen storage properties will be detailed in the next section.

3.1.2 The Mg_6Pd intermetallic compound

Although it is too expensive for large scale applications, palladium acts as a catalyst and improves magnesium sorption properties, as well as resistance to air oxidation [69].

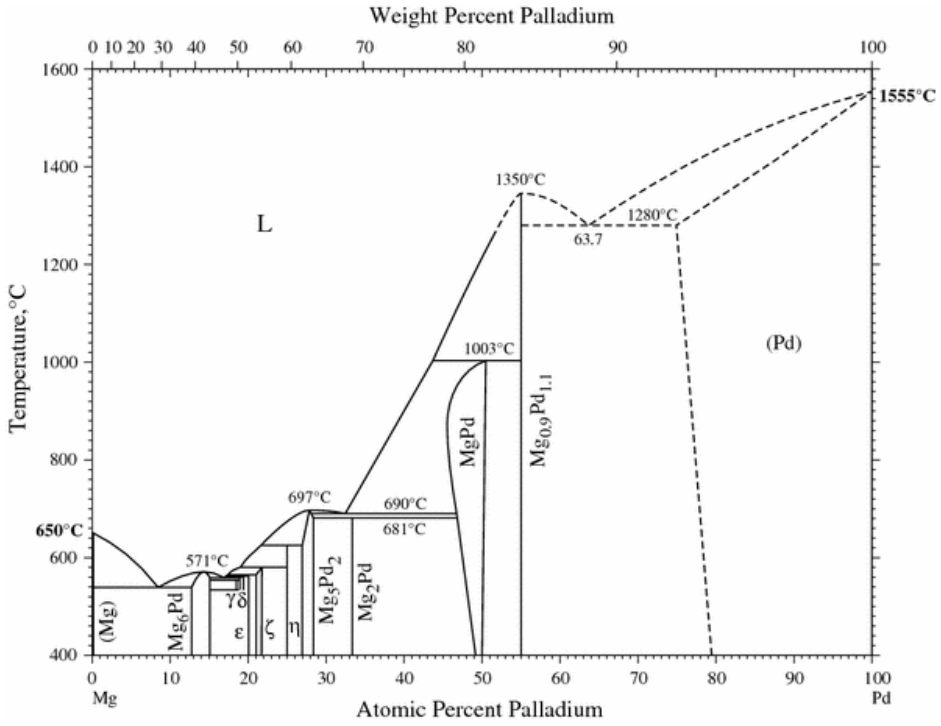

Figure 1.7. The Mg-Pd phase diagram [70].

The binary phase diagram of the Mg-Pd system [70] shows the existence of numerous intermetallic phases (Figure 1.7), among which Mg_6Pd is the richest in Mg.

Hence, this compound has attracted wide interest for hydrogen storage over the last decades, as it is the lightest and also the cheapest Mg-Pd intermetallic.

a. Structural properties

The Mg_6Pd phase crystallizes in a large *fcc* (face centered cubic) unit cell with the space group *F*-43*m*. The crystal structure of this intermetallic was determined by Samson [71]. Its large unit-cell (a = 20.108 Å) contains 340 atoms of Mg and 56 atoms of Pd distributed over 14 crystallographic sites: 10 for Mg atoms, 3 for Pd atoms and one with mixed occupancies. The corresponding structural parameters as described by Samson are reported in Table 1.2. Site 12 can be simultaneously occupied by Mg and Pd, and constitutional Mg vacancies are formed on site 14. This two sites act as buffer for Mg concentration through the wide homogeneity range which extends from 85.0 to 87.4 at.% Mg.

Table 1.2. Atomic sites, Wyckoff positions, Site Occupancy Factors (SOF) and atomic coordinates of the Mg_6Pd crystal structure [71].

Site n°	Atom	Wyckoff position	SOF	Atomic coordinates		
				x	***y***	***z***
1	Mg	48*h*	1	0.1436	*x*	0.0340
2	Mg	48*h*	1	0.0940	*x*	0.2739
3	Mg	48*h*	1	0.1510	*x*	0.5281
4	Mg	48*h*	1	0.0566	*x*	0.7676
5	Mg	48*h*	1	0.2002	*x*	0.9072
6	Mg	24*f*	1	0.1072	0	0
7	Mg	24*f*	1	0.3813	0	0
8	Mg	24*g*	1	0.0648	1/4	1/4
9	Mg	16*e*	1	0.3025	*x*	*x*
10	Pd	16*e*	1	0.1679	*x*	*x*
11	Pd	16*e*	1	0.4065	*x*	*x*
12	Pd	16*e*	0.49	0.6687	*x*	*x*
	Mg		0.51		*x*	*x*
13	Pd	16*e*	1	0.9004	*x*	*x*
14	Mg	4*d*	0.97	1/4	1/4	3/4

This structural model has been later revised by Makongo *et al.* [72] to better describe the accommodation of the homogeneity range. In particular, at the Mg-rich boundary, strong disorder affects sites 12 and 14. When the phase composition exceeds

86.2 at.% Mg, Mg vacancies are created on site 14 and site 12 splits into two atomic positions named 12*a* and 12*b*, being the latter exclusively occupied by Mg atoms. Thus, when Mg concentration increases in the Mg_6Pd phase, site occupancy factor (SOF) on site 14 decreases while SOF on site 12*b* increases. This configuration implies the following new restraints for SOF refinements: $\sum$(SOF12*a*, SOF12*b*) = 1 and $\sum$(SOF12*b*, SOF14) = 1. When Mg content is below 86.2 at.%, the chemical composition of the phase is accommodated through SOF of Mg and Pd on site 12*a*. In consequence of the wide homogeneity range of this phase, the lattice parameter varies linearly from 20.045 to 20.199 Å, depending on Mg concentration (from 85.0 to 87.4 at.% Mg, respectively).

Regarding the construction of the Mg_6Pd cell, it can be described by an arrangement of interpenetrated Mackay clusters (Figure 1.8b). A Mackay cluster is made of three concentric shells centred on a Pd atom [72]: the inner shell consists of an icosahedron with 12 Mg atoms at the vertices, the second shell is formed by 30 Mg atoms on the vertices of an icosidodecahedron and the outer shell consists of 6 Pd and 6 Mg on an icosahedron (Figure 1.8a from bottom to top).

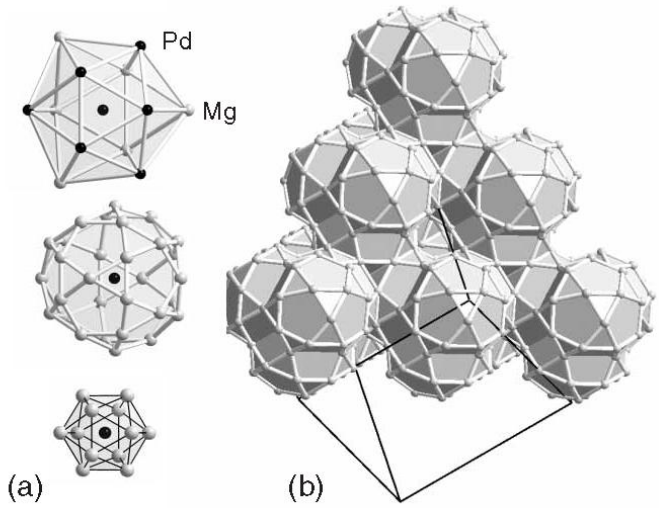

Figure 1.8. a) The three concentric shells of a Mackay cluster and b) arrangement of Mackay clusters in the Mg_6Pd cell [72].

b. Hydrogenation properties

Mg_6Pd absorbs up to 4.3 wt.% H when exposed to 4 MPa of hydrogen pressure and 573 K [73]. The PCI curve measured by Huot *et al.* displays three plateau pressures corresponding to the following successive reactions [74]:

$$Mg_6Pd + 2.35\ H_2 \leftrightarrow Mg_{3.65}Pd + 2.35\ MgH_2 \quad \textbf{(1.5)}$$

$$Mg_{3.65}Pd + 2.35\ MgH_2 + 1.15\ H_2 \leftrightarrow ½\ Mg_5Pd_2 + 3.5\ MgH_2 \quad \textbf{(1.6)}$$

$$½\ Mg_5Pd_2 + 3.5\ MgH_2 + 1.5\ H_2 \leftrightarrow MgPd + 5\ MgH_2 \quad \textbf{(1.7)}$$

The hydrogen uptake corresponding to each reaction is 1.9, 0.9 and 1.2 wt.% H respectively, for a total of 4.0 wt.% H. The difference with experimental capacity was attributed to the formation of Mg_5Pd_2(H) and MgPd(H) solid solutions. An investigation on Mg/Mg_6Pd nanoparticles [75] concluded to a similar hydrogenation mechanism but the occurrence of unidentified Mg-Pd compounds during hydrogenation was also suggested [75; 76].

Regarding the thermodynamics of Mg_6Pd hydrogenation, only few data are available. Kume and Weiss [77] obtained enthalpy and entropy values for the dehydriding reaction of Mg_6Pd catalyzed by tetracyanoethylene (TCNE) using the Van't Hoff equation. PCI curves were measured at relatively low temperature (433 to 468 K) and low pressure (< 0.01 MPa) and were limited to reactions (1.5) and (1.6), although only one plateau pressure was observed. They found that the hydrided Mg_6Pd was more stable than MgH_2 with ΔH = -80.3 kJ/molH_2 and ΔS = - 148 J/KmolH_2.

Kinetics reported for Mg_6Pd is rather slow, even for ball milled material [74]. Though, Roquefere *et al.* achieved significant kinetic improvement by short co-milling of Mg_6Pd with 15 wt.% Fe [78]. The crystallite size was significantly reduced and Fe was expected to have catalytic properties on hydrogen absorption. However, thermodynamic and kinetic properties remain unsatisfactory and further improvements are needed. Investigation based on the Mg_6Pd intermetallic has been continued by exploration of new pseudo-binary isomorphous compounds, with the objective to create less stable hydrides.

3.1.3 $Mg_6Pd_{1-x}Ni_x$ pseudo-binary compounds

New families of intermetallics can be obtained by substitution of Pd by other transition metals that have less affinity for hydrogen. Ni seems to be a suitable

substitution element as, besides having close electronic outer shell configuration to Pd, it has catalytic properties for hydrogen dissociation and it is much cheaper than Pd.

a. Ternary phase diagram

Pd and Ni are totally miscible and form an isomorphous binary system [79], which lead to expect complete miscibility in the $Mg_6Pd_{1-x}Ni_x$ pseudo-binary phase. However, this hypothesis is refuted by the fact that the Mg_6Ni phase does not exist in the Mg-Ni phase diagram. Only a metastable phase, isostructural to Mg_6Pd, can be obtained by melt-spinning and low temperature annealing [80; 81].

The first data reported on the Mg-Ni-Pd ternary system [82; 83] mentioned a Ni solubility in the Mg_6Pd phase limited to 2 at.% Ni (*i.e.* x = 0.13) at 673 K. A deeper investigation on Ni solubility limit in the Mg_6Pd phase demonstrated that the homogeneity range actually extends to 9 at.% Ni at 673 K [84]. The corresponding ternary phase diagram at the Mg-rich corner is represented in Figure 1.9.

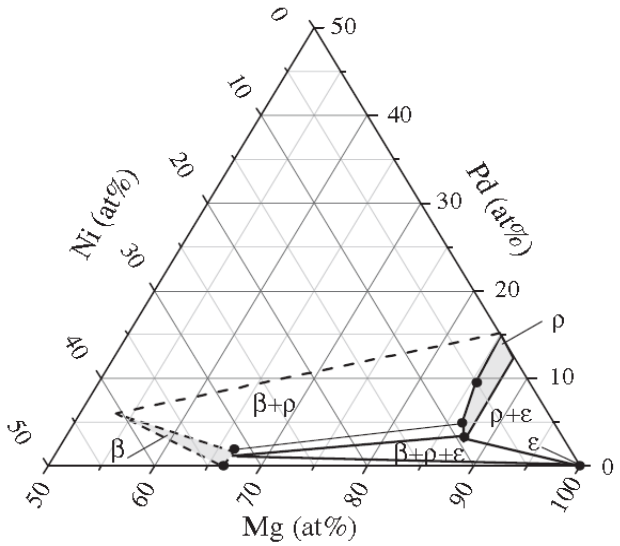

Figure 1.9. Ternary phase diagram of the Mg-Ni-Pd system in the Mg-rich corner at 673 K **[84]**. Labels: ρ for Mg_6Pd phase; β for Mg_2Ni phase; ε for Mg phase.

b. Structural properties

The $Mg_6Pd_{1-x}Ni_x$ crystal structure has been determined for several compositions by X-ray diffraction [84; 85] and by neutron diffraction for x = 0.5 [86]. The space group was the same than for Mg_6Pd crystal. Therefore, the model of Makongo previously

described (Chapter 1, section 3.1.2.a) was applied to this pseudo-binary phase and Ni substitution was allowed on Pd sites. Interestingly, it was found that Ni atoms preferentially locate on sites with low coordination numbers (CN), *i.e.* sites 10 (CN = 12), 11 (CN = 10) and 13 (CN = 12), and that site 12 (CN = 13) was exclusively occupied by Pd and Mg. This distribution was attributed to steric effects: larger atoms will preferentially locate on sites with higher CN because they offer a larger space. In this case, Ni atoms are smaller than Pd ones (r_{Ni} = 1.24 Å and r_{Pd} = 1.37 Å) and therefore locate on site with lower CN. This feature was also confirmed by first-principles calculations on this pseudo-binary compound [87].

As anticipated by the difference of atomic radii, the lattice parameter of the pseudo-binary phase decreases linearly with the amount of Ni substituting Pd [84; 87]. However, Mg concentration in the Mg_6Pd phase affects more importantly the size of the cell due to its much larger radius (r_{Mg} = 1.60 Å) as compared to Ni and Pd ones.

c. Hydrogenation properties

Hitherto, hydrogenation properties have been investigated for the partially substituted $Mg_6Pd_{0.5}Ni_{0.5}$ compound [86; 88]. The sample absorbed up to 4.5 wt.% H at 615 K and under 2 MPa of hydrogen pressure. Hydrogenation led to a totally reversible disproportionation of the initial compound into MgH_2, Mg_2NiH_4 and Mg_5Pd_2 phases. Neutron diffraction analyses highlighted the complex polymorphic properties of the Mg_2NiH_4 phase. Indeed, it was found that under the studied hydrogenation conditions, this hydride phase crystalliszes in the LT2 orthorhombic structure which exhibits microtwinning occurring during the cooling of the cubic HT polymorph (see Chapter 1, section 3.1.1). These structural modifications made crystallographic refinements of this phase difficult. Mg_5Pd_2 and Mg_2NiH_4 final phases did not show any sign of partial substitution of Ni by Pd or *vice versa*. In contrast, Lass reported the formation of the $Mg_2(Ni,Pd)H_4$ phase and the absence of Mg-Pd intermetallics during the hydrogenation of a $Mg_6Pd_{0.3}Ni_{0.7}$ compound [89].

Thermodynamic properties of the $Mg_6Pd_{0.5}Ni_{0.5}$ compound were determined by PCI measurements and using the Van't Hoff equation [88]. Enthalpy and entropy variations during hydrogen absorption (ΔH = -63 ± 3 kJ/molH_2 and ΔS = -114 ± 4 J/K.molH_2) represented a significant decrease in stability as compared to that of pure MgH_2.

3.2 Mg and catalysts

One of the main drawbacks of Mg-based alloys is the loss in gravimetric storage capacity as compared to pure Mg. In addition, hydrogenation of well-crystallized intermetallic compounds generally implies long range diffusion of metallic elements which slows down the reaction kinetics. An alternative to Mg alloys is the addition of catalysts which is generally achieved by ball milling. In this section, different examples of Mg-catalyst systems will be presented.

3.2.1 Transition metal additives

TM are commonly used to catalyse hydrogen absorption or desorption in Mg. Effective catalysis requires a uniform distribution of very small catalyst particles over Mg surface. They generally affect the reaction kinetics by the spill-over mechanism, as described in Chapter 1, section 2.2.3. Because of its widely recognized catalytic properties, Pd was one of the first elements to be added to ball-milled Mg [90; 91]. It was demonstrated that very small amounts of Pd (< 1 wt.%) homogeneously distributed over the Mg surface resulted in significant kinetic improvement and eliminated the need of an activation process. The positive effect of other TM, such as TM from the 3d-block but also Zr or Nb, was also tested. The experimental procedure generally consists in ball milling a small quantity of additive (from 1 to 5 at.% TM) with MgH_2 powder [8; 92–97]. The type of mill as well as the milling conditions, the amount of additive and the initial state of the powders influences the efficiency of the catalyst. Therefore, comparison of results from different experimental procedures must be taken with a lot of care. As a general trend, kinetic improvements are clearly observed when compared to a reference of pure MgH_2 sample and are evidenced by activation energy decrease [97; 98]. Among the abundance of results in this area of investigation, Nb [8; 94; 99; 100], V [92; 96; 98; 100] and Ti [92; 96] elements stands out for their strong ability to facilitate hydrogen absorption. In addition, their immiscibility with Mg allows decorating Mg particles without forming any alloyed phases. For example, a MgH_2 + 5 at.% V mixture milled during 20 hours was able to desorb hydrogen in 33 min at 508 K and subsequently absorb 5.6 wt.% H in about 4 min at 473 K [93]. In addition, these outstanding hydrogenation properties were essentially maintained after 2000 cycles [101]. Similar properties were found out for Nb catalysed MgH_2 [99; 102].

The precise role of these catalysts is still subject to debate and several effects seem to take part in the kinetic enhancement. However several authors agree on the formation of metastable NbH_x or VH_x hydride phases that act as gateway for hydrogen diffusion [8; 96; 99; 102; 103]. Analogous conclusions were drawn from Ti catalysed MgH_2 [92; 96] but more details on the Mg-Ti-H system will be given in section 3.2.3.

Finally, it is worth to precise that none of the publications mentioned above in this section reported any thermodynamic modification on the Mg-H system. However, in some cases it is possible to form Mg-TM metastable phases with better thermodynamic properties. For example, interesting results on metastable $Mg_{0.75}Nb_{0.25}$ *bcc* alloy obtained by co-deposition show a destabilization of the $(Mg_{0.75}Nb_{0.25})H_2$ *bcc* hydride as compared to MgH_2 [104]. The PCI curves measured during hydrogen absorption between 293 and 413 K indicated an enthalpy of -53 kJ/molH_2 with an entropy of -117 J/K.molH_2.

3.2.2 Metal oxide catalysts

Metal oxide catalysts combine the abrasive properties of ceramic materials with the catalytic properties of the metal as seen in the previous section. Investigation in this field is very productive and most of the TM oxides from the 3d-block have been tested [105–108], as well as Nb, Zr, Al or Si oxides. As for TM catalysts, small amounts of oxides are generally added before a BM process with MgH_2. Considering the large amount of data and the diversity of experimental procedures, systematic studies are the most suitable way to compare the efficiency of the different catalysts. For example, Oelerich *et al.* compared the effects of 0.2 at.% of different oxides when ball milled during 100 h with MgH_2. They found that Cr_2O_3 led to fast hydrogen absorption while Fe_3O_4 was the most efficient to improve hydrogen desorption rate [108]. Then, Barkhordarian *et al.* continued the systematic study by comparing the two previous oxides with Nb_2O_5 using the same conditions of preparation and characterization [109]. It was found that the last one was much better than all the previously investigated catalysts on MgH_2 showing a complete hydrogen absorption in 1 min at 573 K. Figure 1.10 illustrates the strikingly superior desorption rate of MgH_2 catalysed with Nb_2O_5. From this moment, Nb_2O_5 passed to be the most promising catalyst to improve sorption reaction kinetics in Mg. Oxide concentration did not significantly influence the

hydrogen absorption rate. Nevertheless, it was optimized to 0.5 at.% in MgH_2 to reach the fastest desorption [110]. This concentration is low enough to limit the loss in gravimetric capacity which was maintained at 7 wt.% H.

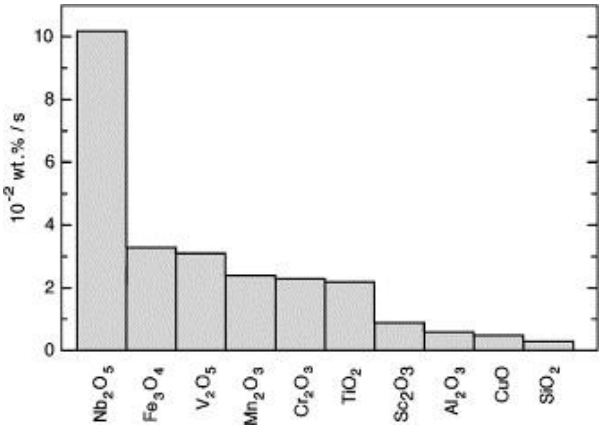

Figure 1.10. Desorption rate of MgH_2 catalysed with different metal oxides at 573 K into vacuum **[109]**.

Several hypotheses have been suggested to explain the outstanding kinetics of such composites. The first proposed mechanism concerns the ceramic nature of metal oxides which favour the nanostructuration of the material during BM process and hence reduce the diffusion length path of hydrogen atoms. In addition, the introduction of a high density of structural defects is expected to change the electronic structure of the metal ion and increase the catalytic activity of the metal oxide [111]. The formation of a hydrogen depleted MgH_{2-x} phase, identified by XRD and calorimetry, has also been reported to highly increase H diffusion [107; 112]. Finally, the catalytic mechanism of metal oxides also involves the ability of the metal cation to have multiple valence states which helps to dissociate hydrogen molecules and to transfer hydrogen atoms to the Mg phase. This intermediate state allows fast hydrogen dissociation and recombination. The role of oxygen anions is then to tailor the electronic structure of the metal ions [111].

3.2.3 The Mg-Ti system

Owing to its light weight among the TM and its relatively low cost, Ti is an attractive additive to improve Mg hydrogenation properties. As Nb or V catalysts, Ti forms several hydride phases and the existence of a metastable TiH_x ($0.7 < x < 1.1$,

depending on the particle size) phase has been reported [113]. In addition, the fluorite-type face centred cubic (*fcc*) structure of TiH_2 exhibits much faster hydrogen diffusion rate (1.7×10^{-13} m²/s at 600 K [114]) than the rutile-type body centred tetragonal (*bct*) MgH_2. Therefore, it is expected to be a good H carrier and favour the kinetics of hydrogen diffusion. As magnesium, pure Ti crystallizes at room temperature in the hexagonal close packed (*hcp*) structure (S.G. $P6_3mmc$). However, Mg and Ti form an immiscible system [115], characterised by a large positive heat of mixing ($\Delta H > 20$ kJ/mol atom). The nearly inexistent solubility of one element into the other was attributed to their different valence (4 electrons for Ti and 2 electrons for Mg) [116]. In consequence, no Mg-Ti stable phases can be formed but, as suggested by first principles investigation [117], obtaining Ti-doped MgH_2 opens field to possible thermodynamic destabilization of the hydride. To this purpose, solubility of one element into the other can be extended using non-equilibrium processing techniques such as vapour deposition or mechanochemistry.

In the first part of this section we will see some achievements of metastable Mg-Ti alloys and ternary Mg-Ti-H hydrides obtained either by ball milling or as thin films. The second part will be dedicated to the most recent results obtained on MgH_2-TiH_2 nanocomposites.

a. Metastable Mg-Ti alloys and Mg-Ti-H hydrides

Mg-Ti thin films have attracted wide interest not only for hydrogen storage investigation but also for their peculiar optical properties for solar collector applications or optical switchable devices [118]. While the as-deposited films are metallic and highly reflective, the hydrided state becomes strongly absorbing. For both types of applications, the understanding of structural properties and hydrogenation mechanism of this system is essential.

Metastable $Mg_{1-x}Ti_x$ thin film alloys have been obtained by Notten and co-workers using dc magnetron sputtering deposition method with x = 0 to 0.5 [119–121]. The as-deposited thin films crystallized in a single phase *hcp* structure at ambient temperature [119]. It was demonstrated that the cell parameters of the $Mg_{1-x}Ti_x$ phase closely followed a linear variation with x according to Vegard's law. When these films were hydrogenated at low temperature, a different structure transformation was induced

for Mg-rich alloys ($x < 0.1$) which formed a rutile *bct* MgH_2 phase, while a fluorite *fcc* hydride was formed for samples with $x > 0.13$. This structural dependence was also related to different discharge rates during electrochemical dehydrogenation: the *fcc* structure revealed a much better ability to rapidly desorb hydrogen than samples with *bct* structure [121]. This fact confirmed the importance of the crystal structure on hydrogen diffusion properties. Combining structural, optical and electrical data, Borsa *et al.* suggested the formation of a coherent crystalline structure between TiH_2 and Mg phases, which induced the formation of a cubic MgH_2 structure, isomorphous to TiH_2, upon hydrogenation of samples with $x > 0.13$ [120]. This coherent structure was assumed to be responsible for enhanced hydrogenation properties. Recently, a *fcc* $Mg_{1-x}Ti_xH_y$ phase with reduced enthalpy of hydrogenation has been achieved by hydrogenation of a $Mg_{1-x}Ti_x$ + Mg + Ti nanocomposite synthesized by spark discharge generation [122]. However, if the enthalpy was reduced to -45 $kJ/molH_2$, the entropy value also decreased to -84 $J/K.molH_2$. This destabilization was attributed to the high density of interfaces generating lattice strains, the presence of hydrogen vacancies and the excess free volume due to local deformations.

The achievement of large scale hydrogen storage implies to develop bulk materials. Mechanochemistry is a suitable method to prepare Mg-Ti based materials in larger amount than in thin films. Some researchers started to experiment mechanical alloying of pure Mg and Ti and to study the consequent solubility of Mg into Ti and *vice versa*. Solubility of Mg into Ti has been reported to reach 24 at.% when Ti and Mg were ball milled under Ar atmosphere [123]. Similarly, solid solution of Ti into Mg was observed up to 12.5 at.% [124]. In both cases, lattice expansion or contraction for Ti(Mg) and Mg(Ti) solid solutions respectively, in agreement with their respective atomic radii, has been reported. These rich solid solutions were easily explained by the isomorphous crystal structures of Ti and Mg, but the metastable Mg(Ti) phase dissociated into MgH_2 and TiH_2 upon hydrogenation at 563 K [124]. Ti(Mg) solid solution remained thermally stable up to 913 K [123].

In latter studies, Asano *et al.* demonstrated that the final structure of a ball milled Mg-Ti mixture strongly depended on the milling conditions and the Mg:Ti atomic ratio [125]. Thus, they achieved to synthesize *hcp*, *fcc* and *bcc* $Mg_{1-x}Ti_x$ alloys ($0.2 < x < 0.65$), concluding that the crystal structure of milled products is closely

related to the plastic deformation process, *i.e.* to the amount of energy introduced in the system through the milling process. For example, a $Mg_{80}Ti_{20}$ sample ball milled during 200 h with stainless steel balls and vial resulted in a *hcp* structure while zirconia tools led to a *hcp* and *fcc* mixture. They achieved to hydrogenate at low temperature and high pressure (423 K, 8 MPa) a $Mg_{50}Ti_{50}$ *bcc* alloy obtained by mechanical milling to form a *fcc* $Mg_{0.42}Ti_{0.58}H_{1.77}$ hydride phase with the fluorite structure of TiH_2 [126]. They obtained closely related hydride phases (*fcc* $Mg_{0.40}Ti_{0.6}H_{1.13}$) by ball milling MgH_2 + Ti during long times (200 h) [127]. However, no data on the thermal stability of this ternary hydride was given.

In the same direction, Kalisvaart *et al.* obtained different final structures (*hcp* and *fcc*) by varying the initial state of ball milled materials (powder or ribbon) [128].

According to Rousselot *et al.*, a 0.5Mg-0.5Ti mixture ball milled during 20 hours in a vibratory mill resulted in a metastable *hcp* structure with complete solution of Mg and Ti [129]. This phase was irreversibly transformed in a *fcc* structure after electrochemical hydrogenation. They also showed the possibility to directly synthesize ternary hydride phases by high energy ball milling of MgH_2 + Ti, Mg + TiH_2 or MgH_2 + TiH_2 mixtures. In this case, the final products consisted of two different hydride phases in the *fcc* structure with different cell parameters [130].

Another method to prepare Mg-Ti-H hydride was proposed by Kyoi *et al.* by reacting a mixture of MgH_2 and TiH_2 in a high pressure anvil cell at 8 GPa and 873 K [131]. A Mg_7TiH compound was obtained with a *fcc* structure. This material was able to desorb about 5.5 wt.% H at 605 K, which is about 130 K lower than MgH_2 temperature desorption. However, the Mg_7Ti phase did not exist without the stabilizing presence of hydrogen and no information was given on the reversibility of this material.

In summary, the abundance and diversity of results concerning the Mg-Ti-H system does not allow concluding on a simple behaviour, as the synthesis conditions strongly influence the final products. We have seen that Mg(Ti) and Ti(Mg) solid solutions can be extended to a significant range by means of ball milling during long times (from 10 to 200 h). It is also possible to form ternary hydrides Mg-Ti-H but their thermal stability remains limited. The main limitations associated with the previously described materials are the long times required for synthesis, issues of cold welding between the powder

and the milling tools, and the poor stability of the obtained compounds. In addition, only few data on their hydrogenation properties are available.

b. MgH_2-TiH_2 composites

More recently, a new type of Mg-Ti based materials have been developed using reactive ball milling (RBM). This technique is an efficient way to enhance hydrogenation kinetics, but also to avoid thermal activation treatments and oxidation concerns. Different approaches have been used to obtain MgH_2-TiH_2 composites.

Choi and co-workers prepared composites samples by high-energy-high-pressure mechanical milling of MgH_2 and TiH_2 under a hydrogen pressure of 13.8 MPa [130; 131]. After 12 hours of milling, they obtained a nanocrystalline (15-23 nm) mixture of MgH_2 and TiH_2 phases and no ternary hydride was identified. The thermodesorption of the as-milled $7MgH_2$-TiH_2 resulted in much faster kinetics than pure MgH_2 ball milled in the same conditions, with an onset desorption temperature at 400 K at a heating rate of 5 K/min [132]. They evidenced the catalytic properties of TiH_2 showing a decrease in activation energy for dehydrogenation from 96 kJ/mol for ball milled MgH_2 to 81 kJ/mol for $50MgH_2$-TiH_2 composite. The activation energy reduction was more important as the TiH_2 content increased and reached 68 kJ/mol for the $4MgH_2$-TiH_2 composition [132; 133]. In addition, the desorption properties of the composite sample remained almost stable after 5 absorption/desorption cycles. A decrease in desorption enthalpy was also reported for $10MgH_2$-TiH_2 material (69.2 ± 0.5 kJ/molH_2) and was attributed to the destabilizing effect of TiH_2 incorporated into the MgH_2 lattice [133]. These encouraging results led to further investigations on the hydrogenation properties of $10MgH_2$-TiH_2 nanocomposites [134; 135]. Lu *et al.* showed the very good sorption kinetics and high stability on reversible hydrogen sorption over 80 cycles of a $10MgH_2$-TiH_2 composite [134]. In addition, they achieved to hydrogenate more than 50 % of a desorbed composite at room temperature under 2 MPa of hydrogen pressure [135]. The activation energy corresponding to hydrogen absorption was found to be remarkably low (16.4 kJ/molH_2). Lower enthalpy and entropy values were also reported for hydrogen absorption from MgH_2 phase (69.8 kJ/molH_2 and 129 J/KmolH_2) and kinetic improvements were essentially attributed to the catalytic effect of TiH_2.

Lately, RBM has been employed for *in situ* hydrogenation of elemental Mg-Ti mixtures [136; 137]. Shao *et al.* synthesized a $10MgH_2$-TiH_2 nanocomposite by milling during 20 hours a 10Mg-Ti mixture under 30 MPa of hydrogen pressure [136]. They obtained a nanometric composite powder (5 nm) able to desorb at 100 K lower than commercial MgH_2 during thermodesorption. In contrast with previous results from Lu and Choi, they concluded that no modification of the thermodynamic properties occurred as compared to those of pure MgH_2. These results are in agreement with those obtained by Cuevas *et al.* on MgH_2-TiH_2 nanocomposites synthesized by RBM for several Ti contents [137]. The H-cycling properties of a $7MgH_2$-$3TiH_2$ nanocomposite were compared to those of Ti-free MgH_2 synthesized by the same method. The Ti-containing nanocomposite exhibited outstanding sorption kinetics with absorption/desorption reaction times below 100 seconds at 573 K. Furthermore, such fast kinetics remained stable on more than 30 cycles. In contrast, pure MgH_2 obtained by RBM exhibited sorption reaction times over 60 min and slowed down on H-sorption cycling.

All these results coincide on the outstanding properties of MgH_2-TiH_2 composites for hydrogen storage. However, no clear explanation on the effect of TiH_2 on Mg hydrogenation properties was evidenced.

3.3 Nanoconfined Mg

Nanoconfinement in porous media has recently attracted interest as it opens the possibility to synthesize and stabilize Mg particles as small as 2 nm. At this scale, a significant enthalpy reduction is expected, as calculated by Bérubé *et al.* [30] (see Chapter 1, section 2.2.4). We will see here some examples of Mg-based nanoparticles supported into porous carbon matrix. Mg nanoparticles confined into carbons pores have been successfully prepared by de Jongh *et al.* [138] using melt infiltration techniques. They started from a mixture of MgH_2 powder and carbon that was heated up to the Mg melting temperature. They studied the influence of impurities (oxygen and nitrogen) in the carbon and the pore size distribution on the nanoparticles final size and pore filling. They obtained particles from 2 to 5 nm large with a high ratio of pore filling for the high-purity carbons with the smallest pores. The optimum metal loading

was found to be around 15 wt.% Mg. For higher Mg content, large bulk particles were detected out of the carbon.

This promising technique was later extended to form $Mg_{1-x}Ni_x$ confined nanoparticles [139]. In this case, the carbon was previously impregnated with Ni nanoparticles (5 nm) that were dispersed into the pores using a nickel nitrate solution. In a second time, Mg was infiltrated into the carbon by the same technique than in ref. [138], leading to the formation of an intimate mixture of Mg and Mg_2Ni phases with sizes from 10 to 30 nm (Figure 1.11). This result showed the possibility to confine Mg-based alloys and also that the presence of Ni was facilitating the wetting of the molten Mg in the carbon pores. After hydrogenation at 598 K under 5 MPa of hydrogen pressure of different Mg-Ni compositions, a thermal desorption investigation showed that MgH_2 and Mg_2NiH_4 desorption peaks were easily identified at slightly lower temperatures than bulk materials. In addition, an intermediate broad peak appeared close to the eutectic composition ($Mg_{0.88}Ni_{0.12}$). These hybrid materials exhibited attractive desorption properties although no data were available on their cycling properties.

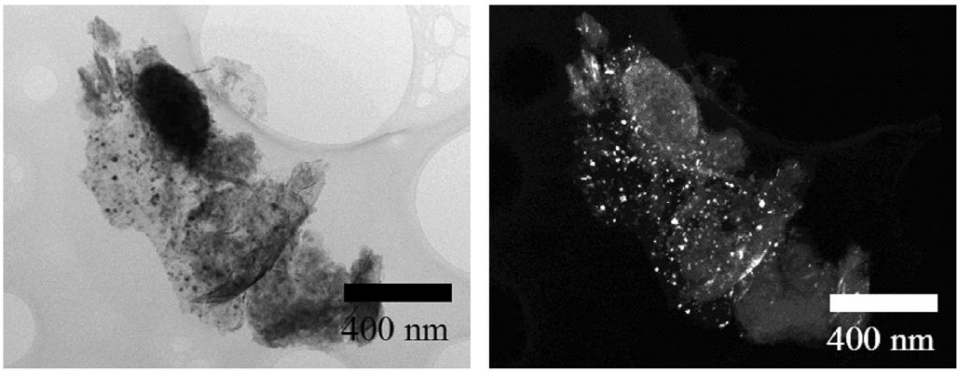

Figure 1.11. Bright field (left) and dark field (right) transmission electron micrographs of $Mg_{0.87}Ni_{0.13}$ nanoparticles supported on a high surface area graphite **[139]**.

Another method to synthesize nanoconfined Mg-based particles has been explored by Zhang *et al.* [140]. MgH_2 particles nanoconfined into a carbon aerogel scaffold were directly obtained by decomposition of an organometallic precursor, dibutylmagnesium ($MgBu_2$), under hydrogen atmosphere at 443 K. The particle size could not be determined but the broad X-ray diffraction peaks suggested the nanometric size of the

MgH_2 phase. Such composite presented faster desorption kinetics than ball-milled MgH_2 and its reversibility was proved over 10 cycles. A similar composite, which consists of 3 nm MgH_2 particles confined into activated carbon fibre, was reported to have significantly reduced enthalpy and entropy of hydrogenation of 63.8 kJ/molH_2 and 117.2 J/KmolH_2 respectively [141]. This thermodynamic change was attributed to the very small particle size (< 3 nm) and to the possible interaction of Mg with the carbon support.

Based on the same preparation technique, other elements have been confined into porous carbons using different organometallic precursors. Hence, Mg-Fe-H and Mg-Ni-H hydrides have been infiltrated into a carbon template by impregnation of $FeCp_2$ and $NiCp_2$ precursors followed by the addition of either $MgEt_2$ or $MgBu_2$ [142]. These results show the possibility to extend nanoconfinement to a wide range of Mg-based alloys.

Nanoconfinement of Mg-based materials into porous matrix is a powerful way to improve hydrogenation kinetics and probably thermodynamics of (de)hydrogenation. However, the gravimetric capacity of these hybrid materials remains too low because the loading of the carbon pores is usually limited to ~15 wt.% of active material. Thus, the hydrogen gravimetric capacity of a carbon loaded with 15 wt.% of MgH_2 would not exceed 1.1 wt.% H. Therefore, the porosity and surface area of the support remain key parameters to reach higher metal loading.

4 Conclusion

After more than fifty years of investigation on Mg-based materials, extensive advances have been achieved on improving their hydrogenation properties. Progresses on kinetics of absorption and desorption are considerable, through the addition of suitable catalysts combined with powder nanostructuration. Concerning thermodynamic improvements, some Mg-based hydrides have been reported to be destabilized as compared to pure MgH_2. However, the operating conditions of the obtained materials remain far from the required working window of 0.1-1 MPa and 273-373 K for feeding fuel cells.

Nevertheless, the use of Mg for solid state hydrogen storage is still relevant. The thermodynamic drawbacks can be minimised, for example, by coupling a metal hydride

tank to a suitable thermal management system which allows recovering the heat released during exothermic absorption and reuse it to initiate endothermic desorption. Indeed, several patents on Mg-based hydrogen tank already exist [143; 144] and some commercial models are by now available for stationary hydrogen storage. Besides, the development of novel Mg-based materials is expected to improve the thermodynamic and kinetic issues related to the Mg-H system. The diversity of potential new compounds, including metastable alloys, is wide and opens many fields for solid state hydrogen storage investigation. Therefore, further comprehension of the mechanisms involved during H-metal reaction is still needed to achieve efficient Mg-based storage media.

In this context, the purpose of the next chapters is on one side to explore novel Mg-based materials by combining different strategies to improve their hydrogenation properties, and on the other side to reach a deep understanding of the mechanisms that lead to enhanced hydrogen storage ability.

References

1. Okamoto H. H-Mg (hydrogen-magnesium). *J. Phase Equilib.* 2001; **22** (**5**): 598–599.
2. Stampfer JF, Holley CE, Suttle JF. The Magnesium-Hydrogen System. *J. Amer. Chem. Soc.* 1960; **82**: 3504–3508.
3. Vajeeston P, Ravindran P, Hauback BC, Fjellvag H, Kjekshus A, Furuseth S, et al. Structural stability and pressure-induced phase transitions in MgH_2. *Phys. Rev. B* 2006; **73** (**22**): 224102.
4. Zhang J, Cuevas F, Zaïdi W, Bonnet J-P, Aymard L, Bobet J-L, et al. Highlighting of a Single Reaction Path during Reactive Ball Milling of Mg and TM by Quantitative H_2 Gas Sorption Analysis to Form Ternary Complex Hydrides (TM = Fe, Co, Ni). *J. Phys. Chem. C* 2011; **115** (**11**): 4971–4979.
5. Doppiu S, Schultz L, Gutfleisch O. In situ pressure and temperature monitoring during the conversion of Mg into MgH_2 by high-pressure reactive ball milling. *J. Alloys Compd.* 2007; **427** (**1-2**): 204–208.
6. Revesz A, Fatay D, Spassov T. Hydriding kinetics of ball-milled nanocrystalline MgH_2 powders. *J. Mater. Res.* 2007; **22** (**11**): 3144–3151.
7. Gennari FC, Castro FJ, Urretavizcaya G. Hydrogen Desorption Behavior from Magnesium Hydrides Synthesized by Reactive Mechanical Alloying. *J. Alloys Compd.* 2001; **321** (**1**): 46–53.
8. Pelletier JF, Huot J, Sutton M, Schulz R, Sandy AR, Lurio LB, et al. Hydrogen Desorption Mechanism in MgH_2-Nb Nanocomposites. *Phys. Rev. B* 2001; **63** (**5**): 052103.
9. Huot J, Liang G, Boily S, Van Neste A, Schulz R. Structural Study and Hydrogen Sorption Kinetics of Ball-Milled Magnesium Hydride. *J. Alloys Compd.* 1999; **293-295**: 495–500.
10. Huot J, Swainson I, Schulz R. Phase transformation in magnesium hydride induced by ball milling. *Ann. Chim.-Sci. Mat.* 2006; **31** (**1**): 135–144.
11. Varin RA, Czujko T, Chiu C, Wronski Z. Particle size effects on the desorption properties of nanostructured magnesium dihydride (MgH_2) synthesized by controlled reactive mechanical milling (CRMM). *J. Alloys Compd.* 2006; **424** (**1-2**): 356–364.

12. Bortz M, Bertheville B, Böttger G, Yvon K. Structure of the high pressure phase γ-MgH_2 by neutron powder diffraction. *J. Alloys Compd.* 1999; **287** (**1-2**): L4–L6.
13. Karen P, Kjekshus A, Huang Q, Karen VL. The crystal structure of magnesium dicarbide. *J. Alloys Compd.* 1999; **282** (**1–2**): 72–75.
14. Ellinger FH, Holley CE, McInteer BB, Pavone D, Potter RM, Staritzky E, et al. The Preparation and Some Properties of Magnesium Hydride. *J. Amer. Chem. Soc.* 1955; **77** (**9**): 2647–2648.
15. Bastide J, Bonnetot B, Letoffe J, Claudy P. Polymorphism of Magnesium Hydride at High-Pressure. *Mater. Res. Bull.* 1980; **15** (**12**): 1779–1787.
16. Cui S, Feng W, Hu H, Feng Z, Wang Y. Structural phase transitions in MgH_2 under high pressure. *Solid State Commun.* 2008; **148** (**9-10**): 403–405.
17. Noritake T, Towata S, Aoki M, Seno Y, Hirose Y, Nishibori E, et al. Charge density measurement in MgH_2 by synchrotron X-ray diffraction. *J. Alloys Compd.* 2003; **356**: 84–86.
18. Gerasimov K, Goldberg E, Ivanov E. On the Kinetic-Model of Magnesium Hydriding. *J. Less-Common Met.* 1987; **131**: 99–107.
19. Bogdanovic B, Bohmhammel K, Christ B, Reiser A, Schlichte K, Vehlen R, et al. Thermodynamic investigation of the magnesium-hydrogen system. *J. Alloys Compd.* 1999; **282** (**1-2**): 84–92.
20. Bohmhammel K, Wolf U, Wolf G, Konigsberger E. Thermodynamic optimization of the system magnesium-hydrogen. *Thermochim. Acta* 1999; **337** (**1-2**): 195–199.
21. Stioui M, Grayevsky A, Resnik A, Shaltiel D, Kaplan N. Macroscopic and Microscopic Kinetics of Hydrogen in Magnesium-Rich Compounds. *J. Less-Common Met.* 1986; **123**: 9–24.
22. Vigeholm B, Jensen K, Larsen B, Pedersen A. Elements of Hydride Formation Mechanisms in Nearly Spherical Magnesium Powder Particles. *J. Less-Common Met.* 1987; **131**: 133–141.
23. Dornheim M. Thermodynamics of Metal Hydrides: Tailoring Reaction Enthalpies of Hydrogen Storage Materials. In: Moreno Pirajn JC (ed). *Thermodynamics - Interaction Studies - Solids, Liquids and Gases*. InTech; 2011.
24. Schlapbach L, Züttel A. Hydrogen-storage materials for mobile applications. *Nature* 2001; **414** (**6861**): 353–358.
25. Reilly JJ, Wiswall RH, Hoffman KC. Metal hydrides as a source of hydrogen fuel. *NASA STI/Recon Technical Report N* 1970; **75**: 20876.
26. Sandrock G. A panoramic overview of hydrogen storage alloys from a gas reaction point of view. *J. Alloys Compd.* 1999; **293–295**: 877–888.
27. Van Mal HH, Buschow KHJ, Miedema AR. Hydrogen absorption in $LaNi_5$ and related compounds: Experimental observations and their explanation. *J. Less-Common Met.* 1974; **35** (**1**): 65–76.
28. Miedema AR, Buschow KHJ, Van Mal HH. Which intermetallic compounds of transition metals form stable hydrides? *J. Less-Common Met.* 1976; **49**: 463–472.
29. Vajo JJ, Mertens F, Ahn CC, Bowman, Fultz B. Altering Hydrogen Storage Properties by Hydride Destabilization through Alloy Formation: LiH and MgH_2 Destabilized with Si. *J. Phys. Chem. B* 2004; **108** (**37**): 13977–13983.
30. Bérubé V, Radtke G, Dresselhaus M, Chen G. Size effects on the hydrogen storage properties of nanostructured metal hydrides: A review. *Int. J. Energ. Res.* 2007; **31** (**6-7**): 637–663.
31. Wagemans RWP, van Lenthe JH, de Jongh PE, van Dillen AJ, de Jong KP. Hydrogen Storage in Magnesium Clusters: Quantum Chemical Study. *J. Am. Chem. Soc.* 2005; **127** (**47**): 16675–16680.
32. Bérubé V, Chen G, Dresselhaus MS. Impact of nanostructuring on the enthalpy of formation of metal hydrides. *Int. J. Hydrogen Energy* 2008; **33** (**15**): 4122–4131.
33. Aguey-Zinsou K-F, Ares-Fernandez J-R. Hydrogen in magnesium: new perspectives toward functional stores. *Energy Environ. Sci.* 2010; **3** (**5**): 526–543.
34. Mintz M, Zeiri Y. Hydriding Kinetics of Powders. *J. Alloys Compd.* 1995; **216** (**2**): 159–175.

35. Barkhordarian G, Klassen T, Bormann R. Kinetic investigation of the effect of milling time on the hydrogen sorption reaction of magnesium catalyzed with different Nb_2O_5 contents. *J. Alloys Compd.* 2006; **407** (**1–2**): 249–255.
36. Fernandez JF, Sanchez C. Rate determining step in the absorption and desorption of hydrogen by magnesium. *J. Alloys Compd.* 2002; **340**: 189–198.
37. Leardini F, Ares JR, Fernández JF, Bodega J, Sánchez C. An investigation on the thermodynamics and kinetics of magnesium hydride decomposition based on isotope effects. *Int. J. Hydrogen Energy* 2011; **36** (**14**): 8351–8357.
38. Rudman P. Hydrogen-Diffusion-Rate-Limited Hydriding and Dehydriding Kinetics. *J. Appl. Phys.* 1979; **50** (**11**): 7195–7199.
39. Zaluski L, Zaluska A, Ström-Olsen JO. Nanocrystalline metal hydrides. *J. Alloys Compd.* 1997; **253–254**: 70–79.
40. Huot J, Ravnsbæk DB, Zhang J, Cuevas F, Latroche M, Jensen TR. Mechanochemical Synthesis of Hydrogen Storage Materials. *Prog. Mater. Sci.* 2013; **58** (**1**): 30–75.
41. Suryanarayana C. Mechanical alloying and milling. *Prog. Mater. Sci.* 2001; **46** (**1–2**): 1–184.
42. Shao H, Xin G, Zheng J, Li X, Akiba E. Nanotechnology in Mg-based materials for hydrogen storage. *Nano Energy* 2012; **1** (**4**): 590–601.
43. Conner WC, Falconer JL. Spillover in Heterogeneous Catalysis. *Chem. Rev.* 1995; **95** (**3**): 759–788.
44. De Jongh PE, Adelhelm P. Nanoparticles and 3D Supported Nanomaterials. In: Hirscher M (ed). *Handbook of Hydrogen Storage*. Wiley-VCH Verlag GmbH & Co. KGaA; 2010. pp. 279–340.
45. De Jongh PE, Adelhelm P. Nanosizing and Nanoconfinement: New Strategies Towards Meeting Hydrogen Storage Goals. *ChemSusChem* 2010; **3** (**12**): 1332–1348.
46. Reilly JJ, Wiswall RH. Reaction of hydrogen with alloys of magnesium and copper. *Inorg. Chem.* 1967; **6** (**12**): 2220–2223.
47. Shao HY, Wang YT, Xu HR, Li XG. Preparation and hydrogen storage properties of nanostructured Mg_2Cu alloy. *J. Solid State Chem.* 2005; **178** (**7**): 2211–2217.
48. Karty A, Grunzweig-Genossar J, Rudman PS. Hydriding and dehydriding kinetics of Mg in a Mg/Mg_2Cu eutectic alloy: Pressure sweep method. *J. Appl. Phys.* 1979; **50** (**11**): 7200–7209.
49. Reilly J, Wiswall R. Reaction of hydrogen with alloys of magnesium and nickel and the formation of Mg_2NiH_4. *Inorg. Chem.* 1968; **7** (**11**): 2254–2256.
50. Zaluska A, Zaluski L, Strom-Olsen JO. Synergy of hydrogen sorption in ball-milled hydrides of Mg and Mg2Ni. *J. Alloy. Compd.* 1999; **289** (**1-2**): 197–206.
51. Huot J, Akiba E, Takada T. Mechanical alloying of Mg-Ni compounds under hydrogen and inert atmosphere. *J. Alloys Compd.* 1995; **231** (**1-2**): 815–819.
52. Selvam P, Viswanathan B, Swamy C, Srinivasan V. Studies on the Thermal-Characteristics of hydrides of Mg, Mg_2Ni, Mg_2Cu and $Mg_2Ni_{1-x}M_x$ (M = Fe, Co, Cu or Zn - $0<x<1$) alloys. *Int. J. Hydrogen Energy* 1988; **13** (**2**): 87–94.
53. Hsu F-K, Hsu C-W, Chang J-K, Lin C-K, Lee S-L, Jiang C-E. Structure and hydrogen storage properties of $Mg_2Cu_{1-x}Ni_x$ (x = 0–1) alloys. *Int. J. Hydrogen Energy* 2010; **35** (**24**): 13247–13254.
54. Darnaudery J, Darriet B, Pezat M. The $Mg_2Ni_{0.75}M_{0.25}$ Alloys (M=3d Element) - Their Application to Hydrogen Storage. *Int. J. Hydrogen Energy* 1983; **8** (**9**): 705–708.
55. Spassov T, Koster U. Thermal stability and hydriding properties of nanocrystalline melt-spun $Mg_{63}Ni_{30}Y_7$ alloy. *J. Alloys Compd.* 1998; **279** (**2**): 279–286.
56. Darnaudery JP, Pezat M, Darriet B. Influence de la substitution du cuivre au nickel dans Mg_2Ni sur le stockage de l'hydrogène. *J. Less-Common Met.* 1983; **92** (**2**): 199–205.
57. Soubeyroux J, Fruchart D, Mikou A, Pezat M, Darriet B, Hagenmuller P. Structural Study on the Mg_2Ni-H_2 System .2. the High-Temperature Variety. *Mater. Res. Bull.* 1984; **19** (**8**): 969–978.
58. Noreus D, Werner P. Structural Studies of Monoclinic Mg_2NiD_4. *J. Less-Common Met.* 1984; **97**: 215–222.

59. Zolliker P, Yvon K, Baerlocher C. Low-Temperature Structure of Mg_2NiH_4 - Evidence for Microtwinning. *J. Less-Common Met.* 1986; **115** (**1**): 65–78.
60. Noréus D, Werner P-E, Sieler J, Steimecke G, Hoyer E. Structural Studies of Hexagonal Mg_2NiH_x. *Acta Chem. Scand.* 1982; **36a**: 847–851.
61. Selvam P, Viswanathan B, Swamy CS, Srinivasan V. Mg_2NiH: a new hydride phase in the Mg_2Ni-H_2 system. *Int. J. Hydrogen Energy* 1988; **13** (**12**): 749–759.
62. Selvam P, Yvon K. Synthesis of Mg_2FeH_6, Mg_2CoH_5 and Mg_2NiH_4 by high-pressure sintering of the elements. *Int. J. Hydrogen Energy* 1991; **16** (**9**): 615–617.
63. Huot J, Hayakawa H, Akiba E. Preparation of the hydrides Mg_2FeH_6 and Mg_2CoH_5 by mechanical alloying followed by sintering. *J. Alloys Compd.* 1997; **248** (**1–2**): 164–167.
64. Gennari FC, Castro FJ, Andrade Gamboa JJ. Synthesis of Mg_2FeH_6 by reactive mechanical alloying: formation and decomposition properties. *J. Alloys Compd.* 2002; **339** (**1–2**): 261–267.
65. Bogdanović B, Reiser A, Schlichte K, Spliethoff B, Tesche B. Thermodynamics and dynamics of the Mg–Fe–H system and its potential for thermochemical thermal energy storage. *J. Alloys Compd.* 2002; **345** (**1–2**): 77–89.
66. Reiser A, Bogdanović B, Schlichte K. The application of Mg-based metal-hydrides as heat energy storage systems. *Int. J. Energ. Res.* 2000; **25** (**5**): 425–430.
67. Fernández IG, Meyer GO, Gennari FC. Reversible hydrogen storage in Mg_2CoH_5 prepared by a combined milling-sintering procedure. *J. Alloys Compd.* 2007; **446–447**: 106–109.
68. Chen J, Takeshita HT, Chartouni D, Kuriyama N, Sakai T. Synthesis and characterization of nanocrystalline Mg_2CoH_5 obtained by mechanical alloying. *J. Mater. Sci.* 2001; **36** (**24**): 5829–5834.
69. Adams BD, Chen A. The role of palladium in a hydrogen economy. *Mater. Today* 2011; **14** (**6**): 282–289.
70. Okamoto H. Mg-Pd (Magnesium-Palladium). *J. Phase Equilib. Diff.* 2010; **31** (**4**): 407–408.
71. Samson S. Complex Cubic A_6B Compounds. II. The crystal structure of Mg_6Pd. *Acta Cryst.* 1972; **B28**: 936.
72. Makongo JPA, Prots Y, Burkhardt U, Niewa R, Kudla C, Kreiner G. A case study of complex metallic alloy phases: structure and disorder phenomena of Mg-Pd compounds. *Philos. Mag.* 2006; **86**: 427–433.
73. Huot J, Yonkeu A, Dufour J. Rietveld analysis of neutron powder diffraction of Mg_6Pd alloy at various hydriding stages. *J. Alloys Compd.* 2008; **475**: 168–172.
74. Dufour J, Huot J. Study of Mg_6Pd alloy synthesized by cold rolling. *J. Alloys Compd.* 2007; **446-447**: 147–151.
75. Callini E, Pasquini L, Rude LH, Nielsen TK, Jensen TR, Bonetti E. Hydrogen storage and phase transformations in Mg–Pd nanoparticles. *J. Appl. Phys.* 2010; **108** (**7**): 073513.
76. Zlotea C, Andersson Y. Microstructural modifications induced by hydrogen absorption in Mg_5Ga_2 and Mg_6Pd. *Acta Mater.* 2006; **54**: 5559–5564.
77. Kume Y, Weiss A. On the interaction of hydrogen with the intermetallic phase Mg_6Pd. *J. Less-Common Met.* 1987; **136**: 51–54.
78. Roquefere J-G, Lang J, Yonkeu A, Dufour J, Huot J. Effect of iron on the hydriding properties of the Mg_6Pd hydrogen storage system. *Int. J. Hydrogen Energy* 2011; **36** (**3**): 2165–2169.
79. Ghosh G, Kantner C, Olson GB. Thermodynamic modeling of the Pd-X (X=Ag, Co, Fe, Ni) systems. *J. Phase Equilib.* 1999; **20** (**3**): 295–308.
80. Kempen ATW, Nitsche H, Sommer F, Mittemeijer EJ. Crystallization kinetics of amorphous magnesium-rich magnesium-copper and magnesium-nickel alloys. *Metall. Mater. Trans. A* 2002; **33** (**4**): 1041–1050.
81. Teresiak A, Uhlemann M, Thomas J, Gebert A. The metastable Mg_6Ni phase - Thermal behaviour, crystal structure and hydrogen reactivity of the rapidly quenched alloy. *J. Alloys Compd.* 2008; **475** (**1-2**): 191–197.

82. Kolesnichenko V, Karonik V, Ivanishchev A. Phase-Diagram of the Mg-Ni-Pd System in the Magnesium-Rich Range. *Russ. Metall.* 1981; (**4**): 207–210.
83. Gupta KP. The Mg-Ni-Pd (Magnesium-Nickel-Palladium) system. *J. Phase Equilib. Diff.* 2004; **25** (**2**): 191–194.
84. Cuevas F, Fernandez JF, Ares JR, Leardini F, Sanchez C. Homogeneity range and crystal structure of Ni substituted Mg_6(Pd,Ni) complex intermetallic compounds. *J. Phys. Chem. Solids* 2010; **71** (**9**): 1259–1263.
85. Fernandez JF, Cuevas F, Leardini F, Bodega J, Ares JR, G. Garces, et al. A new pseudo-binary $Mg_6Pd_{0.5}Ni_{0.5}$ intermetallic compound stabilised by Pd for hydrogen storage. *J. Alloys Compd.* 2010; **495**: 233–241.
86. Cuevas F, Fernandez JF, Ares JR, Leardini F, Latroche M. Crystal structure and hydrogenation properties of pseudo-binary $Mg_6Pd_{0.5}Ni_{0.5}$ complex metallic alloy. *J. Solid State Chem.* 2009; **182**: 2890–2896.
87. Fernandez JF, Widom M, Cuevas F, Ares JR, Bodega J, Leardini F, et al. First-principles phase stability calculations and estimation of finite temperature effects on pseudo-binary $Mg_6(Pd_xNi_{1-x})$ compounds. *Intermetallics* 2011; **19** (**4**): 502–510.
88. Fernandez JF, Ares JR, Cuevas F, Bodega J, Leardini F, Sanchez C. A thermodynamic study of the hydrogeneation of the pseudo-binary $Mg_6Pd_{0.5}Ni_{0.5}$ intermetallic compound. *Intermetallics* 2010; **18**: 233–241.
89. Lass EA. Reversible hydrogen-storage at reduced temperatures in the intermetallic compound Mg_6(Ni,Pd). *Int. J. Hydrogen Energy* 2011; **36** (**22**): 14496–14502.
90. Zaluska A, Zaluski L, Ström–Olsen JO. Nanocrystalline Magnesium for Hydrogen Storage. *J. Alloys Compd.* 1999; **288** (**1–2**): 217–225.
91. Von Zeppelin F, Reule H, Hirscher M. Hydrogen desorption kinetics of nanostructured MgH_2 composite materials. *J. Alloys Compd.* 2002; **330–332**: 723–726.
92. Liang G, Huot J, Boily S, Van Neste A, Schulz R. Catalytic effect of transition metals on hydrogen sorption in nanocrystalline ball milled MgH_2-TM (TM=Ti, V, Mn, Fe and Ni) systems. *J. Alloys Compd.* 1999; **292** (**1-2**): 247–252.
93. Liang G, Huot J, Boily S, Van Neste A, Schulz R. Hydrogen Storage Properties of the Mechanically Milled MgH_2-V Nanocomposite. *J. Alloys Compd.* 1999; **291** (**1-2**): 295–299.
94. Huot J, Pelletier JF, Liang G, Sutton M, Schulz R. Structure of nanocomposite metal hydrides. *J. Alloys Compd.* 2002; **330–332**: 727–731.
95. Rivoirard S, de Rango P, Fruchart D, Charbonnier J, Vempaire D. Catalytic Effect of Additives on the Hydrogen Absorption Properties of Nano-crystalline MgH_2(X) composites. *J. Alloys Compd.* 2003; **356–357**: 622–625.
96. Charbonnier J, de Rango P, Fruchart D, Miraglia S, Pontonnier L, Rivoirard S, et al. Hydrogenation of Transition Element Additives (Ti, V) during Ball Milling of Magnesium Hydride. *J. Alloys Compd.* 2004; **383** (**1-2**): 205–208.
97. Hanada N, Ichikawa T, Fujii H. Catalytic effect of nanoparticle 3d-transition metals on hydrogen storage properties in magnesium hydride MgH_2 prepared by mechanical milling. *J. Phys. Chem. B* 2005; **109** (**15**): 7188–7194.
98. Liang G, Huot J, Boily S, Schulz R. Hydrogen desorption kinetics of a mechanically milled MgH_2-5at.%V nanocomposite. *J. Alloys Compd.* 2000; **305** (**1-2**): 239–245.
99. Huot J, Pelletier JF, Lurio LB, Sutton M, Schulz R. Investigation of dehydrogenation mechanism of MgH_2-Nb nanocomposites. *J. Alloys Compd.* 2003; **348** (**1-2**): 319–324.
100. Schimmel HG, Huot J, Chapon LC, Tichelaar FD, Mulder FM. Hydrogen Cycling of Niobium and Vanadium Catalyzed Nanostructured Magnesium. *J. Amer. Chem. Soc.* 2005; **127** (**41**): 14348–14354.
101. Dehouche Z, Djaozandry R, Huot J, Boily S, Goyette J, Bose T., et al. Influence of cycling on the thermodynamic and structure properties of nanocrystalline magnesium based hydride. *J. Alloys Compd.* 2000; **305** (**1–2**): 264–271.

102. De Rango P, Chaise A, Charbonnier J, Fruchart D, Jehan M, Marty P, et al. Nanostructured magnesium hydride for pilot tank development. *J. Alloys Compd.* 2007; **446**: 52–57.
103. Charbonnier J, de Rango P, Fruchart D, Miraglia S, Skryabina N, Huot J, et al. Structural Analysis of Activated Mg(Nb)H_2. *J. Alloys Compd.* 2005; **404–406**: 541–544.
104. Tan X, Wang L, Holt CMB, Zahiri B, Eikerling MH, Mitlin D. Body centered cubic magnesium niobium hydride with facile room temperature absorption and four weight percent reversible capacity. *Phys. Chem. Chem. Phys.* 2012; **14** (**31**): 10904–10909.
105. Bellemare J, Huot J. Hydrogen storage properties of cold rolled magnesium hydrides with oxides catalysts. *J. Alloys Compd.* 2012; **512** (**1**): 33–38.
106. Croston DL, Grant DM, Walker GS. The catalytic effect of titanium oxide based additives on the dehydrogenation and hydrogenation of milled MgH_2. *J. Alloys Compd.* 2010; **492** (**1–2**): 251–258.
107. Borgschulte A, Bösenberg U, Barkhordarian G, Dornheim M, Bormann R. Enhanced Hydrogen Sorption Kinetics of Magnesium by Destabilized $MgH_{2-\delta}$. *Catal. Today* 2007; **120** (**3–4**): 262–269.
108. Oelerich W, Klassen T, Bormann R. Metal Oxides as Catalysts for Improved Hydrogen Sorption in Nanocrystalline Mg-based Materials. *J. Alloys Compd.* 2001; **315** (**1-2**): 237–242.
109. Barkhordarian G, Klassen T, Bormann R. Fast hydrogen sorption kinetics of nanocrystalline Mg using Nb_2O_5 as catalyst. *Scripta Mater.* 2003; **49** (**3**): 213–217.
110. Barkhordarian G, Klassen T, Bormann R. Effect of Nb_2O_5 content on hydrogen reaction kinetics of Mg. *J. Alloys Compd.* 2004; **364** (**1–2**): 242–246.
111. Barkhordarian G, Klassen T, Bormann R. Catalytic mechanism of transition-metal compounds on Mg hydrogen sorption reaction. *J. Phys. Chem. B* 2006; **110** (**22**): 11020–11024.
112. Corey RL, Ivancic TM, Shane DT, Carl EA, Bowman RC, Bellosta von Colbe JM, et al. Hydrogen Motion in Magnesium Hydride by NMR. *J. Phys. Chem. C* 2008; **112** (**49**): 19784–19790.
113. Bhosle V, Baburaj EG, Miranova M, Salama K. Dehydrogenation of TiH_2. *Mat. Sci. Eng. A-Struct.* 2003; **356** (**1–2**): 190–199.
114. Kaess U, Majer G, Stoll M, Peterson DT, Barnes RG. Hydrogen and deuterium diffusion in titanium dihydrides/dideuterides. *J. Alloys Compd.* 1997; **259** (**1–2**): 74–82.
115. Murray J. The Mg−Ti (Magnesium-Titanium) System. *J. Phase Equilib.* 1986; **7** (**3**): 245–248.
116. Suryanarayana C, Froes FH. Nanocrystalline titanium-magnesium alloys through mechanical alloying. *J. Mater. Res.* 1990; **5** (**09**): 1880–1886.
117. Song Y, Guo ZX, Yang R. Influence of Titanium on the Hydrogen Storage Characteristics of Magnesium Hydride: a First Principles Investigation. *Mat. Sci. Eng. A-Struct.* 2004; **365** (**1–2**): 73–79.
118. Baldi A, Borsa DM, Schreuders H, Rector JH, Atmakidis T, Bakker M, et al. Mg–Ti–H thin films as switchable solar absorbers. *Int. J. Hydrogen Energy* 2008; **33** (**12**): 3188–3192.
119. Vermeulen P, Graat PCJ, Wondergem HJ, Notten PHL. Crystal Structures of Mg_yTi_{100-y} Thin Film Alloys in the As-deposited and Hydrogenated State. *Int. J. Hydrogen Energy* 2008; **33** (**20**): 5646–5650.
120. Borsa DM, Gremaud R, Baldi A, Schreuders H, Rector JH, Kooi B, et al. Structural, Optical, and Electrical Properties of $Mg_yTi_{1-y}H_x$ Thin Films. *Phys. Rev. B* 2007; **75** (**20**): 205408.
121. Vermeulen P, Niessen RAH, Notten PHL. Hydrogen Storage in Metastable Mg_yTi_{1-y} Thin Films. *Electrochem. Commun.* 2006; **8**: 27–32.
122. Anastasopol A, Pfeiffer TV, Middelkoop J, Lafont U, Canales-Perez RJ, Schmidt-Ott A, et al. Reduced Enthalpy of Metal Hydride Formation for Mg–Ti Nanocomposites Produced by Spark Discharge Generation. *J. Am. Chem. Soc.* 2013; **135** (**21**): 7891–7900.
123. Sun F, Froes FH (Sam). Synthesis and Characterization of Mechanical-Alloyed Ti-xMg Alloys. *J. Alloys Compd.* 2002; **340**: 220–225.
124. Liang G, Schulz R. Synthesis of Mg-Ti Alloy by Mechanical Alloying. *J. Mater. Sci.* 2003; **38** (**6**): 1179–1184.

125. Asano K, Enoki H, Akiba E. Synthesis of HCP, FCC and BCC Structure Alloys in the Mg-Ti Binary System by Means of Ball Milling. *J. Alloys Compd.* 2009; **480** (**2**): 558–563.
126. Asano K, Enoki H, Akiba E. Synthesis of Mg-Ti FCC Hydrides from Mg-Ti BCC Alloys. *J. Alloys Compd.* 2009; **478** (**1-2**): 117–120.
127. Asano K, Akiba E. Direct Synthesis of Mg-Ti-H FCC Hydrides from MgH_2 and Ti by Means of Ball Milling. *J. Alloys Compd.* 2009; **481** (**1-2**): L8–L11.
128. Kalisvaart WP, Notten PHL. Mechanical alloying and electrochemical hydrogen storage of Mg-based systems. *J. Mater. Res.* 2008; **23** (**8**): 2179–2187.
129. Rousselot S, Bichat MP, Guay D, Roue L. Structure and electrochemical behaviour of metastable $Mg_{50}Ti_{50}$ alloy prepared by ball milling. *J. Power Sources* 2008; **175** (**1**): 621–624.
130. Rousselot S, Guay D, Roue L. Synthesis of fcc Mg-Ti-H alloys by high energy ball milling: Structure and electrochemical hydrogen storage properties. *J. Power Sources* 2010; **195** (**13**): 4370–4374.
131. Kyoi D, Sato T, Rönnebro E, Kitamura N, Ueda A, Ito M, et al. A new ternary magnesium-titanium hydride Mg_7TiH_x with hydrogen desorption properties better than both binary magnesium and titanium hydrides. *J. Alloys Compd.* 2003; **372**: 213–217.
132. Choi YJ, Lu J, Sohn HY, Fang ZZ. Hydrogen storage properties of the Mg-Ti-H system prepared by high-energy-high-pressure reactive milling. *J. Power Sources* 2008; **180**: 491–497.
133. Choi YJ, Lu J, Sohn HY, Fang ZZG, Ronnebro E. Effect of Milling Parameters on the Dehydrogenation Properties of the Mg-Ti-H System. *J. Phys. Chem. C* 2009; **113** (**44**): 19344–19350.
134. Lu J, Choi YJ, Fang ZZ, Sohn HY, Ronnebro E. Hydrogen Storage Properties of Nanosized MgH_2-0.1TiH_2 Prepared by Ultrahigh-Energy-High-Pressure Milling. *J. Amer. Chem. Soc.* 2009; **131** (**43**): 15843–15852.
135. Lu J, Choi YJ, Fang ZZ, Sohn HY, Roennebro E. Hydrogenation of Nanocrystalline Mg at Room Temperature in the Presence of TiH_2. *J. Am. Chem. Soc.* 2010; **132** (**19**): 6616–6617.
136. Shao H, Felderhoff M, Schüth F. Hydrogen Storage Properties of Nanostructured MgH_2/TiH_2 Composite Prepared by Ball Milling under High Hydrogen Pressure. *Int. J. Hydrogen Energy* 2011; **36** (**17**): 10828–10833.
137. Cuevas F, Korablov D, Latroche M. Synthesis, Structural and Hydrogenation Properties of Mg-rich MgH_2-TiH_2 Nanocomposites Prepared by Reactive Ball Milling under Hydrogen Gas. *Phys. Chem. Chem. Phys.* 2012; **14** (**3**): 1200.
138. De Jongh PE, Wagemans RWP, Eggenhuisen TM, Dauvillier BS, Radstake PB, Meeldijk JD, et al. The Preparation of Carbon-Supported Magnesium Nanoparticles using Melt Infiltration. *Chem. Mater.* 2007; **19** (**24**): 6052–6057.
139. Bogerd R, Adelhelm P, Meeldijk JH, de Jong KP, de Jongh PE. The structural characterization and H_2 sorption properties of carbon-supported $Mg_{1-x}Ni_x$ nanocrystallites. *Nanotechnology* 2009; **20** (**20**): 204019.
140. Zhang S, Gross AF, Van Atta SL, Lopez M, Liu P, Ahn CC, et al. The synthesis and hydrogen storage properties of a MgH_2 incorporated carbon aerogel scaffold. *Nanotechnology* 2009; **20** (**20**): 204027.
141. Zhao-Karger Z, Hu J, Roth A, Wang D, Kübel C, Lohstroh W, et al. Altered thermodynamic and kinetic properties of MgH_2 infiltrated in microporous scaffold. *Chem. Commun.* 2010; **46** (**44**): 8353–8355.
142. Zlotea C, Chevalier-Cesar C, Leonel E, Leroy E, Cuevas F, Dibandjo P, et al. Synthesis of small metallic Mg-based nanoparticles confined in porous carbon materials for hydrogen sorption. *Faraday Discuss.* 2011; **151**: 117–131.
143. Bienvenu G, Chaise A, De Rango P, Fruchart D, Garrier S, Jehan M, et al. Réservoir adiabatique d'hydrure métallique. 2012;
144. Jehan M, Peyreaud L, De Rango P, Bienvenu G, Dibandjo P. Réservoir de stockage et de destockage d'hydrogène et/ou de chaleur. 2011;

Chapter 2.

Experimental techniques

OUTLINE

In this chapter we present the technical and theoretical tools that have been used throughout this Thesis. The different methods used for materials synthesis are first described. Then, we will present the techniques employed to characterize their morphology, chemical composition and structural properties. Finally, we detail the procedures used to determine the hydrogenation properties of each investigated material.

1 Material preparation

Different methods of synthesis are employed in this Thesis, giving rise to diverse natures of materials with their own specificities.

1.1 Alloy synthesis

The preparation of $Mg_6Pd_{1-x}TM_x$ bulk alloys was performed by melting of the constituent elements. The low melting point of Mg as compared to the transition metals used in this thesis has to be considered. Indeed, Mg melts at 923 K while Pd and Ni melting point is over 1700 K and Cu and Ag melt at temperatures over 1200 K. In consequence, one has to adopt specific methods in order to avoid strong Mg evaporation during heating. In this thesis, two techniques have been used depending on the amount of alloy to be prepared and the initial form of the products (see Table 2.1).

Table 2.1. Commercial products used for alloy syntheses

Element	Provider	Purity	Form
Mg	Alfa Aesar	> 99.8 %	chips
Pd	Sempsa	> 99.9 %	foil
Ni	Cerac	> 99.9 %	foil
Ag	-	> 99.9 %	powder
Cu	CENIM	> 99.9 %	foil

1.1.1 Induction melting

Induction melting was used to synthesize relatively large amounts of alloy (50 - 100 g), owing to the dimensions of the furnace (Figure 2.1). The raw or pre-alloyed elements were mechanically cleaned of eventual oxide layer and weighted to obtain the desired nominal composition. To offset the Mg loss during melting, about

1 at.% excess of Mg was added to the initial composition. All reactants were then introduced into a graphite crucible covered with a thin layer of boron nitride to avoid possible carbon contamination. The chamber of the furnace was flushed three times with Ar and finally kept with 75 kPa of Ar pressure to limit Mg evaporation during melting. Melting was achieved by increasing the alternative current passing through the induction coil around the crucible, which generates a strong magnetic field into the coil axis and heats up the metallic constituents. After 10 minutes at the molten state, the metal was cast in a stainless steel mould where it cooled down rapidly, still under Ar atmosphere. This last step provides to the alloy a good homogenisation of all the molten phases. In addition, a two or three days annealing was performed under secondary vacuum to reach a better thermodynamic equilibrium.

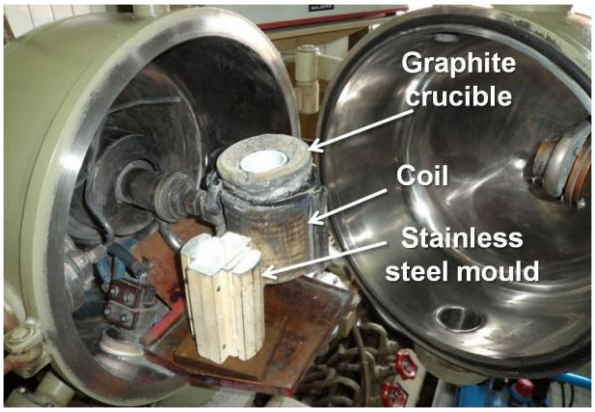

Figure 2.1. View of the open chamber of the induction furnace.

1.1.2 Sealed crucibles

Another technique was used to synthesize smaller amounts of Mg-based alloys (1 - 5 g). In this case, initial compounds were introduced into a steel crucible that was then hermetically sealed under argon and placed in a high temperature electric furnace (Figure 2.2). It was then heated up over the melting temperature of the alloy (typically at 1000 K) during 3 hours and cooled down to the annealing temperature where it was maintained for two days. The sealed crucible allows for melting Mg-based alloys, prevents sample oxidation and avoids Mg loss by evaporation.

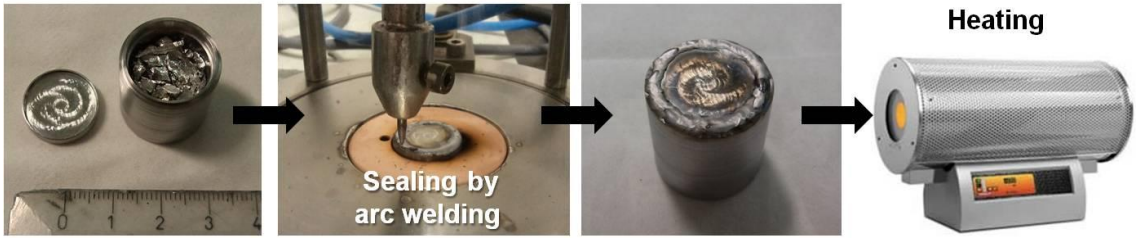

Figure 2.2. Procedure for the alloy preparation in sealed steel crucible.

1.2 Reactive ball milling

The reactive ball milling (RBM) technique was used for the synthesis of MgH_2-TiH_2 nanocomposites. Indeed, Mg and Ti elements are immiscible and alloying these two elements by melting techniques is impossible. RBM allows for fast *in situ* hydrogenation of Mg-Ti mixtures at room temperature. The mechanical treatment induces highly energetic collisions which favour the formation of fresh surfaces directly available for hydrogen absorption as well as homogeneous mixing of the solid constituents at the nanoscale.

RBM experiments under hydrogen or deuterium gas have been performed in a high-pressure milling vial commercialized by Evicomagnetics (Figure 2.3 left). This vial is equipped with gas pressure and temperature sensors which allows for *in situ* monitoring of hydrogen (deuterium) uptake as a function of milling time. An experimental method which takes into account the real gas behaviour of hydrogen (deuterium) and the calibration of the gas temperature was developed to reach a typical accuracy in the determination of H-content of 95 % [1].

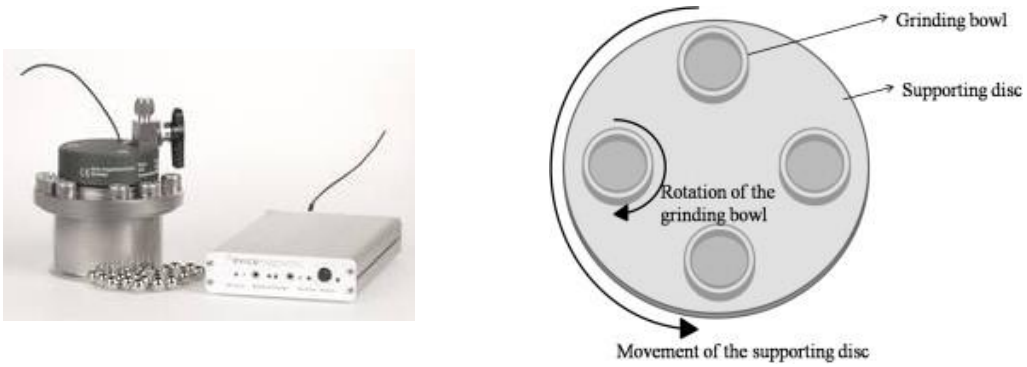

Figure 2.3. The Evicomagnetics milling vial and the telemetric receptor (left). Schematic representation of the principle of a planetary mill (right).

Mg (Alfa Aesar, < 800 μm, 99.8 % purity metal basis) and Ti (Aldrich, < 150 μm, 99.7 % purity metal basis) powders together with the 12 mm stainless steel balls were loaded in the milling vial inside the glove box. The ball to powder mass ratio was 37.5 for all Mg-Ti powder mixtures and 60 for pure Mg powder and the typical sample mass was 8 g. The vial was then connected to a manometric hydrogenation device to calibrate the empty volume inside the vial (typically 170 mL) and introduce the initial gas pressure (typically 6-8 MPa). The milling was carried out in a Fritsch Pulverisette 4 planetary mill at respective disk and vial rotation speeds of 400 and 800 rpm as illustrated in Figure 2.3 on the right. Milling was performed in two milling cycles of 120 min with 120 min pause in between for cooling of the milling tools. Hydrogenation was completed during the first cycle and the second cycle was used for calibration purpose. Finally, the remaining hydrogen (deuterium) was evacuated and the powder unloaded inside the glove box.

1.3 Intermetallic nanoconfinement in porous carbon

The preparation of nanoconfined Mg-based alloys in an activated carbon requires a two-step specific procedure that has been recently developed [2; 3]. Figure 2.4 summarizes the experimental procedure followed to obtain nanoconfined Mg_6Pd particles. The first step consists in the impregnation of the porous carbon (HSAG500 from TIMCAL) by a home-made precursor Pd-containing solution (H_2PdCl_4) followed by the reduction of $[PdCl_4]^{2-}$ ions in Ar/H_2 flow (0.5 L/min) at 573 K to obtain Pd@C hybrids. The sample was then degassed under secondary vacuum for several hours and protected from air contact for all further sample handling.

The second step consists in melt-infiltration of MgH_2 in this hybrid to get Mg_6Pd@C intermetallic/carbon materials. Mg mass was calculated according to the stoichiometry of the required alloy. In the glove box, the MgH_2 (Alfa Aesar 98 %) was mixed with the Pd@C hybrid and loaded in a graphite crucible which was then put in a non-hermetic stainless steel holder and introduced into a quartz tube. The mixture was then placed in a furnace under an Ar flow and heated up to 930 K to decompose MgH_2 and to reach infiltration of the molten Mg into the pores. After 40 minutes of dwelling, the sample was cooled down slowly and extracted inside the glove box.

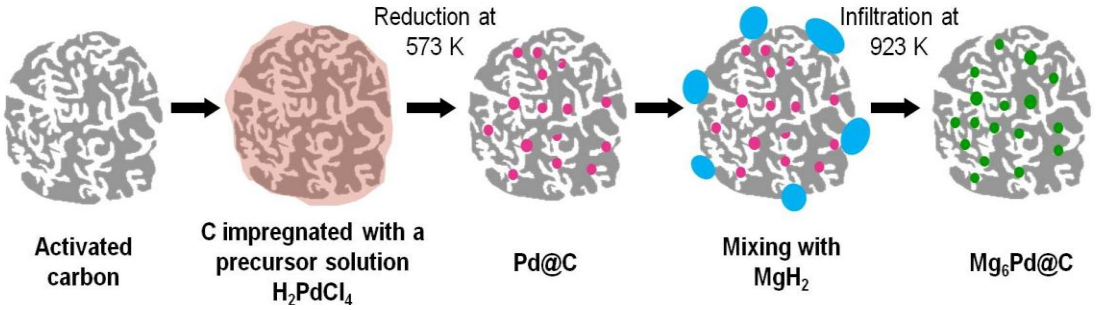

Figure 2.4. The precursor impregnation followed by the melt-infiltration process. Pink circles stand for the Pd precursor particles, MgH_2 is represented in blue and green colour symbolises the alloy nanoparticles.

Finally, the hybrid material was hydrogenated overnight in a high pressure autoclave (Parr) at 573 K under a hydrogen pressure of 5 MPa.

2 Chemical and structural characterization

2.1 Scanning electron microscopy

Scanning electron microscopy (SEM) coupled with energy dispersive X-ray analysis (EDX) has been used to characterize the morphology and the chemical composition of the alloys.

2.1.1 Basics of SEM

SEM is a powerful technique of observation that uses a high energy electron beam (from 0.3 to 30 keV) to scan the surface of a sample and produce an image through the different types of emitted electrons [4]. The different types of interactions of the electrons with the atoms of a sample are represented in Figure 2.5. The most common imaging technique is the one produced by secondary electrons (SE). These electrons result from inelastic interactions between the sample atoms and the primary electrons from the beam. Owing to their low energy, the SE are emitted within a few nanometers from the sample surface. Therefore, this technique is mainly used to observe the morphology and topography of a surface.

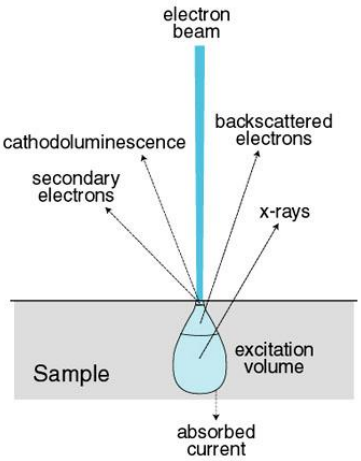

Figure 2.5. The different interactions of an incident electron beam with a sample [5].

Backscattered electrons (BSE) are emitted as a result of elastic interactions between the incident electron beam and the sample atoms. Larger atoms, because of their larger cross-sectional area, have a higher probability to generate a collision with primary electrons. In consequence, the number of emitted BSE is proportional to the mean atomic number Z of the sample. Thus, BSE images are an excellent tool to generate Z-contrast maps of sample compositions, where phases containing heavy elements appear in bright grey and dark areas correspond to light elements. This method probes a sample thickness of about 1 μm.

EDX analysis, a complementary tool to SEM, uses the X-ray emission characteristic of each element to determine the chemical composition of a sample. The inelastic collisions of the incident beam with electrons from the inner layer of atoms in the specimen generate electron excitation. As the excited electrons return to lower energy states, photons are emitted with fixed wavelength, related to the difference in energy levels of electrons in different shells for a given element. The emitted X-rays are detected by an energy dispersive spectrometer (EDS). The technique allows determining the relative atomic composition of the samples with a typical error of 1 at.% and spatial resolution about 1 μm^3.

2.1.2 Sample preparation and instrument

The use of BSE images and EDX analysis requires working with flat and polished surface. To this purpose, the samples were embedded in epoxy resin and polished with

diamond paste under ethanol down to 1/4 μm when possible. In some cases, the sample was too sensitive to oxidation, due to the large amount of Mg, and polishing had to be stopped at 3 μm. In addition, the analysed specimen has to be conductive, which is not the case of epoxy resin. Thus, the polished sample had to be coated with a 10 nm layer of Au by evaporation under vacuum. The instruments used during this Thesis were a Hitachi S-3000N 0K coupled to an EDS Oxford Instruments, INCA x-sight.

2.2 Electron probe micro analysis

2.2.1 Basics of EPMA

Electron probe micro analysis (EPMA) is a quantitative and non-destructive technique [6] that provides accurate chemical composition of samples and phases which elements atomic mass (Z) is higher than 5. This technology works according to the same principle than SEM-EDX, but allows for better accuracy because it is equipped with a wavelength dispersive spectrometer (WDS) instead of EDS. Unlike EDS which produces a broad spectrum of energies simultaneously detected, WDS isolates the X-rays of interest by means of a single crystal. The constructive interference generated at a given wavelength according to the Bragg's law allows detecting and counting a single wavelength at a time. Detection of other wavelengths corresponding to other elements is obtained by changing the position of the crystal. This method avoids overlapping issues that occur when emission lines from two different elements share the same energy. Quantitative analysis of all elemental constituents is achieved after comparison of the measured signal intensity for each element to that of a standard sample. Typical error in chemical analysis is ~0.1 at.% and the spatial resolution is ~1 μm^3.

2.2.2 Sample preparation and instrument

As for SEM-EDX, the sample surface needs to be flat and polished to obtain good quality analyses. Small pieces of the alloy ingots were embedded in a low melting point Wood alloy and polished in the same way than the epoxy resin used for SEM. In this study, the samples were analyzed in a Cameca SX-100 instrument which main features are represented in Figure 2.6.

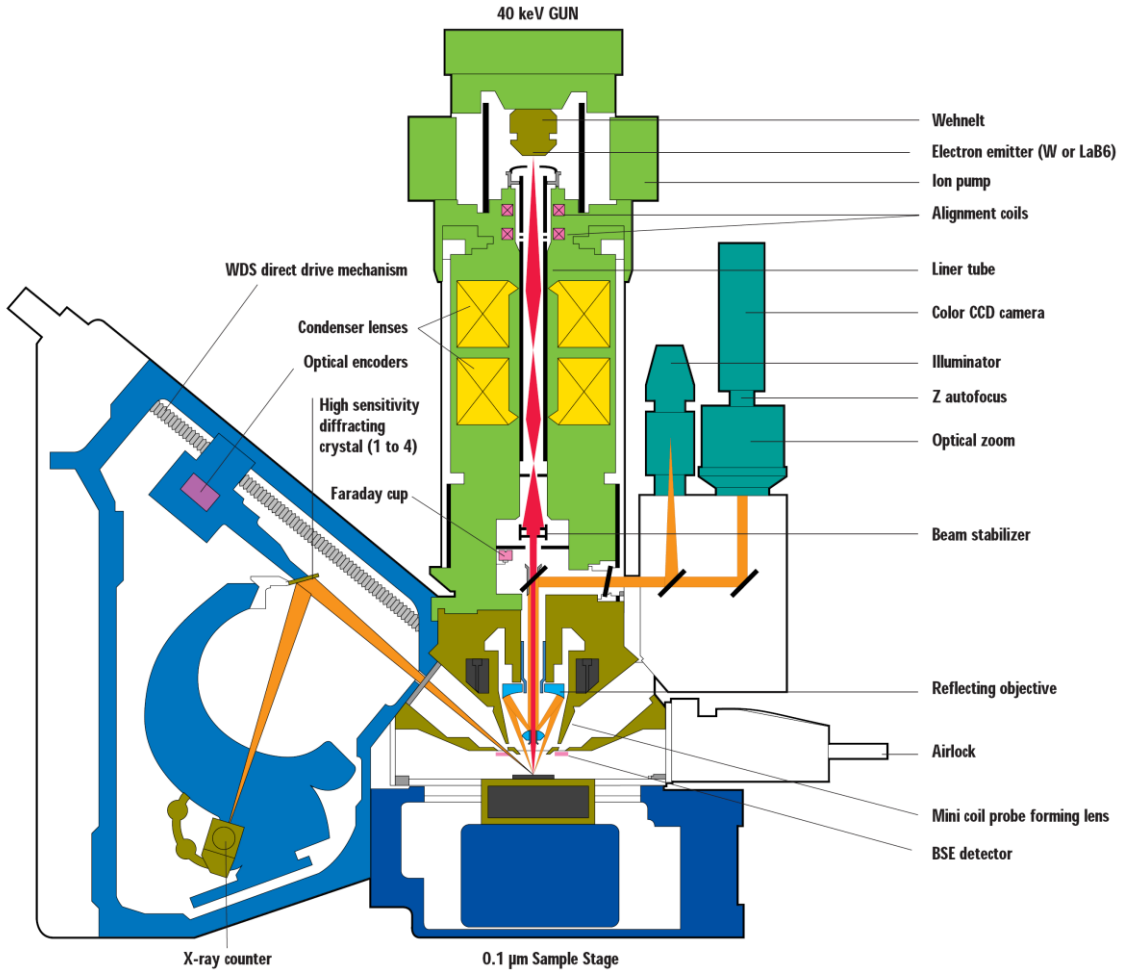

Figure 2.6. Technical drawing of the Cameca SX-100 EPMA instrument.

2.3 Transmission electron microscopy

2.3.1 Basics of transmission electron microscopy

Transmission electron microscopy (TEM) [7] uses a high energy electron beam (from 100 keV to 1 MeV) projected on a very thin (< 200 nm) sample. The electrons are emitted by a source (*e.g.* a field emission gun) and are focused and magnified by a system of magnetic lenses. The incident electrons penetrate the thickness of the sample and give rise to different types of interactions. The different scattering processes (elastic or inelastic) occurring through the material are interpreted to obtain information on defects, grain boundaries, interfaces, *etc.* with atomic scale resolution.

In this Thesis, we focus on the conventional TEM imaging techniques to obtain information about the microstructure of nanosized materials. The bright field (BF) images are formed by a two dimensional projection of the sample obtained by the

transmitted unscattered beam. Thicker regions of the sample or regions with a higher atomic number will appear dark, while thinner regions or with no sample in the beam path will appear bright. The dark field (DF) mode is obtained by selecting one reflection of the diffracted beam. Therefore, only the crystalline parts of the sample which orientation corresponds to the Bragg angle of the selected reflection will appear bright. These two modes produce contrasted images that allow identifying metallic particles and oriented crystallites.

2.3.2 Sample preparation and instrument

The air-sensitivity of the studied samples implied the use of a special sample-holder that could be loaded inside the glove-box and protected from air during the transfer to the TEM vacuum chamber. In addition, the sample-holder was cooled to ~100 K with liquid nitrogen to avoid decomposition of the hydrided samples by the beam irradiation. The thin powder was dispersed on a Cu grid covered with a carbon layer. The instrument used was a FEI Tecnai F20 ST with a field emission gun 200 keV.

2.4 Powder diffraction

2.4.1 General principles of powder diffraction

Both X-ray and neutron diffraction are essential techniques for structural characterization of crystalline materials [8]. Powder diffraction is based on the interaction of sub-atomic particles (photons or neutrons) with the atoms constituent of a crystal, and more particularly on the elastic scattering. Elastic scattering occurs when the energy of an incident radiation is conserved but its direction of propagation may change. When an incident beam hits an atom, the scattered radiations will propagate in all directions. In a crystalline solid where the atoms are arranged in a regular pattern, the interferences of scattered radiations are in majority destructive but they are constructive when Bragg's law is satisfied:

$$n\lambda = 2d \sin \theta \qquad \textbf{(2.1)}$$

where n is an integer, d is the spacing between the scattering planes in the solid, λ is the wavelength of the incident beam (which has to be comparable with d) and θ is the angle between the incident ray and the scattering planes (Figure 2.7). In other words,

diffraction occurs only when the path length difference between two parallel waves is an integer multiple of the wavelength.

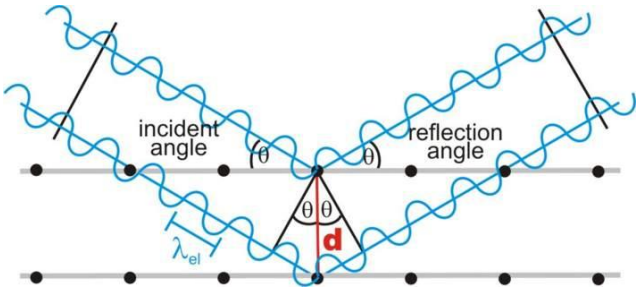

Figure 2.7. Geometric illustration of the Bragg condition with a constructive interference from a parallel incident beam [9].

When this condition is fulfilled, the waves are in phase and produce a Bragg peak, which relative intensity will depend on the nature of the atoms in the diffracting plane. In the case of powder diffraction, the samples are polycrystalline with a random distribution of all *(h,k,l)* planes. Therefore, the diffraction pattern obtained by scanning a large θ range will result in a peak distribution corresponding to the reflections of each *(h,k,l)* plane. Analysis of the diffraction pattern allows, for instance, the determination of relative phase amounts, their atomic and structural parameters and their average crystallite sizes.

2.4.2 X-ray powder diffraction

In the case of X-ray radiation, the incident beam interacts with the electron cloud of the atoms. Therefore, heavy atoms are easily detected while light atoms, such as hydrogen, are hardly perceived. The amplitude of the scattered wave is described by the atomic form factor *f* which is proportional to the atomic number of the atom and decreases with θ angle.

Typical X-ray diffractometers use the Bragg-Brentano geometry. In this geometry, the relationship between θ (the angle between the sample surface and the incident X-ray beam) and 2θ (the angle between the incident beam and the detector) is maintained throughout the analysis. The position of the sample defines the centre of a circle on which the X-ray source and the detector are located. If the X-ray source is fixed while

the sample and detector rotate an angle θ and 2θ, respectively, this is called θ-2θ geometry. If the sample is fixed, while both the X-ray source and detector move an angle θ, then it corresponds to θ-θ geometry (Figure 2.8). All the instruments used in this Thesis were designed in the Bragg-Brentano geometry but they have different configurations.

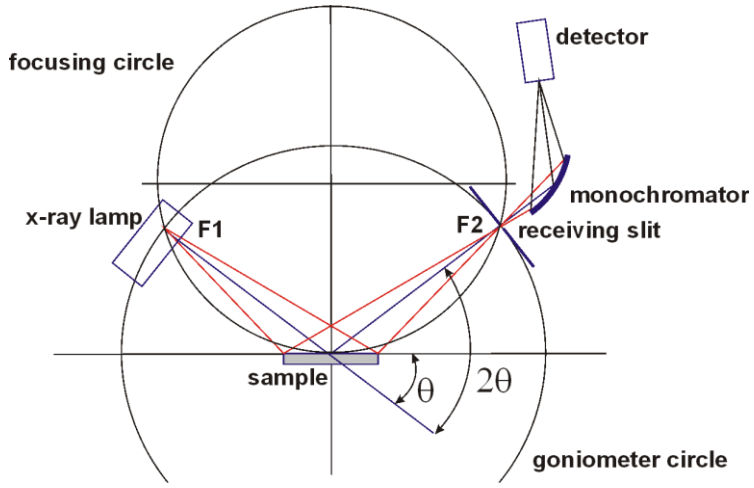

Figure 2.8. Schematic representation of the θ-θ Bragg-Brentano geometry [10].

Most of the X-ray powder diffraction (XRPD) acquisitions concerning the $Mg_6Pd_{1-x}TM_x$ alloys were performed in a Panalytical X'Pert Pro θ-2θ diffractometer with filtered Cu-$K_{\alpha 1}$ radiation ($\lambda_{K\alpha 1}$ = 1.54050 Å). The samples were prepared by dispersing the metal powder on a thin layer of vacuum grease spread on a glass support. The powder was previously ground in an agate mortar and sieved to particle size below 63 μm. This technique ensures a random orientation of the crystallites.

The XRPD analyses of the ball milled composites and nanoconfined hybrids were obtained in a Bruker D8 Advance θ-θ diffractometer with Cu-K_α radiation ($\lambda_{K\alpha 1}$ = 1.54051 Å, $\lambda_{K\alpha 2}$ = 1.54433 Å) and graphite rear monochromator. Owing to the pyrophoric character of these samples, a special air-tight sample-holder commercialized by Bruker was used to avoid samples to be in contact with air. This sample-holder was loaded with about 200 mg of powder inside the glove box and hermetically closed with a X-ray transparent cap.

2.4.3 Neutron powder diffraction

a. Basics of neutron diffraction

Unlike X-rays, neutrons are scattered by the nuclei of the atoms. Analogically to the form factor *f* in X-ray diffraction, the amplitude of the diffracted neutrons is proportional to the scattering length *b*. This characteristic value is independent of the scattering angle, allowing for better peak resolution at high angles. As can be noticed in Figure 2.9, there is no straightforward relation between the atomic number Z of the atoms and the scattering length *b* of neutrons. This property makes neutron diffraction a very helpful tool to detect light atoms such as hydrogen or deuterium that exhibits a strong contrast. However, the hydrogen atom neutron scattering is dominated by a very large incoherent scattering cross section ($\sigma_{inc(H)} = 79.7 \times 10^{-28}$ m^{-2}) which results in an important background contribution. In consequence, the studies of hydrides are almost always performed on deuterated materials as deuterium incoherent scattering cross section is much smaller ($\sigma_{inc(D)} = 2.0 \times 10^{-28}$ m^{-2}).

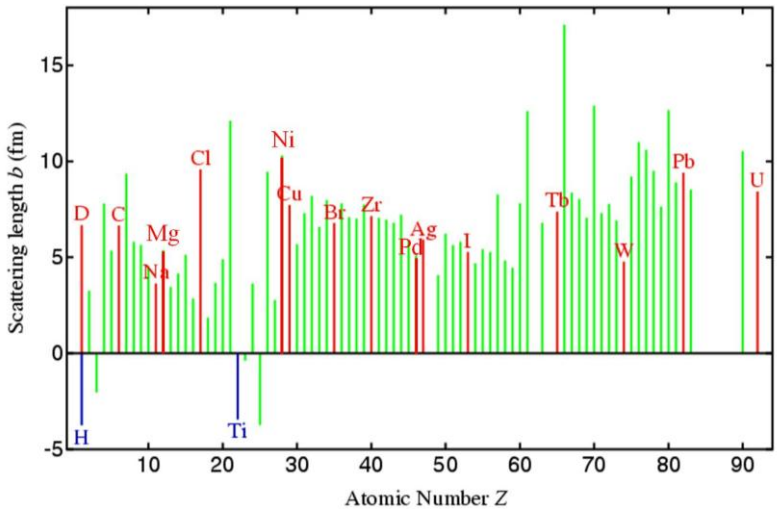

Figure 2.9. Neutron scattering length *b* as a function of the atomic number Z [11].

In addition, since neutrons do not have any electric charge, they can penetrate several centimetres through the condensed matter. This is an advantage to probe the bulk of a sample instead of the few μm analysed by XRPD.

Most of the neutron powder diffractometers use the Debye Scherrer geometry (Figure 2.10). A parallel monochromatic neutron beam hits the sample contained in a cylindrical holder and a series of detectors are located on a detection cylinder. In

consequence, diffracted neutrons are counted simultaneously for the whole θ range, allowing for fast diffractogram acquisition.

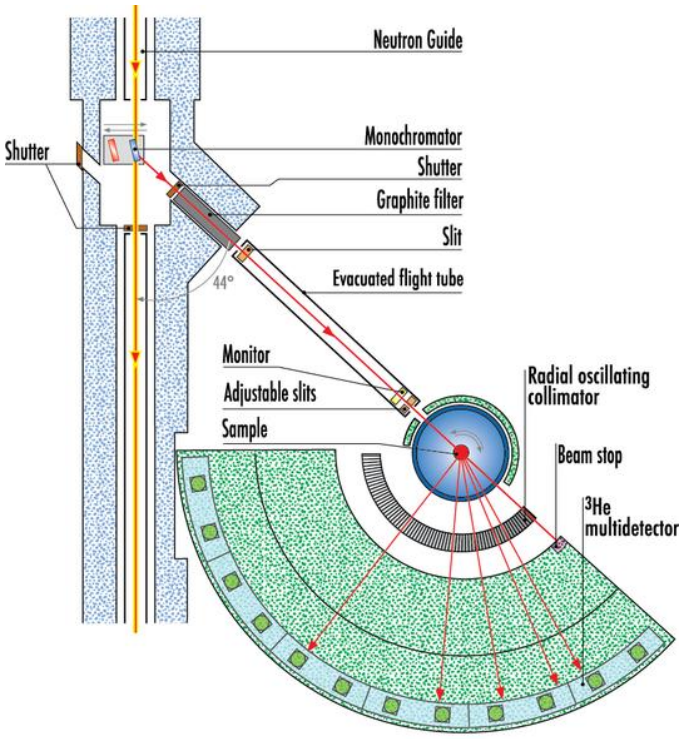

Figure 2.10. Technical drawing of the D1B diffractometer showing the Debye-Scherrer geometry.

In this Thesis, two types of neutron diffraction measurements have been performed. On one hand, high resolution powder diffraction was used for *ex situ* acquisition at room temperature. On the other hand, *in situ* neutron measurements were carried out to determine structural evolutions during (ab)desorption experiments.

b. *Ex situ* neutron diffraction: sample preparation and instruments

Ex situ measurements have been performed on deuterated samples synthesized by RBM. The sample powder was introduced in a vanadium tube hermetically sealed in an Ar protective atmosphere. Sample masses varied from 2 to 5 g, depending on molar mass of the compound and sample-holder size.

The 3T2 diffractometer at Laboratoire Léon Brillouin (Saclay, France) was used to measure composites MgD_2-TiD_2 samples in neutron beam with wavelength $\lambda = 1.225$ Å.

The 2θ angle ranges from 5° to 122° and scattered neutrons counting was obtained by 50 ^{3}He detectors. The MgD_2 sample was measured in the HRPT diffractometer at Paul Scherrer Institute (Villingen, Switzerland) with λ = 1.494 Å. The diffractogram was obtained in the 0 - 165° 2θ-range by 1600 ^{3}He detectors.

c. *In situ* neutron diffraction: sample preparation and instruments

In situ neutron diffraction experiments were carried out in the diffractometer D1B at Institut Laue Langevin (Grenoble, France). The sample-holder, specially designed for that purpose, was made of stainless steel and equipped with an external thermocouple and a valve for deuterium input and output. It was connected to a volumetric rig allowing deuterium uptake control by manometric methods. A vanadium furnace, transparent to neutrons, was used to control the thermal environment of the sample. A general view of the diffractometer is presented in Figure 2.11.

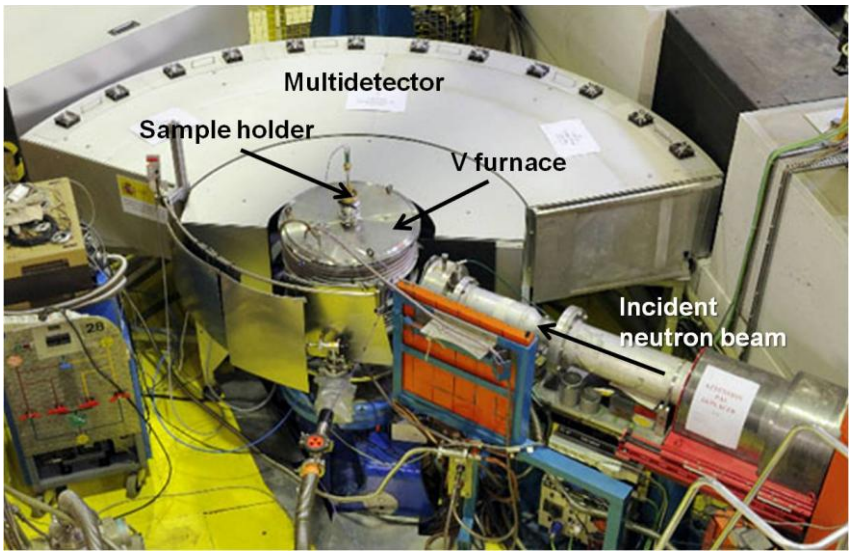

Figure 2.11. General view of the diffractometer D1B equipped with the V furnace.

D1B is a high resolution diffractometer equipped with He/CF_4 position-sensitive detector composed of a system of multi-electrodes with 1280 cells with a separation of 0.1º, covering in total 128º ranged from 0.8 to 128.8º in 2θ. Three pyrolitic graphite monochromators provide a flux of 6.5×10^6 n $cm^{-2}s^{-1}$ for a wavelength of 2.52 Å. At the expense of the neutron flux (reduced to 0.4×10^6 n $cm^{-2}s^{-1}$), a second wavelength, λ = 1.28 Å, is available by using a germanium monochromator. This elevated neutron flux

allows for short time acquisitions (typically 10 min in this study) to follow the structural evolution of the materials with deuterium uptake.

2.4.4 Diffractogram analysis: the Rietveld method

X-ray or neutron powder diffraction can provide a large amount of structural information on polycrystalline materials. To extract this information, it is first necessary to identify the present phases. This step is done by using the Eva (from Brucker) or X'Pert Pro (from Panalytical) software which access to the crystallographic PDF (powder diffraction file) database. Once the phases and their structure are identified, the experimental profile can be fitted to a calculated profile by means of the Rietveld method [12]. In this Thesis, diffraction patterns were analyzed using the Rietveld method with the Fullprof Suite software [13].

The principle of this method is to calculate a theoretical diffractogram from the different variables in the equations of diffraction and taking in account the instrumental characteristics. The structural parameters (lattice parameters, atomic positions, Debye-Waller factors, site occupancy), the scale factor, the background signal and the shape function are progressively refined by a least square method to produce a calculated pattern that should be as close as possible to the experimental diffractogram. This is done by minimising the function *M*:

$$M = \sum_i w_i \, (y_{i,obs} - y_{i,calc})^2 \qquad \textbf{(2.2)}$$

where $y_{i,obs}$ is the observed intensity of point i, $y_{i,calc}$ is the calculated intensity and w_i is a statistical weight given by the inverse of the calculated intensity ($1/y_{i,calc}$).

The intensity at point i, $y_{i,calc}$, is calculated as the sum of the background contribution and all the Bragg peaks from the different phases contributing at this point:

$$y_{i,calc} = y_{bi} + \sum_{\Phi} S_{\Phi} \sum_{k} j_{\Phi k} . Lp_{\Phi k} . |F_{\Phi k}|^2 . \Omega_{i\Phi k} \qquad \textbf{(2.3)}$$

where:

y_{bi} is the background contribution

S_{Φ} is the scale factor of the phase Φ

$j_{\Phi k}$ is the multiplicity of the reflection k

$Lp_{\Phi k}$ is the Lorentz-polarization factor. It modulates the intensity as a function of the θ angle.

$F_{\Phi k}$ is the structure factor of the reflection k

$\Omega_{i\Phi k}$ is the profile shape function

The first summation concerns all the crystalline phases Φ present in the sample and the second one relates to all the reflections *k* contributing to point *i*.

The structure factor $F_{\Phi k}$ relates the intensity of the reflection *k* to the atomic arrangement of the diffracting structure:

$$F_{\Phi k} = \sum_{j=1}^{n} f_j . exp(i2\pi . \vec{k} . \vec{r_j}) . exp(-B_j . sin^2\left(\frac{\theta}{\lambda^2}\right)) \quad \textbf{(2.4)}$$

where:

f_j is the form factor of atom *j* in the case of X-ray, and the scattering length *b* in the case of neutrons.

$\vec{k}$ is the direction of the diffraction

$\vec{r_j}$ indicates the position of atom *j*

B_j is the Debye-Waller factor for atom *j* (in Å²). This factor reflects the thermal vibration of an atom around its crystallographic position. In the case of isotropic vibration, it is written as

$$B = 8\pi^2 U_{iso} \quad \textbf{(2.5)}$$

with U_{iso} the average quadratic amplitude of the vibration.

In the case of anisotropic displacement, the atom vibrates into an ellipsoid volume which shape and orientation can be defined by the following parameters:

$$\beta_{11} = \frac{1}{4} B_{11} a^{*2} \quad \textbf{(2.6)} \qquad \beta_{12} = \frac{1}{4} B_{12} a^{*2} b^{*2} \quad \textbf{(2.7)}$$

$$\beta_{22} = \frac{1}{4} B_{22} b^{*2} \quad \textbf{(2.8)} \qquad \beta_{13} = \frac{1}{4} B_{13} a^{*2} c^{*2} \quad \textbf{(2.9)}$$

$$\beta_{33} = \frac{1}{4} B_{33} c^{*2} \quad \textbf{(2.10)} \qquad \beta_{23} = \frac{1}{4} B_{23} b^{*2} c^{*2} \quad \textbf{(2.11)}$$

with *a**, *b** and *c** the lengths of the reciprocal axes.

The profile shape function $\Omega_{i\Phi k}$ is used to define the peak profile. In this study, the refinements were performed using the "Thomson-Cox-Hastings pseudo-Voigt" function, which considers the peak profile as a weighted sum of a Gaussian and a Lorentzian functions:

$$\Omega = \eta L + (1\text{-}\eta)G \quad \textbf{(2.12)}$$

where η represents the balance between G and L components.

The full-width at half maximum (FWHM) of the Gaussian and Lorentzian components are given as:

$$H_G = (U\tan^2\theta + V\tan\theta + W)^{1/2} \quad \textbf{(2.13)}$$

$$H_L = X\tan\theta + Y\cos\theta \quad \textbf{(2.14)}$$

The parameter U is mainly affected by peak broadening induced by sample microstrains, while Y depends on the crystallite size in the sample. Parameters V, W and X are related to the instrument contribution. In consequence, U and Y parameters are refined and can be used for the determination of the crystallite size and microstrain analysis. The crystallite size is determined from the Lorentzian broadening contribution and the Scherrer formula according to the following relation:

$$D = \frac{360}{\pi^2} \cdot \frac{\lambda}{Y - Y_0} \quad \textbf{(2.15)}$$

with D the diameter in Å of the crystallite considered isotropic, λ the wavelength in Å and Y_0 the instrumental contribution to the Lorentzian component in degrees.

The evaluation of the microstrain in the sample can be obtained from the Gaussian contribution to the peak broadening by the equation:

$$\varepsilon = \frac{\pi^{3/2}}{1.8 \times 8\sqrt{ln2}} \cdot \sqrt{U - U_0} \quad \textbf{(2.16)}$$

where ε is the average microstrain in % and U_0 is the instrumental contribution to the Gaussian component.

To evaluate the validity of a diffraction profile refinement, several reliability factors are calculated. These factors measure the agreement between the experimental and the calculated profiles. The Bragg factor evaluates the validity of the refinement for a given phase. It is probably the best criteria to validate the refined structural model:

$$R_B = 100 \times \frac{\sum_k \left| I_{k,obs} - I_{k,calc} \right|}{\sum_k \left| I_{k,obs} \right|} \quad \textbf{(2.17)}$$

with $I_k = j_k.F_k^2$

The profile factor R_p and the weighted profile factor R_{wp} characterise the quality of the global refinement. They are dominated by the precision of the shape function to

describe the peak shape but they have relatively low sensibility to the structural parameters:

$$R_p = 100 \times \frac{\sum_i |y_{i,obs} - y_{i,calc}|}{\sum_k |y_{i,obs}|} \quad \textbf{(2.18)}$$

$$R_{wp} = 100 \times \left(\frac{\sum_i w_i \left(y_{i,obs} - y_{i,calc}\right)^2}{\sum_i w_i \left(y_{i,obs}\right)^2} \right)^{1/2} \quad \textbf{(2.19)}$$

The expected weighted profile factor reflects the statistical quality of the data:

$$R_{exp} = 100 \times \left(\frac{n - p + c}{\sum_i w_i \left(y_{i,obs}\right)^2} \right)^{1/2} \quad \textbf{(2.20)}$$

where *n* is the number of points used in the refinement, *p* is the number of refined parameters and *c* is the number of constraints.

Finally, the reduced chi-square is a statistic parameter that represents the goodness of fit. Its value should be as close as possible to 1:

$$\chi^2 = \left(\frac{R_{wp}}{R_{exp}} \right)^2 \quad \textbf{(2.21)}$$

2.5 X-ray Absorption Spectroscopy

X-ray Absorption Spectroscopy (XAS) allows the determination of the local structure around an absorbing atom, independently of the crystalline state of the material (amorphous, nanocrystalline, *etc.*). In this technique, the sample is irradiated by a monochromatic but energy-tuneable X-ray beam and the absorbance is recorded as a function of the photon energy. When the beam energy corresponds to the energy of a core-level electron, *i.e.* at the absorption edge, the incident photon is absorbed and the core electron ejected from the atom. At higher energies, the photo-electron is back-scattered by the neighbouring atoms, inducing interferences responsible for the oscillations observed in the absorption spectra above the edge. The X-ray absorption spectrum is typically divided in two regimes: X-ray Absorption Near Edge Spectroscopy (XANES) and Extended X-ray Absorption Fine-structure Spectroscopy (EXAFS). XANES spectrum provides information on the oxidation state, symmetry around the absorbing atom and electronic structure. The EXAFS function χ(k) is the oscillatory part of the absorption spectrum. EXAFS is used to determine atomic

distances, coordination numbers and species of the neighbours of an absorbing atom, as well as disorder parameters through Debye-Waller factors.

This technique has been used to obtain information on the local structure of Mg_6Pd nanoparticles confined in a porous matrix. EXAFS measurements were performed by P. De Jongh's group (Utrecht University) at the DESY-synchrotron facility in Hamburg (DORIS beamline C). The Pd-edge (E = 24350 eV) was measured for a Mg_6Pd bulk reference mixed in boron nitride (30 mg in 20 mg BN), a Mg_6Pd@C composite (160 mg) and a hydrided sample Mg_6PdH_x@C (160 mg). The quantities were calculated in order to obtain an edge jump near 1. All samples were pressed into pellets in the glove box and measured in a closed cell in a He atmosphere.

The study of XAS measurements requires a complex mathematical treatment that is widely described in ref. [14]. The spectra were extracted using standard procedures available in MAX-Cherokee program [15]. All EXAFS fits were performed with MAX-RoundMidnight code [15] by fitting the experimental spectra to the EXAFS standard formula, using first-coordination sphere filtered spectra. Theoretical phases and amplitudes were calculated with FEFF8.4 code [16; 17].

2.6 Porosity analysis by nitrogen physisorption

Physisorption is the process by which gas molecules are adsorbed onto a surface of a solid through weak attractive forces, usually at cryogenic temperatures. This process is used experimentally to quantify the surface area of a solid, its pore size and pore volume distribution. The porosity and surface area analysis is achieved by measuring the adsorption and desorption isotherms of the sample with liquid nitrogen at 77 K. Porous hybrid materials were analysed in this thesis by using a Quantachrome Instruments Autosorb IQ. The amount of adsorbed nitrogen is determined by volumetric measurements as a function of the relative pressure P/P_0, where P_0 is the saturation pressure.

2.6.1 Specific surface area determination

The specific surface area of a porous sample is generally determined through the Brunauer, Emmett and Teller (BET) method [18], with the following equation:

$$\frac{1}{W\left((P_0/P)-1\right)} = \frac{1}{W_m C} + \frac{C-1}{W_m C}\left(\frac{P}{P_0}\right) \quad \textbf{(2.22)}$$

where W is the weight of gas adsorbed measured by volumetric means, W_m is the weight of one monolayer of adsorbate and C is the BET constant which is related to the adsorption energy of the gas.

The plot of $\frac{1}{W((P_0/P)-1)}$ against $\frac{P}{P_0}$ is linear at low pressure, *i.e.* in the 0.05 - 0.25 relative pressure range. From the values of the slope s and the intercept i we can deduce the value of W_m:

$$s = \frac{C-1}{W_m C} \; and \; i = \frac{1}{W_m C} \; therefore \; W_m = \frac{1}{s+i} \quad \textbf{(2.23)}$$

Finally, the specific surface area is expressed as:

$$S = \frac{W_m . N . A_{cs}}{M . w} \quad \textbf{(2.24)}$$

with N Avogadro's number, A_{cs} the cross sectional area of the adsorbate, M its molecular weight and w the sample weight.

2.6.2 Total pore volume, pore size distribution and microporous volume

The total pore volume V_{tot} of the sample is determined from the amount of adsorbed nitrogen close to the saturation pressure (typically at $P/P_0 = 0.99$ in the isotherm). It is expressed as follows:

$$V_{tot} = \frac{V_{ads}}{V_{m(g)}} \times V_{m(l)} \quad \textbf{(2.25)}$$

where V_{ads} is the gaseous volume of adsorbed nitrogen, $V_{m(g)}$ and $V_{m(l)}$ are the molar volumes of gaseous and liquid nitrogen respectively.

The pore size distribution is commonly obtained by the Barrett, Joyner and Halenda (BJH) method [19], based on an adaptation of the Kelvin equation. It is a step by step computational analysis of the desorption branch of the isotherm that relates the pore volume to the pore dimensions. Hence, we obtain a cumulative plot of the pore volume against the mean pore size.

The total volume of micropores is estimated by the Dubinin-Radushkevic (DR) method [20], generally in the 0 - 0.1 relative pressure range. The DR equation gives the following relationship:

$$logW = logW_0 - K\left(log\frac{P_0}{P}\right)^2 \quad \textbf{(2.26)}$$

with W the weight of the liquid adsorbate, W_0 the weight adsorbed in the volume of the micropores, and K the Dubinin-Radushkevich isotherm constant. By plotting $logW$ against $\left(log\frac{P_0}{P}\right)^2$, we obtain the value of W_0 from the intercept with the vertical axis. Thus, from the density of the liquid nitrogen, we obtain the volume of the micropores.

3 Hydrogenation properties

3.1 Sievert's manometric measurements

3.1.1 General principle of the Sievert's method

This method, based on manometric measurements, is used to determine the amount of hydrogen absorbed or desorbed in a sample during solid-gas reaction. A certain amount of hydrogen is first introduced in a calibrated reservoir volume at a given temperature. By measuring the pressure in this volume, it is then possible to know the initial number of hydrogen moles n_i. The gas is then expanded to another calibrated volume containing the sample which can react with hydrogen. H-sorption causes a pressure variation in the total volume and the equilibrium is reached when the pressure does not change anymore. The final number of hydrogen moles n_f is determined from the final equilibrium pressure. Therefore, the accurate determination of n_i and n_f is essential to calculate the hydrogen uptake of a sample. In a first approach, the ideal gas law can be used to calculate the number of hydrogen moles at pressure lower than 1 MPa.

$$n = \frac{PV}{RT} \quad \textbf{(2.27)}$$

with P the hydrogen pressure in the reservoir (Pa), V the volume of the reservoir (m^3), T the temperature of the reservoir (K) and R the gas constant (R = 8.314 J/mol.K). This model assumes that no interaction force exists between the hydrogen molecules and considers the gas molecules as point masses with no significant volume.

To take in account the real gas behaviour of hydrogen at higher pressure (0 - 10 MPa) and temperature (100 - 1000 K), Hemmes [21] developed a model derived from the Van der Waals equation:

$$n = \frac{\left(P + a(P)\frac{n^{\alpha}}{V^{\alpha}}\right)(V - nb(P))}{RT} \quad \textbf{(2.28)}$$

where *a(P)* and *b(P)* depend on the pressure and α on the temperature, according to the following expressions:

$$a(P) = \exp(a_1 + a_2 \ln(P) - \exp(a_3 + a_4 \ln(P)) \text{ for } P > 0.1 \text{ MPa} \quad \textbf{(2.29)}$$

$$b(P) = \sum_{i=0}^{8} b_i (\ln(P))^i \text{ for } P > 10 \text{ MPa}$$
$$b(P) = b(P = 10\ MPa) \text{ for } P < 10 \text{ MPa} \quad \textbf{(2.30)}$$

$$\alpha(T) = \alpha_0 + \alpha_1 T + \alpha_2 T^2 \quad \textbf{(2.31)}$$

The numerical solution of equation (2.28) is obtained according to the Newton method by resolving the following function:

$$f(n) = \left(P + a(P)\frac{n^{\alpha}}{V^{\alpha}}\right)\left(V - nb(P)\right) - nRT \quad \textbf{(2.32)}$$

This is achieved by an iteration process, considering the initial *n* value as $n_0 = PV/RT$. The next estimations of n_i are calculated with the relation $n_{i+1} = n_i - f(n_i)/f'(n_i)$ until a convergence is reached, being $f'(n_i)$ the molar derivative of the function $f(n_i)$.

The Hemmes method has been used to calculate the hydrogen uptake from manometric measurements in a Sievert type apparatus.

3.1.2 Experimental device

A typical Sievert type apparatus (Figure 2.12) is made of calibrated volumes, including a reservoir volume V_r, a sample holder volume V_s and a cross volume V_{cr}. The device is equipped with a pressure sensor that measures the pressure in V_{cr}. The cross volume includes the volume of the pressure sensor. Depending on the amount of sample and on the sensitivity of the measurements, either V_{cr} or $V_{cr} + V_r$ can be used as initial volume before expansion to V_s. The bench is connected to the atmosphere to empty hydrogen pressure when it exceeds 0.1 MPa and to a pump to evacuate the residual gas from the system (P_{vac} ~ 1 Pa). The sample is placed into a sample-holder which is introduced in an electric furnace.

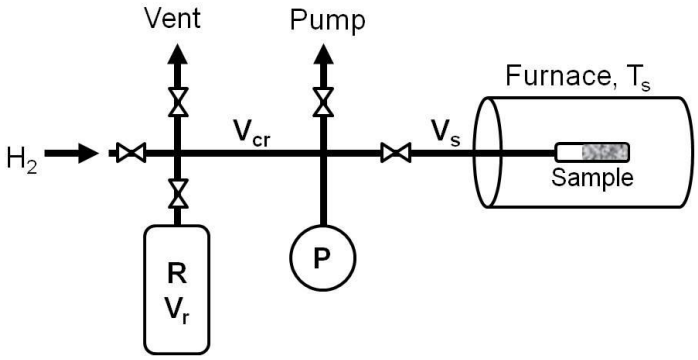

Figure 2.12. Schematic representation of a typical Sievert type apparatus.

3.1.3 Measurement conditions

In this work, several models of hydrogenation bench have been used, with pressure sensors adapted to the working pressure range (1, 3, 6 or 10 MPa) and reservoir volumes chosen in function of the amount of hydrogen to be (ab)desorbed.

For all bulk samples, ~ 0.5 g of alloy was introduced in form of powder (particle size < 63 μm) into the sample-holder closed with a stainless steel filter. The temperature was measured by means of a thermocouple (type K) either fixed on the external wall of the sample-holder or in direct contact with the sample, depending of the bench used. Every hydrogenation was preceded by 3 activation cycles at 620 K under 3 MPa of hydrogen pressure (absorption) and primary vacuum (desorption).

Pressure composition isotherms (PCI) were measured by successive addition of hydrogen in the sample. At each point, hydrogen content is obtained when the equilibrium pressure is reached. A PCI curve consists of about 15 equilibrium points in absorption and the same in desorption. The accuracy of PCI measurements depends on the operating temperature and the time needed to reach equilibrium. Indeed, hydrogen permeation may occur through the steel sample-holder which results in a decrease of the measured hydrogen pressure. Therefore, a shift that can reach 0.5 wt.% H in the final hydrogen content is generally observed at temperature ≥ 623 K.

Kinetic measurements were performed by isothermal absorption with typical initial pressure of 2 MPa. A special attention was paid to reduce at maximum the pressure drop by using a large initial volume.

3.2 Thermal desorption spectroscopy

Thermal Desorption Spectroscopy (TDS) is a commonly used technique to determine the kinetics of decomposition of metal hydrides. Two different setups were used during this Thesis, depending on the sample requirements.

The first one is designed for measurements under Ar flow. It consists of a quadrupole mass spectrometer (QMS 200 Balzers) for gas analysis coupled to a differential scanning calorimeter (DSC4 Perkin Elmer) through a thin capillary tube. A schematic representation of the experimental setup is given in Figure 2.13. The hydrided sample (~ 15 mg) is introduced in a graphite crucible located in a double-furnace system. An empty graphite crucible is used as a reference. A controlled flow of Ar passes through the furnace while a linear heating ramp is imposed on both pans (typically from 323 to 823 K). A fraction of the gas mixture of Ar + H_2 is extracted by the capillary tube to the high vacuum chamber containing the QMS. The H_2 ion current measured by the mass spectrometer (MS) is hence proportional to the desorption rate from the hydride. It is also possible to quantify the amount of desorbed hydrogen by calibration measurements performed with commercial MgH_2 (Alfa Aesar, 95% purity). Therefore, an accurate estimation of the desorbed hydrogen (typical accuracy of 98 %) can be obtained by the following relation:

$$n_{H2} = \varphi_{H2} \int (i_2 - i_2^0)\, dt \qquad \textbf{(2.33)}$$

where φ_{H2} is the calibration factor determined from MgH_2 desorption, i_2 is the hydrogen ion current measured in the MS and i_2^0 is the background signal due to residual H_2 atmosphere in the system. MgH_2 calibration was regularly actualized due to possible changes in the QMS instrument (filament ageing) or in the gas flow (pump maintenance). The sample was weighted before and after the experiment to compare the mass loss to the measured amount of hydrogen desorbed. In this system, contact with air during sample loading cannot be avoided even though it can be minimized by fast transfer to the furnace.

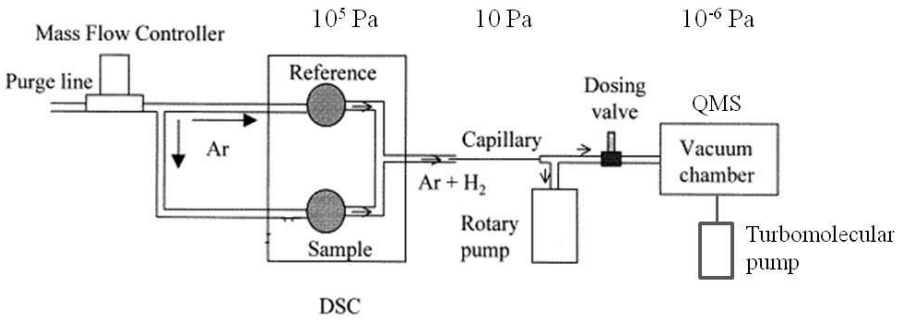

Figure 2.13. Experimental setup of the DSC-MS system [22].

Since the DSC system offers an accurate measurement of the sample temperature, it is also possible to obtain reliable results on activation energy measurements. Indeed, application of the Kissinger method [23] to TDS measurements at different heating rates (5, 10 an 20 K/min) allows to calculate the activation energy of hydrogen desorption according to the equation:

$$ln\left(\frac{\beta}{T_p^2}\right) = ln\left(\frac{AR}{E_a}\right) - \frac{E_a}{RT_p} \quad \textbf{(2.34)}$$

where E_a is the activation energy (kJ/molH_2), A is the pre-exponential factor (min^{-1}), β is the heating rate (K/min), T_p is the peak temperature (K) and R is the gas constant. Hence, the plot of $ln\left(\frac{\beta}{T_p^2}\right)$ against $\frac{1}{T_p}$ gives a straight lines which intercept is proportionnal to the activation energy.

The second setup consists of a QMS (MKS Microvision Plus RGA) connected through a series of valves to a silica tube where the sample is placed in a Ta pan. The heating ramp imposed to the sample is programmed and controlled by an electric furnace around the silica tube. Contrary to the other setup, the whole system works under dynamic high vacuum (10^{-6} - 10^{-4} Pa). The temperature is monitored by a thermocouple (type K) in close contact with the sample. This setup offers the possibility to load the sample inside the glove box, which is particularly interesting for air-sensitive nanoparticles. However, this system was used only for qualitative measurement as the accuracy on the partial H_2 pressure and mass sample were too low.

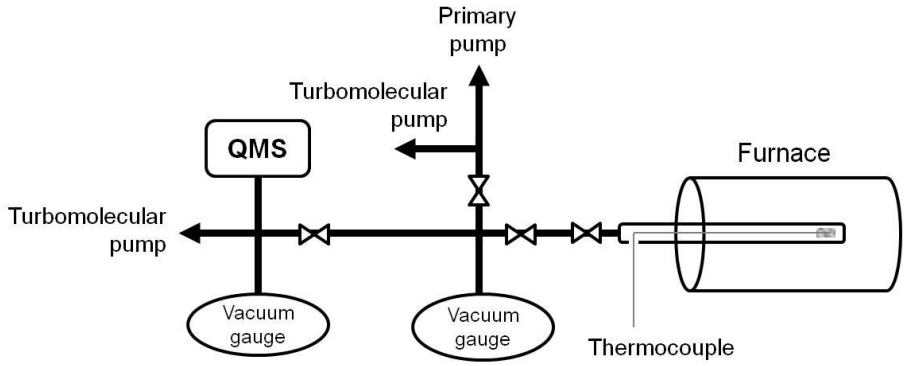

Figure 2.14. Experimental setup of the high vacuum TDS system.

3.3 Differential scanning calorimetry

3.3.1 Standard DSC

The thermal stability of some alloys has been tested by means of differential scanning calorimetry (DSC) in Ar flow. This thermoanalytical technique measures the difference in the amount of heat required to maintain a sample at the same temperature than a reference during a ramp of temperature. The recorded heat flow can be associated to thermal events in the material such as phase decomposition or melting.

Few mg of the sample is introduced in a graphite crucible and placed in a DSC TA Instrument Q100. The heat flow is recorded as a function of temperature during heating and cooling ramps between 323 and 823 K at a constant rate of 5 K/min. A baseline was measured in the same experimental conditions with an empty crucible before each experiment.

3.3.2 High pressure DSC

High pressure DSC (HP-DSC) is based on the same principle than standard DSC but allows for measurements under hydrogen pressure. In consequence, it is possible to measure the heat flow associated to hydrogen absorption or desorption during heating and cooling ramps of temperature. The sample (typical mass ~10 mg) is introduced in a high pressure cell that fits into the DSC furnace of the SENSYS evo DSC instrument from Setaram. The reference cell is identical and placed into the reference furnace. The cell containing the sample is connected to a high pressure gas panel equipped with a pressure sensor and a large reservoir volume to maintain the pressure as steady as possible during the length of the experiment. The cell containing the sample is flushed

with hydrogen gas twice before starting the measurement. Then, a given hydrogen pressure is introduced in the system and maintained during all the experiment. Temperature ramps are programmed in the desired temperature range to observe absorption and desorption events.

This technique allows characterizing the cycling properties of a material by observation of the shape, position and size evolution of the heat-flow peaks.

References

1. Zhang J, Cuevas F, Zaïdi W, Bonnet J-P, Aymard L, Bobet J-L, et al. Highlighting of a Single Reaction Path during Reactive Ball Milling of Mg and TM by Quantitative H_2 Gas Sorption Analysis to Form Ternary Complex Hydrides (TM = Fe, Co, Ni). *J. Phys. Chem. C* 2011; **115** (**11**): 4971–4979.
2. De Jongh PE, Wagemans RWP, Eggenhuisen TM, Dauvillier BS, Radstake PB, Meeldijk JD, et al. The Preparation of Carbon-Supported Magnesium Nanoparticles using Melt Infiltration. *Chem. Mater.* 2007; **19** (**24**): 6052–6057.
3. Bogerd R, Adelhelm P, Meeldijk JH, de Jong KP, de Jongh PE. The structural characterization and H_2 sorption properties of carbon-supported $Mg_{1-x}Ni_x$ nanocrystallites. *Nanotechnology* 2009; **20** (**20**): 204019.
4. Egerton R. *Physical Principles of Electron Microscopy - An Introduction to TEM, SEM, and AEM*. Springer; 2005.
5. Wittke JH. Department of Geology, Northern Arizona University. *http://www4.nau.edu/microanalysis*
6. Reed SJB. *Electron Microprobe Analysis and Scanning Electron Microscopy in Geology*. Cambridge University Press. 1996.
7. Williams DB, Carter CB. *Transmission Electron Microscopy - A Textbook for Materials Science*. 2nd ed. Springer; 2009.
8. Bish DL, Post JE. *Modern powder diffraction*. Mineralogical Society of America; 1989.
9. ETH Zürich. The Electron Microscopy Site. *http://www.microscopy.ethz.ch/bragg.htm*
10. Department of Experimental Physics, Comenius University. Laboratory of X-ray Scattering methods. *http://www.dep.fmph.uniba.sk/mambo/index.php?option=content&task=view&id=259*
11. Cockcroft JK, Birkbeck College, London, United Kingdom. Powder Diffraction Course Material. *http://pd.chem.ucl.ac.uk*
12. Rietveld HM. A profile refinement method for nuclear and magnetic structures. *J. Appl. Crystallogr.* 1969; **2** (**2**): 65–71.
13. Roisnel T, Rodríguez-Carvajal J. WinPLOTR: A Windows Tool for Powder Diffraction Pattern Analysis. *Mater. Sci. Forum* 2001; **378-381**: 118–123.
14. Teo BK. *EXAFS: basic principles and data analysis*. Springer-Verlag; 1986.
15. Michalowicz A, Moscovici J, Muller-Bouvet D, Provost. MAX: Multiplatform Applications for XAFS. *J. Phys.: Conf. Ser.* 2009; **190** (**1**): 012034.
16. Ankudinov AL, Rehr JJ, Conradson SD. Real-space multiple-scattering calculation and interpretation of x-ray-absorption near-edge structure. *Phys. Rev. B* 1998; **58** (**12**): 7565–7576.
17. Ankudinov AL, Bouldin CE, Rehr JJ, Sims J, Hung H. Parallel calculation of electron multiple scattering using Lanczos algorithms. *Phys. Rev. B* 2002; **65** (**10**): 104107.
18. Brunauer S, Emmet PH, Teller E. Adsorption of gases in multimolecular layers. *J. Am. Chem. Soc.* 1938; **60**: 309–319.

19. Barrett EP, Joyner LG, Halenda PH. The Determination of Pore Volume and Area Distributions in Porous Substances .1. Computations from Nitrogen Isotherms. *J. Am. Chem. Soc.* 1951; **73**: 373–380.
20. Rouquerol F, Rouquerol J, Sing KSW. *Adsorption by Powders and Porous Solids: Principles, Methodology and Applications*. Academic Press; 1999.
21. Hemmes H, Driessen A, Griessen R. Thermodynamic properties of hydrogen at pressures up to 1 Mbar and temperatures between 100 and 1000K. *J. Phys. C: Solid State Phys.* 1986; **19** (**19**): 3571.
22. Fernández J., Cuevas F, Sánchez C. Simultaneous differential scanning calorimetry and thermal desorption spectroscopy measurements for the study of the decomposition of metal hydrides. *J. Alloys Compd.* 2000; **298** (**1–2**): 244–253.
23. Blaine RL, Kissinger HE. Homer Kissinger and the Kissinger equation. *Thermochim. Acta* 2012; **540**: 1–6.

Chapter 3.

Pseudo-binary $Mg_6Pd_{1-x}TM_x$ compounds for H-storage

OUTLINE

Among all the Mg-TM systems, Mg-Pd exhibits the largest number of intermetallic phases, with eleven identified compounds. Besides, Mg_6Pd is the Mg-richest intermetallic phase among the referenced Mg-TM phases. The catalytic properties of Pd for hydrogen dissociation are an additional advantage to make attractive the Mg_6Pd compound for hydrogen storage. This chapter presents the properties of several pseudo-binary compounds based on the Mg_6Pd intermetallic with substitution of Pd atoms by other TM (TM = Ag, Cu and Ni) [1; 2]. We are interested here in the structural properties of the $Mg_6Pd_{1-x}TM_x$ compounds in relation with the TM solubility. Their hydrogenation properties are then investigated and compared to those of Mg. The Mg_6Pd intermetallic compound is first characterized as a reference for the following substituted compounds.

1 Mg_6Pd intermetallic compound

The Mg_6Pd compound has been synthesized by induction melting followed by an annealing at 773 K in an Ar atmosphere. The nominal composition has been set close to the Mg-rich limit of the Mg_6Pd homogeneity range, with 87.3 at.% Mg, in order to counterbalance eventual Mg loss during melting due to its ability to evaporate at moderate temperature.

1.1 Characterization of the alloy

1.1.1 Micro-structure and chemical composition

A cross-sectional slice of the Mg_6Pd ingot was polished with diamond paste and observed using the BSE technique of the EPMA instrument. A representative image of the sample is shown in Figure 3.1. The sample is single phase (in grey on Figure 3.1). The average atomic composition as obtained by EPMA measurements on 50 random points at the ingot core is $Mg_{85.7(3)}Pd_{14.3(3)}$. This composition is slightly below the nominal one and corresponds to the exact 6:1 stoichiometry.

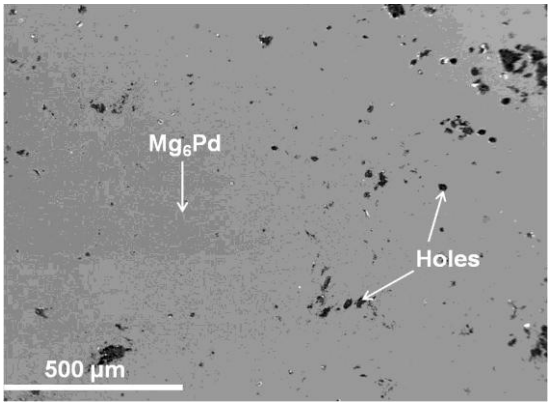

Figure 3.1. BSE image of a polished Mg_6Pd sample from the ingot core.

1.1.2 Structural properties

XRPD analysis confirmed that the alloy only consists of the ρ-Mg_6Pd phase, with a lattice parameter of a = 20.1502(2) Å. The obtained diffractogram and the corresponding Rietveld refinement output are represented in Figure 3.2.

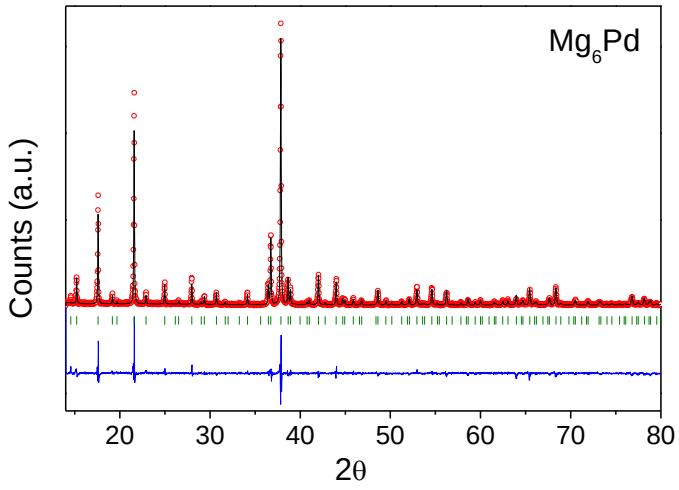

Figure 3.2. XRPD Rietveld refinement of the Mg_6Pd compound (Cu K_α radiation). Continuous line shows the calculated diffraction pattern, vertical bars correspond to the Bragg positions for the Mg_6Pd phase. The difference between experimental and calculated patterns is given below.

In order to validate the structural models proposed by Samson [3] and Makongo *et al.* [4], both have been probed to refine the Mg_6Pd structure (see section 3.1.2.a in Chapter 1). Table 3.1 displays the refined atomic coordinates and SOF obtained according to each model. In Samson's model, the homogeneity range is accommodated

by Mg vacancies at site 14 and mixed Mg and Pd occupancy at site 12. In Makongo's model, which is more accurate, site 12 splits into 12*a* and 12*b* sites, being the former occupied by Mg and Pd atoms and the latter exclusively occupied by Mg. Nevertheless, both models yield in our case very similar structural parameters. In particular, the refinement of Mg and Pd occupancy on sites 12 and 14 leads in both models to very close atomic compositions, which are consistent with EPMA results. In addition, it has to be noted that both models lead to equivalent agreement factors. This indicates that the collected XRPD data does not allow confirming the most detailed model given by Makongo. Thus, to refine our data it is more appropriate to use the simplest model (Samson's one) which involves a lower number of fitting parameters. This choice has been followed all over this manuscript.

Table 3.1. Atomic sites, Wyckoff positions, SOF and atomic coordinates of the Mg_6Pd phase obtained by Rietveld refinement, according to Makongo's and Samson's crystallographic models. The refined atomic compositions and agreement factors are also given at the end of the table. Along this Thesis, numbers inside parentheses stand for the error in the last digit.

Site n°	Atom	Wyckoff position	Makongo's model				Samson's model			
			SOF	Atomic coordinates			SOF	Atomic coordinates		
				x	*y*	*z*		*x*	*y*	*z*
1	Mg	48*h*	1	0.141(1)	*x*	0.038(1)	1	0.142(1)	*x*	0.039(1)
2	Mg	48*h*	1	0.094(1)	*x*	0.275(1)	1	0.094(1)	*x*	0.275(1)
3	Mg	48*h*	1	0.153(1)	*x*	0.522(1)	1	0.153(1)	*x*	0.522(1)
4	Mg	48*h*	1	0.058(1)	*x*	0.769(1)	1	0.058(1)	*x*	0.770(1)
5	Mg	48*h*	1	0.203(1)	*x*	0.910(1)	1	0.203(1)	*x*	0.910(1)
6	Mg	24*f*	1	0.107(1)	0	0	1	0.107(1)	0	0
7	Mg	24*f*	1	0.380(1)	0	0	1	0.381(1)	0	0
8	Mg	24*g*	1	0.057(1)	1/4	1/4	1	0.056(1)	1/4	1/4
9	Mg	16*e*	1	0.304(1)	*x*	*x*	1	0.304(1)	*x*	*x*
10	Pd	16*e*	1	0.168(1)	*x*	*x*	1	0.168(1)	*x*	*x*
11	Pd	16*e*	1	0.406(1)	*x*	*x*	1	0.406(1)	*x*	*x*
12	Pd	16*e*	-	-	-	-	0.34(2)	0.669(1)	*x*	*x*
	Mg		-	-	-	-	0.66(2)	0.669(1)	*x*	*x*
12a	Pd	16*e*	0.38(6)	0.664(1)	*x*	*x*	-	-	-	-
	Mg		0	0.664(1)	*x*	*x*	-	-	-	-
12b	Mg	16*e*	0.62(6)	0.681(2)	*x*	*x*	-	-	-	-
13	Pd	16*e*	1	0.901(1)	*x*	*x*	1	0.901(1)	*x*	*x*
14	Mg	4*d*	0.38(6)	1/4	1/4	3/4	0.4(1)	1/4	1/4	3/4
Refined atomic composition		**Mg (at.%)**	86.3(3)				86.4(2)			
		Pd (at.%)	13.7(3)				13.6(1)			
Agreement factors		R_B	8.76				8.99			
		R_{wp}	17.5				17.6			

1.2 Hydrogenation properties

1.2.1 Thermodynamics: PCI curves

The pressure-composition isotherms have been measured in a Sievert's manometric apparatus at three different temperatures between 0.01 and 3 MPa (Figure 3.3). In this pressure range, the compound absorbs up to 3.2 wt.% H with two equilibrium plateau pressures. This result is in agreement with the PCI at 573 K reported by Dufour *et al.* [5] where two plateau pressures were observed between 0 and 3.0 wt.% H. The hysteresis between equilibrium pressures of absorption and desorption is particularly pronounced for the high pressure plateau. This phenomenon is probably the result of

slowest (de)hydriding kinetics in this region of the PCI, making difficult to reach equilibrium at each measured point (typical equilibrium time was 24 hours).

Furthermore, we can observe that the hydrogen content at the end of the desorption isotherms is not equal to zero, in particular at T = 648 K. This difference is explained by the experimental error due mainly to some hydrogen permeation through the steel sample holder at high temperature. This error increases with temperature and accumulates on each measured point of the PCI, making the last points of desorption affected by a larger error. For the sake of clarity, error bars are not represented in Figure 3.3 and analogous figures along this chapter, but we easily observe that this error can reach 0.5 wt.% H at the end of an isotherm.

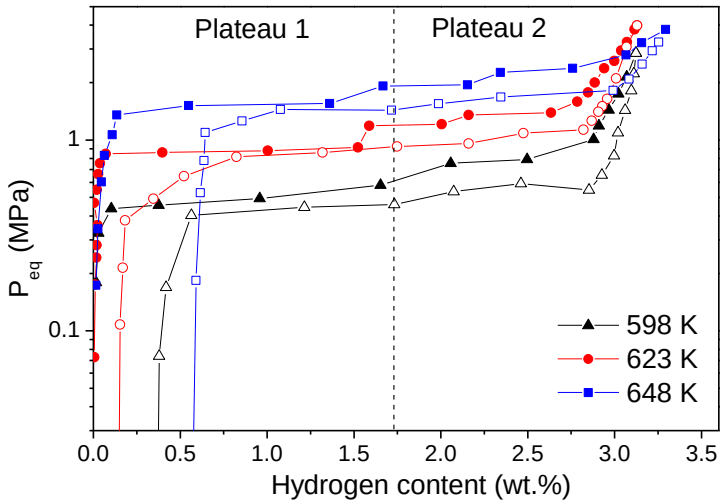

Figure 3.3. PCI curves of the Mg_6Pd compound during absorption (full symbols) and desorption (empty symbols) at 598, 623 and 648 K.

The equilibrium pressures at the middle of each plateau of absorption (1 wt.% H for plateau 1 and 2.5 wt.% H for plateau 2) are reported in Table 3.2. These values are used to plot the Van't Hoff lines in Figure 3.4, according to equation (1.2), and to deduce the enthalpy and entropy of hydrogenation. The enthalpy variation corresponding to plateau 1, ΔH_1 = -72(1) kJ/molH_2, is rather close to the formation enthalpy of MgH_2 (-74.5 kJ/molH_2). The enthalpy variation of plateau 2 is slightly less negative with ΔH_2 = -68(1) kJ/molH_2, showing a small destabilization of the hydrided state for H-rich composition. Entropy values (ΔS_1 = -133(2) J/KmolH_2 and ΔS_2 = -131(2) J/KmolH_2)

are in very good agreement with the entropy variation attributed to hydrogen molecule dissociation in metal-hydrogen systems.

This result diverges from the only thermodynamic values previously reported in literature for TCNE-catalysed Mg_6Pd. Significantly more negative values were found with ΔH = -80 kJ/molH_2 and ΔS = -148 J/KmolH_2 for the first plateau [6]. This discrepancy can be explained by a large experimental error in ref. [6] due to relatively low working temperatures (433 - 468 K) and consequent long equilibrium times (> 50 hours).

Table 3.2. Equilibrium pressures corresponding to absorption plateaus 1 and 2 of the Mg_6Pd PCI curves.

	P_{eq} (MPa)	
T (K)	**Plateau 1 @1 wt.% H**	**Plateau 2 @2.5 wt.% H**
598	0.502	0.804
623	0.884	1.372
648	1.531	2.304

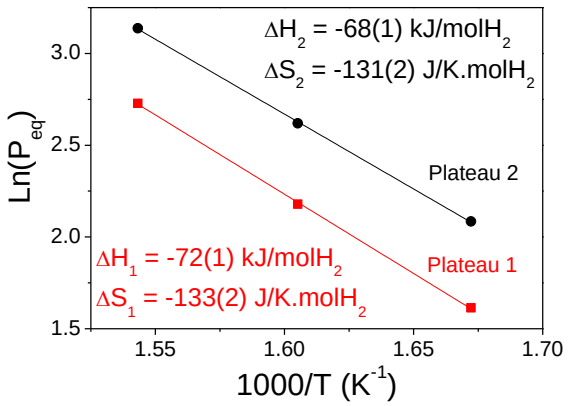

Figure 3.4. Van't Hoff plots corresponding to the two absorption plateaus of the Mg_6Pd isotherms.

1.2.2 Hydrogenation mechanism

As presented in section 3.1.2.b of Chapter 1, the hydrogenation reaction of the Mg_6Pd compound takes place in several steps, leading to the formation of several Mg-Pd intermetallic phases. Based on the amount of hydrogen absorbed during the first plateau and considering the different possible reactions, Dufour and Huot suggested the formation of ζ-$Mg_{3.65}Pd$ as intermediate phase during the first plateau of hydrogenation

[5]. However, this phase consists of an extremely complex crystallographic structure, described by Makongo with 89 atomic sites in the orthorhombic S.G. *Fmmm* [7], and has never been clearly identified during Mg_6Pd hydrogenation. In contrast, the formation of the Mg_5Pd_2 phase during the second plateau has been confirmed by neutron diffraction data [8] and its structure is well known. Huot *et al.* have also reported the occurrence of a third plateau at high pressure (P = 3 MPa at T = 573 K) [8], which is not reached in our study. This plateau would correspond to the decomposition of the Mg_5Pd_2 phase into MgH_2 and MgPd intermetallic compound.

In order to confirm this mechanism, a sample of Mg_6Pd has been hydrogenated at 623 K under 2 MPa of hydrogen pressure. The hydrogen content calculated from manometric measurements was 3.2 wt.% H, which corresponds to the end of the second plateau observed on PCI curves. Considering the hydrogenation conditions of pressure and temperature, MgH_2 and Mg_5Pd_2 phases are expected as final products. This was confirmed by the XRPD measurements presented in Figure 3.5 and the corresponding refined phase amounts of 58.0 wt.% for Mg_5Pd_2 and 41.5 wt.% for MgH_2 (Table 3.3). Additionally, a small amount of a third phase was also detected with the presence of diffraction peaks at 2θ = 24.6° and 39.1°, as can be observed on the detailed plot of Figure 3.5. This phase has been refined as the hexagonal η-Mg_3Pd phase which structure has been determined by Makongo *et al*. [9]. Its structure is rather simple (only 5 atomic positions in the S.G. $P6_3cm$) as compared to the ζ-$Mg_{3.65}Pd$ phase. However, the high Bragg agreement factor (R_B = 31.1) attributed to this phase leads to think that the refined structure is not the correct one. Indeed, several other intermetallic phases have close compositions (ζ-$Mg_{3.65}Pd$ and ε-$Mg_{3.97}Pd$) with their main diffraction peaks also located around 24.5° and 39° with Cu-K_α radiation. In view of the very complex structures of the ζ- and ε-phases and the small amount of this phase present in our sample, we will consider the η-Mg_3Pd phase as an approximate structure and composition for this third phase. The presence of a Mg rich compound as Mg_3Pd at this stage of hydrogenation suggests that the second plateau of absorption is not totally completed.

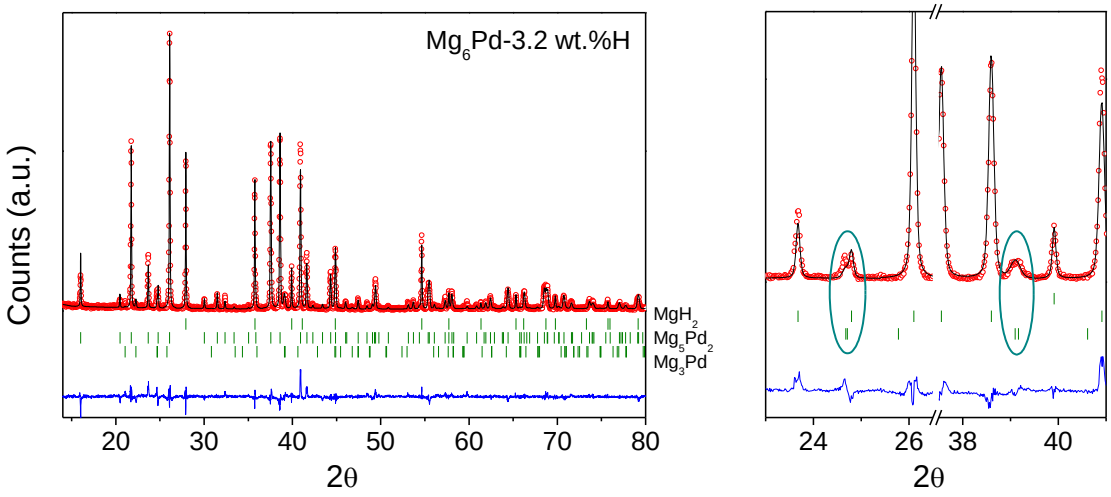

Figure 3.5. XRPD Rietveld refinement of the hydrided (3.2 wt.% H) Mg_6Pd compound (Cu K_α radiation). The plot on the right shows a detailed view of the Mg_3Pd main peaks. Continuous line shows the calculated diffraction pattern and vertical bars correspond to the Bragg positions. The difference between experimental and calculated patterns is given below.

Table 3.3. Rietveld refinement results of the hydrided (3.2 wt.% H) Mg_6Pd compound.

Phase	**S.G.**	**Phase amount (wt.%)**	**Cell parameters (Å)**	R_B	R_{wp}	χ^2
MgH_2	$P4_2/mnm$	41.5(5)	a = 4.5135(1) c = 3.0197(1)	3.98		
Mg_5Pd_2	$P6_3/mmc$	58.0(5)	a = 8.6704(1) c = 8.1678(1)	10.4	19.1	2.59
η-Mg_3Pd	$P6_3cm$	0.5(1)	a = 7.9743(6) c = 8.437(5)	31.1		

In summary, the phase composition of the hydrided Mg_6Pd is in agreement with the hydrogenation mechanism proposed by Dufour and Huot [5]. Hydrogenation of the Mg_6Pd compound leads to the formation of MgH_2 together with a Mg-Pd intermetallic. With increasing H-uptake, this intermetallic becomes richer in Pd and the amount of MgH_2 gradually rises.

1.2.3 Kinetic characterization

The desorption rate of hydrided Mg_6Pd has been compared with commercial MgH_2 by TDS measurements at 10 K/min (Figure 3.6). The hydrided Mg_6Pd desorbed H at a

temperature which is about 15 K lower than that of commercial MgH_2. This result reflects mainly the faster kinetics of the Pd containing material.

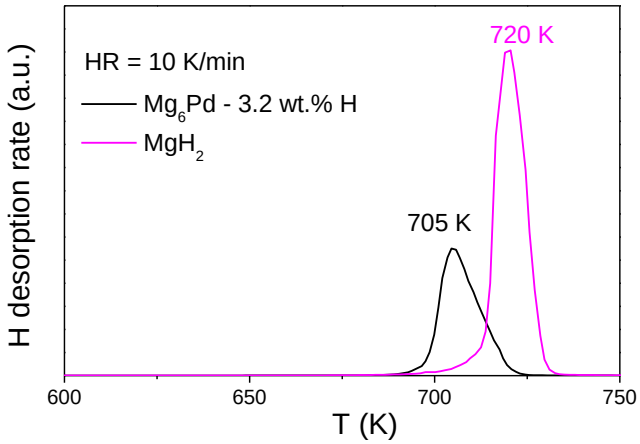

Figure 3.6. TDS spectra of Mg_6Pd hydrided at 3.2 wt.% H compared with commercial MgH_2 at the same heating rate of 10 K/min.

1.3 Discussion on the stability of the Mg_6Pd-H system

The thermodynamic improvement achieved by alloying Mg and Pd is highlighted in the Van't Hoff plots shown in Figure 3.7. Both plateaus of the Mg_6Pd isotherms occur at higher pressures than for pure Mg.

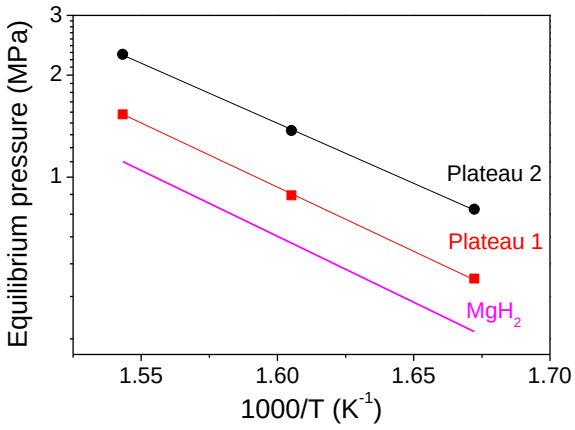

Figure 3.7. Van't Hoff plots of the two absorption plateaus of the Mg_6Pd compound compared with the MgH_2 considering ΔH = -74.5 kJ/molH_2 and ΔS = -135 J/K molH_2 [10].

Although MgH_2 is the only hydride phase formed during the hydrogenation reaction of Mg_6Pd, the net enthalpy of reaction is reduced because of the formation of other phases. Let's consider the hydrogenation reaction of the first plateau:

$$Mg_6Pd + 3\ H_2 \leftrightarrow Mg_3Pd + 3\ MgH_2 \quad \textbf{(3.1)}$$

The corresponding enthalpy of reaction, $\Delta_rH_{(1)}$, can be calculated from the formation enthalpy of each component as reported in Table 3.4 and applying Hess's law. Hence, we obtain:

$$\Delta_rH_{(1)} = \Delta_fH_{(MgH_2)} + \frac{\Delta_fH_{(Mg_3Pd)} - \Delta_fH_{(Mg_6Pd)}}{3} \quad \textbf{(3.2)}$$

Therefore, the reduction of $|\Delta_rH|$ compared to $|\Delta_fH(MgH_2)|$ will only depend on the difference of formation enthalpy between the initial and the final compounds. In this case, if $|\Delta_fH(Mg_3Pd)| < |\Delta_fH(Mg_6Pd)|$, then we will have $|\Delta_rH| < |\Delta_fH(MgH_2)|$. However, according to the enthalpy values reported in Table 3.4, this condition is not fulfilled for these compounds and $\Delta_rH_{(1)}$ = -75.3 kJ/molH_2, a value very close to the formation enthalpy of MgH_2. The difference with the value obtained experimentally for the first plateau of absorption (-72(1) kJ/molH_2) is explained by the uncertainty concerning the Mg-Pd intermetallic formed at the end of the first plateau and the uncertainties on the calculated enthalpy values. We have seen previously (in section 1.2.2 of this chapter) that the Mg-Pd phase diagram exhibits several intermetallic phases with composition close to Mg_3Pd (η-Mg_3Pd, ζ-$Mg_{3.65}Pd$ and ε-$Mg_{3.97}Pd$) and complex crystallographic structures. Besides, the ζ-$Mg_{3.65}Pd$ phase was in fact reported by Dufour and Huot to be the end-product of the first plateau as deduced from mass balance considerations [5]. The same authors also mentioned that the existence of a homogeneity range for the ζ-$Mg_{3.65}Pd$, Mg_5Pd_2 and MgPd phases–contrary to the other Mg-Pd intermetallic phases– may be responsible for the formation of the three observed plateau pressures. According to this argument, the reaction enthalpy of the first plateau should be calculated taking into account the formation enthalpy of the ζ-$Mg_{3.65}Pd$ phase, for which no value is available at the moment. Therefore, the calculated $\Delta_rH_{(1)}$ constitutes an approximation for the first plateau of absorption.

Table 3.4. Enthalpy of formation of the different compounds involved in the Mg_6Pd hydrogenation reaction at 300 K. Enthalpy values for the intermetallic phases are determined by thermodynamic modelling of finite temperature effects and extrapolation from the values at T = 0 K given in Ref. [11].

Compound	Enthalpy 300 K ($kJ/mol_{compound}$) [Ref]
MgH_2	-74.5 [10]
ρ-Mg_6Pd	-173.7 [12]
γ-$Mg_{4.4}Pd$	-182.1 [12]
η-Mg_3Pd	-176 [12]
Mg_5Pd_2	-343 [12]
MgPd	-150 [12]

A similar calculation can be applied for the next two plateaus of absorption according to the following hydrogenation reactions:

$$Mg_3Pd + 3\ MgH_2 + 0.5\ H_2 \leftrightarrow ½\ Mg_5Pd_2 + 3.5\ MgH_2 \quad \textbf{(3.3)}$$

$$½\ Mg_5Pd_2 + 3.5\ MgH_2 + 1.5\ H_2 \leftrightarrow MgPd + 5\ MgH_2 \quad \textbf{(3.4)}$$

Using the formation enthalpy values of Table 3.4 and Hess's law, we obtain $\Delta_rH_{(2)}$ = -65.5 kJ/molH_2 and $\Delta_rH_{(3)}$ = -60.7 kJ/molH_2 for plateaus 2 and 3, respectively. The hydrogenation enthalpy corresponding to the second plateau is in good agreement with the experimental value (-68(1) kJ/molH_2). This result shows the increasing destabilization with higher H-concentration, due to the contribution to enthalpy of the Mg-Pd compounds formation while depleting in Mg. In other words, the enthalpy variation of the decomposition of Mg-Pd phases into Pd-richer intermetallic phases counterbalances the stability of MgH_2.

The study of the Mg_6Pd compound has demonstrated that both kinetic and thermodynamic properties are slightly improved as compared to those of pure Mg. In the next sections of this chapter, effort will be focused on reducing the Pd amount in such compound by creating new pseudo-binary intermetallic alloys of the type $Mg_6Pd_{1-x}TM_x$. One important advantage will be obviously to reduce the cost of such alloys, but other effects are also expected, in particular on the energy involved during hydrogenation reactions. Indeed, hydrogenation of these alloys will lead to the

formation of different Mg-TM intermetallic compounds which may possibly alter the net enthalpy of the global (de)hydrogenation reaction.

2 Substituting Pd by Ag

Owing to the similarities in electronic configuration of Ag and Pd and their complete miscibility in the liquid and solid states [13], we expect a relatively easy substitution of Pd by Ag in the ρ-phase. In fact, a previous assessment of the Mg-Pd-Ag ternary phase diagram showed the existence of a wide homogeneity range for the $Mg_6Pd_{1-x}Ag_x$ pseudo-binary ρ-phase up to x = 0.56 [14].

To study the hydrogenation properties of this phase, a pseudo-binary Ag-rich $Mg_6Pd_{1-x}Ag_x$ alloy was synthesized by induction melting of Mg and Pd elements together with a pre-alloyed eutectic mixture Mg_4Ag/Mg. An ingot of about 50 g has been prepared for the nominal atomic composition $Mg_{86.2}Pd_{6.9}Ag_{6.9}$, which corresponds to the x = 0.5 stoichiometry. The alloy was annealed during 2 days at 648 K.

2.1 Characterization of the alloy

2.1.1 Micro-structure and chemical composition

A polished cross sectional slice of the $Mg_{86.2}Pd_{6.9}Ag_{6.9}$ ingot has been studied by SEM. BSE images on Figure 3.8 give an overview of the material morphology at the ingot core. It is composed of a homogeneous matrix (in grey on the image) and Mg precipitates located at the grain boundaries (in black). The chemical composition of the matrix has been determined by EPMA on 30 points distributed over a sample area of about 300 x 200 nm. The average atomic composition is $Mg_{83.2(3)}Pd_{9.6(2)}Ag_{7.2(3)}$. The Mg concentration is lower than in nominal composition, a fact attributed to partial evaporation of Mg during the melting of the alloy and to the precipitation of pure Mg on grain boundaries. A small depletion of Ag content is also observed as compared to nominal composition due to minor segregation of Ag rich compounds at the ingot surface.

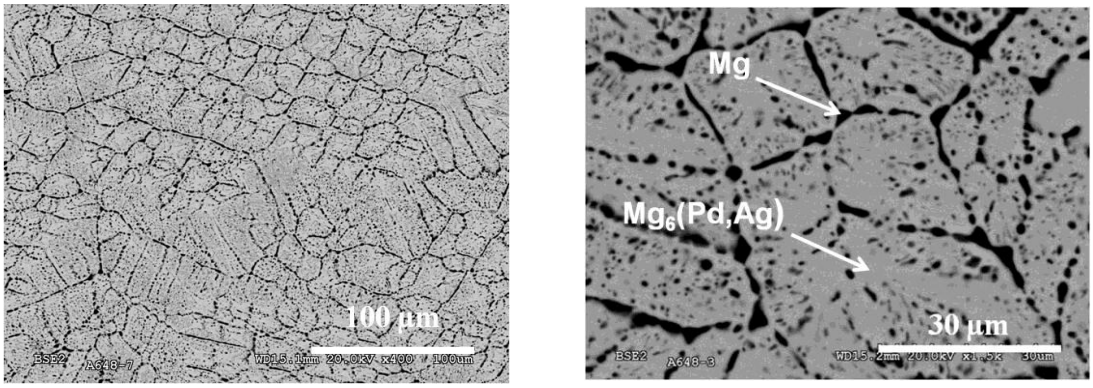

Figure 3.8. BSE images of an ingot slice of the $Mg_6Pd_{0.5}Ag_{0.5}$ alloy.

2.1.2 Structural properties

The XRPD pattern of the alloy with Ag substitution has been analysed using the Rietveld method (Figure 3.9). The diffractogram displays sharp peaks that can be indexed with two phases: Mg (S.G. *P*6$_3$/*mmc*, hexagonal) and ρ-Mg_6Pd (S.G. *F*-43*m*, cubic).

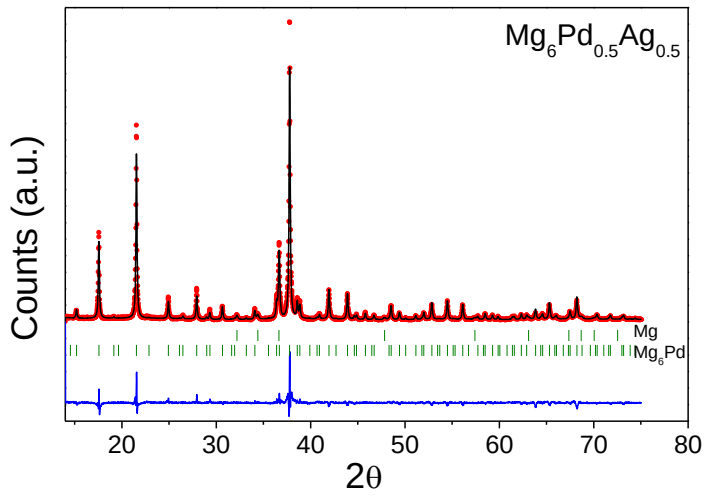

Figure 3.9. XRPD pattern (Cu K_α radiation) of the $Mg_6Pd_{0.5}Ag_{0.5}$ alloy (dots) and the corresponding Rietveld refinement (solid line). Bragg peak positions are plotted as vertical bars for Mg and Mg_6Pd phases. The line below represents the difference between the calculated and the experimental patterns.

Table 3.5. Summary of Rietveld refinement results for the $Mg_6Pd_{0.5}Ag_{0.5}$ alloy.

Phase	S.G.	Phase amount (wt.%)	Cell parameters (Å)	R_B	R_{wp}
Mg	$P6_3/mmc$	11.1(4)	a = 3.208(1) c = 5.208(1)	9.0	13.1
ρ-Mg_6Pd	F-43m	88.9(8)	a = 20.188(1)	8.8	

Table 3.5 shows good agreement factors between observed and calculated patterns. The Mg phase appears in a significant but nevertheless acceptable amount (11.1 wt.%). The main phase, Mg_6Pd with Ag substitution, exhibits a larger cell parameter than for the binary intermetallic at the same Mg content. Makongo *et al.* reported that the *a*-axis of Mg_6Pd phase increases linearly from 20.045 to 20.1985 Å when Mg concentration varies within the homogeneity range from 85.0 to 87.4 at.% Mg [4]. Considering the EPMA results, the Mg concentration is at the poor side of the homogeneity range. Therefore one would expect a smaller lattice parameter than the one obtained by Rietveld refinement (a = 20.188 Å). The observed difference indicates that Ag partially substitutes Pd, as Ag has a larger atomic radius than Pd (r_{Ag} = 1.44 Å and r_{Pd} = 1.37 Å). Unfortunately, these two elements possess very close number of electrons (Z = 46 and 47 for Pd and Ag, respectively), making not possible to refine Ag site occupancy on Pd sites. In consequence, the Mg_6Pd phase has been refined using the structural model proposed by Samson [3] without considering Pd by Ag substitution. Therefore, Mg occupancy has been refined on site 14 and occupancy on site 12 has been refined for Mg and Pd atoms. The obtained structural parameters are presented in Table 3.6. Atomic coordinates are in very good agreement with those reported by Samson for the Mg_6Pd phase and the refined Mg concentration is in fairly good agreement with EPMA result (Mg_{XRD} = 84.3(2) at.%, Mg_{EPMA} = 83.2(3) at.%). Comparison with the previous non-substituted Mg_6Pd sample shows that a lower Mg concentration leads to a higher Mg occupancy at site 14 and lower occupancy at site 12, in accordance with the results obtained by Makongo [7] throughout the homogeneity range of the intermetallic phase.

Table 3.6. Refined positional parameters and occupancies of the $Mg_6Pd_{0.5}Ag_{0.5}$ phase. The refined atomic composition is also given at the end of the table.

Site n°	Atom	Wyckoff position	SOF	Atomic coordinates		
				x	*y*	*z*
1	Mg	48*h*	1	0.144(2)	*x*	0.034(3)
2	Mg	48*h*	1	0.090(2)	*x*	0.273(2)
3	Mg	48*h*	1	0.153(2)	*x*	0.528(3)
4	Mg	48*h*	1	0.056(2)	*x*	0.764(2)
5	Mg	48*h*	1	0.202(2)	*x*	0.908(2)
6	Mg	24*f*	1	0.106(3)	0	0
7	Mg	24*f*	1	0.378(3)	0	0
8	Mg	24*g*	1	0.059(3)	1/4	1/4
9	Mg	16*e*	1	0.305(2)	*x*	*x*
10	Pd	16*e*	1	0.167(1)	*x*	*x*
11	Pd	16*e*	1	0.407(1)	*x*	*x*
12	Pd	16*e*	0.90(5)	0.670(1)	*x*	*x*
	Mg		0.10(5)		*x*	*x*
13	Pd	16*e*	1	0.899(1)	*x*	*x*
14	Mg	4*d*	0.96(5)	1/4	1/4	3/4
Refined atomic composition		**Mg (at.%)**	84.3(2)			
		Pd (at.%)	15.7(1)			

2.1.3 Thermal stability

The thermal behaviour of the alloy has been analyzed by DSC. The heat flow recorded as a function of temperature is plotted in Figure 3.10.

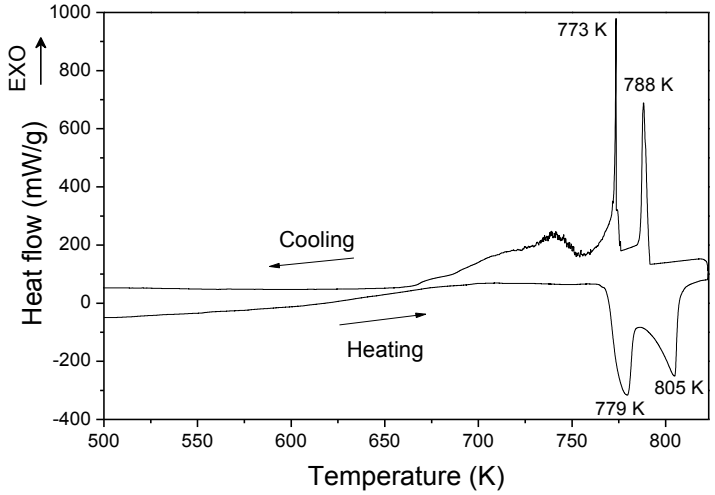

Figure 3.10. DSC scan of $Mg_6Pd_{0.5}Ag_{0.5}$ sample during heating and cooling at 5 K/min.

On heating, two endothermic peaks are detected at 779 K and 805 K. They are attributed to melting events, which however are much broader than typical melting peaks. Thus, it can be inferred that melting occurs simultaneously with the disproportionation of the pseudo-binary compound into intermetallic phases. Owing to the phase complexity of both Mg-Pd and Mg-Ag systems, and even more of the ternary Mg-Pd-Ag system, it seems ambitious to describe the exact disproportionation mechanism that occurs during heating. However, some hints allow us to propose an approximate reaction path for the $Mg_6Pd_{1-x}Ag_x$ disproportionation. The onset temperature of the first peak, 764 K, concurs with the reported melting temperature of the Mg_3Ag phase at 767 K [15]. We have confirmed the formation of this phase above 728 K by *in situ* high-temperature XRPD measurements (Figure 3.11). In addition, it appeared that the alloy disproportionates into Mg_3Ag phase and Mg, implying that Pd should be fully dissolved in the Mg_3Ag phase. Unfortunately, the formation of MgO could not be avoided during the *in situ* XRPD experiment, which probably affected the thermodynamic of the reaction. Therefore, we cannot rule out the persistence of the $Mg_6(Pd,Ag)$ compound together with $Mg_3(Ag,Pd)$ and Mg phases during heating in the absence of oxygen, *i.e.* during DSC measurements. The second endothermic peak may correspond to the melting of the Mg phase mixed with $Mg_6(Pd,Ag)$. To this respect, the eutectic melting of Mg_6Pd and Mg phases occurs at 812 K [16], in fairly good agreement with the temperature of the second peak at 805 K. In consequence, it can be proposed that the homogeneity range of the $Mg_6Pd_{1-x}Ag_x$ phase shrinks during heating, leading to the alloy disproportionation into Mg, $Mg_6(Pd,Ag)$ and $Mg_3(Ag,Pd)$ phases. According to *in situ* XRPD measurements, the thermal stability of the pseudo-binary alloy $Mg_6Pd_{1-x}Ag_x$ with $x = 0.5$ is maintained up to 728 K.

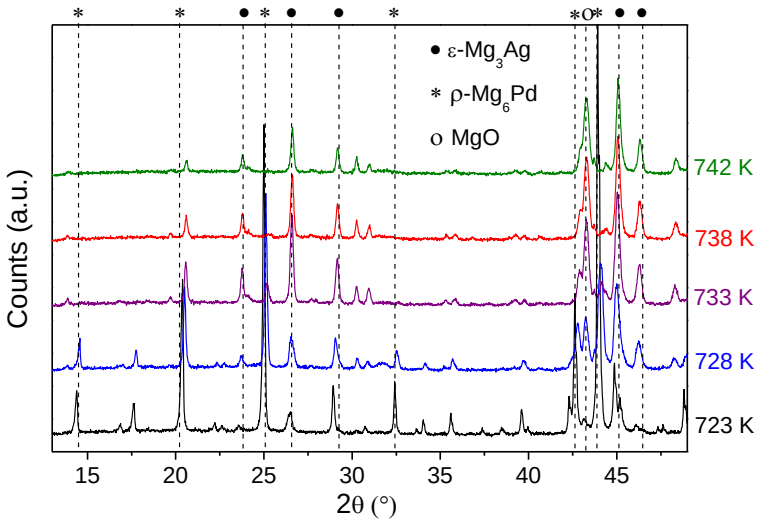

Figure 3.11. XRPD patterns (Co K_α radiation) of the $Mg_6Pd_{0.5}Ag_{0.5}$ sample obtained during heating at 5 K/min under He flow.

During cooling, two sharp exothermic peaks are observed at 788 K and 773 K. They are attributed to the solidification of Mg, Mg_6(Pd,Ag) and Mg_3(Ag,Pd) phases mentioned above. They are followed by an exothermic bump at lower temperature, which is attributed to the reformation of the pseudo-binary ρ-phase by a solid state reaction between the solidified phases. XRPD analysis of the sample after DSC scan (Figure 3.12) shows that the initial material was reformed after cooling and no trace of Mg_3Ag was found.

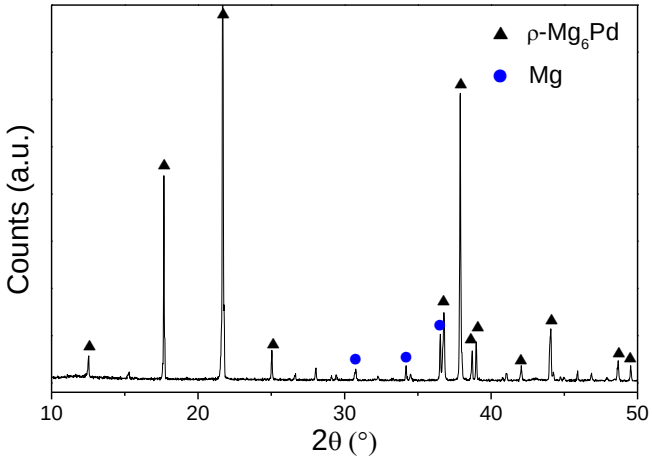

Figure 3.12. XRPD pattern (Cu K_α radiation) of the $Mg_6Pd_{0.5}Ag_{0.5}$ sample after heating at 823 K during DSC experiment.

2.1.4 Ag solubility – ternary phase diagram

The ternary Mg-Pd-Ag phase diagram at 673 K assessed by Prince in 1988 [14] displays a homogeneity range for the $Mg_6Pd_{1-x}Ag_x$ phase with a maximum Ag solubility of 8 at.% (x = 0.56) for a Mg content of 84 at.% (Figure 3.13). Our experimental results for the composition of the pseudo-binary phase annealed at 648 K according to EPMA gives a slightly lower Ag content (7.2 at.% Ag) and a smaller Mg concentration (83.2 at.% Mg). Though, such small differences can be explained by the lower annealing temperature used in our work as compared to the isothermal section determined by Prince.

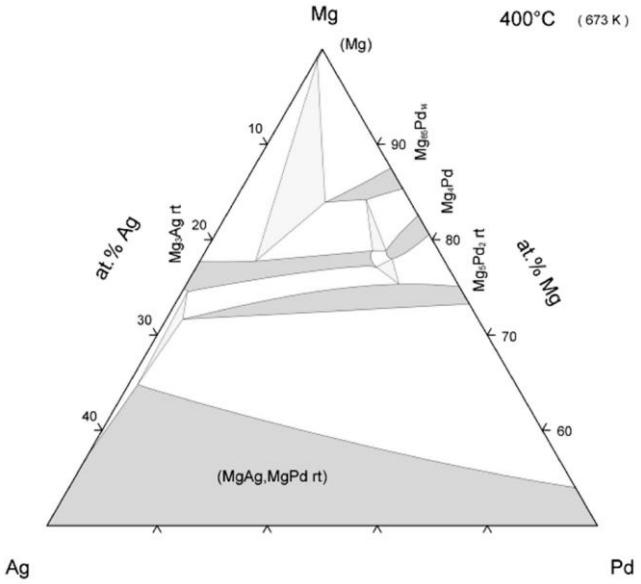

Figure 3.13. Ternary phase diagram of the Mg-Pd-Ag system at 673 K [14].

2.2 Hydrogenation properties

2.2.1 Thermodynamics: PCI curves

The PCI curves of the $Mg_6Pd_{0.5}Ag_{0.5}$ alloy have been measured at 598, 623 and 648 K between 0.01 and 3 MPa of hydrogen pressure. Figure 3.14 displays the resulting isotherms in absorption and desorption. The sample absorbs up to 3.0 wt.% H according to two plateau pressures. The first plateau occurs for H-contents below 1.5 wt.% H and is rather flat. The second one occurs above 2 wt.% H and is more tilted. It could result of the merging of two shorter plateaus that unfortunately could not be resolved. As

observed for Mg_6Pd, a large experimental error is attributed on the last points of desorption at the highest temperature, due to hydrogen permeation through the sample holder.

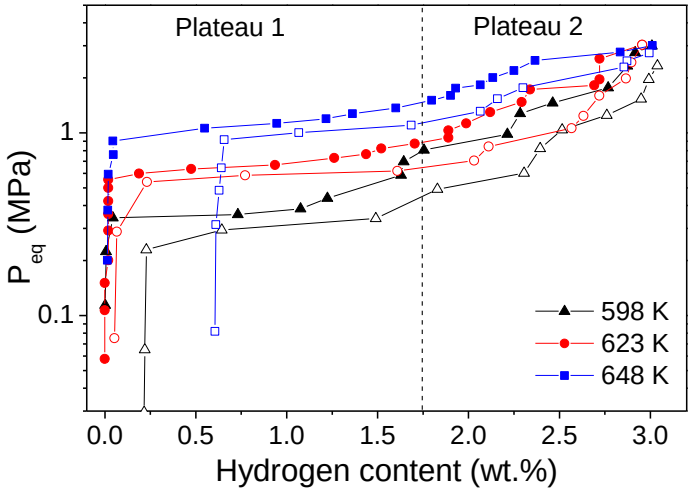

Figure 3.14. PCI curves of the $Mg_6Pd_{0.5}Ag_{0.5}$ sample during absorption (full symbols) and desorption (empty symbols) at 598, 623 and 648 K.

Using the equilibrium pressures of the two plateaus at 1 wt.% H and 2.5 wt.% H (Table 3.7) and the corresponding Van't Hoff plots (Figure 3.15), enthalpies and entropies of hydrogenation have been calculated. The resulting values for plateau 1, ΔH_1 = -72(2) kJ/molH_2 and ΔS_1 = -132(2) J/K.molH_2, are similar to those of Mg_6Pd. Thus, Ag substitution does not change the thermodynamics of the first hydrogenation reaction. In contrast, the second plateau exhibits much less negative values of enthalpy and entropy with ΔH_2 = -35(4) kJ/molH_2 and ΔS_2 = -81(6) J/K.molH_2, suggesting that Ag significantly affects the equilibrium of the second hydrogenation reaction. However, last results should be taken with care in view of the slope and extent in hydrogen content of the second plateau.

Table 3.7. Equilibrium pressures corresponding to absorption plateaus 1 and 2 of the $Mg_6Pd_{0.5}Ag_{0.5}$ PCI curves.

	P_{eq} (MPa)	
T (K)	**Plateau 1 @1 wt.% H**	**Plateau 2 @2.5 wt.% H**
598	0.375	1.498
623	0.682	1.770
648	1.150	2.580

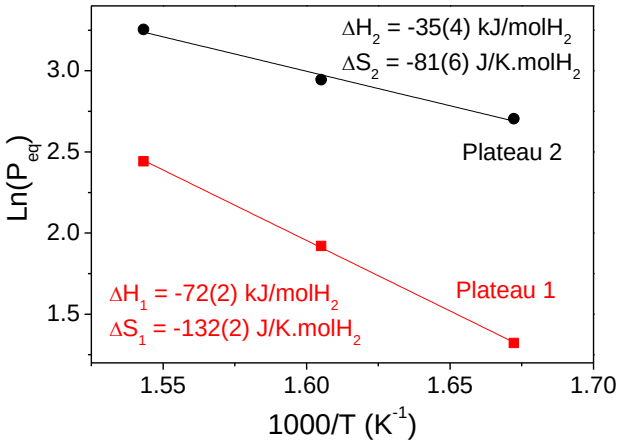

Figure 3.15. Van't Hoff plots corresponding to the two absorption plateaus of the $Mg_6Pd_{0.5}Ag_{0.5}$ isotherms.

2.2.2 Hydrogenation mechanism

Several samples with different hydrogen contents have been prepared in order to identify the phases that are formed during hydrogenation at 623 K of the $Mg_6Pd_{0.5}Ag_{0.5}$ compound. In addition, one sample has been fully hydrided under 4 MPa of hydrogen pressure at 623 K, leading to an H-uptake of 4.4 wt.% H. Their labels and hydrogen contents are detailed in Table 3.8.

Table 3.8. Hydrogen content of the annealed and partially hydrided $Mg_6Pd_{0.5}Ag_{0.5}$ samples.

Label	**H content (wt.% H)**
MPA	0
MPAH1.8	1.8(2)
MPAH2	2.0(2)
MPAH3	3.0(2)
MPAH4.4	4.4(3)

The XRPD patterns and peak identification of these samples are presented in Figure 3.16. During the first plateau of hydrogenation (from 0 to 2 wt.% H), we clearly identify the formation of MgH_2 together with the cubic ε-Mg_3Ag phase while the initial ρ-Mg_6Pd progressively disappears. The Mg_5Pd_2 phase is formed during the second plateau (up to 3 wt.% H) and finally the MgPd phase appears for the highest H-content (4.4 wt.% H).

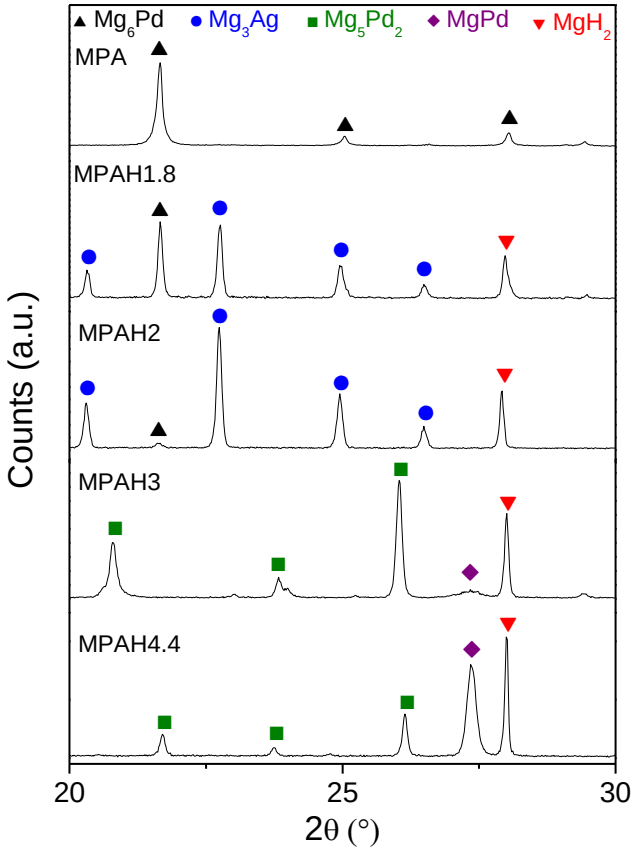

Figure 3.16. XRPD patterns (Cu K_α radiation) of the $Mg_6Pd_{0.5}Ag_{0.5}$ sample at different hydrogen contents.

The relative phase amounts and structural properties have been determined by Rietveld analysis of the XRPD patterns. Main results are displayed in Table 3.9. The decrease of the Mg_6Pd lattice parameter ($\Delta a/a$ = -0.5 %) observed in MPAH1.8 and MPAH2 samples as compared to the parent compound is attributed to Mg depletion in this phase on hydriding (r_{Mg} = 1.60 Å while r_{Ag} = 1.44 Å and r_{Pd} = 1.37 Å). The ε-Mg_3Ag phase is also observed to exhibit a cell shrinkage ($\Delta a/a$ = -0.7 %) as compared

to the cubic ε-Mg_3Ag compound (a = 17.61 Å [17]). This is attributed to Pd solubility in this phase ($r_{Pd} < r_{Ag}$). Even more interesting is the behaviour of the lattice parameters of the Mg_5Pd_2 phase. The occurrence of this phase is detected at 3.0 and 4.4 wt.% H. At 3.0 wt.% H, strong anisotropic cell expansion ($\Delta a/a$ = -0.1 %, $\Delta c/c$ = 4.8 %) is observed by comparison with the reported lattice parameters of Mg_5Pd_2 compound (a = 8.65 Å, c = 8.17 Å [18]). At higher H-content (4.4 wt.% H), the unit cell seems to relax ($\Delta a/a$ = 0.2 %, $\Delta c/c$ = 0.5 %). This distortion is too important to be linked to the Mg homogeneity range of this phase (related cell variations below 0.3 % [18]). Instead, it suggests Ag-solubility ($r_{Ag} > r_{Pd}$) in the Mg_5Pd_2 compound, which extent depends on the progress of the hydrogenation reaction. Finally, the MgPd and MgAg phases are isostructural (CsCl-type) and possess complete solubility [14]. Using the data reported in ref. [19], its approximate composition is $MgPd_{0.3}Ag_{0.7}$.

Table 3.9. Rietveld refinements results of partially hydrided $Mg_6Pd_{0.5}Ag_{0.5}$ samples.

Sample	Phase	S.G.	Phase amount (wt.%)	Cell parameters (Å)	R_B	R_{wp}
MPAH1.8	ρ-Mg_6Pd	*F*-43*m*	30.2(3)	*a* = 20.1012(3)	13.7	15.3
	MgH_2	*P*4$_2$/*mnm*	25.2(4)	*a* = 4.5107(1) *c* = 3.0185(1)	3.5	
	ε-Mg_3Ag	*Fm*-3	44.6(4)	*a* = 17.4801(2)	7.84	
MPAH2	ρ-Mg_6Pd	*F*-43*m*	1.8(1)	*a* = 20.0822(1)	33.7	16.1
	MgH_2	*P*4$_2$/*mnm*	30.3(4)	*a* = 4.5110(1) *c* = 3.0183(1)	7.34	
	ε-Mg_3Ag	*Fm*-3	67.9(5)	*a* = 17.4448(2)	7.68	
MPAH3	MgH_2	*P*4$_2$/*mnm*	42.7(5)	*a* = 4.5157(1) *c* = 3.0208(1)	6.79	19.1
	Mg_5Pd_2	*P*6$_3$/*mmc*	51.0(5)	*a* = 8.6451(2) *c* = 8.5661(2)	6.04	
	$MgPd_{0.3}Ag_{0.7}$	*Pm*-3*m*	6.3(2)	*a* = 3.2695(2)	9.43	
MPAH4.4	MgH_2	*P*4$_2$/*mnm*	50.8(5)	*a* = 4.5152(1) *c* = 3.0209(1)	4.79	16.2
	Mg_5Pd_2	*P*6$_3$/*mmc*	15.7(2)	*a* = 8.6748(2) *c* = 8.2108(2)	13.2	
	$MgPd_{0.3}Ag_{0.7}$	*Pm*-3*m*	33.5(3)	*a* = 3.2648(1)	7.32	

XRPD results clearly show the formation of the MgH_2 phase along with different intermetallic phases during hydrogenation. Though, they are not conclusive regarding Pd and Ag solubility due to the impossibility to refine their respective site occupancy. A

relevant approximation of the chemical composition of these samples has been obtained by means of SEM-EDX analyses. The BSE images are presented in Figure 3.17 and chemical compositions of the identified phases are reported in Table 3.10. The images show the increasing surface of the dark area, identified as MgH_2, with the increasing H-content. In addition, several phases with different tones of grey are observed and identified in agreement with the XRPD results. Besides, EDX analyses detect the presence of both Pd and Ag elements in all intermetallic $Mg_x(Pd,Ag)_y$ phases, confirming the high level of solubility of these two TMs that was anticipated by Prince in the ternary Mg-Pd-Ag phase diagram [14]. However, the full structural characterization of such substituted compounds requires more complex techniques than conventional XRPD, like anomalous diffraction tools [20], diffuse scattering or EXAFS, to determine the site occupancy of Pd and Ag atoms.

Table 3.10. Chemical composition of the partially hydrided $Mg_6Pd_{0.5}Ag_{0.5}$ samples as obtained by SEM-EDX analyses.

Sample	Phase	Mg (at.%)	Pd (at.%)	Ag (at.%)
MPAH1.8	ε-Mg_3Ag	76(4)	9(2)	15(3)
	ρ-Mg_6Pd	80(3)	12(1)	8(1)
	MgH_2	95(4)	3(2)	2(1)
MPAH2	ε-Mg_3Ag	74(2)	11(2)	15(2)
	ρ-Mg_6Pd	80(3)	13(2)	7(1)
	MgH_2	100	0	0
MPAH3	Mg_5Pd_2	69(4)	16(2)	15(2)
	MgH_2	99(4)	0,7(2)	0,6(5)

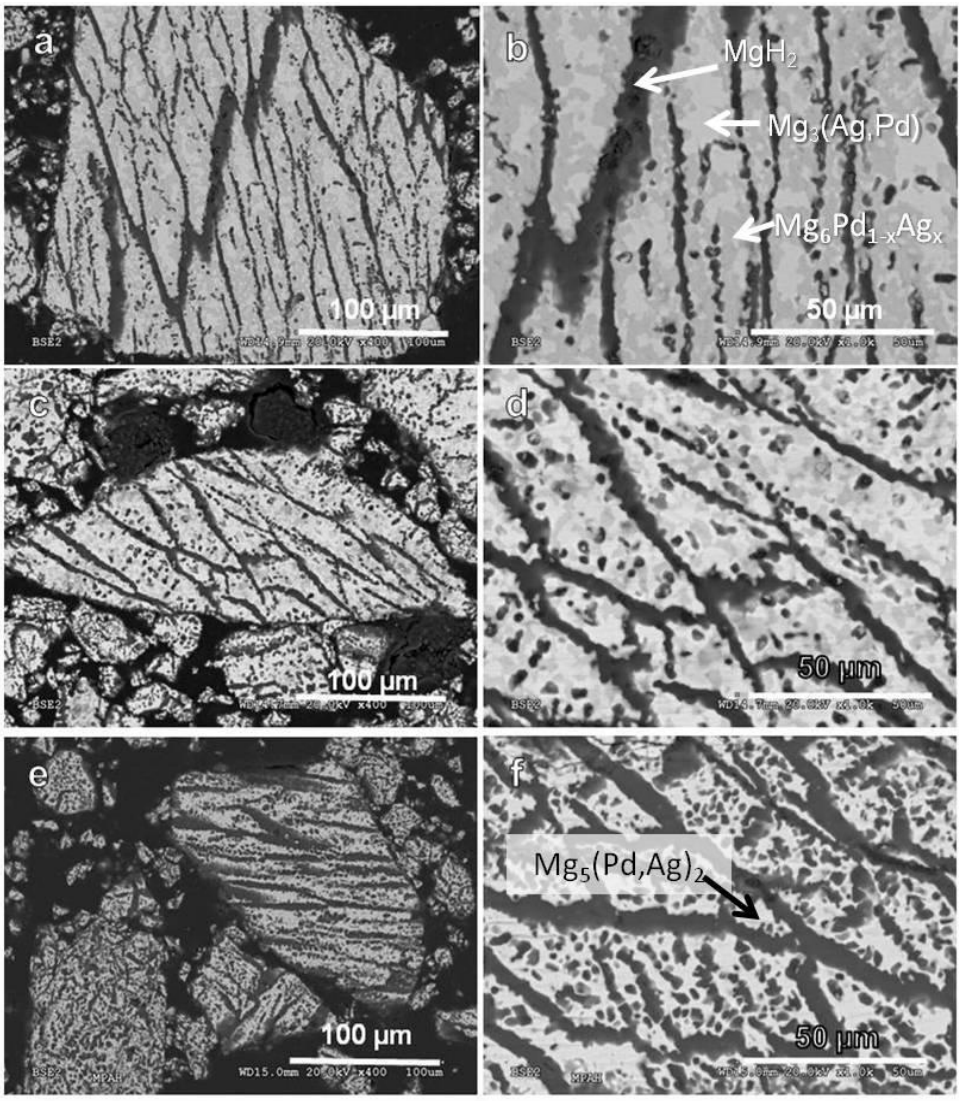

Figure 3.17. BSE images of a) and b) MPAH1.8, c) and d) MPAH2, e) and f) MPAH3.

At the light of this detailed information on the composition of samples at different hydrogenation stages, the following hydrogenation reactions are proposed:

$$Mg_6Pd_{0.5}Ag_{0.5} + 3\ H_2 \leftrightarrow Mg_3Ag_{0.5}Pd_{0.5} + 3\ MgH_2 \quad \textbf{(3.5)}$$

$$Mg_3Ag_{0.5}Pd_{0.5} + 3\ MgH_2 + 0.5\ H_2 \leftrightarrow \tfrac{1}{2}\ Mg_5PdAg + 3.5\ MgH_2 \quad \textbf{(3.6)}$$

$$\tfrac{1}{2}\ Mg_5PdAg + 3.5\ MgH_2 + 1.5\ H_2 \leftrightarrow MgPd_{0.5}Ag_{0.5} + 5\ MgH_2 \quad \textbf{(3.7)}$$

For the sake of simplicity, equiatomic Pd and Ag contents have been fixed for the composition of $Mg_x(Pd,Ag)_y$ phases. This mechanism is analogous to the one of Mg_6Pd and leads to a similar hydrogen storage capacity. The successive transformations are schematically represented in Figure 3.18. The progressive Mg depletion of the

intermetallic phases with hydrogen concentration results in the formation of additional MgH_2.

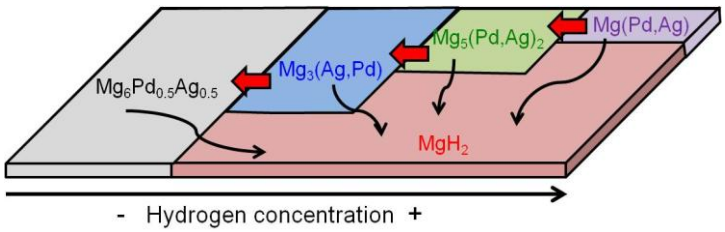

Figure 3.18. Schematic illustration of the phase growth during hydrogenation of the $Mg_6Pd_{0.5}Ag_{0.5}$ compound. Large arrows represent the growing direction of the phases. Thin arrows symbolize the diffusion of Mg atoms.

2.2.3 Reversibility

A totally desorbed sample (MPAdes) has been prepared after 3 activation cycles and analysed by SEM-EDX and XRPD. Desorption was performed at 623 K by two successive desorption steps at P < 0.15 MPa and finally evacuating during approximately 30 minutes. As observed on the BSE images (Figure 3.19) and EDX results (Table 3.11), the composition of the desorbed sample differs from the one of the parent compound as significant amounts of Mg and $Mg_3(Ag,Pd)$ phases are detected along with the $Mg_6Pd_{1-x}Ag_x$ main phase. XRPD refinement results (Table 3.12) show that 75.3 wt.% of the ρ-phase was reformed after desorption, with a lattice parameter (a = 20.191 Å) close to the one of the former pseudo-binary compound (a = 20.188 Å). This last data, together with chemical composition obtained by EDX, suggests a similar composition in the main phase than in the parent compound.

Table 3.11. Chemical composition of the desorbed $Mg_6Pd_{0.5}Ag_{0.5}$ sample as obtained by SEM-EDX analyses.

Sample	Phase	Mg (at.%)	Pd (at.%)	Ag (at.%)
MPAdes	ε-Mg_3Ag	78(3)	10(2)	12(2)
	ρ-Mg_6Pd	82(3)	10(1)	8(1)
	Mg	95(4)	2(2)	3(2)

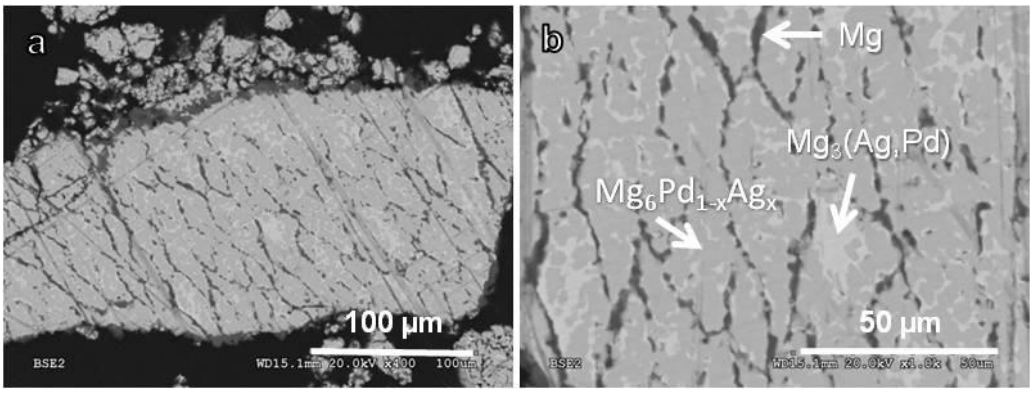

Figure 3.19. BSE images of the desorbed $Mg_6Pd_{0.5}Ag_{0.5}$ sample.

Table 3.12. Rietveld refinement results of the desorbed $Mg_6Pd_{0.5}Ag_{0.5}$ sample.

Sample	Phase	S.G.	Phase amount (wt.%)	Cell parameters (Å)	R_B	R_{wp}
MPAdes	Mg	*P*6$_3$/*mmc*	14.0(4)	*a* = 3.2081(1) *c* = 5.2088(2)	4.89	21.6
	ρ-Mg_6Pd	*F*-43*m*	75.3(6)	*a* = 20.1910(1)	6.63	
	ε-Mg_3Ag	*Fm*-3	10.7(2)	*a* = 17.5454(3)	12.9	

However, this limited reversibility on the alloy composition did not affect the reversible hydrogen capacity which was maintained after at least 3 cycles of absorption and desorption. This also confirms that the residual ε-Mg_3(Ag,Pd) phase should be active towards hydrogenation, since its occurrence is not detrimental for the reversible capacity.

2.2.4 Kinetic characterization

The desorption kinetics of the MPAH3 sample has been analysed by means of thermal desorption spectroscopy at different heating rates. The obtained hydrogen desorption spectra are represented in Figure 3.20. The spectra consist of a single desorption peak, with onset temperature at 665 K at the slowest heating rate. The activation energy of hydrogen desorption has been calculated using the Kissinger equation. This energy, 169(8) kJ/molH_2, is comparable with that reported for H-desorption from MgH_2, which ranges from 140 to 172 kJ/molH_2 [21–26]. This suggests that the controlling step for H-desorption is the nucleation and growth of the Mg phase controlled by the Mg-MgH_2 interface displacement.

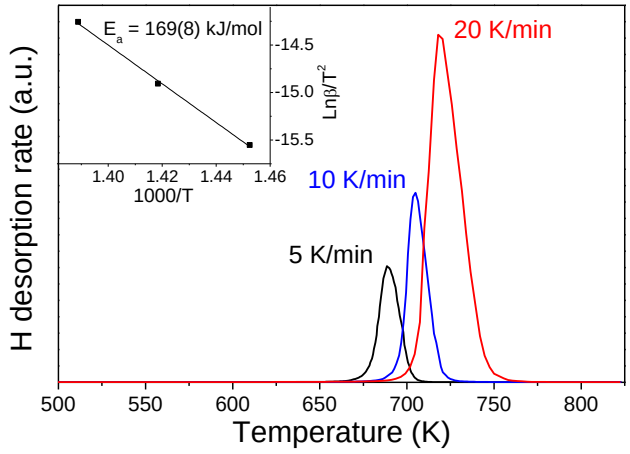

Figure 3.20. TDS spectra of the MPAH3 sample measured at heating rates of 5, 10 and 20 K/min. The inset displays the Kissinger plot with the corresponding activation energy.

As for kinetics during absorption, no improvement is achieved with Ag substitution, as can be observed in Figure 3.21. The absorption is slightly faster for $Mg_6Pd_{0.5}Ag_{0.5}$ than for Mg_6Pd during the first half of the reaction but then slows down and 90 % of the sample is hydrided in about 100 min, which is significantly slower than the 60 min observed for the Mg_6Pd.

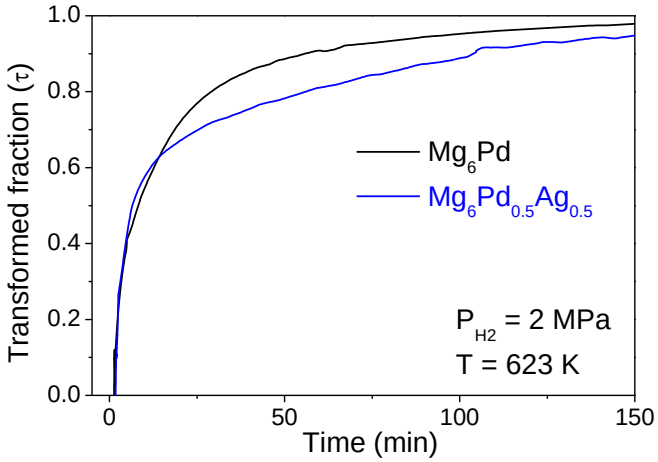

Figure 3.21. Comparison of the kinetics for the Mg_6Pd and $Mg_6Pd_{0.5}Ag_{0.5}$ samples during the third absorption at 623 K and 2 MPa of hydrogen pressure.

2.3 Discussion on the stability of the $Mg_6Pd_{1-x}Ag_x$-H system

Substituting Pd by Ag atoms in the Mg_6Pd structure is possible up to a solubility limit of 7.2 at.% Ag. The hydrogenation of this pseudo-binary compound leads to a similar reaction pathway than the one observed for the Mg_6Pd compound. However, the resulting thermodynamics differ significantly. The first absorption plateau, corresponding to reaction (3.5), is similar to the Mg/MgH_2 equilibrium as can be observed in Figure 3.22. According to Hess's law and reaction (3.5), this implies that $\Delta_fH(Mg_3Ag_{0.5}Pd_{0.5})$ and $\Delta_fH(Mg_6Pd_{0.5}Ag_{0.5})$ must have very close values, as it was calculated for the non-substituted compound. For the second plateau, corresponding to reaction (3.6), the destabilization seems obvious, with a strong slope reduction in the Van't Hoff plot (Figure 3.22) that reflects a much less negative enthalpy of absorption (ΔH_2 = -35(4) kJ/molH_2). However, because of the lower entropy variation associated to the second plateau (ΔS_2 = -84(6) J/K.molH_2), the equilibrium pressure at a given temperature does not increase as much as expected for such enthalpy reduction.

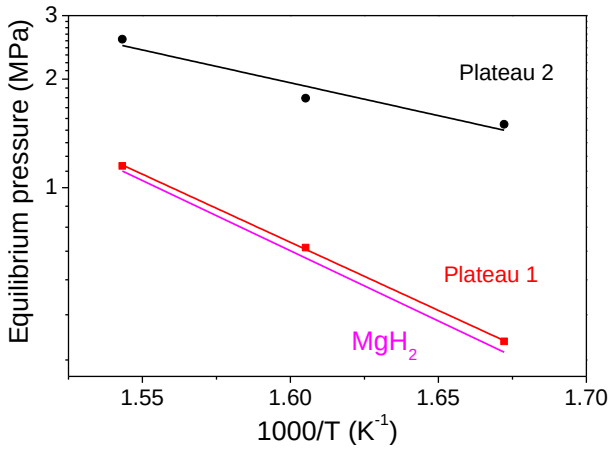

Figure 3.22. Van't Hoff plots of the two absorption plateaus of the $Mg_6Pd_{0.5}Ag_{0.5}$ compound compared with the Mg/MgH_2 system considering ΔH = -74.5 kJ/molH_2 and ΔS = -135 J/K molH_2 [10].

It should be noted that the measured entropy variation is strikingly low. It almost approaches that reported for adsorbents ($\Delta S \sim 8R$ = 66.5 J/K.molH_2 [27]). This less negative value of ΔS is probably related to the contribution of the solid reactants. Certainly, the complexity of the disproportionation reaction path leading to a multi-phase and fine microstructure, the atomic disorder due to the presence of pseudo-binary

compounds and the occurrence of linear defects in the end-products (microstrains as high as 0.20 and 0.28 % for Mg_3(Ag,Pd) and Mg(Pd,Ag) phases have been evaluated), might lead to a significant reduction of the reaction entropy. However, the occurrence of sloping and ill-defined plateaus in this system imposes to consider the entropy value as only approximate. Further confirmation by using calorimetric measurements and/or *ab-initio* calculations is needed. Questionable results related to low entropy variations have been reported in the past as concerns, for instance, the $ZrMn_{2+x}$-H system [28].

3 Substituting Pd by Cu

Though Pd and Cu do not belong to the same period and group, they are located close in the periodic table. Moreover, they are fully miscible in the liquid state [29]. Because of that, it is expected that Cu can substitute Pd atoms in the Mg_6Pd intermetallic phase. As presented in Chapter 1 section 3.1.1, Cu-Mg alloys have already been investigated for hydrogen storage [30–32], and Cu was found to destabilize MgH_2 and to have catalytic properties for hydrogen sorption [31]. Although no Mg-Pd-Cu ternary phase diagram has been reported in the literature, the existence of a pseudo-binary $Mg_6Pd_{1-x}Cu_x$ phase is expected.

$Mg_6Pd_{1-x}Cu_x$ alloy ingots have been prepared for three different Cu contents with nominal compositions: $Mg_{85.7}Pd_{7.1}Cu_{7.1}$, $Mg_{85.8}Pd_{10.3}Cu_{3.9}$ and $Mg_{85.7}Pd_{11.8}Cu_{2.5}$. They will be designated as x = 0.5, x = 0.3 and x = 0.2, respectively. The x = 0.5 sample was obtained with the same procedure than for Ag-substituted sample. In the case of the other two compositions, pre-alloyed Mg_6Pd compound as well as Mg and Cu elements were introduced in a steel crucible that was then hermetically sealed under argon and placed in a high temperature electric furnace. They were then heated at 1000 K during 3 hours. All samples were submitted to a 2 days annealing at 673 K before structural characterization.

3.1 Characterization of the alloy

3.1.1 Micro-structure and chemical composition

Figure 3.23 shows the BSE images of the three studied $Mg_6Pd_{1-x}Cu_x$ samples. In all cases, three phases, which proportion depends on Cu content, are observed as black, dark grey and light grey areas. EDX analyses proved that these phases are Mg,

Mg_6(Pd,Cu) and Mg_2(Cu,Pd), respectively. Thus, for x = 0.5, large Mg dendrites are observed in black (Figure 3.23a). These dendrites are surrounded by small precipitates (< 5 µm) belonging to the three different phases (Figure 3.23b). At lower Cu content (*i.e.* for x = 0.3 and 0.2), a large amount of the dark grey Mg_6(Pd,Cu) phase dominates with still minor eutectic areas of light grey Mg_2(Cu,Pd) and black Mg phases. EDX analyses of the matrix (dark grey) in both samples indicate that the Mg_6(Pd,Cu)-type phase has a low Cu solubility.

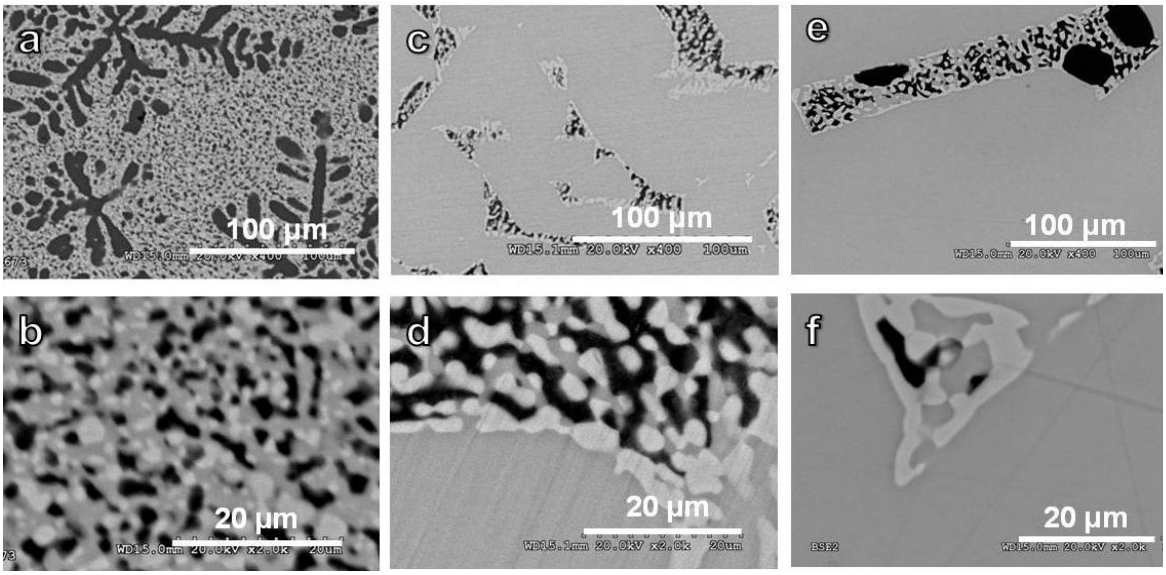

Figure 3.23. BSE images of $Mg_6Pd_{1-x}Cu_x$ compounds with x = 0.5 (a and b), x = 0.3 (c and d) and x = 0.2 (e and f). Top and bottom images show different magnification views.

Accurate chemical compositions have been obtained for the three samples by EPMA and results are gathered in Table 3.13. For all samples, the Mg concentration of the pseudo-binary ρ-phase is around 86.0 at.%. In contrast, the relative amount of Cu and Pd varies depending on the nominal composition of the alloy. The Cu concentration gradually decreases from 3.9(5) at.% for x = 0.5 down to 1.8(4) at.% for x = 0.2. As for the Mg_2(Cu,Pd) phase, its composition is roughly the same for all samples with 67.5 at.% Mg, 27.5 at.% Cu and only 5 at.% Pd.

Table 3.13. Chemical compositions of $Mg_6(Pd,Cu)$ and $Mg_2(Cu,Pd)$ pseudo-binary phases obtained by EPMA on x = 0.5, 0.3 and 0.2 samples.

Sample	Phase	Mg (at.%)	Pd (at.%)	Cu (at.%)
x = 0.5	ρ-$Mg_6Pd_{1-x}Cu_x$	86.0(5)	10.2(2)	3.9(5)
	$Mg_2Cu_{1-y}Pd_y$	67.9(8)	4.7(8)	27.4(2)
x = 0.3	ρ-$Mg_6Pd_{1-x}Cu_x$	86.1(1)	11.6(2)	2.3(2)
	$Mg_2Cu_{1-y}Pd_y$	67.3(5)	5.0(3)	27.7(8)
x = 0.2	ρ-$Mg_6Pd_{1-x}Cu_x$	85.9(1)	12.3(4)	1.8(4)
	$Mg_2Cu_{1-y}Pd_y$	67.2(1.0)	4.8(3)	28.0(9)

3.1.2 Structural properties

The crystal structure of all Cu-substituted samples has been analysed by XRPD and refined using the Rietveld method. The analysed diffraction patterns are presented in Figure 3.24. The width of the diffraction peaks reflects the microstructures previously observed by SEM. The presence of small precipitates in the x = 0.5 sample leads to wider diffraction peaks than for the other two samples. The three phases previously identified by SEM-EDX are also indexed by XRPD. Details on their cell parameters and relative amounts are summarized in Table 3.14. At the highest Cu concentration (*i.e.* x = 0.5), the three phases are present in significant amounts, with nearly 50 wt.% of the pseudo-binary $Mg_6Pd_{1-x}Cu_x$ phase. When x = 0.3, the amount of Mg is negligible, and that of $Mg_6Pd_{1-x}Cu_x$ is close to 90 wt.%. For x = 0.2, the alloy is almost $Mg_6Pd_{1-x}Cu_x$ single phase.

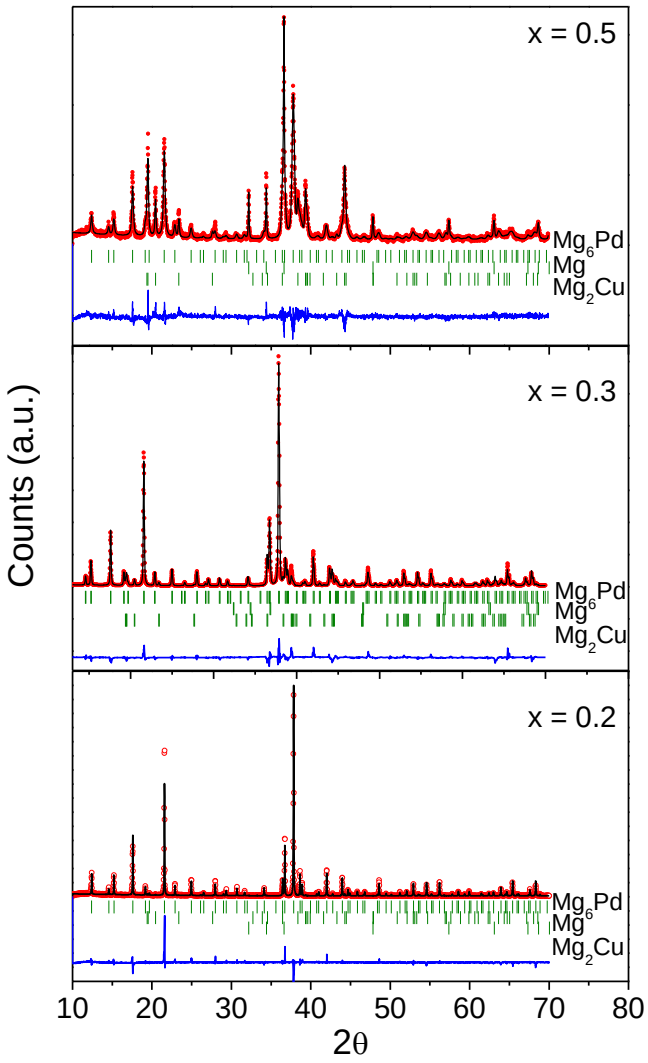

Figure 3.24. XRPD patterns (Cu K_α radiation) of the $Mg_6Pd_{1-x}Cu_x$ alloys for x = 0.5, 0.3 and 0.2 (dots) and the corresponding Rietveld refinement (solid line). Bragg peak positions are plotted as vertical bars. The line below represents the difference between the calculated and the experimental patterns.

Table 3.14. Rietveld refinements results of the $Mg_6Pd_{1-x}Cu_x$ alloys for x = 0.5, 0.3 and 0.2 samples.

Sample	Phase	S.G.	Phase amount (wt.%)	Cell parameters (Å)	R_B	R_{wp}
x = 0.5	ρ-$Mg_6Pd_{1-x}Cu_x$	*F*-43*m*	49.3(1.0)	*a* = 20.182(1)	6.5	13.5
	Mg	*P*6$_3$/*mmc*	26.7(6)	*a* = 3.209(1) *c* = 5.210(1)	5.5	
	$Mg_2Cu_{1-y}Pd_y$	*P*6$_2$22	24.0(9)	*a* = 5.285(1) *c* = 13.648(1)	9.2	
x = 0.3	ρ-$Mg_6Pd_{1-x}Cu_x$	*F*-43*m*	88.9(9)	*a* = 20.161(1)	8.1	13.7
	Mg	*P*6$_3$/*mmc*	0.2(1)	*a* = 3.209* *c* = 5.210*	20.9	
	$Mg_2Cu_{1-y}Pd_y$	*P*6$_2$22	10.9(2)	*a* = 5.283(1) *c* = 13.648(1)	18.6	
x = 0.2	ρ-$Mg_6Pd_{1-x}Cu_x$	*F*-43*m*	98(2)	*a* = 20.161(1)	8.9	17.2
	Mg	*P*6$_3$/*mmc*	0.8(2)	*a* = 3.209(1) *c* = 5.210(1)	32.6	
	$Mg_2Cu_{1-y}Pd_y$	*P*6$_2$22	1.2(2)	*a* = 5.285(1) *c* = 13.645(1)	34.1	

* Not refined

As for $Mg_6Pd_{1-x}Ag_x$, the ρ-phase crystallizes in the *F*-43*m* space group. In this case, the electron density of Cu and Pd atoms differs sufficiently to refine their respective occupancy on Pd sites. Hence, refinements have been performed taking into account the previously explained structural constraints on Mg and Pd positions and by allowing Pd by Cu partial substitution on Pd sites. Table 3.15 displays atomic sites as well as their atomic coordinates and refined SOF. The chemical composition of the phase resulting from Rietveld refinement is also given. Occupancy on site 12 has been restricted to Pd and Mg atoms, considering that Cu, which has a smaller radius than Pd, will preferentially locate on sites with low coordination number (CN) (*i.e*. sites 10, 11 and 13 with CN = 12, 10 and 12, respectively). Indeed, it was previously demonstrated for Pd by Ni substitution in the Mg_6Pd phase that Ni occupancy on site 12 (CN = 13) was almost negligible [33]. Site 11, which has the lower CN (CN = 10), shows the highest Cu occupancy while site 13 remains mostly occupied by Pd atoms.

Table 3.15. Refined positional parameters and occupancy factors (SOF) for the $Mg_6Pd_{1-x}Cu_x$ phase in x = 0.5, 0.3 and 0.2 samples. The last three rows correspond to the chemical composition of the phase according to Rietveld refinements.

Site n°	Atom	Wyckoff position	x = 0.5				x = 0.3				x = 0.2			
			SOF	Atomic coordinates			SOF	Atomic coordinates			SOF	Atomic coordinates		
				x	*y*	*z*		*x*	*y*	*z*		*x*	*y*	*z*
1	Mg	48*h*	1	0.137(1)	*x*	0.037(2)	1	0.145(1)	*x*	0.032(1)	1	0.143(1)	*x*	0.033(1)
2	Mg	48*h*	1	0.096(1)	*x*	0.276(2)	1	0.095(1)	*x*	0.273(1)	1	0.094(1)	*x*	0.272(1)
3	Mg	48*h*	1	0.160(1)	*x*	0.525(2)	1	0.150(1)	*x*	0.525(1)	1	0.152(1)	*x*	0.527(1)
4	Mg	48*h*	1	0.054(1)	*x*	0.768(2)	1	0.055(1)	*x*	0.766(1)	1	0.053(1)	*x*	0.769(1)
5	Mg	48*h*	1	0.201(1)	*x*	0.911(2)	1	0.202(1)	*x*	0.915(1)	1	0.201(1)	*x*	0.913(1)
6	Mg	24*f*	1	0.100(2)	0	0	1	0.099(1)	0	0	1	0.103(1)	0	0
7	Mg	24*f*	1	0.387(2)	0	0	1	0.387(1)	0	0	1	0.385(1)	0	0
8	Mg	24*g*	1	0.067(2)	0.25	0.25	1	0.055(1)	0.25	0.25	1	0.058(1)	0.25	0.25
9	Mg	16*e*	1	0.304(2)	*x*	*x*	1	0.301(1)	*x*	*x*	1	0.302(1)	*x*	*x*
10	Pd Cu	16*e*	0.8(1) 0.2(1)	0.167(1)	*x*	*x*	0.89(2) 0.11(2)	0.168(1)	*x*	*x*	1 0	0.168(1)	*x*	*x*
11	Pd Cu	16*e*	0.2(2) 0.8(2)	0.404(1)	*x*	*x*	0.67(2) 0.33(2)	0.407(1)	*x*	*x*	0.85(9) 0.15(9)	0.406(1)	*x*	*x*
12	Pd Cu Mg	16*e*	0.18(3) 0 0.82(3)	0.673(1)	*x*	*x*	0.13(2) 0 0.87(2)	0.673(1)	*x*	*x*	0.20(3) 0 0.80(3)	0.673(1)	*x*	*x*
13	Pd Cu	16*e*	1 0	0.901(1)	*x*	*x*	0.92(2) 0.08(2)	0.900(1)	*x*	*x*	0.99(9) 0.01(9)	0.900(1)	*x*	*x*
14	Mg	4*d*	0.4(4)	0.25	0.25	0.75	0.7(2)	0.25	0.25	0.75	0.8(2)	0.25	0.25	0.75
Refined atomic composition		**Mg (at.%)** **Pd (at.%)** **Cu (at.%)**	87.1(7) 8.9(1.4) 4.0(1.4)				87.3(3) 10.6(7) 2.1(6)				87.1(4) 12.3(8) 0.6(7)			

The evolution of the $Mg_6Pd_{1-x}Cu_x$ phase composition as determined from XRPD Rietveld refinements follows the same trend than from EPMA analysis (Figure 3.25), though Mg concentration seems to be over-estimated in Rietveld refinements. It can be concluded that Pd by Cu substitution increases with Cu-content in the alloy.

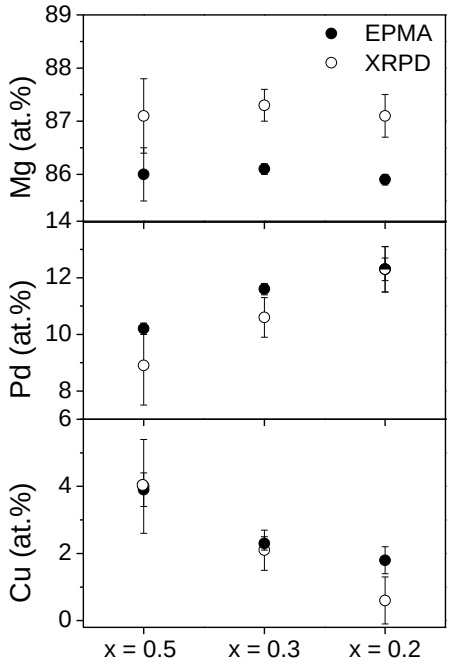

Figure 3.25. Chemical composition of the $Mg_6Pd_{1-x}Cu_x$ ρ-phase measured by EPMA and by XRPD Rietveld refinements for x = 0.5, 0.3 and 0.2 samples.

The lattice parameter of the ρ-phase obtained by XRPD refinements (Table 3.14) exhibits identical values for x = 0.3 and 0.2 (a = 20.161(1) Å). This suggests that the composition of the phase is almost the same, in agreement with EPMA results. In contrast, the sample with x = 0.5 exhibits a significantly larger cell (a = 20.182 Å). Considering the atomic radii of the phase constituents (r_{Mg} = 1.60 Å, r_{Pd} = 1.37 Å and r_{Cu} =1.28 Å), a cell reduction is expected for constant Mg content when the Cu content increases. Strikingly, the opposite behaviour is observed, which can only be explained by a higher Mg content in the x = 0.5 sample. This discrepancy can be understood by the larger error in EPMA measurements for the x = 0.5 sample as a result of its finer microstructure (see Figure 3.23 a and b).

As for the $Mg_2Cu_{1-y}Pd_y$ secondary phase, it is worth mentioning that its crystal structure differs from those of the end binary compounds: Mg_2Cu crystallizes in the orthorhombic symmetry (S.G. *Fddd*) whereas Mg_2Pd crystallizes in the cubic one (S.G. *Fd*-3*m*). Indeed, the crystal structure of the $Mg_2Cu_{1-y}Pd_y$ phase with 5 at.% Pd was found to be hexagonal and the corresponding diffraction peaks can be indexed in the same space group as the Mg_2Ni phase (S.G. $P6_222$). In other words, the (Cu,Pd)-pseudo atom behaves as a Ni one from the structural point of view. Further investigations on the structural stability of this phase as function of Pd/Cu ratio are in progress but beyond the scope of the present thesis.

3.1.3 Thermal stability

The thermal stability of the Cu-substituted compound has been probed on the quasi-single phase sample (x = 0.2) by DSC (Figure 3.26).

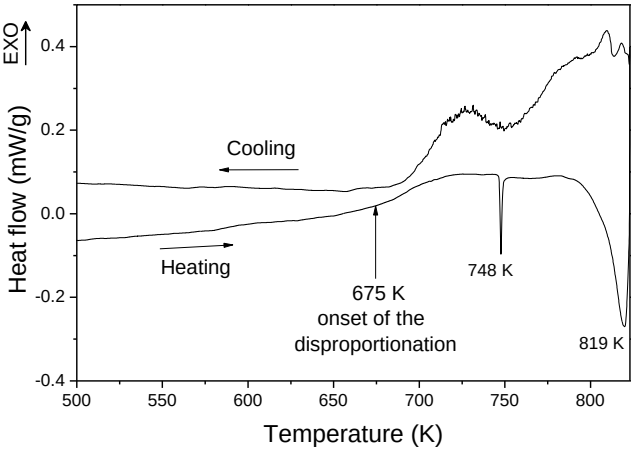

Figure 3.26. DSC scan of the $Mg_6Pd_{0.8}Cu_{0.2}$ sample during heating and cooling at 5 K/min.

As for the Mg-Pd-Ag system, the complexity of the Mg-Pd-Cu system does not allow us to provide a complete description of the disproportionation mechanism of the ρ-phase. However some interesting information can be extracted from this data on the thermal stability of this material. On heating, an exothermic bump appears above 675 K. Next, we observe two endothermic peaks: a sharp one at 748 K and a broad one at 819 K. The bump temperature matches with the annealing treatment for sample synthesis and may suggest that the ρ-phase starts decomposing into Mg_6Pd, Mg_2Cu and Mg

phases just above the alloy annealing temperature. Next, the first endothermic peak can be attributed to the melting of a Mg_2Cu/Mg mixture, which is reported to occur at 758 K [34]. The width of the second peak leads to assume a progressive melting of Mg_6Pd phase with remaining Mg. Once again, the eutectic melting of Mg and Mg_6Pd phases at 812 K is in fairly good agreement with the temperature of the second peak at 819 K.

On cooling, a complex behaviour is observed with several broad and overlapped exothermic peaks, making difficult to identify with certainty the solidification and reformation of the different phases.

3.1.4 Cu solubility – ternary phase diagram

At the light of the results obtained for several ternary alloys of the Mg-Pd-Cu system, a phase diagram in the Mg-rich corner is proposed for the first time in Figure 3.27. The phase composition of the x = 0.5 sample establishes the composition of the three phased (Mg, Mg_6(Pd,Cu) and Mg_2(Cu,Pd)) domain, while that of x = 0.3 sample shows the equilibrium between Mg_6(Pd,Cu) and Mg_2(Cu,Pd) phases. The x = 0.2 sample can be considered within the homogeneity range of the ρ-phase.

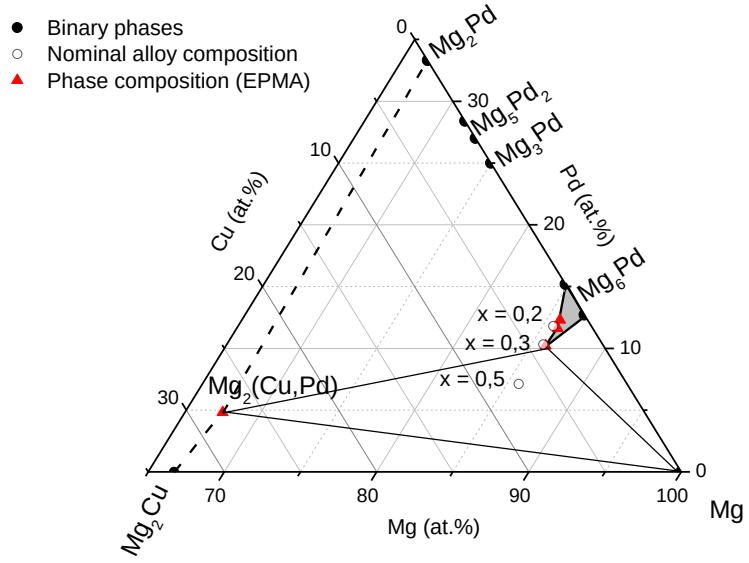

Figure 3.27. Isothermal section at 673 K of the Mg-Pd-Cu ternary phase diagram in the Mg-rich corner. Experimental points for the ρ-phase and Mg_2(Cu,Pd) are obtained from EPMA analyses (triangle symbols). The nominal composition of each sample is marked by empty dots.

The most relevant feature of this phase diagram concerns the rather small solubility limit of Cu in Mg_6Pd as compared to other TM substitutions such as Ni (9 at.%) [35] or Ag (7.2 at.%). Indeed, the Cu solubility limit only attains 3.9 at.%. In addition, at least three different phases should exist along the Mg_2Cu-Mg_2Pd line, since three compounds with distinct crystal structures (Mg_2Cu, Mg_2Pd and $Mg_2(Cu,Pd)$ with 5 at.% Pd) have been evidenced.

3.2 Hydrogenation properties

The hydrogenation properties of the $Mg_6Pd_{1-x}Cu_x$ ρ-phase have been determined using the x = 0.3 sample. This sample contains close to 90 wt.% of the ρ-phase.

3.2.1 Thermodynamics: PCI curves

The thermodynamic properties have been evaluated by measuring the PCI curves at 595, 628 and 648 K between 0.01 and 3 MPa of hydrogen pressure (Figure 3.28). The isotherms exhibit two plateau pressures and a maximum hydrogen content of 3.2 wt.%.

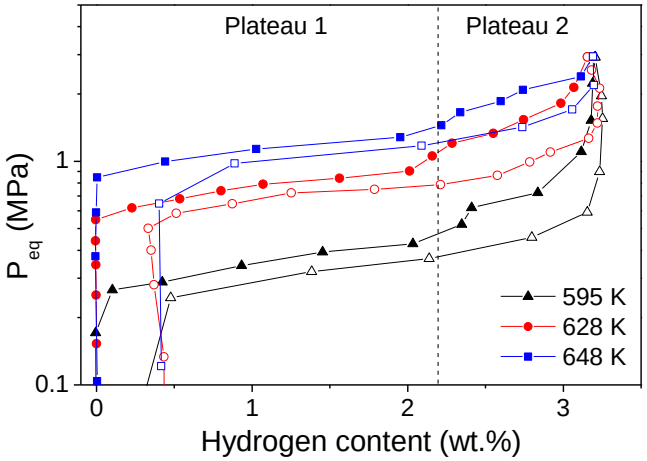

Figure 3.28. PCI curves of the $Mg_6Pd_{0.7}Cu_{0.3}$ compound during absorption (full symbols) and desorption (empty symbols) at 595, 628 and 648 K.

The equilibrium pressures at the middle of each plateau of absorption (Table 3.16) have been used to draw the Van't Hoff plots and calculate the corresponding enthalpy and entropy changes (Figure 3.29). The obtained values for the first plateau (ΔH_1 = -71(3) kJ/molH_2 and ΔS_1 = -130(5) J/K.molH_2) are comparable with those of the

Mg_6Pd and $Mg_6Pd_{0.5}Ag_{0.5}$ compounds. The equilibrium of the second plateau (ΔH_2 = -62(4) kJ/molH_2 and ΔS_2 = -120(6) J/K.molH_2) is slightly destabilized as compared to Mg_6Pd, but still more stable than for $Mg_6Pd_{0.5}Ag_{0.5}$.

Table 3.16. Equilibrium pressures corresponding to absorption plateaus 1 and 2 of the $Mg_6Pd_{0.7}Cu_{0.3}$ PCI curves.

	P_{eq} (MPa)	
T (K)	**Plateau 1 @1 wt.% H**	**Plateau 2 @2.5 wt.% H**
595	0.350	0.641
628	0.775	1.300
648	1.126	1.780

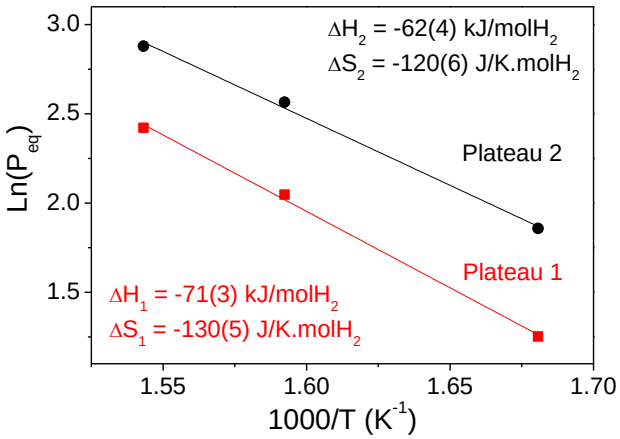

Figure 3.29. Van't Hoff plots corresponding to the two absorption plateaus of the $Mg_6Pd_{0.7}Cu_{0.3}$ isotherms.

3.2.2 Hydrogenation mechanism

The hydrogenation path of the $Mg_6Pd_{1-x}Cu_x$ compound has been determined by analysing the composition of partially (1.4 wt.% H, labelled as MPCH1.4) and totally (3.2 wt.% H, labelled as MPCH3.2) hydrided samples. MPCH1.4 corresponds to the middle of the first plateau and MPCH3.2 matches with the end of the second plateau. Their XRPD patterns compared to the parent alloy are displayed in Figure 3.30 while the corresponding Rietveld refinements results are detailed in Table 3.17. The partially hydrided sample (MPCH1.4) is composed of MgH_2 together with the Mg_2Cu phase and a large amount of remaining $Mg_6Pd_{1-x}Cu_x$. A small amount of the cubic γ-$Mg_{57}Pd_{13}$ is also observed. At further hydrogenation, the Mg_5Pd_2 phase is formed along with more

Mg_2Cu and MgH_2, at the expense of the ρ-phase which totally disappeared. As a general trend, $Mg_6Pd_{1-x}Cu_x$ decomposes progressively to form the MgH_2 phase together with Mg_2Cu and a Mg-Pd intermetallic compound which depletes in Mg with increasing H-content. The cell parameter of the ρ-phase (a = 20.107(1) Å) is significantly reduced in the MPCH1.4 sample as compared to the same phase before hydrogenation (a = 20.161(1) Å), suggesting a depletion in Mg which atomic radius is the largest.

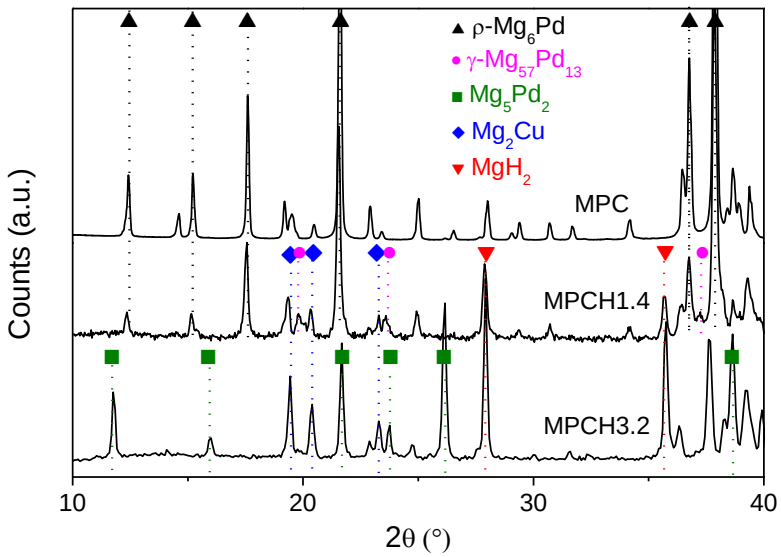

Figure 3.30. XRPD patterns (Cu K_α radiation) of the $Mg_6Pd_{0.7}Cu_{0.3}$ alloy before hydrogenation and hydrided to 1.4 wt.% H and 3.2 wt.% H.

Table 3.17. Rietveld refinements results of partially hydrided $Mg_6Pd_{0.7}Cu_{0.3}$ samples.

Sample	Phase	S.G.	Phase amount (wt.%)	Cell parameters (Å)	R_B	R_{wp}
MPCH1.4	ρ-$Mg_6Pd_{1-x}Cu_x$	*F-43m*	60(2)	a = 20.107(1)	10.3	7.5
	$Mg_2Cu_{1-y}Pd_y$	*P6₂22*	16(1)	a = 5.2873(3) c = 13.684(1)	12.5	
	γ-$Mg_{57}Pd_{13}$	*Pm-3*	7(1)	a = 14.049(1)	17.2	
	MgH_2	*P4₂/mnm*	17(1)	a =4.5123(4) c = 3.0186(4)	10.8	
MPCH3.2	$Mg_5Pd_{2-z}Cu_z$	*P6₃/mmc*	36(1)	a = 8.649(4) c = 8.188(5)	12.4	8.9
	$Mg_2Cu_{1-y}Pd_y$	*P6₂22*	22(2)	a = 5.300(1) c = 13.679(1)	16.7	
	MgH_2	*P4₂/mnm*	42(1)	a =4.5143(2) c = 3.0204(2)	4.97	

The same phases have been identified on the BSE images of Figure 3.31, except the γ-$Mg_{57}Pd_{13}$ phase which amount is too low. All the intermetallic phases exhibit Pd by Cu substitution and *vice versa*. The amount of substituted atoms has been determined by EPMA analyses on both hydrided samples for the three main pseudo-binary phases (Table 3.18). The amount of Cu substituting Pd in the ρ-phase was slightly reduced in the MPCH1.4 sample (1.8(3) at.% Cu) as compared to the same phase in the parent alloy (2.3(2) at.% Cu). But the decrease in Mg concentration is more significant as it loses close to 2 at.% Mg in the partially hydrided sample. This result is consistent with the cell parameter reduction previously mentioned. As regard to the $Mg_2Cu_{1-y}Pd_y$ phase, its composition remains almost constant, independently of the hydrogen concentration in the sample, with ~10 at.% Pd (*i.e.* y = 0.3). Finally, the $Mg_5Pd_{2-z}Cu_z$ phase exhibits little Cu solubility with a Cu concentration of 5 at.%, corresponding to z = 0.3.

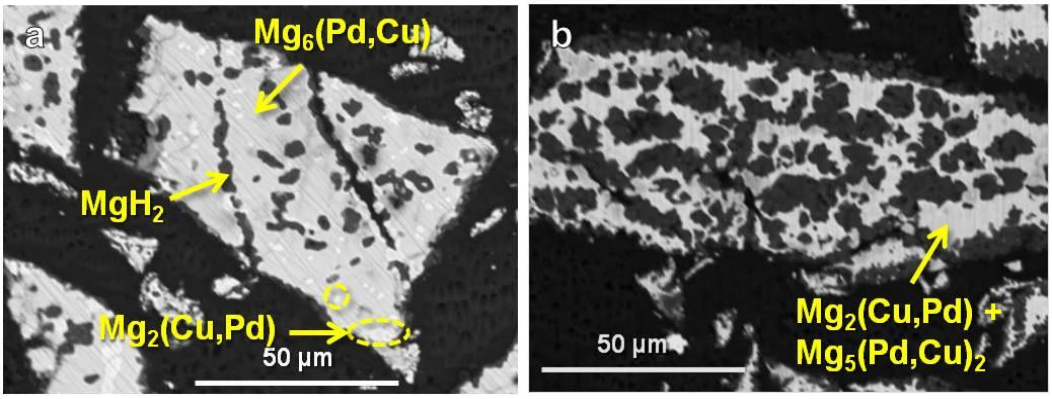

Figure 3.31. BSE images of a) MPCH1.4 and c) MPCH3.2 samples.

Table 3.18. Chemical composition of partially hydrided $Mg_6Pd_{0.7}Cu_{0.3}$ samples as obtained by EPMA analyses.

Sample	Phase	Mg (at.%)	Pd (at.%)	Cu (at.%)
MPCH1.4	ρ-$Mg_6Pd_{1-x}Cu_x$	84.2(2)	14.0(2)	1.8(3)
	$Mg_2Cu_{1-y}Pd_y$	67(1)	9(2)	24(2)
MPCH3.2	$Mg_2Cu_{1-y}Pd_y$	67(3)	10(2)	23(3)
	$Mg_5Pd_{2-z}Cu_z$	71(1)	24(2)	5(2)

Based on these results, the hydrogenation mechanism can be described through the following hydrogenation reactions (for the sake of simplicity, γ-$Mg_{57}Pd_{13}$ is written as $Mg_{4.4}Pd$ and no Cu solubility is considered in the Mg-Pd intermetallic phases):

$$7\ Mg_6Pd_{0.7}Cu_{0.3} + 18.4\ H_2 \leftrightarrow 3\ Mg_2Cu_{0.7}Pd_{0.3} + 4\ Mg_{4.4}Pd + 18.4\ MgH_2 \quad \textbf{(3.8)}$$

$$3\ Mg_2Cu_{0.7}Pd_{0.3} + 4\ Mg_{4.4}Pd + 18.4\ MgH_2 + 7.6\ H_2 \leftrightarrow 3\ Mg_2Cu_{0.7}Pd_{0.3} + 2\ Mg_5Pd_2 + 26\ MgH_2 \quad \textbf{(3.9)}$$

Reaction (3.8) leads to a theoretical hydrogen absorption of 2.2 wt.% H, matching perfectly with the end of the first plateau of absorption. This plateau corresponds to the decomposition of the initial pseudo-binary $Mg_6Pd_{1-x}Cu_x$ phase into the Cu-rich $Mg_2Cu_{1-y}Pd_y$ and a Pd-rich $Mg_{4.4}Pd$ phase. Concerning this last phase, no information allows to state on the occurrence of Cu solubility.

The additional hydrogen uptake corresponding to reaction (3.9) is of 0.9 wt.% H, in agreement with the hydrogen content at the end of the second plateau of absorption. During this stage of hydrogenation, the $Mg_{4.4}Pd$ depletes in Mg which is immediately hydrided, and forms the Mg_5Pd_2 intermetallic containing a small amount of Cu.

In spite of having no result at higher H-content, we can assume that a third plateau would occur by the decomposition of the Mg_5Pd_2 into MgPd and more MgH_2, as it happens for the Mg_6Pd compound. In addition, the decomposition of the $Mg_2Cu_{1-y}Pd_y$ is also expected, as Mg_2Cu is known to react with hydrogen to form MgH_2 and $MgCu_2$. However, this possibility is only speculative as we do not have information on the stability of the pseudo-binary $Mg_2Cu_{1-y}Pd_y$ phase. The following hypothetic reaction can be proposed:

$$3\ Mg_2Cu_{0.7}Pd_{0.3} + 2\ Mg_5Pd_2 + 26\ MgH_2 + 10.5\ H_2 \leftrightarrow 1.5\ MgCu_{1.4}Pd_{0.6} + 4\ MgPd + 36.5\ MgH_2 \quad \textbf{(3.10)}$$

This last reaction would provide an additional hydrogen capacity 1.2 wt.% H, for a total of 4.3 wt.% H corresponding to the global reaction.

The overall hydrogenation mechanism is illustrated in Figure 3.32. In summary, the $Mg_6Pd_{1-x}Cu_x$ compound reacts with hydrogen to form MgH_2 together with Cu-rich ($Mg_2(Cu,Pd)$ and $Mg(Cu,Pd)_2$) and Pd-rich ($Mg_{4.4}Pd$, Mg_5Pd_2 and MgPd) intermetallic phases which occurrence and amount depend on the progress of the hydrogenation process.

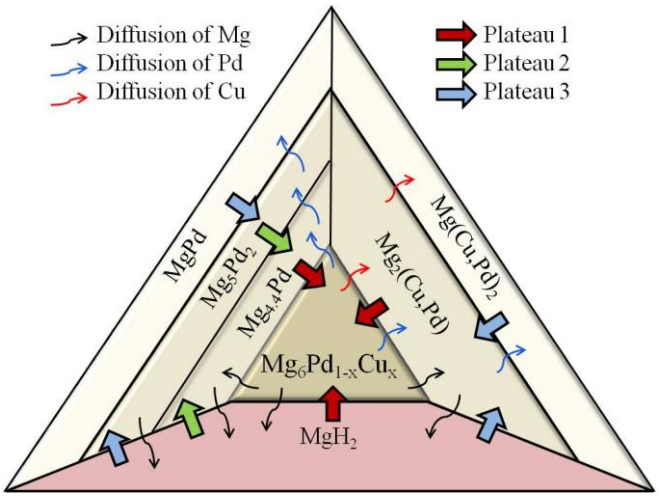

Figure 3.32. Schematic illustration of the phase growth during hydrogenation of the $Mg_6Pd_{1-x}Cu_x$ compound. Large arrows represent the growing direction of the phases. Thin arrows symbolize the diffusion of each element.

3.2.3 Reversibility

A totally desorbed sample (MPCdes) has been prepared at T = 623 K by two successive desorption steps (P < 0.15 MPa) and final vacuum during 30 minutes. Its phase composition has been analysed by EPMA. The major part of the compound consisted of the $Mg_6Pd_{1-x}Cu_x$ ρ-phase. In addition, a small amount of $Mg_2Cu_{1-y}Pd_y$ was also detected, which appears in light grey areas on the BSE image of Figure 3.33. The chemical atomic composition of the ρ-phase was found to be $Mg_{86.1(6)}Pd_{11.6(5)}Cu_{2.3(3)}$, showing that we recover exactly the same composition as in the parent compound.

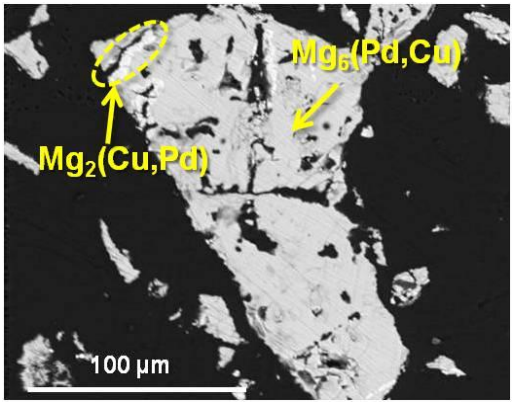

Figure 3.33. BSE image of the $Mg_6Pd_{0.7}Cu_{0.3}$ compound after desorption.

XRPD refinement on the desorbed sample (Table 3.19) shows that the relative phase amounts are very close to the composition of the original compound with about 90 wt.% of the ρ-phase. The cell parameter of this phase is only 0.01 Å larger than in the parent compound.

Table 3.19. Rietveld refinement results of the desorbed $Mg_6Pd_{0.7}Cu_{0.3}$ compound.

Sample	Phase	S.G.	Phase amount (wt.%)	Cell parameters (Å)	R_B	R_{wp}
MPCdes	ρ-$Mg_6Pd_{1-x}Cu_x$	*F*-43*m*	92(2)	*a* = 20.1716(3)	9.84	7.08
	$Mg_2Cu_{1-y}Pd_y$	$P6_222$	8(1)	*a* = 5.2846(3) c = 13.656(1)	13	

Thus, full reversibility of the $Mg_6Pd_{0.7}Cu_{0.3}$ compound after hydrogen absorption and desorption has been achieved while the Cu solubility is maintained in the ρ-phase.

3.2.4 Kinetic characterization

The activation energy involved during hydrogen desorption from the MPCH3.2 sample has been determined using the Kissinger equation applied to the TDS spectra of Figure 3.34.

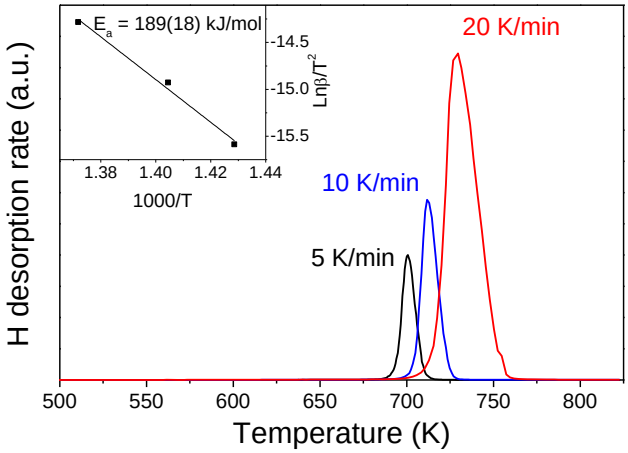

Figure 3.34. TDS spectra of the $Mg_6Pd_{0.7}Cu_{0.3}$ compound hydrided at 3.2 wt.% H measured at heating rates of 5, 10 and 20 K/min. The inset displays the Kissinger plot and corresponding activation energy.

The obtained value, 189(18) kJ/molH_2, is of the same order as for the Ag-substituted compound, taking in account the large error attributed to this measurement. This result shows that the limiting step for hydrogen desorption might be similar to that of $Mg_6Pd_{0.5}Ag_{0.5}$ and MgH_2, *i.e.* the Mg-MgH_2 interface displacement.

Concerning the absorption, slightly faster kinetics is observed for the Cu-substituted material than for the Mg_6Pd sample (Figure 3.35). About 90 % of the alloy is hydrided in less than 40 minutes while almost 60 minutes is needed to transform the same fraction of the Mg_6Pd compound.

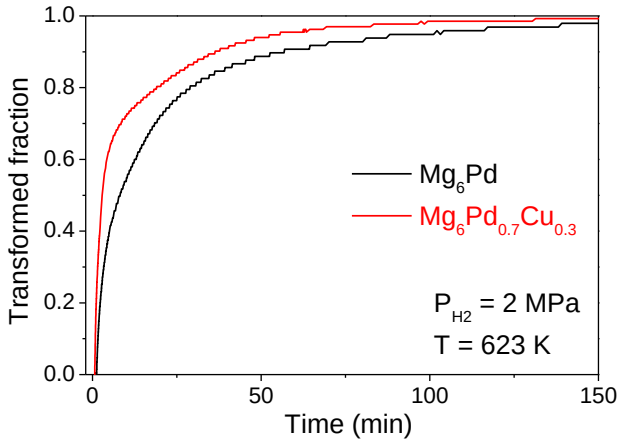

Figure 3.35. Comparison of the kinetics for the Mg_6Pd and $Mg_6Pd_{0.7}Cu_{0.3}$ compounds during the third absorption at 623 K and 2 MPa of hydrogen pressure.

3.3 Discussion on the stability of the $Mg_6Pd_{1-x}Cu_x$-H system

In the case of the Cu-substituted compound, the global stability of the hydrided system is expected to be altered by the formation of the $Mg_2Cu_{1-y}Pd_y$ phase, besides the Mg-Pd intermetallics. Indeed, the reported heat of formation of Mg_2Cu is -29.4 kJ/$mol_{compound}$ [36], which is significantly less stable than all the known Mg-Pd intermetallics (see Table 3.4). Applying Hess's law to equation (3.8) considering pure intermetallic compounds (*i.e.* with no Cu and Pd solubility) would give the following reaction enthalpy:

$$\Delta_r H_{(1)} = \Delta_f H_{(MgH_2)} + \frac{3\Delta_f H_{(Mg_2Cu)} + 4\Delta_f H_{(Mg_{4.4}Pd)} - 7\Delta_f H_{(Mg_6Pd)}}{18.4} \qquad \textbf{(3.11)}$$

The resulting value, -52.8 kJ/molH_2, differs significantly from the experimental result (-71(3) kJ/molH_2), showing that miscibility of Pd and Cu atoms in the reactants

and products must notably change the thermodynamic of the system. In this case, it is expected that Cu substitution in the Mg_6Pd phase will destabilize the compound and consequently increase $|\Delta_r H_{(1)}|$. *Ab initio* calculations are here fundamental to understand the thermodynamics of this system.

Finally, if the hypothetical reaction (3.10) takes place, it should occur at higher pressure than the other two plateaus, resulting in an even less stable hydride.

4 Substituting Pd by Ni

Ni is an interesting candidate for Pd substitution in the M_6Pd intermetallic compound as it possesses good catalytic properties for H_2 dissociation [37; 38]. It has been recently demonstrated that, at 623 K, the maximum solubility of Ni in the Mg_6Pd phase reaches 9 at.% Ni, corresponding to $Mg_6Pd_{0.25}Ni_{0.75}$ composition [11; 35]. The structural and hydrogenation properties of the pseudo-binary phase at the maximum Ni solubility are investigated in this section. The compound with nominal composition $Mg_6Pd_{0.25}Ni_{0.75}$ was prepared by induction melting, mixing pure Mg and Pd elements with a pre-alloyed Mg_2Ni/Mg eutectic mixture.

4.1 Characterization of the alloy

4.1.1 Micro-structure and chemical composition

The BSE image of a polished sample from the original ingot (Figure 3.36) showed a homogeneous main phase with minor occurrence of black precipitates and eutectic zones. The average atomic composition for the main phase was found to be $Mg_{87.0(3)}Pd_{4.4(3)}Ni_{8.6(3)}$, as determined by EDX analyses on 20 points of the ingot. EDX analyses of black precipitates and eutectic zones revealed that they are formed by pure Mg and eutectic Mg/Mg_2Ni, respectively.

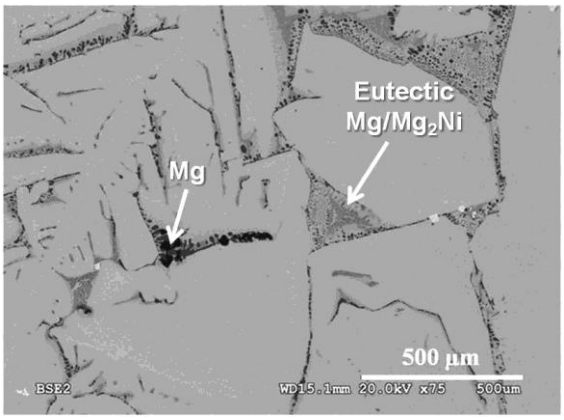

Figure 3.36. BSE image of an ingot slice of the $Mg_6Pd_{0.25}Ni_{0.75}$ alloy.

4.1.2 Structural properties

XRPD data analysed by the Rietveld method (Figure 3.37 and Table 3.20) confirmed the low amount of Mg and Mg_2Ni phases (5.9 and 4.7 wt.%, respectively). The main phase crystallizes in the same structure as the binary Mg_6Pd compound (S.G. *F*-43*m*), with a lattice parameter of 20.106 Å. The crystal refinement of the $Mg_6Pd_{1-x}Ni_x$ phase, as displayed in Table 3.21, has been performed following the model of Samson [3], assuming that Ni and Pd atoms share atomic sites 10, 11 and 13 whereas site 12 was shared by Mg and Pd atoms. Refined site occupancy of Ni shows good agreement with the nominal Ni content. In addition, the site with the lowest CN (site 11) exhibits the highest Ni occupancy. The refined atomic composition $Mg_{87.6(2)}Pd_{4.1(9)}Ni_{8.3(8)}$ is consistent with EDX analysis.

Table 3.20. Summary of Rietveld refinement results for the $Mg_6Pd_{0.25}Ni_{0.75}$ alloy.

Phase	**S.G.**	**Phase amount (wt.%)**	**Cell parameters (Å)**	R_B	R_{wp}
Mg	$P6_3/mmc$	5.8(4)	a = 3.209(1) c = 5.212(1)	12.4	17.3
Mg_2Ni	$P6_222$	4.7(4)	a = 5.224(2) c = 13.30(1)	33.6	
ρ-$Mg_{6.19(1)}Pd_{0.29(7)}Ni_{0.59(6)}$	*F*-43*m*	89.4(1.5)	a = 20.106(1)	14.0	

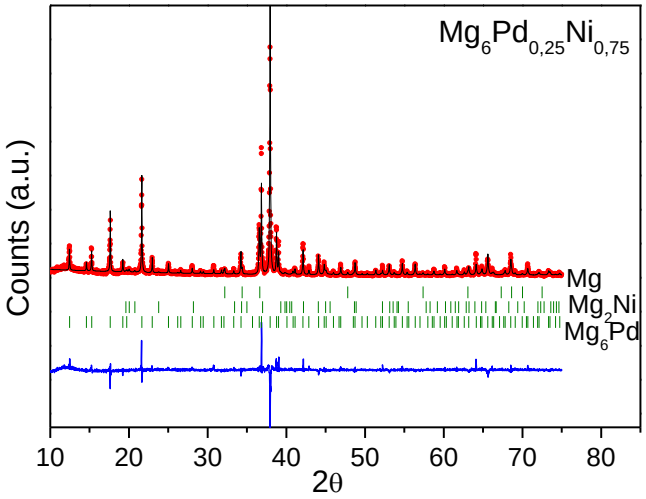

Figure 3.37. XRPD pattern (Cu K_α radiation) of the $Mg_6Pd_{0.25}Ni_{0.75}$ alloy (dots) and the corresponding Rietveld refinement (solid line). Bragg peak positions are plotted as vertical bars for Mg, Mg_2Ni and Mg_6Pd phases. The line below represents the difference between the calculated and the experimental patterns.

Table 3.21. SOF and atomic coordinates of the $Mg_6Pd_{1-x}Ni_x$ ρ-phase for x = 0.75.

Site n°	Atom	Wyckoff position	SOF	Atomic coordinates		
				x	***y***	***z***
1	Mg	48*h*	1	0.144(1)	*x*	0.034(1)
2	Mg	48*h*	1	0.095(1)	*x*	0.274(1)
3	Mg	48*h*	1	0.149(1)	*x*	0.525(1)
4	Mg	48*h*	1	0.0545(1)	*x*	0.769(1)
5	Mg	48*h*	1	0.201(1)	*x*	0.913(1)
6	Mg	24*f*	1	0.102(2)	0	0
7	Mg	24*f*	1	0.387(1)	0	0
8	Mg	24*g*	1	0.064(2)	0.25	0.25
9	Mg	16*e*	1	0.305(1)	*x*	*x*
10	Pd	16*e*	0.42(2)	0.168(1)	*x*	*x*
	Ni		0.58(2)			
11	Pd	16*e*	0.22(2)	0.406(1)	*x*	*x*
	Ni		0.78(2)			
12	Pd	16*e*	0.08(1)	0.678(6)	*x*	*x*
	Ni		0			
	Mg		0.92(1)			
13	Pd	16*e*	0.29(2)	0.900(1)	*x*	*x*
	Ni		0.71(2)			
14	Mg	4*d*	1	0.25	0.25	0.75
Refined atomic composition		**Mg (at.%)**	87.6(2)			
		Pd (at.%)	4.1(9)			
		Ni (at.%)	8.3(8)			

4.1.3 Ni solubility – ternary phase diagram

The Ni content is very close to its maximum solubility in the Mg_6Pd phase that was reported to be 9 at.% Ni at 673 K [35]. Therefore, the three-phase microstructure shown in Figure 3.36 is compatible with the nominal alloy composition ($Mg_{85.7}Pd_{3.6}Ni_{10.7}$ in at.% units) and the Mg-Ni-Pd phase diagram of Figure 1.9.

4.2 Hydrogenation properties

4.2.1 Thermodynamics: PCI curves

Figure 3.38 shows the absorption and desorption PCI curves of the $Mg_6Pd_{0.25}Ni_{0.75}$ alloy. The isotherms exhibit two plateau pressures and a full capacity of about 5.6 wt.% H. This storage capacity is slightly higher than the one reported by Lass for a similar compound (4.9 wt.% H under 2 MPa of hydrogen pressure at 473 K in the $Mg_{5.95}Pd_{0.7}Ni_{0.35}$ alloy) [39], but it can be justified by the higher hydrogen pressure used in our study. The first plateau pressure extends from 0 to 3.2 wt.% H and is rather flat, while the second plateau pressure is more tilted and exhibits a more pronounced hysteresis.

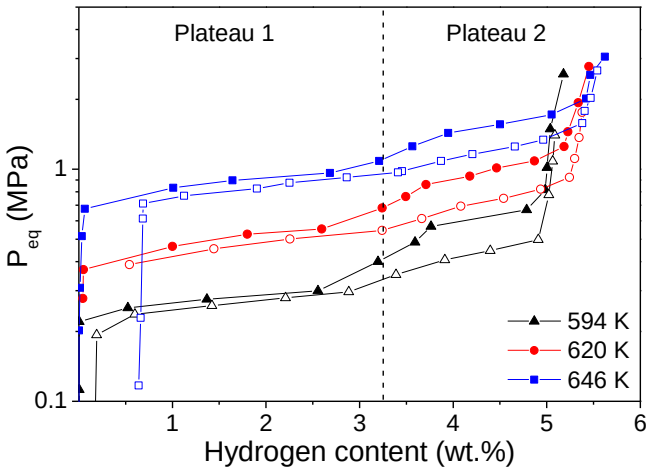

Figure 3.38. PCI curves of the $Mg_6Pd_{0.25}Ni_{0.75}$ compound during absorption (full symbols) and desorption (empty symbols) at 594, 620 and 646 K.

The enthalpy and entropy changes during hydrogen absorption were calculated using the Van't Hoff equation from the equilibrium pressures reported in Table 3.22. The corresponding Van't Hoff plot is shown in Figure 3.39. The thermodynamic values

of the low pressure plateau (ΔH_1 = -72(2) kJ/molH_2 and ΔS_1 = -129(2) J/K.molH_2) are very close to those of MgH_2 formation. As for the high pressure plateau, enthalpy and entropy reach much less negative values (ΔH_2 = -55(1) kJ/molH_2 and ΔS_2 = -108(1) J/K.molH_2) than for MgH_2, indicating a significant destabilizing effect.

Table 3.22. Equilibrium pressures corresponding to the two absorption plateaus 1 and 2 of the $Mg_6Pd_{0.25}Ni_{0.75}$ PCI curves.

	P_{eq} (MPa)	
T (K)	**Plateau 1 @1.8 wt.% H**	**Plateau 2 @4.5 wt.% H**
594	0.283	0.635
620	0.528	1.022
646	0.908	1.560

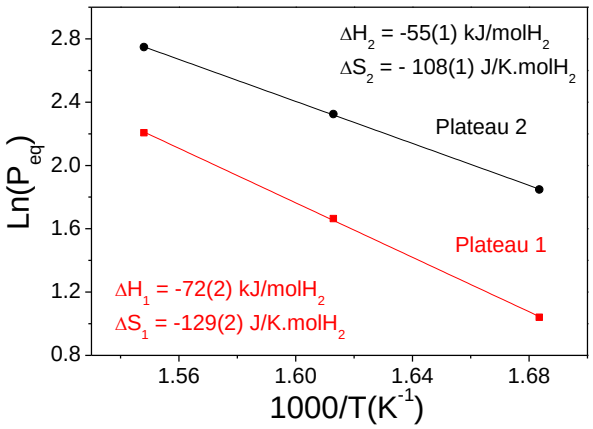

Figure 3.39. Van't Hoff plots corresponding to the two absorption plateaus of the $Mg_6Pd_{0.25}Ni_{0.75}$ isotherms.

4.2.2 Hydrogenation mechanism

In order to determine the reactions that occur during each of the observed plateau pressure, five samples with different H contents were synthesized. Their hydrogen contents, as established by manometric means, are displayed in Table 3.23.

Table 3.23. Hydrogen content of the as-cast and partially hydrided $Mg_6Pd_{0.25}Ni_{0.75}$ samples.

Label	H content (wt.% H)
MPN	0
MPNH1.9	1.9(1)
MPNH2.5	2.5(2)
MPNH3.5	3.5(2)
MPNH4	4.0(3)
MPNH5.6	5.6(2)

These samples have been analysed by means of XRPD which patterns and main peaks identification are displayed in Figure 3.40. The corresponding phase amount evolution with H-content is represented in Figure 3.41. It is observed that hydrogen absorption causes complex phase transformations with the occurrence of several Mg-Pd intermetallic phases and two hydride phases. MgH_2 is formed during the first plateau of hydrogenation, together with the Mg_2Ni phase, while the relative amount of the $Mg_6Pd_{1-x}Ni_x$ phase decreases. The second hydride, Mg_2NiH_4, starts to form during the second plateau, along with η-Mg_3Pd, Mg_5Pd_2 and finally MgPd.

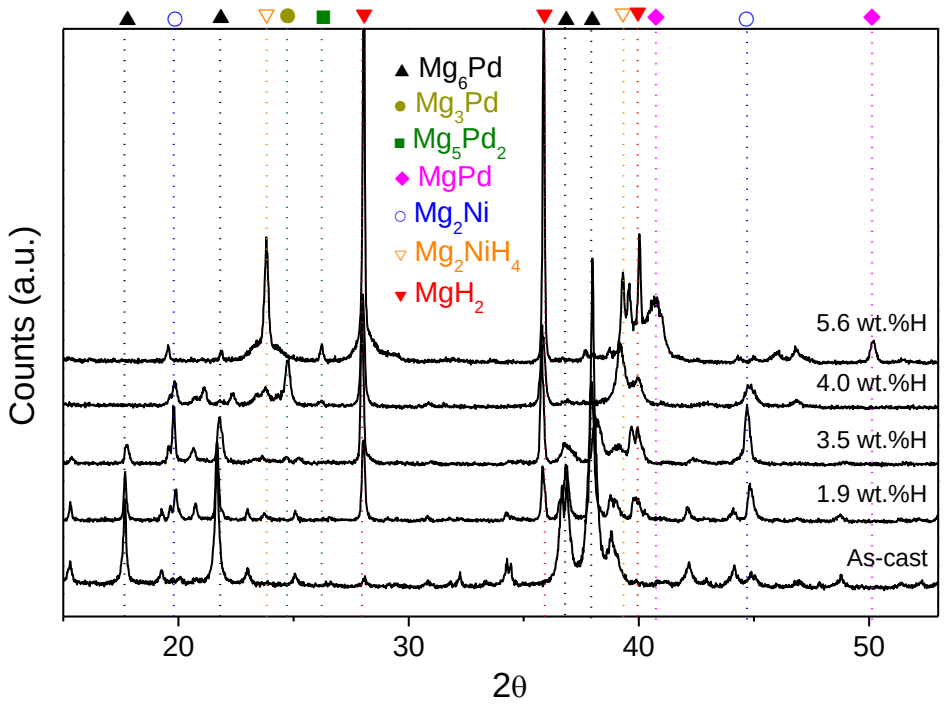

Figure 3.40. XRPD patterns (Cu K_α radiation) of the $Mg_6Pd_{0.25}Ni_{0.75}$ compound at different H-contents during absorption. Phase identification of main diffraction peaks is expressly indicated.

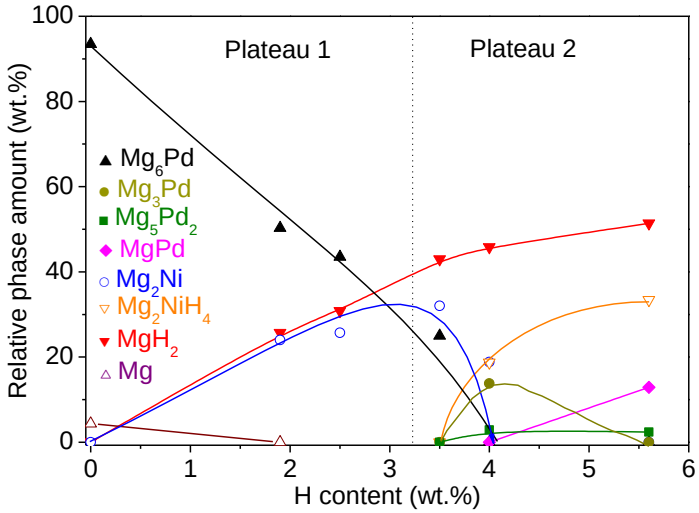

Figure 3.41. Evolution of the relative phase amounts with hydrogen absorption, as determined by Rietveld refinement of the XRPD patterns.

The corresponding Rietveld refinements results are gathered in Table 3.24, from which the following relevant information can be extracted:

i) The composition of the ρ-phase, which has been refined as described for the parent alloy, depletes in Ni and Mg contents during the first plateau of hydrogenation. In fact, these elements segregate out to form Mg_2Ni and MgH_2 phases. Thus, the lattice parameter of the ρ-phase changes due to the different atomic radii of the components (r_{Pd} = 1.37 Å, r_{Ni} = 1.25 Å and r_{Mg} = 1.60 Å). The more Pd (and the less Ni) the phase contains, the larger the cell volume is. However, these correlations are only valid as long as the Mg-content in the ρ-phase remains constant. At higher H-content (3.5 wt.% H), the Mg content drops and the cell volume strongly decreases. We can justify this strong dependence of the cell volume with Mg content by the much larger atomic radius of this atom as compared with Ni and Pd. This partial disproportionation of the intermetallic compound into Pd-rich $Mg_6(Pd,Ni)$ and Mg_2Ni phases reflects that hydrogen absorption shrinks the homogeneity range of the ρ-phase, both in Mg and Ni contents.

ii) The Mg_2Ni phase of the partially hydrided samples exhibits a larger crystal cell than the one reported in literature (a = 5.211 Å, c = 13.244 Å [40]) or observed in the as-cast material (Table 3.20). This fact is explained by the

solid solution of hydrogen in the Mg_2Ni phase, which has been described by Noreus *et al.* as $Mg_2NiH_{0.3}$ [40].

iii) A similar observation can be done for the Mg_5Pd_2 and MgPd phases, which cell parameters are slightly higher than those reported in the literature (a = 8.6598 Å and c = 8.1688 Å [18] for Mg_5Pd_2 and a = 3.12 Å for MgPd [41]). H-solid solution in those phases was already reported by Huot *et al.* [8].

It is also worth mentioning that the Mg_2NiH_4 phase could be reasonably but not perfectly refined in the orthorhombic LT2 modification. The structure of this phase could be in fact more intricate than described in section 3.1.1 of Chapter 1. Finally, no Ni solubility was detected in Mg-Pd phases.

Table 3.24. Rietveld refinements results of partially hydrided $Mg_6Pd_{0.25}Ni_{0.75}$ samples.

Sample	Phase	S.G.	Phase amount (wt.%)	Cell parameters (Å)	R_B	R_{wp}
MPNH1.9	MgH_2	$P4_2/mnm$	25.7(5)	a = 4.5139(2) c = 3.0201(2)	11.2	18.7
	Mg_2Ni	$P6_222$	24.0(5)	a = 5.2404(3) c = 13.445(2)	11.8	
	ρ-$Mg_{6.18(1)}Pd_{0.55(2)}Ni_{0.32(2)}$	F-43m	50.3(6)	a = 20.1456(7)	13.4	
MPNH2.5	MgH_2	$P4_2/mnm$	30.8(5)	a = 4.5171(2) c = 3.0218(2)	8.14	22
	Mg_2Ni	$P6_222$	25.7(5)	a = 5.2459(3) c = 13.464(2)	10.2	
	ρ-$Mg_{6.18(2)}Pd_{0.68(5)}Ni_{0.21(4)}$	F-43m	43.5(5)	a = 20.155(1)	11.5	
MPNH3.5	MgH_2	$P4_2/mnm$	43.0(5)	a = 4.5149(2) c = 3.0208(2)	7.53	20.5
	Mg_2Ni	$P6_222$	32.0(5)	a = 5.2493(3) c = 13.476(1)	15.1	
	ρ-$Mg_{5.98(3)}Pd_{0.76(7)}Ni_{0.30(5)}$	F-43m	25.0(4)	a = 20.002(2)	18.9	
MPNH4	MgH_2	$P4_2/mnm$	44.9(6)	a = 4.5180(3) c = 3.0214(2)	6.55	15.3
	Mg_2Ni	$P6_222$	16.5(5)	a = 5.2499(8) c = 13.475(3)	12.1	
	Mg_2NiH_4	$Pcc2$	21.9(7)	a = 13.53(3) b = 6.55(1) c = 6.18(1)	5.28	
	Mg_5Pd_2	$P6_3/m$	1.7(2)	a = 8.677(5) c = 8.167(7)	17.7	
	η-Mg_3Pd	$P6_3\ cm$	15.1(3)	a = 7.9815(8) c = 8.446(1)	15.3	
MPNH5.6	MgH_2	$P4_2/mnm$	52.1(7)	a = 4.5191(2) c = 3.0228(2)	9.1	23.4
	Mg_2NiH_4	$Pcc2$	31.9(6)	a = 13.139(5) b = 6.436(3) c = 6.478(3)	14.4	
	Mg_5Pd_2	$P6_3/m$	2.1(2)	a = 8.677(2) c = 8.187(4)	33.7	
	MgPd	Pm-3	13.9(3)	a = 3.1583(4)	2.35	

The BSE images in Figure 3.42 show the complex morphology of partially hydrided samples. The sample microstructure depends on its hydrogen content. The MPNH1.9 sample contains dark precipitates with typical sizes from 1 to 20 μm, preferentially located near interfaces (grain boundaries and cracks). EDX analyses indicate that they correspond to the MgH_2 phase. The surrounding matrix is composed of the $Mg_6Pd_{1-x}Ni_x$ phase with Mg_2Ni inclusions (light grey in Figure 3.42b). As the sample is getting hydrided, the grey matrix shrinks at the benefit of filament-like areas leading to a sub-micrometric microstructure in the fully hydrided sample (Figure 3.42f). According to

the XRPD results, the white areas are assigned to the occurrence of both Mg_2NiH_4 and Mg-Pd phases.

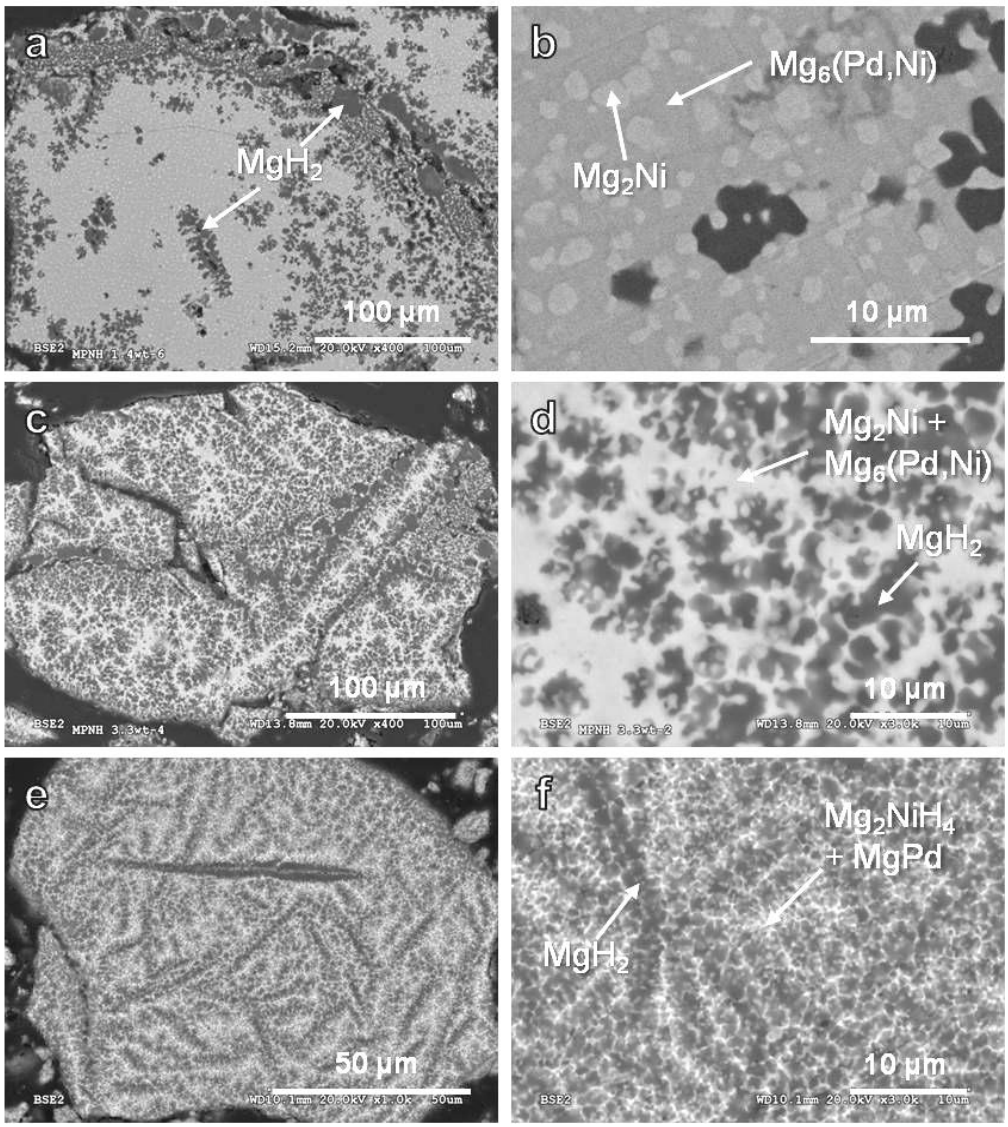

Figure 3.42. BSE images of a) and b) MPNH1.9, c) and d) MPNH3.5, e) and f) MPNH5.6.

These results demonstrate that the $Mg_6Pd_{0.25}Ni_{0.75}$ compound reacts with hydrogen through a complex mechanism. The study of samples at different stages of hydrogenation and results from Rietveld analyses constitute a solid basis to propose a series of reactions, corresponding to the hydrogenation pathway of the alloy.

According to the phases present in samples MPN, MPNH1.9, MPNH2.5 and MPNH3.5, the first step for hydrogen absorption, corresponding to the first plateau, can be described as follows:

$$2.6\ Mg_{6.19}Pd_{0.29}Ni_{0.59} + 7.7\ H_2 \leftrightarrow Mg_{5.98}Pd_{0.76}Ni_{0.30} + 1.2\ Mg_2Ni + 7.7\ MgH_2 \quad \textbf{(3.12)}$$

Reaction (3.12) reveals the depletion of Mg and Ni in the ρ-phase. The hydrogen uptake during the first plateau essentially results from MgH_2 formation. Ni and some Mg react together to form Mg_2Ni which absorbs little hydrogen as a solid solution. At the end of this plateau, the calculated hydrogen content according to reaction (3.12) is 2.75 wt.% H. Taking in account that the parent alloy originally contained pure Mg and Mg_2Ni phases, this value matches satisfactorily with the hydrogen absorbed at the end of the first plateau during the PCI curves (Figure 3.38).

During the second plateau, two simultaneous paths occur. On one side, the Mg_2Ni is getting hydrided while on the other side, the Mg-Pd intermetallic phases deplete in Mg to form Pd-richer phases and MgH_2. This process can be approximated through the following reactions:

$$Mg_{5.98}Pd_{0.76}Ni_{0.30} + 1.2\ Mg_2Ni + 7.7\ MgH_2 + 4.3\ H_2 \leftrightarrow 0.6\ Mg_2NiH_4 + 0.9\ Mg_2Ni + 10.8\ MgH_2 + 0.76\ Mg_3Pd \quad \textbf{(3.13)}$$

$$0.6\ Mg_2NiH_4 + 0.9\ Mg_2Ni + 10.8\ MgH_2 + 0.76\ Mg_3Pd + 1.2\ H_2 \leftrightarrow Mg_2NiH_4 + 0.5\ Mg_2Ni + 11.2\ MgH_2 + 0.38\ Mg_5Pd_2 \quad \textbf{(3.14)}$$

$$Mg_2NiH_4 + 0.5\ Mg_2Ni + 11.2\ MgH_2 + 0.38\ Mg_5Pd_2 + 2.1\ H_2 \leftrightarrow 1.5\ Mg_2NiH_4 + 12.3\ MgH_2 + 0.76\ MgPd \quad \textbf{(3.15)}$$

for which the increasing amount of Mg_2NiH_4 is arbitrarily given.

During reaction (3.13), the ρ-phase totally disproportionates into Mg_2Ni, MgH_2 and Mg_3Pd phases. Besides, the Mg_2Ni phase partially hydrogenates to form Mg_2NiH_4. The Mg_3Pd phase decomposes into Mg_5Pd_2 and more MgH_2 during reaction (3.14). In reaction (3.15), the formation of the Mg_2NiH_4 hydride is completed and the amount MgH_2 hydride continues to grow as a result of the disproportionation of Mg_5Pd_2 into the Pd-richest MgPd compound. The slope of the second plateau is then explained by the successive transformations of the Mg-Pd phases that occur during this stage of absorption.

The calculated absorption corresponding to the reactions mentioned above represents a total hydrogen capacity of 5.4 wt.% H. This value is in good agreement with the experimental value at the end of the second plateau (5.6(2) wt.% H).

The overall hydrogenation process can be summarized as schematically represented in Figure 3.43. Phase growth during the first plateau results from Mg_2Ni and MgH_2 formation through Mg and Ni migration from the ρ-phase in the parent compound. As a consequence, the ρ-phase shrinks, depletes in Mg and Ni, and enriches in Pd. As for the second plateau, the ρ-phase totally disproportionates and forms Mg-Pd (Mg_3Pd, Mg_5Pd_2 and MgPd) intermetallic phases. At the same time, the Mg_2Ni transforms into Mg_2NiH_4 hydride.

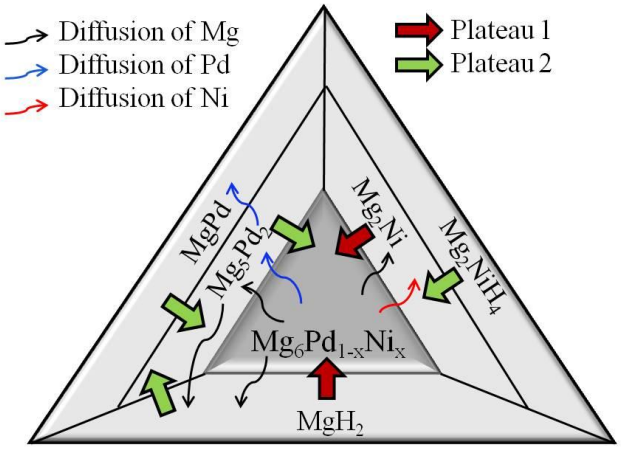

Figure 3.43. Schematic illustration of the phase growth during hydrogenation of the $Mg_6Pd_{1-x}Ni_x$ compound. Large arrows represent the growing direction of the phases. Thin arrows symbolize the diffusion of each element.

In contrast with the reaction scheme proposed by Lass [39], MgH_2 and Mg_2NiH_4 do not form simultaneously but in two different steps. Furthermore, no evidence of Pd solubility in Mg_2NiH_4 phase has been found. This last difference may be justified by the higher temperature used in our study (620 K) as compared to that of Lass (473 K).

4.2.3 Reversibility

Partially dehydrided samples have been prepared to check the reversibility of the previously described mechanism. Their hydrogen contents, deduced from manometric measurements, are reported in Table 3.25.

Table 3.25. Hydrogen content of the desorbed and partially dehydrided $Mg_6Pd_{0.25}Ni_{0.75}$ samples.

Label	H content (wt.% H)
MPNH3.9des	3.9(5)
MPNH0.7des	0.7(3)
MPNdes	0

Rietveld refinements (Table 3.26) of the corresponding XRPD patterns (Figure 3.44) evidence that desorption also occurs in two main steps:

i) The composition of the MPNH3.9des sample, *i.e.* between the two plateau pressures, is similar to the composition of the sample with close H-content formed during absorption (MPNH3.5). The Mg_2NiH_4 phase is totally desorbed while MgH_2 remains in large amount (41.4 wt.%) but nevertheless lower than in the totally hydrided sample. Therefore, hydrogen desorption from the Mg_2NiH_4 hydride is completed during the second plateau and about 23 wt.% of the pseudo-binary phase is already reformed.

ii) The MPNH0.7des sample, which hydrogen content lies at the beginning of the low pressure plateau, exhibits a large amount of the pseudo-binary phase (about 60 wt.%) which results from the recombination of the Mg_2Ni and $Mg_{6.02}Pd_{0,97}Ni_{0.09}$ phases. Both MgH_2 and Mg phases are observed, showing that the decomposition of the MgH_2 phase mainly occurs during this stage.

As occurs in partially hydrided samples, the Mg_2Ni phase exhibits a cell volume expansion with hydrogen content attributed to the presence of H in solid solution. It is also observed that the $Mg_6Pd_{1-x}Ni_x$ phase gradually recovered its initial composition which is refined as $Mg_{87.8(1)}Pd_{3.8(2)}Ni_{8.4(2)}$ (in at.%) in the totally desorbed material. Finally, more than 90 % of the initial $Mg_6Pd_{1-x}Ni_x$ phase is recovered, which demonstrates the reversibility of the hydrogenation reaction. Minor amounts of Mg and Mg_2Ni phases remain after desorption.

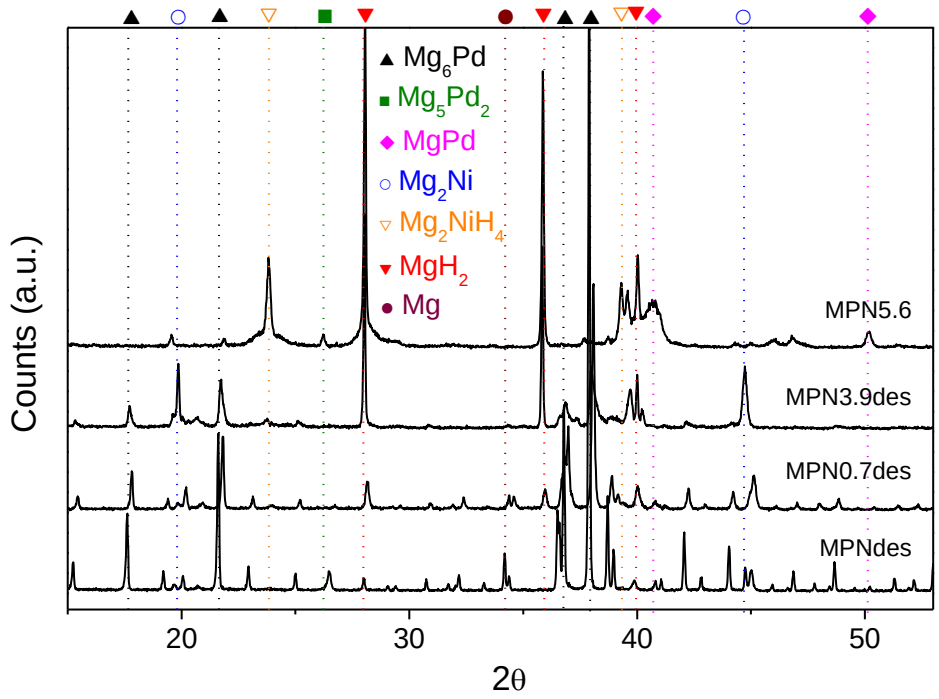

Figure 3.44. XRPD patterns (Cu K_α radiation) of the $Mg_6Pd_{0.25}Ni_{0.75}$ compound at different H-contents during desorption. Phase identification of main diffraction peaks is expressly indicated.

Table 3.26. Rietveld refinements results of the desorbed and partially dehydrided $Mg_6Pd_{0.25}Ni_{0.75}$ samples.

Sample	Phases	S.G.	Phase amount (wt.%)	Cell parameters (Å)	R_B	R_{wp}
MPNH3.9des	MgH_2	$P4_2/mnm$	41.4(6)	a = 4.5158(1) c = 3.0213(1)	9.94	21.5
	Mg_2Ni	$P6_222$	35.4(6)	a = 5.537(3) c = 13.473(2)	21.2	
	ρ-$Mg_{6.02(2)}Pd_{0,97(4)}Ni_{0.09(2)}$	F-43m	23.2(5)	a = 20.106(2)	21	
MPNH0.7des	Mg	$P6_3/mmc$	12.7(4)	a = 3.2102(2) c = 5.2125(5)	8.02	16.2
	MgH_2	$P4_2/mnm$	10.7(3)	a = 4.5158(4) c = 3.0200(4)	3.72	
	Mg_2Ni	$P6_222$	17.5(4)	a = 5.229(1) c = 13.332(2)	17.7	
	ρ-$Mg_{6.18(1)}Pd_{0.32(3)}Ni_{0.54(2)}$	F-43m	59.1(6)	a = 20.151(1)	12.5	
MPNdes	Mg	$P6_3/mmc$	8.4(4)	a = 3.2107(2) c = 5.2133(4)	5.28	21.6
	Mg_2Ni	$P6_222$	6.3(3)	a = 5.218(1) c = 13.270(3)	25.1	
	ρ-$Mg_{6.19(1)}Pd_{0.27(1)}Ni_{0.59(1)}$	F-43m	85.3(8)	a = 20.132(1)	10	

The microstructure of the compound after complete desorption was analysed by SEM-EDX and the corresponding BSE images are displayed in Figure 3.45. The small amount of remaining Mg_2Ni phase appears as small crystallites of about 1 μm large, surrounded by the ρ-phase (Figure 3.45b). The Mg phase is observed in form of larger precipitates.

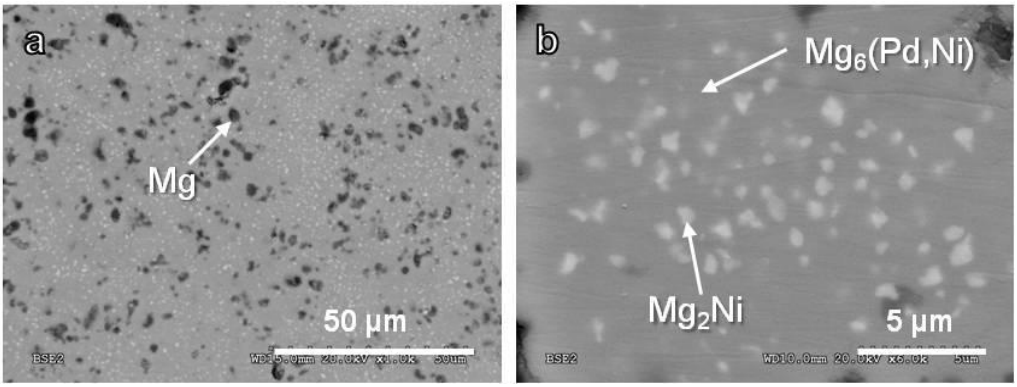

Figure 3.45. BSE images of the $Mg_6Pd_{0.25}Ni_{0.75}$ compound after total desorption (MPNdes).

Owing to the high number of phases that coexist in the material during H-desorption, the present data does not allow to accurately identify the actual desorption mechanism. To gain further insight on this issue, *in situ* neutron diffraction experiments have been performed during desorption from D-loaded Mg_6Pd and $Mg_6Pd_{1-x}Ni_x$ alloys.

4.2.4 *In situ* neutron diffraction during thermal desorption

To determine the complex desorption mechanism of the Ni-substituted compound, an *in situ* thermodesorption experiment has been performed on deuterated $Mg_6Pd_{0.75}Ni_{0.25}$ alloy, taken from the same ingot than the one used in the rest of the study. A deuterated Mg_6Pd sample has also been measured in the same conditions for reference purposes. The same Mg_6Pd alloy as the one studied in section 1 of this chapter was used. Both samples were heated up from 300 to 723 K at a heating rate of 0.5 K/min under dynamic vacuum and the D-desorption rate was determined from changes in the residual pressure. The resulting 2D neutron diffraction patterns are represented in Figure 3.46 together with the desorption curves for both studied samples. We can first appreciate the shift to lower temperature of the $Mg_6Pd_{0.75}Ni_{0.25}$ desorption peak, which takes place at about 60 K lower than non-substituted Mg_6Pd, showing the significantly

faster kinetics in presence of Ni. Next, we observe that both desorption peaks match with the transformation of the hydrides and Mg_5Pd_2 phases into the Mg_6Pd-type phase. In the case of the Ni-containing sample, Mg_2Ni and Mg also appear as intermediate phases.

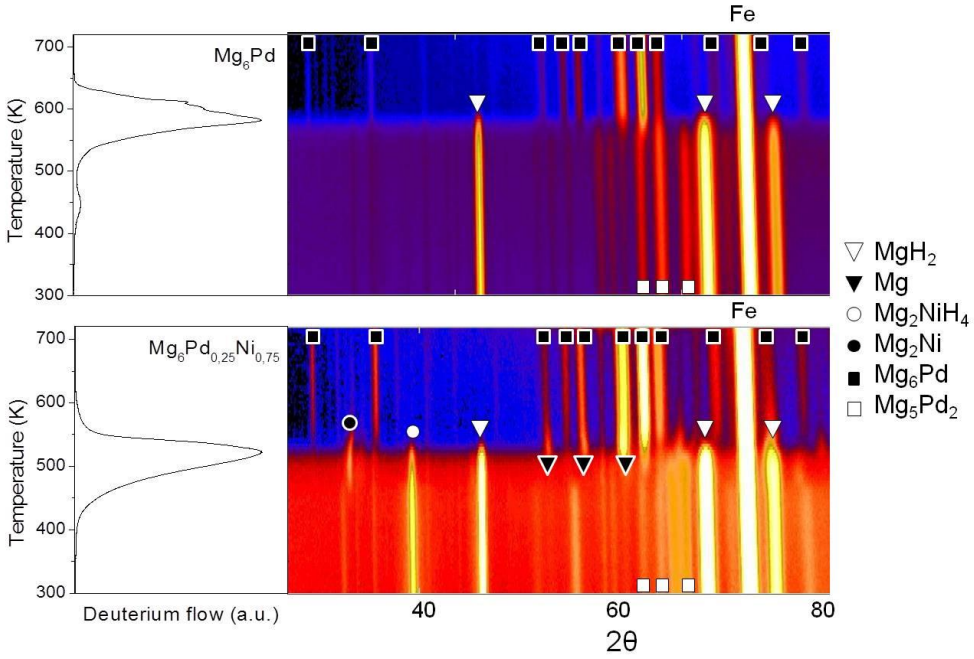

Figure 3.46. Thermal desorption curves and corresponding 2D projections of neutron diffraction patterns obtained during *in situ* thermal desorption at 0.5 K/min of deuterated Mg_6Pd (top) and $Mg_6Pd_{0.25}Ni_{0.75}$ (bottom) alloys. The intensity of the reflection is indicated by the colour scale from blue (lowest intensity) to yellow (strongest intensity). The Fe reflection is due to diffraction from the sample holder.

The evolution of the relative phase amounts as obtained by Rietveld refinements is plotted in Figure 3.47. The desorption mechanism of the Mg_6Pd compound seems to be rather straightforward with the simultaneous disappearing of MgD_2 and Mg_5Pd_2 phases, resulting in the direct recombination of Mg and Mg_5Pd_2 into Mg_6Pd. In fact, the Mg_6Pd phase amount matches very well with the deuterium desorbed fraction. In spite of its very low amount, the MgPd phase seems to disappear at lower temperature. Contrary to absorption experiment (section 1.2.2 of this chapter), the Mg_3Pd-type phase is not observed during desorption. As for the Ni-substituted compound, desorption starts at temperature as low as 450 K, with the decomposition of Mg_2NiD_4 into Mg_2Ni.

Simultaneously, the Mg_5Pd_2 amount starts to decrease and probably forms a Mg-richer intermetallic phase which could not be identified due to the low resolution and the complexity of the diffractograms. The increase of the MgD_2 phase amount at temperatures below 480 K is reasonably attributed to a mass balance effect due to the loss of deuterium in the total mass of the material. At temperature above 480 K, MgD_2 decomposes while $Mg_6Pd_{1-x}Ni_x$ reforms. Surprisingly, the Mg phase also increases between 500 and 550 K, showing that in this case the recombination of the original alloy is not simultaneous to hydrogen desorption. At 550 K, desorption is mostly completed but significant amounts of Mg and Mg_2Ni remain present. The original ρ-phase is then recovered at higher temperatures by Mg, Mg_2Ni and Pd-rich $Mg_6Pd_{1-x}Ni_x$ recombination.

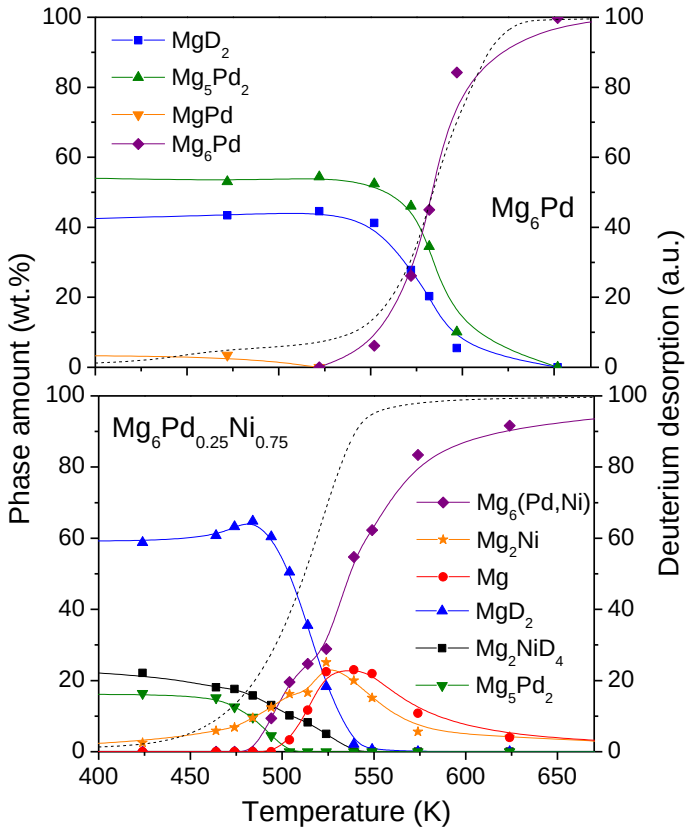

Figure 3.47. Temperature evolution of the relative phase amounts during *in situ* thermodesorption experiments (heating rate: 0.5 K/min) for Mg_6Pd (top) and $Mg_6Pd_{0.25}Ni_{0.75}$ (bottom) alloys. Dashed lines show the desorbed fraction of deuterium.

These results demonstrate that desorption from MgD_2 occurs at significantly lower temperature in the Ni-substituted compound than in Mg_6Pd. Contrary to absorption mechanism where MgD_2 was found to form before Mg_2NiD_4, desorption process exhibits an overlapping of H-desorption from both hydrides. The Mg_2NiD_4 initiates the desorption process from 450 K and MgD_2 decomposes from 500 K. Both compounds are totally desorbed at 550 K. This mechanism suggests the activating properties of some phases that are only present at high H-content, *i.e.* Mg_2NiD_4 or Mg-Pd intermetallic phases. Taking in account that desorption from hydrided Mg_6Pd occurs at much higher temperature, the activating effect of the Mg-Pd phases can be discarded. Therefore, a synergetic effect between Mg_2NiH_4 and MgH_2 can be considered. For example, it is probable that H-desorption from the Mg_2NiH_4 phase prior to MgH_2 decomposition may activate the nucleation of the Mg phase. This cooperative desorption behaviour between these two hydrides had already been observed by Zaluska *et al.* on ball-milled MgH_2 and Mg_2NiH_4 [42]. We also show here that, in dynamic conditions, the recombination of the pseudo-binary phase takes place after the total D-desorption. In consequence, this step is not rate-limiting for the desorption process, but the recombination of the alloy is strongly slowed down by the diffusion of metal atoms.

4.2.5 Kinetic characterization

TDS experiments were carried out for all H-loaded samples. Figure 3.48 depicts the desorption spectra measured at 10 K/min. Samples which hydrogen content was below 4 wt.% H exhibited a single high-temperature (HT) peak around 670 K with onset temperature at 630 K. Above this hydrogen content, desorption spectra were more complex with the occurrence of two peaks. Hydrogen desorption started from 500 K and displayed a broad low-temperature (LT) peak centred at ~ 550 K. A second peak occurred at ~ 625 K for the fully hydrided sample and at ~ 650 K for MPNH4, *i.e.* at lower temperature than for samples containing less than 4 wt.% H. According to previous results during *in situ* thermodesorption, the LT peak can be assigned to desorption from the Mg_2NiH_4 phase which corresponds to weak bonded hydrogen. Similarly, the HT peak is mainly related to desorption from the MgH_2 phase, but also from remaining Mg_2NiH_4.

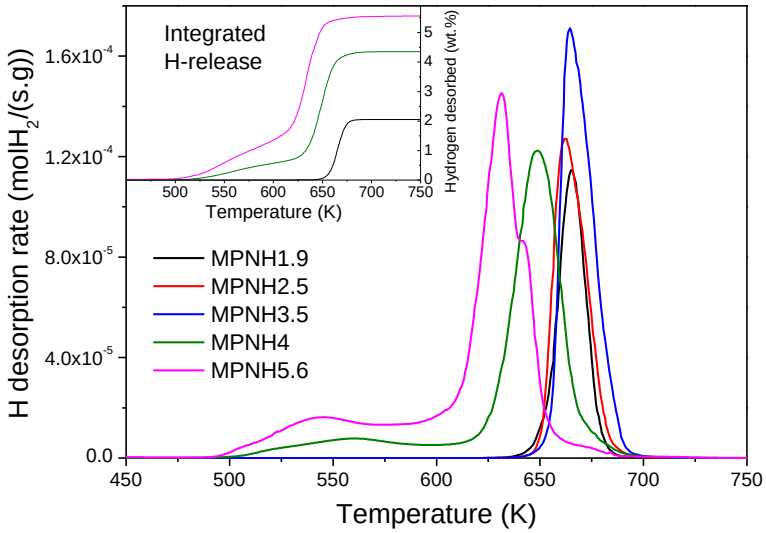

Figure 3.48. TDS spectra measured at 10 K/min for several partially hydrided $Mg_6Pd_{0.25}Ni_{0.75}$ compounds. The inset represents the amount of hydrogen desorbed (wt.% H) as a function of the temperature.

Activation energies have been determined for all partially hydrided samples by measurements at several heating rates. Figure 3.49 illustrates the thermal desorption spectra of the MPNH5.6 sample and the corresponding Kissinger plot. Activation energies have been calculated from the HT peak exclusively and the results are gathered in Table 3.27. For low H-contents (≤ 3.5 wt.% H), the activation energies can be directly related to the MgH_2 decomposition, as the values are compatible with those reported for pure MgH_2 (from 140 to 172 kJ/molH_2 [21–26]).

For high H-contents (≥ 4 wt.% H), much lower activation energies are obtained, which values are typical of ball-milled MgH_2 in presence of additives [43; 44]. This result confirms the catalytic effect of the Mg_2NiH_4 phase on MgH_2 desorption, as suggested in the previous section. Indeed, the Mg_2NiH_4 phase is only present at high H-contents, explaining that the reduced energy of activation is only observed for MPNH4 and MPNH5.6 samples. To this respect, it is also worth noting, the strong microstructure refining in this system (Figure 3.42f) that accompanies hydrogen absorption at high hydrogen contents.

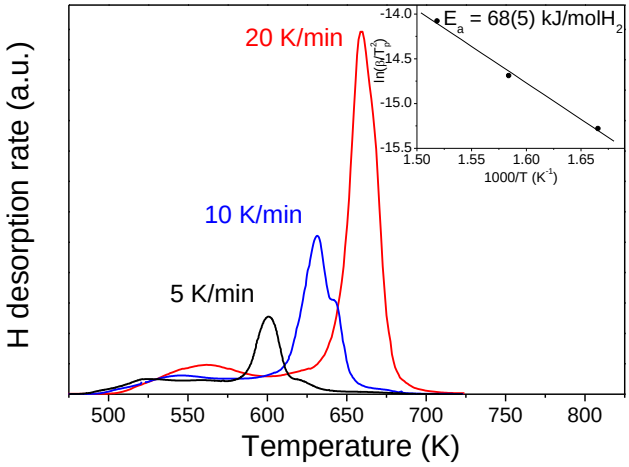

Figure 3.49. TDS spectra of the $Mg_6Pd_{0.25}Ni_{0.75}$ compound hydrided at 5.6 wt.% H measured at heating rates of 5, 10 and 20 K/min. The inset displays the Kissinger plot and corresponding activation energy.

Table 3.27. Activation energies of hydrogen desorption from partially hydrided $Mg_6Pd_{0.25}Ni_{0.75}$ compounds calculated from TDS high-temperature peak using the Kissinger equation. The amount of desorbed hydrogen is deduced from TDS results.

Sample	**H_2 release (wt.%)**	**Activation energy ($kJ/molH_2$)**
MPNH1.9	1,9(1)	136(5)
MPNH2.5	2,7(1)	152(2)
MPNH3.5	3,5(1)	161(1)
MPNH4	4,2(1)	54(1)
MPNH5.6	5,5(1)	68(5)

4.3 Discussion on the stability of the $Mg_6Pd_{1-x}Ni_x$-H system

The standard enthalpy and entropy changes of the hydrogenation reactions leading to the low pressure (reaction (3.12)) and high pressure (reactions (3.13) + (3.14) + (3.15)) plateaus can be calculated using Hess's law and the formation enthalpy and entropy of the involved compounds (see Table 3.28). Thus, the reaction enthalpies corresponding to plateaus 1 and 2 are evaluated, respectively, as:

$$\Delta_r H_{(1)} = \Delta_f H_{(MgH_2)} + \frac{\Delta_f H_{(Mg_{5.98}Pd_{0.76}Ni_{0.30})} + 1.2\Delta_f H_{(Mg_2Ni)} - 2.6\Delta_f H_{(Mg_{6.19}Pd_{0.29}Ni_{0.59})}}{7.7} \quad \textbf{(3.16)}$$

$$\Delta_r H_{(2)} = \frac{0.76\Delta_f H_{(MgPd)} + 4.6\Delta_f H_{(MgH_2)} + 1.5\Delta_f H_{(Mg_2NiH_4)} - 1.2\Delta_f H_{(Mg_2Ni)} - \Delta_f H_{(Mg_{5.98}Pd_{0.76}Ni_{0.30})}}{7.6} \quad \textbf{(3.17)}$$

Table 3.28. Enthalpy and entropy of formation ($Mg_6Pd_{1-x}Ni_x$, MgH_2, Mg_2Ni and MgPd phases) and reaction (Mg_2NiH_4). For $Mg_6Pd_{1-x}Ni_x$, Mg_2Ni and MgPd compounds, values are determined by thermodynamic modelling of finite temperature effects and extrapolation from the values at T = 0 K given in Ref. [11]. All values are given at 298 K.

Compound	Enthalpy ($kJ/mol_{compound}$) [Ref]		Entropy ($J/K\ mol_{compound}$) [Ref]	
ρ-$Mg_{6.19}Pd_{0.29}Ni_{0.59}$	-76	[12]	-15	[12]
ρ-$Mg_{5.98}Pd_{0.76}Ni_{0.30}$	-161	[12]	-21	[12]
MgH_2	-74.5	[10]	-135	[10]
Mg_2NiH_4	-128	[45]	-244	[45]
Mg_2Ni	-61	[12]	-0.8	[12]
MgPd	-150	[12]	-24	[12]

The obtained enthalpy values for both plateaus are $\Delta_rH_{(1)}$ = -79.1 kJ/molH_2 and $\Delta_rH_{(2)}$ = -54.7 kJ/molH_2, in rather good agreement with the experimental values (ΔH_1 = -72(2) kJ/molH_2 and ΔH_2 = -55(3) kJ/molH_2). Entropy changes, which were analogously calculated, are -132.8 and -129.4 J/KmolH_2 for plateau 1 and 2, respectively. The first value concurs also fairly well with the experimental values of ΔS_1 = -129(2) as deduced from the PCI measurements, but the second one differs from the experimental value ΔS_2 = -108(1) J/KmolH_2, showing that additional contributions to entropy must be taken in account during the second plateau.

In the case of the first plateau of absorption, the enthalpy of reaction strongly depends on the enthalpy of decomposition of the Ni-rich initial compound into Mg_2Ni and $Mg_{5.98}Pd_{0.76}Ni_{0.30}$. Thus, the formation enthalpy of the Pd-rich $Mg_6Pd_{1-x}Ni_x$ compound is much more negative than the one of the Ni-rich $Mg_6Pd_{1-x}Ni_x$, resulting in an endothermic disproportionation reaction. Consequently, the calculated enthalpy variation associated to the first plateau of absorption is more endothermic than it is for MgH_2 formation. However, the experimental value ΔH_1 is not as negative as the calculated one, probably because of the uncertainty on the $Mg_6Pd_{1-x}Ni_x$ phase composition and on the corresponding calculated formation enthalpy values.

In contrast, the enthalpy involved during the second plateau of hydrogenation is significantly smaller than $|\Delta_fH(MgH_2)|$. Main contribution to this enthalpy decrease comes from the hydrogenation of the Mg_2Ni phase and the decomposition of the remaining Mg_6Pd into MgPd and MgH_2 phases.

5 Discussion on the effects of alloying on Mg hydriding properties

5.1 Structural occupation factors in $Mg_6Pd_{1-x}TM_x$ compounds

The structural properties of the $Mg_6Pd_{1-x}TM_x$ ρ-phase are altered by the nature of the substituting TM. Figure 3.50 shows, for Ni and Cu substitutions and different nominal compositions, a comparison of the occupancy distribution as obtained by Rietveld refinement on sites 10, 11 and 13. These are the Pd sites where TM substitution was observed. We remind that, owing to its high CN (CN = 13), site 12 was considered to be exclusively occupied by the larger Pd and Mg atoms. The samples with Cu-substitution and the $Mg_6Pd_{0.25}Ni_{0.75}$ sample are obtained in this thesis, while the data on the $Mg_6Pd_{0.5}Ni_{0.5}$ sample comes from a previous work [33]. As a general trend, one can observe that SOF of the TM is higher at site 11. This result is in agreement with the low CN of site 11 (CN = 10) and the smaller radius of Cu and Ni atoms as compared to Pd one. Obviously, we observe that the higher is the TM content in the alloy, the higher is the TM occupancy at all sites. For example, the Ni occupancy for the x = 0.75 composition is shifted to higher values for the three sites as compared to the x = 0.5 composition. Strikingly, the preferential occupation of site 11 (CN =10) as compared to sites 10 and 13 (CN = 12) is higher for Cu than for Ni despite the larger atomic radius of the former (r_{Cu} = 1.28 Å and r_{Ni} = 1.25 Å). This contradicts geometric expectations pointing to the fact that electronic properties have to be considered. Indeed, one should notice for all studied compositions the very low occupancy factors for Cu at sites with CN = 12. This fact may account for the low solubility of Cu in the ρ-Mg_6Pd phase.

In summary, the atomic size of a TM element is not the only parameter which determines the maximum Pd by TM substitution ratio. Indeed, even though Cu and Ni atoms possess close atomic radii, Ni solubility reaches 9 at.% while Cu is limited to 3.9 at.%. The ability of a TM to substitute Pd atoms will also depend on electronic effects. The closer the chemical properties of the substituting TM elements and Pd are, the higher the solubility limit of the TM in the ρ-Mg_6Pd phase is. This statement is illustrated by the Pd-TM miscibility properties (TM = Ag, Ni and Cu) in their respective binary phase diagrams. Thus, full miscibility in the solid state exists in Pd-Ag and Pd-Ni systems [13], *i.e.* for TM with high solubility in the ρ-phase. In contrast, ordered

intermetallic compounds exist in the Pd-Cu system [29], which concurs with the low Cu solubility in the ρ-phase.

However, steric effects remain a deciding factor concerning preferential site occupancy, as observed for Cu and Ni atoms. Therefore, it can be anticipated that Ag atoms, which radius is significantly larger than Pd, Cu or Ni one (r_{Ag} = 1.44 Å), might preferentially occupy the Pd site with the highest CN, *i.e.* site 12.

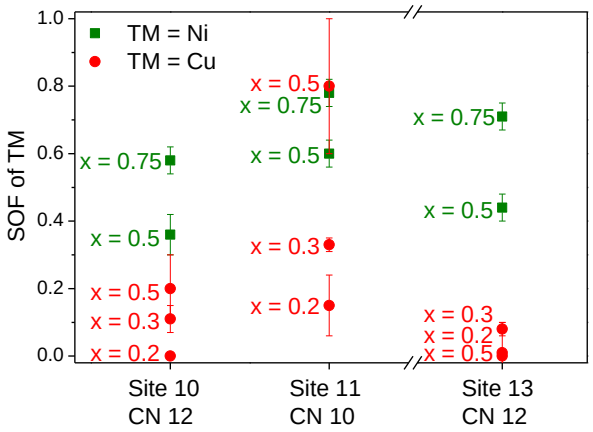

Figure 3.50. Comparison of the SOF of TM = Cu and Ni at sites 10, 11 and 13 in the $Mg_6Pd_{1-x}TM_x$ phase for different nominal alloy compositions. The nominal composition of Cu- and Ni-substituted compounds is labelled at the left of the data point.

5.2 Effects on thermodynamics

We have seen along the previous sections that substituting Pd atoms by different TM in the Mg_6Pd compound gives rise to different hydrogenation mechanisms and thermodynamic properties. Thus, while the Ag-substituted compound forms MgH_2 and Mg(Pd,Ag) intermetallic without chemical constraints in the (Pd,Ag) pseudo-atom, the Cu-substituted alloy dissociates into MgH_2 and two intermetallic phases, one rich in Cu ($Mg_2Cu_{1-y}Pd_y$) and the other one rich in Pd ($Mg_5Pd_{2-z}Cu_z$) with limited solubility of both TMs. On the other hand, the pseudo-binary compound containing Ni forms two hydride phases (MgH_2 and Mg_2NiH_4) and MgPd intermetallic with no Ni solubility. The study of these different hydrogenation paths and their associated thermodynamics leads to relevant information concerning the destabilization mechanism of Mg-based alloys.

In Figure 3.51, we can appreciate the thermodynamic features of the different $Mg_6Pd_{1-x}TM_x$ compounds as compared to the MgH_2 reference. It is obvious that at a

given temperature hydrogen absorption during the first plateau occurs at similar pressure for all the investigated materials. The hydrided Ni-containing compound is even more stable than pure MgH_2. The thermodynamic values reported in Table 3.29 are very close to those of MgH_2, showing that the equilibrium pressure of the first plateau is mainly determined by the formation of MgH_2.

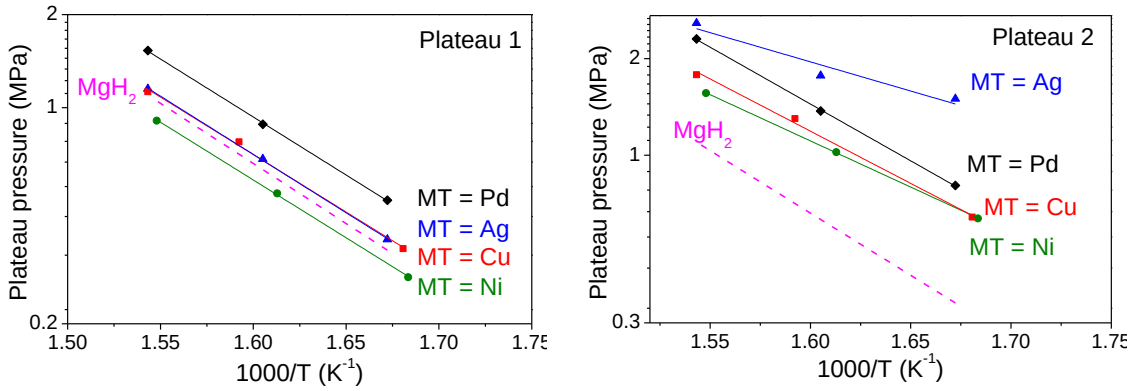

Figure 3.51. Van't Hoff plots of the $Mg_6Pd_{1-x}TM_x$ compounds (TM = Pd, Ag, Cu and Ni) corresponding to each of the experimentally observed absorption plateau pressures. They are compared to the MgH_2 (dashed line) considering ΔH = -74.5 kJ/molH_2 and ΔS = -135 J/KmolH_2 [10].

Table 3.29. Summary of the experimental and calculated enthalpy and entropy values of the $Mg_6Pd_{1-x}TM_x$ compounds (TM = Pd, Ag, Cu and Ni) for each plateau pressure.

	Plateau 1				**Plateau 2**			
	ΔH_1 (kJ/molH_2)		**ΔS_1 (J/KmolH_2)**		**ΔH_2 (kJ/molH_2)**		**ΔS_2 (J/KmolH_2)**	
TM	**Exp.**	**Calc.**	**Exp.**	**Calc.**	**Exp.**	**Calc.**	**Exp.**	**Calc.**
Pd	-72(1)	-75.8	-133(2)	-124.5	-68(1)	-66.0	-131(2)	-135
Ag	-72(2)	-	-132(2)	-	-35(4)	-	-84(6)	-
Cu	-71(3)	-	-130(5)	-	-62(4)	-	-120(6)	-
Ni	-72(2)	-79.1	-129(2)	-132.8	-55(1)	-54.7	-108(1)	-129.4

On the contrary, the second plateau of absorption leads to a significant modification of the MgH_2 equilibrium for all the compositions. The non parallelism of the Van't Hoff plots reflects the different enthalpy of hydrogenation. The lowest slope, *i.e.* the smallest enthalpy, is found for the Ag-substituted compound, and the highest for pure Mg_6Pd. The $|\Delta H|$ decrease in the hydrogenation reaction is due to the reduced formation enthalpy of the final intermetallic products (*e.g.* $\Delta_fH(MgPd)$ = -150 kJ/$mol_{compound}$ in the

case of non-substituted Mg_6Pd) as compared to the initial reactant (*e.g.* $\Delta_fH(Mg_6Pd)$ = -173.7 $kJ/mol_{compound}$).

We also observe that the straight lines do not converge to the same point on the vertical axis due to their different entropy values, as reported in Table 3.29. The lowest entropy of hydrogenation reaction is found for pure Mg_6Pd while the highest occurs for the Ag-substituted compound, *i.e.* the same trend as for the enthalpy behaviour. Indeed, it is interesting to note that, for all studied $Mg_6Pd_{1-x}TM_x$ compounds, the smallest is the enthalpy change, the smallest is the entropy loss. This is illustrated on Figure 3.52, where a linear relation between enthalpy and entropy values occurs. While it is commonly accepted that in simple metal-hydrogen systems the entropy variation is due to the transition from gaseous dihydrogen to chemisorbed hydrogen atoms, it seems that other mechanisms may contribute to the entropy in the studied pseudo-binary compounds. Although the obtained thermodynamic values are somehow questionable for the Ag-substitution for which the PCI curves are not well defined (Figure 3.14), they are more reliable for the Ni-substitution for which isotherms are well defined (Figure 3.38). In the latter case, the reduced entropy decrease during the second plateau of the $Mg_6Pd_{0.75}Ni_{0.25}$ compound may be related to the formation of highly disordered Mg_2NiH_4 structure which exhibits complex polymorphic properties and microtwinning defects [46; 47].

To summarize, thermodynamic analysis of $Mg_6Pd_{1-x}TM_x$ compounds indicates that the product phases that allow for destabilization of the hydrided state, because of their lower stability as compared to the reactants, are also characterised by a high disorder. According to the pressure-temperature dependence as defined by the Van't Hoff equation (1.2), a reduction of $|\Delta S|$ leads to an increase of the equilibrium temperature at a given pressure and ΔH. In other words, if both $|\Delta H|$ and $|\Delta S|$ decrease, the effective change on equilibrium pressure and temperature of a metal-hydride system will be limited.

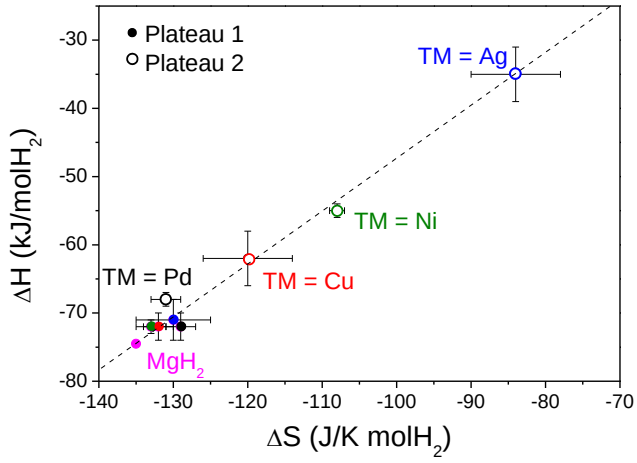

Figure 3.52. Linear correlation between enthalpy and entropy of hydrogenation experimentally obtained for $Mg_6Pd_{1-x}TM_x$ compounds (TM = Pd, Ag, Cu and Ni) compared to MgH_2 [10]. Full symbols correspond to the low pressure plateau (plateau 1) and empty symbols are for the high pressure plateau (plateau 2). The different TM substitutions are identified by the symbol colours.

In the quest for MgH_2 destabilization, alloying Mg with TM to form intermediate compounds during H-absorption is an efficient strategy to tailor the thermodynamics of a hydrogenation reaction. However, an important difficulty comes from the fact that the intermediate compounds might increase the global entropy of the system which results in an equilibrium temperature increase at a given working pressure. The pseudo-binary compounds investigated in this Thesis exhibit interesting thermodynamic improvements only for the high pressure plateau of absorption, *i.e.* at high H-content range. For example, the hydrided $Mg_6Pd_{0.25}Ni_{0.75}$ compound can desorb about 2.5 wt.% H under atmospheric pressure at a temperature of 510 K, which is 40 K lower than pure MgH_2 desorption. The remaining 3 wt.% H would need a higher temperature (560 K) to be desorbed.

The good agreement between experimental and calculated thermodynamic values (Table 3.29 for TM = Pd and Ni) is encouraging for further prediction by *ab initio* calculations of the thermodynamic properties of the different investigated systems. By calculating the formation enthalpy and entropy of initial and final components, it is possible to anticipate the thermodynamic conditions for hydrogenation of potential alloys. An important result coming out from this Doctoral Thesis is the clear evidence of the negative role played by the disorder of the resulting products on the stability of

the hydrided state. Future studies on destabilization of metal-hydrogen systems should consider the choice of appropriate elements or phases which yield well-ordered phases upon hydrogenation.

5.3 Effects on kinetics

We can observe on Figure 3.53 that for all $Mg_6Pd_{1-x}TM_x$ compounds, the thermal desorption of hydrided samples occur at lower temperature than for commercial MgH_2. However, the desorption peaks of samples with TM = Pd, Ag and Cu take place at rather close temperatures, only 10 to 15 K lower than pure MgH_2. This observation concurs with the activation energy values reported in the table attached to Figure 3.53. They are of the same order than activation energies reported for MgH_2 [21–26]. Therefore, it is tempting to attribute to these compounds a similar desorption mechanism than for MgH_2, *i.e.* nucleation and growth of Mg controlled by the displacement of Mg/MgH_2 interface. Besides, *in situ* neutron diffraction experiments demonstrated that, in the case of $Mg_6Pd_{1-x}Ni_x$ alloy, the recombination of the initial pseudo-binary phase only occurs once the desorption is completed. Thus, the diffusion of metal atoms cannot be the rate limiting step during desorption. A similar mechanism can be expected for the other TM-substitutions. On another hand, the presence of Pd and other TM is expected to catalyse the recombination of hydrogen molecules, although at high desorption temperatures this process is expected to be fast.

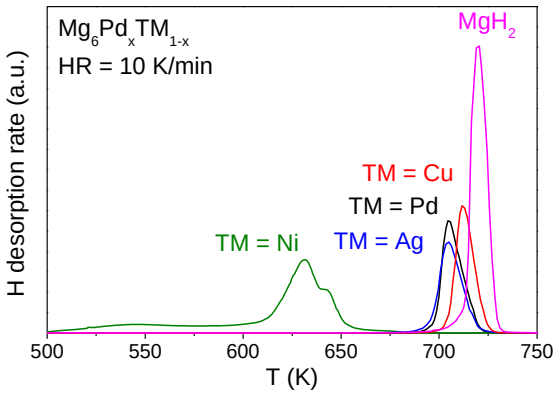

TM	E_a ($kJ/molH_2$)
Ag	169(8)
Cu	189(18)
Ni	68(5)

Figure 3.53. Comparison of the TDS spectra of the totally hydrided $Mg_6Pd_{1-x}TM_x$ compounds (TM = Pd, Ag, Cu and Ni) and commercial MgH_2. The activation energies obtained by TDS measurements at different heating rates are reported in the table on the right-hand side.

The Ni-containing sample possesses however a particular and interesting kinetic behaviour. It exhibits a significantly lower desorption peak, about 90 K below the one of MgH_2, and a much lower activation energy. The effect of alloying on the kinetics of desorption is minor in the case where only MgH_2 is formed as hydride phase (*i.e.* for TM = Ag, Cu and Pd) but significative in presence of additional Mg_2NiH_4. This last one may actuate as a catalyst for Mg nucleation and Mg/MgH_2 interface displacement, which is also reflected by the lower activation energy. It has been shown that the formation of Mg_2NiH_4 is accompanied by a strong microstructure refinement of the fully hydride sample (Figure 3.42f) and that its desorption onset precedes that of MgH_2 (Figure 3.47). Thus, hydrogen desorption from MgH_2 phase may be facilitated through the Mg_2NiH_4 phase, favouring Mg nucleation at the numerous MgH_2/Mg_2NiH_4 grain boundaries. Then, Mg/MgH_2 interface displacement occurs in short time thanks to sub-micrometric grain size of the MgH_2 phase.

The comparison of the kinetics during absorption of the four studied $Mg_6Pd_{1-x}TM_x$ compounds (Figure 3.54) shows important differences for the same hydrogenation conditions. The fastest to reach 90 % of transformed fraction is the Ni-substituted compound, with only 11 minutes, while the Ag-substituted compound spends more than 100 minutes.

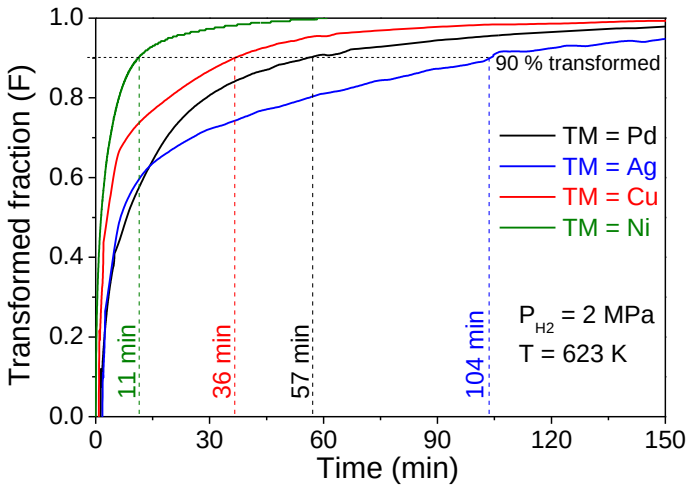

Figure 3.54. Time-evolution of the transformed fraction during H-absorption in the $Mg_6Pd_{1-x}TM_x$ compounds (TM = Pd, Ag, Cu and Ni) at 623 K under 2 MPa of hydrogen pressure.

Information on the rate limiting step of the absorption reaction can be obtained by fitting the kinetic curves to the model equations describing solid-gas reactions. The general kinetics equation gives the time evolution of the reacted fraction F as:

$$F = 1 - \exp(-Bt^m) \quad \textbf{(3.18)}$$

where B is a constant that depends on the nucleation frequency and linear rate of the grain growth and *m* is a constant that varies with the geometry of the system. According to the method proposed by Hancock and Sharp [48], the plot of ln(–ln(1–F)) *vs.* ln(t) for $0.15 < F < 0.5$ gives a straight line which slope *m* allows identifying the absorption mechanism by comparison with theoretical tabulated values [48]. This method has been applied to the isothermal absorption curves of Figure 3.54 and the corresponding plots are represented in Figure 3.55. The obtained *m*-values are included between 0.47 and 0.56, which clearly indicates an absorption mechanism controlled by diffusion. This result is consistent with the fact that hydrogen absorption in such compounds implies the diffusion of heavy atoms (as compared to hydrogen) to dissociate into new intermetallic and hydride phases. Thus, the MgH_2 phase cannot be formed if the TM atoms have not migrated from the ρ-phase to another phase. This was also confirmed by the microstructure of partially hydrided compounds where MgH_2 appeared mainly on cracks and grain boundaries. Hydrogen atoms penetrate through these interfaces and react with available Mg after TM diffusion towards intermetallic phases. In other words, the growth of the MgH_2 phase during absorption is controlled by the diffusion of TM. Therefore, absorption will be faster if the diffusion coefficient is high and if the diffusion path is short. The first parameter depends on the nature of the metal while the second one depends on the microstructure of the material. Regarding the diffusion of TM, the speed of the absorption rate (Figure 3.54) can be tentatively related to the weight of the metallic atoms present in the compound. Thus, the slowest kinetics is obtained for the heaviest Ag-substituted compound and the fastest for the Ni-containing sample. Besides, the microstructure of the hydrided compounds was finer for the Ni-containing material than for Cu or Ag-substituted alloys (Figures 3.17, 3.31 and 3.42).

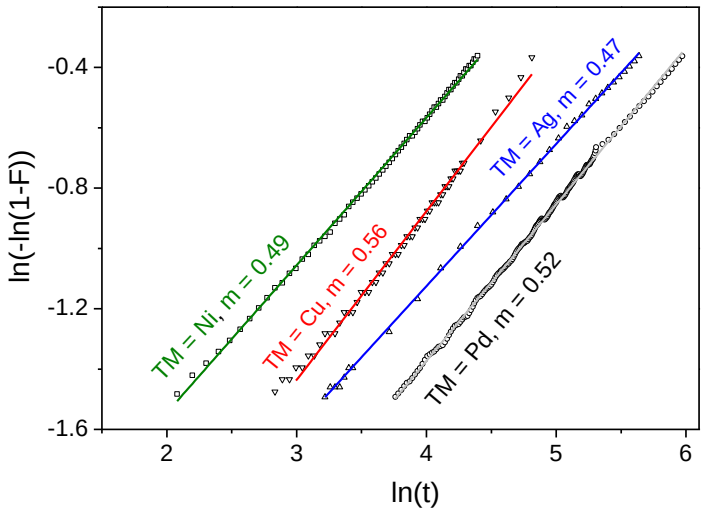

Figure 3.55. Plots of ln(-ln(1-F)) *vs.* ln(t) (with 0.2 < F < 0.5) for the hydrogen absorption curves obtained at 623 K under 2 MPa of hydrogen pressure for the $Mg_6Pd_{1-x}TM_x$ compounds.

The effect of Mg alloying on the (de)hydriding kinetics strongly depends on the nature of the phases that are formed during hydrogenation and their ability to catalyse the sorption reaction. Different mechanisms have been identified for absorption and desorption reactions. The desorption of the samples with TM = Pd, Ag and Cu is driven by the nucleation and growth of the Mg phase and the rate is limited by the MgH_2/Mg interface displacement. In the case of Ni substitution, the decomposition of the MgH_2 phase is catalysed by the Mg_2NiH_4 phase and the related microstructure refinement, and occurs at much lower temperature. During absorption, the diffusion of metal atoms is rate-limiting for the decomposition of the parent alloys into hydride and intermetallic phases.

6 Conclusion

This chapter has brought an exhaustive characterization of a new family of Mg-based alloys of the type $Mg_6Pd_{1-x}TM_x$ with TM = Pd, Ag, Cu and Ni. From a structural and compositional points of view, we have shown that the Mg_6Pd compound admits Pd atoms substitution by at least three different TM. The Ni solubility is the highest, with 9 at.% (*i.e.* x = 0.75) while Ag solubility reaches 7.2 at.% (*i.e.* x = 0.5) and Cu solubility is limited to 3.9 at.% (*i.e.* x = 0.3). The solubility limit does not scale with the atomic

radii of the TM and follows the same trends as the miscibility of Pd-TM binary systems. This suggests that electronic rather than geometric factors should be considered to explain the reported solubility limits. The structural properties of such pseudo-binary phases have been determined using the crystallographic model proposed by Samson [3]. Ni and Cu TM atoms preferentially occupy the site of lowest coordination number, particularly in the case of Cu.

Next, the hydrogenation properties of the alloys have been determined by different solid-gas reaction methods. Each pseudo-binary compound exhibits a different hydrogenation mechanism leading to different intermetallic and hydride phases. For example, hydrogenation of the Cu-substituted compound results in the formation of MgH_2 together with two intermetallic phases, one rich in Cu ($Mg_2Cu_{1-y}Pd_y$) and one rich in Pd ($Mg_5Pd_{2-z}Cu_z$). In the case of substitution by Ni, two hydride phases are formed, MgH_2 and Mg_2NiH_4, along with MgPd intermetallic. Finally, the complete miscibility of the Pd-Ag system leads to the formation of a unique intermetallic $MgPd_{0.5}Ag_{0.5}$ phase besides MgH_2.

The thermodynamics of the four compounds have been experimentally determined by means of PCI measurements using the Van't Hoff equation. Hydrogen absorption isotherms exhibit two equilibrium plateau pressures between 0.01 and 3 MPa, at temperatures between 595 and 650 K. The enthalpy and entropy of the low pressure plateau are, for all compounds, very close to those of the MgH_2. In contrast, significant destabilization is found for the high pressure plateau, which exhibits much lower enthalpy variation but also, and unfortunately, smaller entropy loss. It was highlighted that thermodynamic destabilization systematically entailed an increase of disorder in the final intermetallic (*e.g.* $MgPd_{0.5}Ag_{0.5}$) or hydride (*e.g.* Mg_2NiH_4) phases. In consequence, the effective improvement on the operating temperature and pressure is limited. The knowledge of this effect allows now to focus effort on reducing the disorder in the final products of the hydrided state.

In the cases of TM = Pd and Ni, the enthalpy of the hydrogenation reactions has been calculated using the enthalpies of formation of the different compounds involved and applying Hess's law. The agreement between the calculated and experimental values is very good and encourages performing further *ab initio* calculations to anticipate possible destabilization by Mg-TM alloying.

Unquestionably, the Ni-substituted alloy possesses the strong advantage of a much higher hydrogen storage capacity (5.6 wt%. H at T = 623 K and P_{H2} = 3 MPa) as compared to the other studied compounds (3.2 wt.% and 3.0 wt.% H in the same P-T conditions for Cu and Ag, respectively). However, it is probable that the absorption capacity of the $Mg_6Pd_{1-x}Cu_x$ compound can increase up to 4.3 wt.% H at higher hydrogen pressure, and we have seen that $Mg_6Pd_{1-x}Ag_x$ absorbed 4.4 wt.% H under 4 MPa at 623 K. Although no thermodynamic data were obtained on this area of the PCI curves, the hydride formed at higher pressures will obviously be less stable.

Kinetic improvements are limited for Ag and Cu substitutions. In contrast, the Ni-substituted compound exhibits much faster absorption kinetics and a low activation energy for desorption (E_a = 68(5) kJ/molH_2). This very interesting property is attributed to a catalytic effect of the Mg_2NiH_4 phase, which is formed during the alloy disproportionation on hydriding, on the Mg/MgH_2 nucleation. For all compounds, absorption reaction kinetics are controlled by diffusion of TM atoms, whereas the rate-limiting parameter during H-desorption is the MgH_2/Mg interface displacement.

References

1. Ponthieu M, Fernández JF, Cuevas F, Ares JR, Leardini F, Bodega J, et al. Reversible hydrogen storage in the Ni-rich pseudo-binary $Mg_6Pd_{0.25}Ni_{0.75}$ intermetallic compound: Reaction pathway, thermodynamic and kinetic properties. *J. Alloys Compd.* 2013; **548** (**0**): 96–104.
2. Ponthieu M, Fernandez JF, Cuevas F, Bodega J, Ares JR, Adeva P, et al. Structural and Chemical Characterization of $Mg_6Pd_{1-x}TM_x$ (TM = Ag, Cu) Pseudo-binary Compounds at TM Solubility Limit. *Intermetallics* 2013; Submitted.
3. Samson S. Complex Cubic A_6B Compounds. II. The crystal structure of Mg_6Pd. *Acta Cryst.* 1972; **B28**: 936.
4. Makongo JPA, Prots Y, Burkhardt U, Niewa R, Kudla C, Kreiner G. A case study of complex metallic alloy phases: structure and disorder phenomena of Mg-Pd compounds. *Philos. Mag.* 2006; **86**: 427–433.
5. Dufour J, Huot J. Study of Mg_6Pd alloy synthesized by cold rolling. *J. Alloys Compd.* 2007; **446-447**: 147–151.
6. Kume Y, Weiss A. On the interaction of hydrogen with the intermetallic phase Mg_6Pd. *J. Less-Common Met.* 1987; **136**: 51–54.
7. Makongo JPA. A case study of complex metallic alloy phases: Structure and disorder phenomena of Mg-Pd compounds. 2009; University of Technology, Dresden.
8. Huot J, Yonkeu A, Dufour J. Rietveld analysis of neutron powder diffraction of Mg_6Pd alloy at various hydriding stages. *J. Alloys Compd.* 2008; **475**: 168–172.
9. Makongo JPA, Kudla C, Prots Y, Niewa R, Burkhardt U, Kreiner G. Crystal structure of trimagnesium monopalladium, Mg_3Pd. *Z. Krist.-New Cryst. Struct.* 2005; **220** (**3**): 289–290.
10. Stampfer JF, Holley CE, Suttle JF. The Magnesium-Hydrogen System. *J. Amer. Chem. Soc.* 1960; **82**: 3504–3508.

11. Fernandez JF, Widom M, Cuevas F, Ares JR, Bodega J, Leardini F, et al. First-principles phase stability calculations and estimation of finite temperature effects on pseudo-binary $Mg_6(Pd_xNi_{1-x})$ compounds. *Intermetallics* 2011; **19** (**4**): 502–510.
12. Fernandez JF. Results from not published internal studies. 2013;
13. Ghosh G, Kantner C, Olson GB. Thermodynamic modeling of the Pd-X (X=Ag, Co, Fe, Ni) systems. *J. Phase Equilib.* 1999; **20** (**3**): 295–308.
14. Prince A. Silver-Magnesium-Palladium. *VCH* 1988; **2**: 359–362.
15. Nayeb-Hashemi AA, Clark JB. The Ag-Mg (Silver-Magnesium) system. *Bull. Alloy Phase Diagr.* 1984; **5** (**4**): 348–358.
16. Okamoto H. Mg-Pd (Magnesium-Palladium). *J. Phase Equilib. Diff.* 2010; **31** (**4**): 407–408.
17. Kreiner G, Spiekermann S. Crystal structure of epsilon-$Ag_{7+x}Mg_{26-x}$ - A binary alloy phase of the Mackay cluster type. *Z. Anorg. Allg. Chem.* 2001; **627** (**11**): 2460–2468.
18. Westin L. A Palladium-Magnesium Alloy phase of Co_2Al_5 type. *Acta Chem. Scand.* 1968; **22**: 2574–2580.
19. Sharma S, Weiss A. Thermal and X-Ray-Investigations of the Quasi-Binary System $Ag_{1-x}Pd_xMg$ ($0 < x < 0.5$). *J. Less-Common Met.* 1984; **104** (**1**): L5–L8.
20. Latroche M, Joubert JM, Percheron-Guegan A, Notten PHL. Crystal structure of nonstoichiometric copper-substituted $La(Ni_{1-z}Cu_z)_x$ compounds studied by neutron and synchrotron anomalous powder diffraction. *J. Solid State Chem.* 1999; **146** (**2**): 313–321.
21. Huot J, Liang G, Boily S, Van Neste A, Schulz R. Structural Study and Hydrogen Sorption Kinetics of Ball-Milled Magnesium Hydride. *J. Alloys Compd.* 1999; **293-295**: 495–500.
22. Fernandez JF, Sanchez C. Simultaneous TDS-DSC measurements in magnesium hydride. *J. Alloys Compd.* 2002; 348–352.
23. Han JS, Pezat M, Lee JY. Thermal-Desorption of Hydrogen from Magnesium Hydride. *Scripta Metallurgica* 1986; **20** (**7**): 951–956.
24. Fernandez JF, Sanchez C. Rate determining step in the absorption and desorption of hydrogen by magnesium. *J. Alloys Compd.* 2002; **340**: 189–198.
25. Yoo Y, Tuck M, Kondakindi R, Seo CY, Dehouche Z, Belkacemi K. Enhanced hydrogen reaction kinetics of nanostructured Mg-based composites with nanoparticle metal catalysts dispersed on supports. *J. Alloys Compd.* 2007; **446**: 84–89.
26. Leardini F, Ares JR, Fernández JF, Bodega J, Sánchez C. An investigation on the thermodynamics and kinetics of magnesium hydride decomposition based on isotope effects. *Int. J. Hydrogen Energy* 2011; **36** (**14**): 8351–8357.
27. Eberle U, Felderhoff M, Schüth F. Chemical and Physical Solutions for Hydrogen Storage. *Angew. Chem. Int. Ed.* 2009; **48** (**36**): 6608–6630.
28. Flanagan TB, Oates WA. Thermodynamics of Intermetallic Compound-Hydrogen Systems. In: Schlapbach DL (ed). *Hydrogen in Intermetallic Compounds I*. Springer Berlin Heidelberg; 1988. pp. 49–85.
29. Subramanian PR, Laughlin DE. Cu-Pd (Copper-Palladium). *J. Phase Equilib.* 1991; **12** (**2**): 231–243.
30. Reilly JJ, Wiswall RH. Reaction of hydrogen with alloys of magnesium and copper. *Inorg. Chem.* 1967; **6** (**12**): 2220–2223.
31. Selvam P, Viswanathan B, Swamy C, Srinivasan V. Studies on the Thermal-Characteristics of hydrides of Mg, Mg_2Ni, Mg_2Cu and $Mg_2Ni_{1-x}M_x$ (M = Fe, Co, Cu or Zn - $0<x<1$) alloys. *Int. J. Hydrogen Energy* 1988; **13** (**2**): 87–94.
32. Shao HY, Wang YT, Xu HR, Li XG. Preparation and hydrogen storage properties of nanostructured Mg_2Cu alloy. *J. Solid State Chem.* 2005; **178** (**7**): 2211–2217.
33. Cuevas F, Fernandez JF, Ares JR, Leardini F, Latroche M. Crystal structure and hydrogenation properties of pseudo-binary $Mg_6Pd_{0.5}Ni_{0.5}$ complex metallic alloy. *J. Solid State Chem.* 2009; **182**: 2890–2896.
34. Okamoto H. Cu-Mg (copper-magnesium). *J. Phase Equilib.* 1992; **13** (**2**): 213–214.

35. Cuevas F, Fernandez JF, Ares JR, Leardini F, Sanchez C. Homogeneity range and crystal structure of Ni substituted Mg_6(Pd,Ni) complex intermetallic compounds. *J. Phys. Chem. Solids* 2010; **71** (**9**): 1259–1263.
36. Feufel H, Sommer F. Thermodynamic Investigations of Binary-Liquid and Solid Cu-Mg and Mg-Ni Alloys and Ternary Liquid Cu-Mg-Ni Alloys. *J. Alloys Compd.* 1995; **224** (**1**): 42–54.
37. Pozzo M, Alfè D. Hydrogen Dissociation and Diffusion on Transition Metal (= Ti, Zr, V, Fe, Ru, Co, Rh, Ni, Pd, Cu, Ag)-doped Mg(0001) Surfaces. *Int. J. Hydrogen Energy* 2009; **34** (**4**): 1922–1930.
38. Milanese C, Girella A, Bruni G, Cofrancesco P, Berbenni V, Matteazzi P, et al. Mg–Ni–Cu mixtures for hydrogen storage: A kinetic study. *Intermetallics* 2010; **18** (**2**): 203–211.
39. Lass EA. Reversible hydrogen-storage at reduced temperatures in the intermetallic compound Mg_6(Ni,Pd). *Int. J. Hydrogen Energy* 2011; **36** (**22**): 14496–14502.
40. Noréus D, Werner P-E, Sieler J, Steimecke G, Hoyer E. Structural Studies of Hexagonal Mg_2NiH_x. *Acta Chem. Scand.* 1982; **36a**: 847–851.
41. Stadelmaier HH, Hardy WK. Ternare Kohlenstofflegierungen Von Palladium Und Platin Mit Magnesium, Aluminium, Zink, Gallium, Germanium, Kadmium, Indium, Zinn, Quecksilber, Thallium Und Blei. *Z. MetaIlkd.* 1961; **52** (**6**): 391–396.
42. Zaluska A, Zaluski L, Ström-Olsen JO. Synergy of hydrogen sorption in ball-milled hydrides of Mg and Mg_2Ni. *J. Alloys Compd.* 1999; **289** (**1–2**): 197–206.
43. Liang G, Huot J, Boily S, Schulz R. Hydrogen desorption kinetics of a mechanically milled MgH_2-5at.%V nanocomposite. *J. Alloys Compd.* 2000; **305** (**1-2**): 239–245.
44. Liang G, Huot J, Boily S, Van Neste A, Schulz R. Catalytic effect of transition metals on hydrogen sorption in nanocrystalline ball milled MgH_2-TM (TM=Ti, V, Mn, Fe and Ni) systems. *J. Alloys Compd.* 1999; **292** (**1-2**): 247–252.
45. Zeng K, Klassen T, Oelerich W, Bormann R. Thermodynamic analysis of the hydriding process of Mg-Ni alloys. *J. Alloys Compd.* 1999; **283** (**1-2**): 213–224.
46. Zolliker P, Yvon K. Comments on the structure ambiguity of cubic Mg_2NiH_4 as found by neutron powder diffraction analysis. *Mater. Res. Bull.* 1986; **21** (**4**): 415–419.
47. Zolliker P, Yvon K, Baerlocher C. Low-Temperature Structure of Mg_2NiH_4 - Evidence for Microtwinning. *J. Less-Common Met.* 1986; **115** (**1**): 65–78.
48. Hancock J, Sharp J. Method of Comparing Solid-State Kinetic Data and Its Application to Decomposition of Kaolinite, Brucite, and $BaCO_3$. *J. Am. Ceram. Soc.* 1972; **55** (**2**): 74–77.

Chapter 4.

Nanoconfinement of Mg_6Pd particles in porous carbon

OUTLINE

In this chapter, the effect of nanosizing on the kinetics and thermodynamics of (de)hydrogenation of Mg-based materials is approached. One main issue related to the use of nanoparticles is the fast sintering of the nanostructures with temperature and/or cycling. Indeed, large particles are energetically more favourable due to their lower surface energy. To avoid this coalescence phenomenon, nanosized compounds can be stabilized into the pores of a light and inert matrix. This study focuses on the Mg_6Pd intermetallic compound which bulk properties have already been investigated in the previous chapter. The aim is to achieve kinetics improvement as well as destabilization of the hydrided state.

1 Carbon characteristics

The micro-structural properties of infiltrated metal nanoparticles strongly depend on the morphology of the supporting matrix. The available volume into the pores will define the maximum metal loading of the hybrid compound while the support pore size distribution will restrict the particle size and its distribution. In this investigation, a commercial activated carbon (High Surface Area Graphite, HSAG500 from TIMCAL) has been chosen for its high porosity and purity (> 99.9 %). Micro-structural observations were performed by Transmission Electron Microscopy. Figure 4.1 shows the bright field image of pristine HSAG500 carbon.

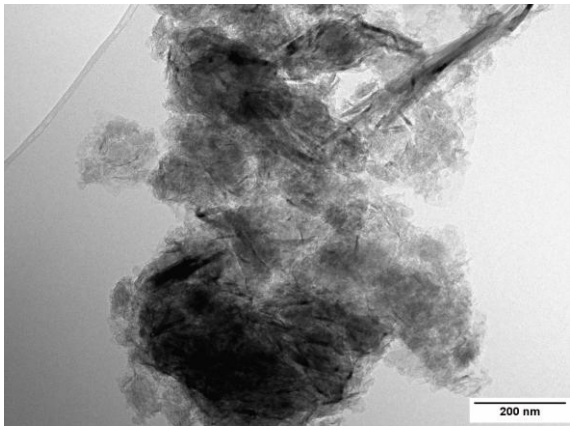

Figure 4.1. TEM image of HSAG500.

As can be observed on the XRPD pattern of Figure 4.2, the crystal structure of the HSAG500 corresponds to the common hexagonal graphite.

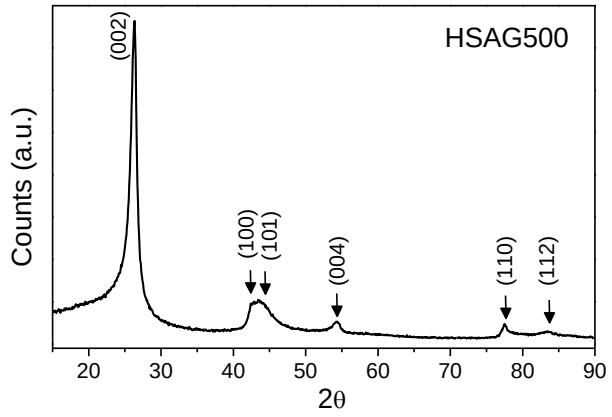

Figure 4.2. XRPD patterns (Cu K_α radiation) of pristine HSAG500.

The surface area and porosity of pristine carbon have been determined by nitrogen adsorption isotherm at 77 K (Figure 4.3). The curve exhibits a hysteresis loop of type H2 according to IUPAC classification, which is attributed to an irregular and wide pore size distribution. The specific surface area was obtained by the Brunauer-Emmett-Teller (BET) method in the 0.05-0.25 relative pressure range. The BET surface area was 500(10) m^2/g, in agreement with the manufacturer data (500 m^2/g).

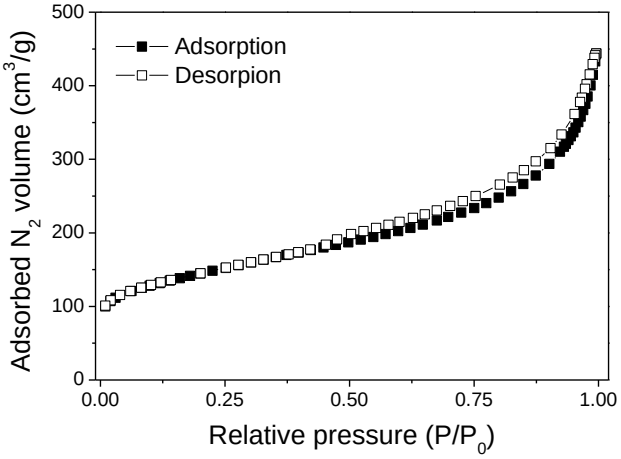

Figure 4.3. Nitrogen physisorption isotherm of pristine HSAG500.

The pore size distribution displayed in Figure 4.4 was determined by the Barrett-Joyner-Halenda (BJH) method. The modal value of the pore size distribution is around 4 nm and the total porous volume is 0.69 cm^3/g. The microporous volume (*i.e.* with pore diameters smaller than 2 nm) reached 0.19(1) cm^3/g.

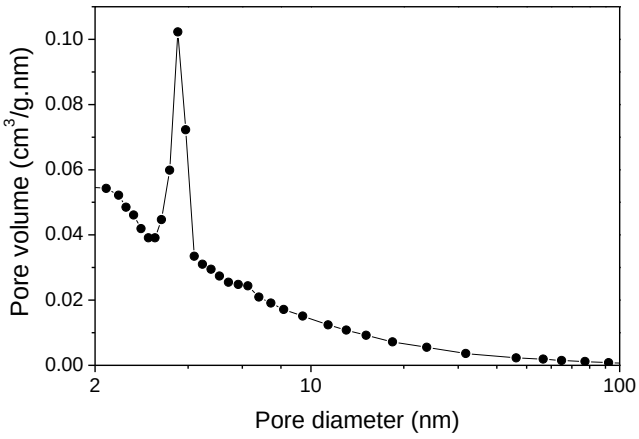

Figure 4.4. Pore size distribution of pristine HSAG500 determined by the BJH model.

2 Structural properties of the synthesized materials

The confinement of Mg_6Pd intermetallic nanoparticles was achieved by the Pd-impregnation of the carbon followed by melt-infiltration process. After the precursor impregnation step with the solution of H_2PdCl_4, the Pd content in the Pd@C hybrid was determined by ICP-OES (inductively coupled plasma optical emission spectrometer) as 8.6(3) wt.% Pd. The Pd@C was then mixed with MgH_2 powder which mass was calculated to obtain the Mg_6Pd stoichiometry. After melt-infiltration of Mg, the final metal loading (*i.e.* $m_{Mg+Pd}/m_{Mg+Pd+C}$) in the Mg_6Pd@C hybrid was 18.3(5) wt.%, as calculated from the weighted mass of MgH_2 and the mass of impregnated Pd deduced from ICP-OES data. The obtained hybrid material has been then hydrogenated overnight in an autoclave at 573 K under a hydrogen pressure of 5 MPa.

The bulk Mg_6Pd used as a reference sample was a single phase alloy ball-milled during 5 min and sieved to reach a grain size below 63 μm.

2.1 Textural properties

The N_2-physisorption isotherms (Figure 4.5 top) have been measured on the hybrid compounds after each step of the synthesis. In addition, one sample was leached from all metal particles using an acidic solution. The main results extracted from BET and BJH calculations are presented in Table 4.1 and the pore size distribution is displayed at the bottom of Figure 4.5. Comparison of the isotherms shows a loss in the total pore volume after Pd impregnation, passing from 0.69 to 0.61 cm^3/g. This volume reduction

is more important than it would be expected from the volume occupied by the amount of Pd. We can interpret this observation by the obstruction of the micropores by the Pd nanoparticles. The pore size distribution shows that the volume reduction mainly concerns the pores smaller than 10 nm, but we also observe a shift to lower value of the modal pore size. This last point suggests that the pores are occupied by Pd nanoparticles but that they are not totally filled, which results in smaller pores and only a slightly surface area decrease (460 m^2/g). After Mg infiltration, the total pore volume decreases to 0.51 cm^3/g and the surface area is strongly reduced to 320 m^2/g. The pore size distribution is similar to the one of Pd@C but with a reduced volume. This indicates that Mg infiltrated the same pores as those containing the Pd nanoparticles, making possible the reaction of both elements. In the hydrided sample, the BET surface area slightly decreases to 263 m^2/g and the total pore volume is reduced to 0.41 cm^3/g. Indeed, H-absorption is expected to expand the volume of the active material and pore obstruction also contributes to the pore volume decrease. Surprisingly, the modal pore size recovers the same value as in the pristine carbon, indicating that the active material might have got out of the 4 nm pores and occupies instead larger pores as shown by the volume decrease for diameters from 5 to 10 nm. In addition, the pores smaller than 3 nm are blocked by the hydrided particles. This process can occur during the reaction of the alloy with hydrogen to form MgH_2. Finally, the leached sample exhibits a similar BET surface area and total pore volume than in the pristine carbon, showing that the porous structure of the carbon was preserved during the different treatments of the synthesis.

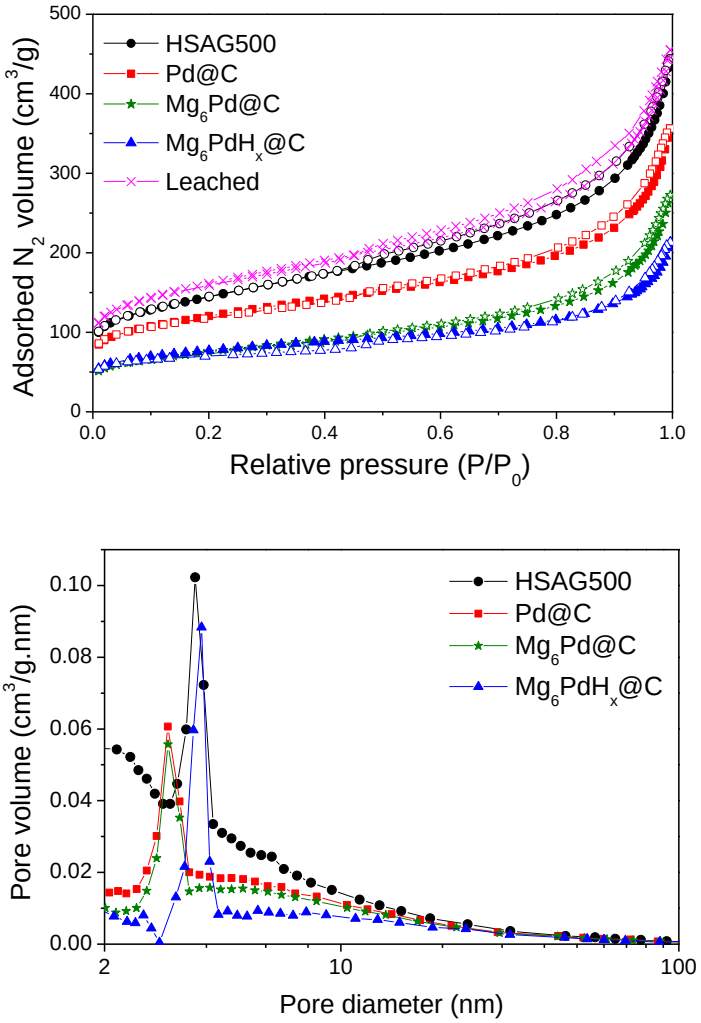

Figure 4.5. Nitrogen physisorption isotherms (top) and pore size distribution (bottom) of pristine HSAG500, after Pd impregnation (Pd@C), after infiltration of Mg (Mg_6Pd@C), after hydrogenation (Mg_6PdH_x@C) and after removal of all metal species (leached). Full symbols correspond to adsorption and empty symbols to desorption.

Table 4.1. BET surface area, total pore volume and mean pore size obtained from N_2-physisorption measurements on hybrid samples at different stages. All values are given per gram of carbon.

Sample	S (BET) (m^2/g)	Total pore volume (cm^3/g)	Expected volume loss (cm^3/g)	Modal pore size (nm)
HSAG500	500(10)	0.69(1)	-	4
Pd@C	460(10)	0.61(1)	0.01	3
Mg_6Pd@C	320(7)	0.51(1)	0.07	3
Mg_6PdH_x@C	262(6)	0.41(1)	-	4
Leached	500(10)	0.70(1)	-	3

2.2 Micro-structural characterization

TEM imaging was performed on the hybrid samples (Figure 4.6) in order to determine the distribution of the nanoparticles in the carbon matrix and their size. The histograms displayed at the right side of Figure 4.6 are obtained by measuring the diameters of random particles.

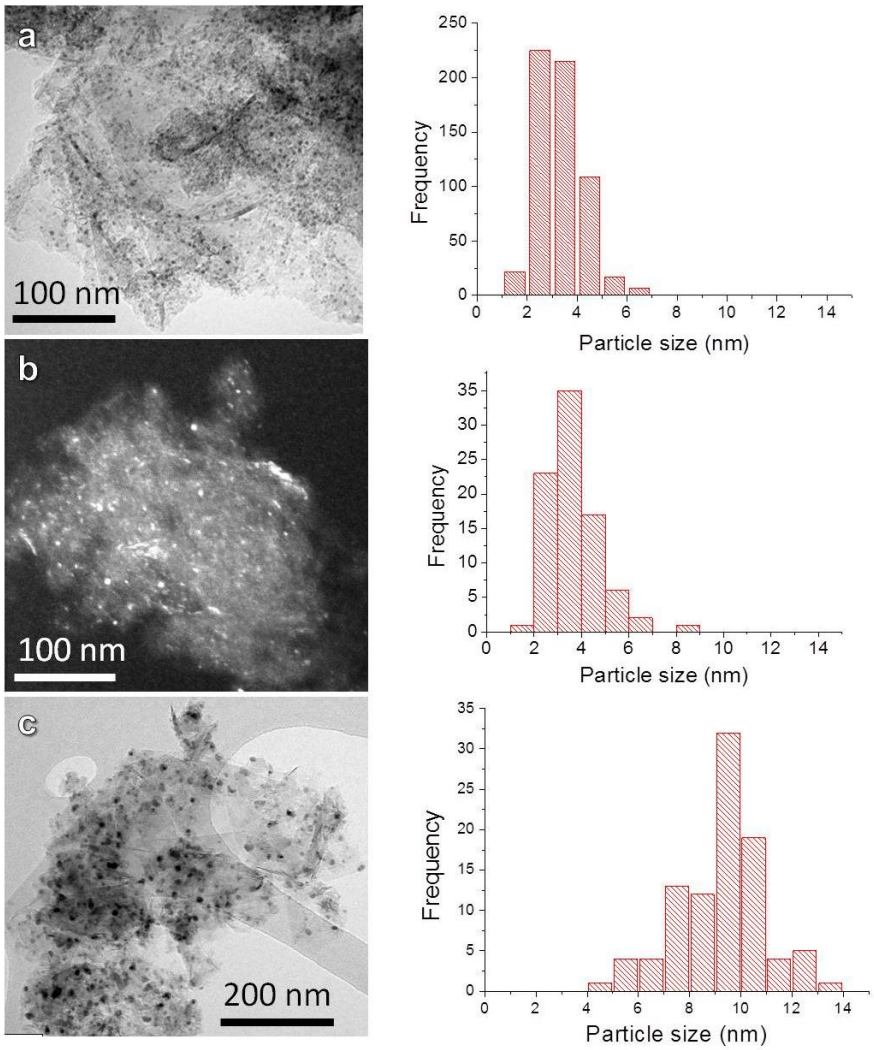

Figure 4.6. TEM images of a) Pd@C, b) Mg_6Pd@C and c) Mg_6PdH_x@C samples. The histograms on the right display the size distribution of the nanoparticles.

The Pd@C hybrid resulted in a homogeneous distribution of Pd nanoparticles which diameter was centred at 3 nm. After Mg infiltration, the mean particle size slightly increases to 4 nm and the homogeneous distribution is maintained all over the carbon.

After hydrogenation, the particle size clearly increases to ~ 10 nm. In consequence, these particles do not fit any more in the 4 nm pores and have to be located in larger pores. This observation confirms the previous assumption that hydrogenation causes the extraction of the active material from the 4 nm pores and a coarsening of the particles.

2.3 Structural properties

2.3.1 XRPD analyses

Figure 4.7 shows the XRPD patterns of the hybrid compounds at different stages of the synthesis. The broad diffraction lines corresponding to Pd in the Pd@C hybrid are typical of low-range nanometric crystals, in agreement with the TEM observations. Similarly, the XRPD pattern of the infiltrated alloy Mg_6Pd@C exhibits only two broad peaks corresponding to the strongest lines of the Mg_6Pd intermetallic compound: reflections of the (422) and (822) planes at $2\theta = 21.63°$ and 39.94°, respectively. The fact that no Mg neither Pd unary phases were detected indicates that both elements did react during the melt-infiltration process. However, X-ray diffraction data are insufficient to determine the crystal structure of the obtained Mg-Pd phase as some Mg_xPd_y intermetallic phases such as Mg_5Pd_2 possess their main diffraction peaks around $2\theta = 21$ and 39°. The occurrence of broad diffraction peaks both for Pd@C and Mg_6Pd@C concurs with the formation of nanocrystalline metal particles within the pores of the carbon host.

Regarding the hydrided compound, the MgH_2 phase is clearly identified, with much more narrow peaks, reflecting the larger crystallite size of this phase. The MgPd intermetallic is also detected in a large amount, as deduced from the intensity of the corresponding peaks. A small amount of MgO is also detected, especially in the hydrided compound, owing to the possible air contamination of the sample during handling.

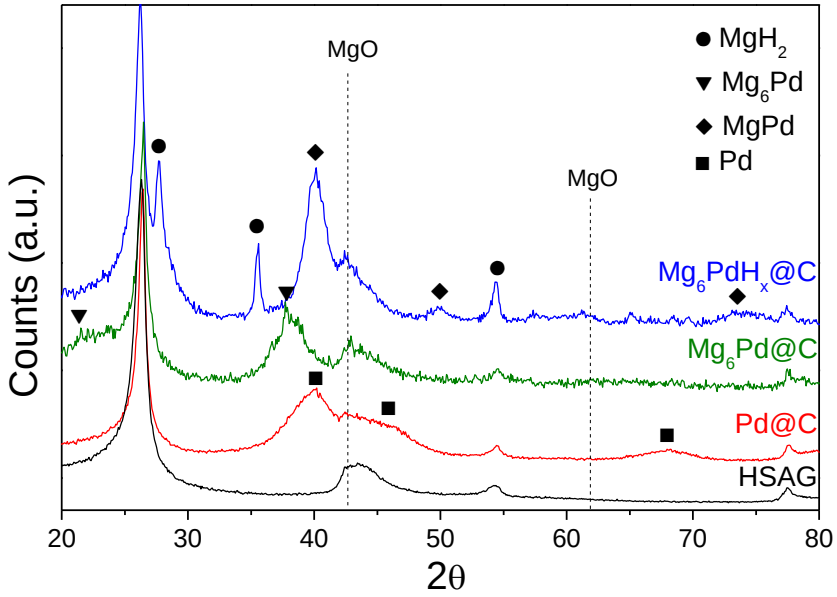

Figure 4.7. XRPD patterns (Cu K_α radiation) and phase identification of pristine HSAG, Pd@C, Mg_6Pd@C and Mg_6PdH_x@C hybrids.

2.3.2 XAS measurements

In an attempt to obtain more detailed information on the nature of the Mg-Pd phase formed during melt-infiltration, XAS measurements at the Pd K-edge have been performed. This technique offers the possibility to analyse the local order of amorphous or nanocrystalline structure that cannot be determined by XRPD.

The as-synthesized Mg_6Pd@C hybrid was measured and compared to a bulk Mg_6Pd reference as well as a Pd foil standard. Figure 4.8a displays the experimental XANES spectra near the Pd-edge obtained for the Pd foil, the bulk Mg_6Pd reference and the hybrid Mg_6Pd@C compound. Mg_6Pd and Mg_6Pd@C present similar edges, with a shoulder around 24359 eV which is not observed in the Pd foil edge. Above the edge, signal oscillations related to the local atomic order are observed. The signals for Mg_6Pd and Mg_6Pd@C only slightly differ and are in phase opposition to those of the Pd foil. This fact suggests for the hybrid material that the first coordination sphere around the Pd atom contains Mg. This preliminary result indicates that Mg and Pd species coexist in the same phase and hence that a Mg-Pd alloy is formed in the nanoconfined particles.

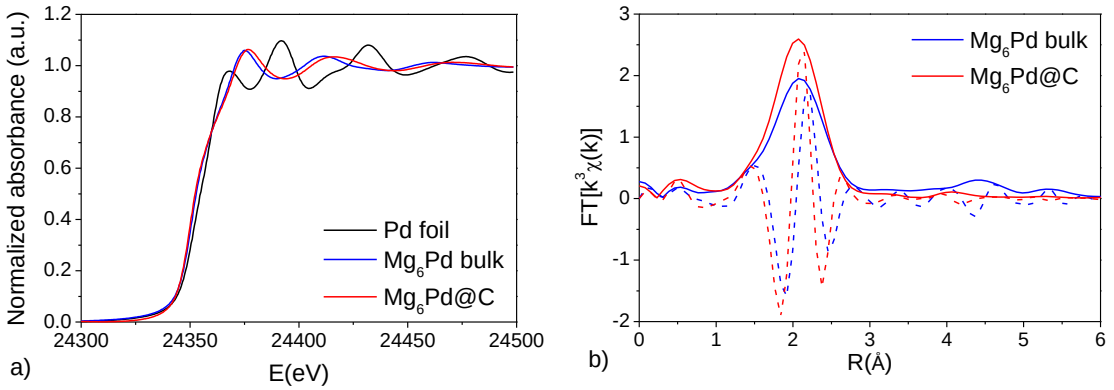

Figure 4.8. a) XANES spectra near Pd-edge of bulk and nanoconfined Mg_6Pd compared to the Pd metal signal. b) Fourier transform of the EXAFS function $\chi(k)$ (k^3-weighted calculated on 2.8-11.5 $Å^{-1}$ domain) of bulk and nanoconfined Mg_6Pd. Continuous and dashed lines correspond to modulus and imaginary part, respectively.

The Fourier transforms of bulk Mg_6Pd and Mg_6Pd@C EXAFS signals are shown in Figure 4.8b. The observed intensity of the main peak (*i.e.* the signal due to the first sphere) is stronger for the nanoparticles than for the bulk alloy. At longer distances in the R-space (*i.e.* at longer distances from the Pd atoms), the signal intensity is weaker for the Mg_6Pd@C hybrid than for the bulk alloy, as a result of higher disorder at longer distances characteristic of nanosized materials.

Next, the signals of the Mg_6Pd reference and Mg_6Pd@C hybrid have been fitted according to a model that focuses on the first coordination sphere around Pd atoms. The filtered experimental spectra are compared to theoretical ones, calculated from the crystallographic data of the Mg_6Pd compound. As described in section 3.1.2 of Chapter 1 and illustrated in Figure 4.9, the Mg_6Pd structure comprises 3 sites (10, 11, 13) exclusively occupied by Pd atoms and one shared with Mg (12).

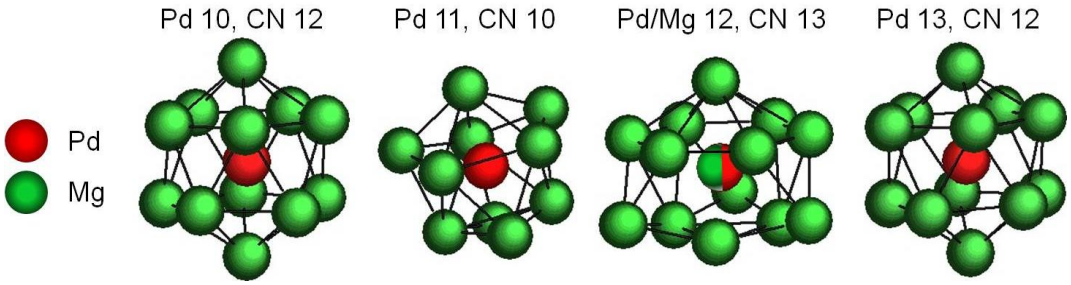

Figure 4.9. Representation of the first coordination sphere around each Pd site in the Mg_6Pd structure.

All together, these 4 independent sites provide 14 different Pd-Mg interatomic distances in the 2.5-3.5 Å range. Taking into account the multiplicity and SOF of each site, it results in an average coordination number of 10.8 Mg atoms (approximated to 11 for EXAFS fits). In order to reduce the number of independent fitted parameters, the environment of a Pd atom has been simplified to 3 average Pd-Mg distances (R_i) for which the Mg atom distribution (N_i) is described in the first row of Table 4.2.

Table 4.2. Environment within the first shell of a Pd atom as calculated from crystallographic data and as fitted for Mg_6Pd bulk and nanoparticles. N_i is the number of Mg atoms situated at a distance R_i of a Pd centre. σ^2 is the Debye-Waller factor and QF_k and QF_R are the quality factors in k- and R-spaces, respectively.

	N_1	R_1 (Å)	N_2	R_2 (Å)	N_3	R_3 (Å)	σ^2 (Å^2)	QF_k	QF_R
Crystallographic average distances	5.7	2.79(10)	3.4	2.96(3)	1.7	3.12(1)	-	-	-
Mg_6Pd bulk	4(3)	2.76(8)	5(1)	2.95(11)	2	3.18(17)	0.012(9)	0.61	0.3
Mg_6Pd@C	8(7)	2.73(2)	3	3.00(5)	-	-	0.017(3)	0.8	0.68

Initially, a preliminary fit was performed to determine whether Pd atoms were present within the first sphere of each Pd site. This was achieved by refining the number of Pd and Mg atoms and their distances in the first coordination sphere, considering only a unique average distance for Pd-Mg or Pd-Pd. As expected for the bulk compound, the fitted number of Pd atoms converged to zero, in agreement with the structure previously described. The same fit was performed for the nanoconfined particles and a similar result was found, confirming that the neighbouring atoms within the first sphere around a Pd atom only consist of Mg. Thus, the nanoconfined compound is definitely a Mg-rich alloy.

Then, the local ordering of the Mg atoms around Pd ones has been fitted in both compounds by optimising the number of Pd-Mg distances used in the calculated signals to minimise the quality factors (QF) of the refinement [1]. In both cases, the total number of Mg atoms was set to 11. The graphical outputs of the bulk and nanoparticles fits are represented in Figure 4.10 and the main fit results are gathered in Table 4.2. For the bulk material, the best fit was obtained with a model that allows for 3 average distances, and the refined distances R_i were in good agreement with the average

crystallographic ones. This result is particularly satisfying in view of the complexity of the Mg_6Pd structure.

In the case of the nanoconfined particles, the experimental spectrum was also well fitted to the theoretical spectrum of the Mg_6Pd structure but the model was optimized, *i.e.* the QF minimised, by reducing the number of average distances to 2. This result shows the less complex atomic arrangement in the nanoparticles than in the bulk phase. The stronger intensity of the main peak observed for the nanoparticles (Figure 4.8b) also results from its simpler atomic arrangement as compared to bulk Mg_6Pd. Indeed, calculated signals from the Mg_6Pd crystallographic structure show the occurrence of destructive interferences that reduce the signal intensity of the FT main peak. The two different distances obtained from Mg_6Pd@C result in less destructive interferences, and thus a more intense FT main peak. In addition, the Debye-Waller factor (σ^2) was higher for the nanoparticles than in the bulk material. This last point indicates a higher atomic disorder in the hybrid sample than in the bulk Mg_6Pd compound, as commonly observed in nanoparticles. Finally, the refined average distances were smaller in the nanoparticles than the crystallographic ones.

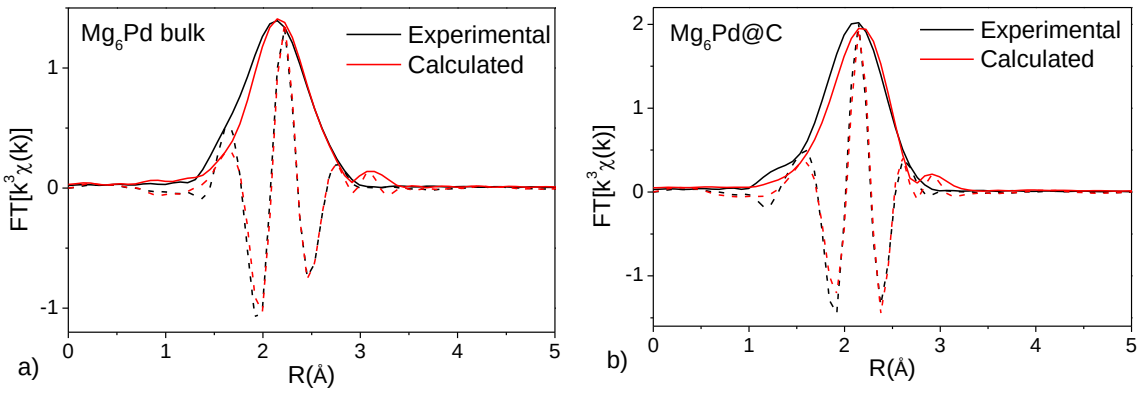

Figure 4.10. First shell refinements of EXAFS spectra obtained for a) bulk Mg_6Pd and b) Mg_6Pd@C hybrid. The black line corresponds to the experimental signal and the red line is the calculated one. Continuous and dashed lines correspond to modulus and imaginary part, respectively.

In summary, it was found that the structure of the nanoparticles is very close but somehow less complex than that of the bulk phase. Indeed, the large cell (a = 20.15 Å)

of the Mg_6Pd phase implies that a 4 nm nanoparticle contains two Mg_6Pd unit-cells. Following this geometric considerations, it is very likely that the atomic order of the complex Mg_6Pd crystal structure is not preserved in the hybrid material. Therefore, the nanoconfined phase corresponds to a Mg-rich Mg-Pd alloy which structure is simpler (*i.e.* lower number of different Pd-Mg distances) but more disordered (*i.e.* higher Debye-Waller factor) than the complex Mg_6Pd intermetallic.

3 Hydrogenation properties compared to bulk material

3.1 Kinetic properties and cyclability

3.1.1 Isothermal hydrogen absorption

Kinetics of absorption has been tested in a Sievert's apparatus at 573 K over 10 cycles of hydrogenation under 4.5 MPa of hydrogen pressure. The kinetic performance of the nanoconfined Mg_6Pd has been compared to that of the bulk alloy. The absorption curves of cycles 2, 5 and 10 are displayed in Figure 4.11. Desorption was achieved at P_{des} = 0.03 MPa. The first absorption corresponded to the activation cycle for the bulk sample and is not represented. In the nanosized sample, this step was not necessary and the first absorption was similar to the second one. The absorption kinetics in the nanoconfined material is strikingly enhanced, with a transformation about five times faster than in the bulk sample during the second absorption. This fast kinetics is attributed to the nanometric particle size which provides higher active surface for H-chemisorption and shorter H-diffusion path.

In addition, we observe a rapid decay of the absorption kinetics in the bulk material after only few cycles (Figure 4.11). The tenth absorption requires about 3 hours to reach 80 % of reacted fraction. This deterioration can be explained by the progressive disproportionation of the initial Mg_6Pd alloy into Mg and another Mg-Pd intermetallic phase. Indeed, it is probable that the alloy recombination step is not fully completed after each desorption owing to the slow diffusion kinetics of metallic atoms. In contrast, the nanoconfined Mg_6Pd exhibits steady absorption rates, even after 10 cycles. This result suggests that the nanometric size of the active material is maintained, by means of the physical barrier provided by the carbon pores to avoid coalescence. In consequence, the diffusion length of the metallic atoms remains very short and allows for fast alloy recombination and short H-diffusion length.

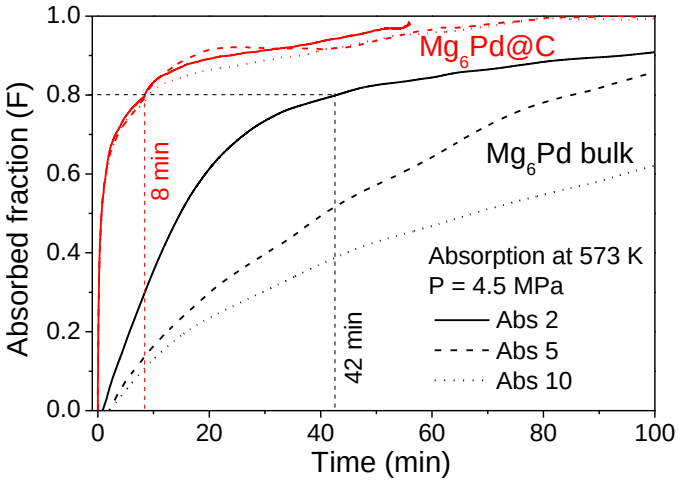

Figure 4.11. Time-evolution of the transformed fraction during H-absorption at 573 K in bulk and nanoconfined Mg_6Pd. Absorption curves during cycles 2, 5 and 10 are represented as solid, dash and dot lines, respectively.

Figure 4.12 shows the XRPD pattern of the desorbed Mg_6Pd@C after 10 cycles of absorption and desorption at 573 K. The presence of the Mg_6Pd phase seems quite clear, but we also detect the three characteristic peaks of the Mg phase at 2θ = 32.19, 34.40 and 36.62°. In addition, a broad peak is observed around 40° and a shoulder appears on both sides of the main carbon peak. According to mass balance considerations, these peaks must belong to a Pd-rich phase. Thus, the Mg_2Pd phase possesses its main diffraction peaks at 2θ = 25.58 and 38.78° [2] and the η-Mg_3Pd phase at 2θ = 24.66 and 39.02° [3]. However, the width and overlapping of the diffraction peaks do not allow concluding with certainty on the origin of these peaks. Anyway, this result shows the limited reversibility of the hybrid system as Mg segregation occurs. However, the persistence of broad diffraction peaks leads to believe that the nanoconfinement was preserved which allows for fast hydriding kinetics. We also see that the formation of MgO could not be avoided, in spite of the protective atmosphere used at each step of handling.

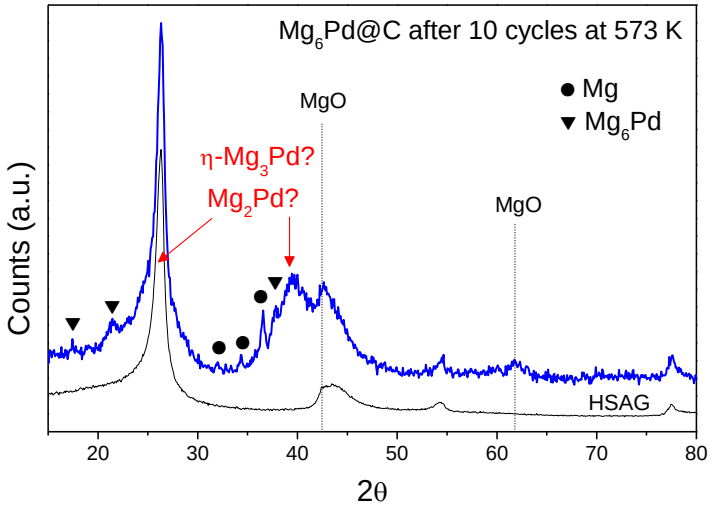

Figure 4.12. XRPD pattern (Cu K_α radiation) and phase identification of Mg_6Pd@C after 10 cycles of ab/desorption at 573 K. The pattern for the pristine HSAG is shown below.

Finally, it was found that the H-absorption capacity is significantly higher in the bulk sample than in the nanoparticles. The average amount of H-absorbed over the 10 cycles is 3.7(2) wt.% H for the bulk Mg_6Pd and 2.6(5) wt.% H in the nanoparticles of the hybrid compound (taking in account only the mass of active material). Similar observation has already been reported by Jurczyk *et al.* on nanocrystalline ball milled Mg_2Cu alloy and was attributed to the large amount of defects, strains and chemical disorder in the lattice of the nanoparticles [4]. It is probable that the highly disordered nanoconfined Mg_6Pd suffers from the same drawback which results in a reduced absorption capacity.

3.1.2 Thermal desorption

The H-desorption properties have also been analysed by means of TDS measurements (Figure 4.13) under secondary vacuum ($P_{res} = 2.10^{-4}$ Pa). For the bulk sample, the desorption begins around 650 K with a single and rather sharp peak. The Mg_6Pd@C hybrid starts to desorb at much lower temperature with a first broad peak between 370 and 515 K, followed by a more intense peak around 600 K. For both compounds, the main peak at high temperature is attributed to H-desorption from the MgH_2 phase. However, desorption from the nanoparticles occurs at about 100 K lower than from the bulk powder. This is attributed to the shortening of H-diffusion path for

the hybrid material. In addition, the broadening of the desorption peak as compared to bulk Mg_6Pd probably results of the size distribution of the hydride nanoparticles. The contribution of carbon on the accelerated desorption process also has to be considered, as it has already been reported to facilitate H-release [5; 6]. However, this effect was recognized to be of minor importance in comparison with the nanosizing effect. Regarding the low temperature peak observed during H-desorption from the hybrid material, it can be reasonably attributed to surface $MgH_2/Mg(OH)_2$ interface reactions [7]. Indeed, $Mg(OH)_2$ is unavoidably formed on the particles surface by reaction of MgH_2 with moisture impurities during handling. It was demonstrated that interaction between these two phases leads to H-desorption at low temperature. This effect is usually inappreciable but owing to the high specific surface area of the nanoparticles, the amount of hydrogen desorbed from this process results in a significant desorption peak at low temperature.

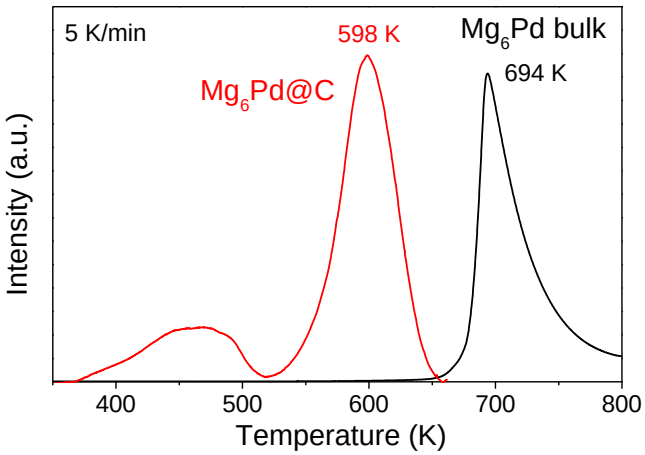

Figure 4.13. Thermal desorption hydrogen spectra at 5 K/min of bulk (black line) and nanoconfined (red line) Mg_6Pd.

3.2 Thermodynamic properties

The stability of the nanoconfined alloy has been compared to the already studied Mg_6Pd in its bulk form. Figure 4.14 shows the pressure-composition isotherm measured between 0.01 and 1 MPa of hydrogen pressure at 548 K. While the bulk alloy displays a flat plateau in this pressure range, the nanostructured compound exhibits a sloping plateau with a significantly higher equilibrium pressure. This result highlights the

equilibrium modification related to the nanosizing effect. In addition, the absence of well resolved plateau pressure also reflects the disordered structure of the nanoparticles.

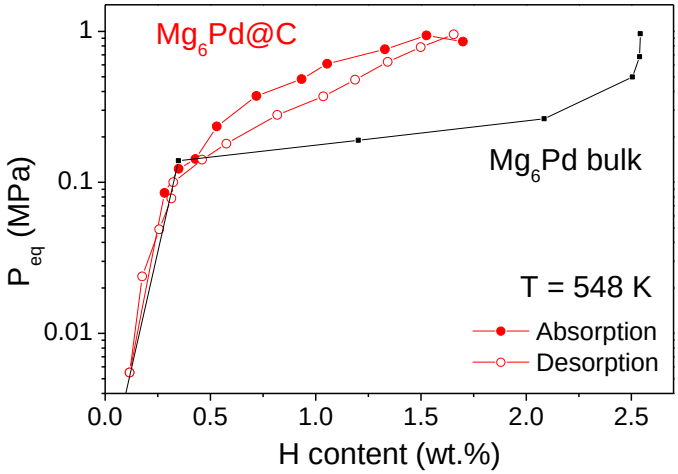

Figure 4.14. PCI curves at 548 K of the bulk (black line) and nanoconfined (red line) Mg_6Pd.

Another hint of hydride destabilization due to nanosizing effect has been evidenced through HP-DSC analysis. Figure 4.15 shows desorption/absorption cycles obtained in the same conditions for both nanoconfined and bulk Mg_6Pd. The desorption peak results in an endothermic signal while absorption is exothermic.

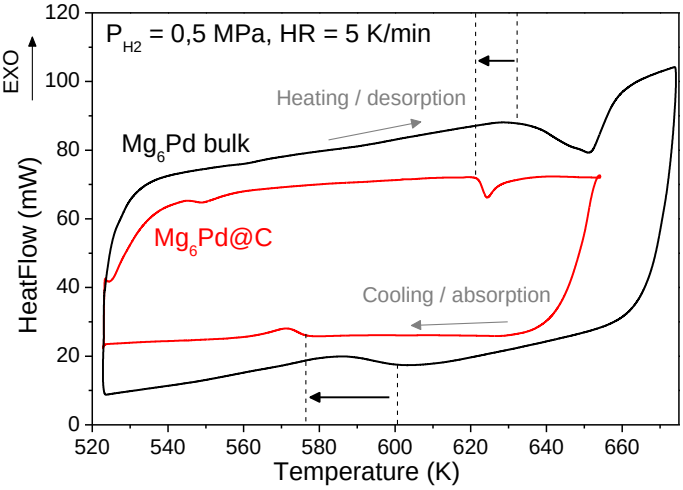

Figure 4.15. HP-DSC measurements obtained during heating and cooling ramps under 0.5 MPa of hydrogen pressure on bulk (black line) and nanoconfined (red line) Mg_6Pd.

On one hand, the narrow peak observed for the hybrid compound as compared to the bulk sample reflects the faster sorption kinetics of nanometric particles due to the shortening of diffusion paths. On the other hand, we observe that the onsets of both desorption and absorption peaks are shifted to lower temperature values in the case of the Mg_6Pd@C compound. This result indicates the destabilization of the nanoconfined alloy as compared to the bulk one. Indeed, as demonstrated by the Van't Hoff relationship (equation 1.2), for two metal-hydrogen systems working under isobaric conditions, the plateau temperature of the less stable one will be lower. Thus, this result confirms that the equilibrium of the nanoconfined alloy has been changed to a less stable hydrided state due to nanosizing effect.

4 Discussion

4.1 Synthesis and hydrogenation mechanism

The melt-infiltration method is a novel approach to synthesize stabilized Mg-based nanoparticles confined into a porous matrix. We demonstrated that it is relatively easy to infiltrate Mg at the molten state and make it react with the previously confined TM precursor into the pores of the carbon. This technique has already been successfully applied to Mg-Ni [8] and Mg-Cu [6] nanoparticles. The advantage to use Pd lies in its well-known catalytic properties and in its ability to form Mg-rich intermetallic phases. The targeted stoichiometry was the Mg richer intermetallic compound, *i.e.* the Mg_6Pd phase. However, maintaining the complex crystal structure of the Mg_6Pd phase at the nanometric scale seems improbable owing to its large cell parameter. Indeed, it is difficult to believe that a 2 nm side cubic cell can preserve its crystal structure when constrained to fit into a pore as small as 4 nm. Though, we were able to demonstrate the formation of Mg-rich Mg-Pd alloyed nanoparticles with sizes ranging from 2 to 8 nm. Phase identification by X-ray diffraction was rather complicated because of the low crystallinity of the alloy and the complexity of the Mg_6Pd structure. However, EXAFS analyses allowed stating that the nanocrystalline structure was close to that of the bulk Mg_6Pd (S.G. *F*-43*m*), though with a simpler atomic ordering.

We saw in Chapter 3 that hydrogenation of the Mg_6Pd compound led to the formation of MgH_2 together with a Mg_xPd_y intermetallic phase which composition depends on the pressure and temperature conditions. Therefore, this reaction requires

the diffusion of Mg and Pd atoms to form these two phases. In the case of the nanoconfined alloy, a similar mechanism occurs as we clearly observed the formation of MgH_2 and MgPd phases by XRPD (Figure 4.7). However, TEM images (Figure 4.6) and pore size distribution analysis (Figure 4.5) show that hydrogenation causes an increase in the particle size accompanied by a migration of the active material to larger pores. Considering the Mg segregation observed in the desorbed sample (Figure 4.12), we can assume that only a part of the MgH_2 phase migrates while the Pd-containing phase remains into the smallest pores. This process is responsible for the limited reversibility of the hybrid compound, making difficult to fully recover the original phase composition. However, it seems that the size of the particles remains in the nanometric scale, allowing for fast hydrogenation kinetics after at least 10 cycles.

4.2 Kinetic improvement

The faster kinetics of the nanoparticles as compared to the bulk material is striking. Not only the absorption takes place in less than 10 min at 573 K, but also the desorption occurs at about 100 K lower than in the bulk material. In addition, this fast kinetics was maintained during at least 10 cycles. The isothermal absorption curves of both compounds have been fitted according to the method proposed by Hancock and Sharp [9] and described in the section 5.3 of Chapter 3. The obtained fits for $0.2 < F < 0.5$ are displayed in Figure 4.16 with the corresponding *m*-values of the slope. The clearly different values of *m* indicate that different absorption mechanisms occur. In the case of the bulk compound ($m = 0.92$), the reaction seems to be controlled by a phase transformation mechanism[1], either the interface displacement (Mg_6Pd/Mg_xPd_y or Mg_6Pd/MgH_2) or the nucleation of the MgH_2 phase. In contrast, hydrogen absorption in the nanoparticles is limited by a diffusion process ($m = 0.54$), either of the metal or the hydrogen atoms. These two mechanisms can be explained by the difference in particle size. The amount of sites available for the nucleation of the MgH_2 phase is much higher in the nanosized sample than in the bulk material, owing to the high specific surface

[1] The different value of *m* as compared to the one obtained in Chapter 3, Figure 3.55 for the same compound ($m = 0.52$ at 623 K and $P_{H2} = 2$ MPa) is explained by the different temperatures and pressures of measurement.

area of the former one. Therefore, the rapid nucleation in the nanoparticles shifts the rate limiting step to hydrogen or metal diffusion. Although the present data does not allow to further distinction in the rate limiting step of each mechanism, we can conclude to a strong effect of nanosizing on the reaction kinetics.

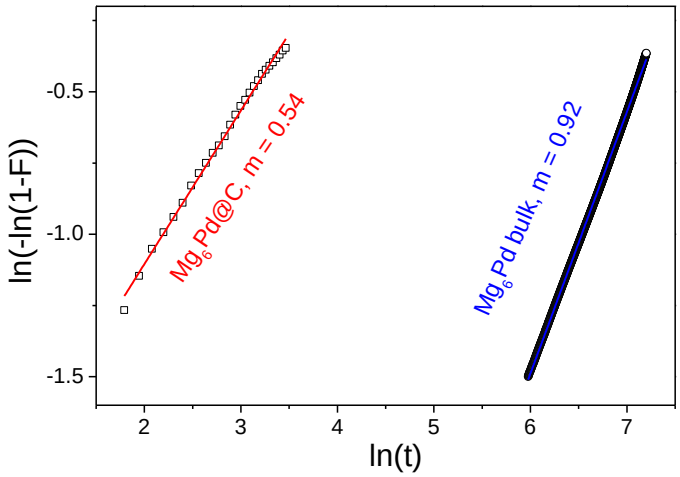

Figure 4.16. Plots of ln(-ln(1-F)) *vs.* ln(t) obtained for the absorption curves at 573 K under 4.5 MPa of hydrogen pressure for the nanoconfined and bulk Mg_6Pd.

The origin of the improved kinetics of the hybrid compound concerns different aspects. First, a catalytic effect of the carbon support on the (de)hydriding reaction is probable, but further experiments would have to be performed to confirm this hypothesis. Then, the nanometric scale of the active material is undoubtedly of great importance to reduce the diffusion path of hydrogen and provide a high surface area for H_2 dissociation/recombination. The role of the porous matrix is also essential to limit the sintering of the nanoparticles upon cycling, even if a small growth could not be avoided during hydrogenation. Finally, the modified structure of the alloy and the high disorder associated to the nanoscale are also expected to have a role on the reaction mechanism.

4.3 Effect on thermodynamics

The experimental results obtained in this chapter do not allow quantifying the effective destabilization as compared to bulk Mg_6Pd, but clear evidences of the thermodynamic modification are given. Thus, the PCI curve measured at 548 K shows a

significantly higher equilibrium pressure in the nanoparticles than in the bulk sample. Besides, the peak shift observed both on absorption and desorption during HP-DSC experiments also confirmed the reduced stability of the nanoconfined material. This destabilization can be attributed to two main phenomena:

i) The non-negligible free surface energy related to the nanosized particles results in a less stable hydride. This effect has already been anticipated by *ab initio* calculations but up to now very few experimental results support this assumption. An enthalpy of absorption of -63.8 kJ/mol_{H2} was reported for MgH_2 nanoparticles smaller than 3 nm [10]. However, this enthalpy reduction was accompanied by an entropy decrease and the effective change on the desorption temperature was only of 11 K at 0.1 MPa of hydrogen pressure. In our case, the effective destabilization seems to be significant

ii) The modified structure of the Mg_6Pd phase at the nano-scale probably alters the stability of the compound. Thus, we showed that the crystal structure of the Mg_6Pd compound was too complex (396 atoms) and too large (a ~ 2 nm) to be maintained in nanoparticles of the same composition. Therefore, the stability of such modified compound may differ from the bulk form.

It is now necessary to determine enthalpy en entropy values by performing further PCI measurements at different temperatures.

5 Conclusion

Nanoconfined Mg_6Pd particles have been successfully synthesized by melt-infiltration process in porous carbon. The particle size was about 4 nm in the as-synthesized compound and increased to 10 nm after hydrogenation. The outstanding kinetic and cycling properties of the hybrid Mg_6Pd@C compound are explained by the reduced H-diffusion path, the high specific surface area available for hydrogen dissociation and nucleation of the MgH_2 phase. In addition, the confinement in a porous scaffold allowed limiting the sintering of the particles, even though small Mg segregation could not be avoided. Thermodynamic destabilization was also achieved, confirming the various *ab initio* predictions on equilibrium and particle size matters.

References

1. Moscovici J, Rougier A, Laruelle S, Michalowicz A. Apparent mismatch between extended x-ray absorption fine structure and diffraction structures of crystalline metastable WO3 phases. *The Journal of Chemical Physics* 2006; **125** (**12**): 124505–124505–8.
2. Makongo JPA, Prots Y, Niewa R, Burkhardt U, Kreiner G. Crystal structure of dimagnesium monopalladium, Mg_2Pd. *Z. Krist.-New Cryst. Struct.* 2005; **220** (**3**): 291–292.
3. Makongo JPA, Kudla C, Prots Y, Niewa R, Burkhardt U, Kreiner G. Crystal structure of trimagnesium monopalladium, Mg_3Pd. *Z. Krist.-New Cryst. Struct.* 2005; **220** (**3**): 289–290.
4. Jurczyk M, Okonska I, Iwasieczko W, Jankowska E, Drulis H. Thermodynamic and electrochemical properties of nanocrystalline Mg_2Cu-type hydrogen storage materials. *J. Alloys Compd*. 2007; **429** (**1–2**): 316–320.
5. Lillo-Rodenas MA, Aguey-Zinsou KF, Cazorla-Amoros D, Linares-Solano A, Guo ZX. Effects of Carbon-Supported Nickel Catalysts on MgH_2 Decomposition. *J. Phys. Chem. C* 2008; **112** (**15**): 5984–5992.
6. Au YS, Ponthieu M, Zwienen R van, Zlotea C, Cuevas F, Jong K de, et al. Synthesis of Mg_2Cu nanoparticles on carbon supports with enhanced hydrogen sorption kinetics. *J. Mater. Chem. A* 2013; **1** (**34**): 9983–9991.
7. Leardini F, Ares JR, Bodega J, Fernandez JF, Ferrer IJ, Sanchez C. Reaction pathways for hydrogen desorption from magnesium hydride/hydroxide composites: bulk and interface effects. *Phys. Chem. Chem. Phys.* 2010; **12**: 572–577.
8. Bogerd R, Adelhelm P, Meeldijk JH, de Jong KP, de Jongh PE. The structural characterization and H_2 sorption properties of carbon-supported $Mg_{1-x}Ni_x$ nanocrystallites. *Nanotechnology* 2009; **20** (**20**): 204019.
9. Hancock J, Sharp J. Method of Comparing Solid-State Kinetic Data and Its Application to Decomposition of Kaolinite, Brucite, and $BaCO_3$. *J. Am. Ceram. Soc.* 1972; **55** (**2**): 74–77.
10. Zhao-Karger Z, Hu J, Roth A, Wang D, Kübel C, Lohstroh W, et al. Altered thermodynamic and kinetic properties of MgH_2 infiltrated in microporous scaffold. *Chem. Commun.* 2010; **46** (**44**): 8353–8355.

Chapter 5.

$Mg(H/D)_2$-$Ti(H/D)_2$ nanocomposites

OUTLINE

The objective of the following investigation is to significantly improve Mg sorption kinetics while preserving a high hydrogen storage capacity for a reduced cost of the material. A twofold approach is then developed: the use of a catalyst to accelerate hydrogen chemisorption, and nanosizing of the material to reduce the length of diffusion of H atoms. As described in Chapter 1, section 3.2.3, the choice of Ti basically relies on its light weight, the *fcc* structure of its hydride known to facilitate H diffusion and its low cost. The catalytic properties of the TiH_2 phase on reversible hydrogenation of MgH_2/Mg have already been reported [1–3] but the mechanisms responsible of the outstanding kinetic improvement remain unclear. In this chapter, the technique of RBM is employed to form $Mg(H/D)_2$-$Ti(H/D)_2$ nanocomposites by *in situ* hydrogenation of Mg and Ti powders during milling. A deep investigation of the structural properties of such nanocomposites is carried out to determine the catalytic role of the TiH_2 phase.

1 Hydrogenation by RBM

1.1 Formation of MgH_2-TiH_2 nanocomposites

The synthesis of MgH_2-TiH_2 nanocomposites was achieved by *in situ* hydrogenation of Mg-Ti powder mixtures during high energy ball milling under reactive atmosphere (hydrogen or deuterium). The monitoring of the pressure and temperature evolution into the vial allows recording the gas absorption as a function of milling time. A typical time evolution of hydrogen pressure and vial temperature recorded during two cycles of Mg-Ti RBM is displayed in Figure 5.1a. The pressure drop observed during the first milling cycle corresponds to the formation of the hydride phases. The concomitant temperature increase is due to ball collisions and frictions and does not exceed 315 K thanks to heat dissipation through the vial wall. During rest time, both temperature and pressure decrease to equilibrium values at ambient conditions. The second cycle does not present any additional hydrogen absorption so it can be used to calibrate the gas temperature that differs from the measured vial temperature. This data is an important parameter to calculate accurately the hydrogen uptake corresponding to the pressure change [4]. The extracted temperature and pressure data are then used to determine the hydrogen uptake as a function of milling time, as presented in Figure 5.1b.

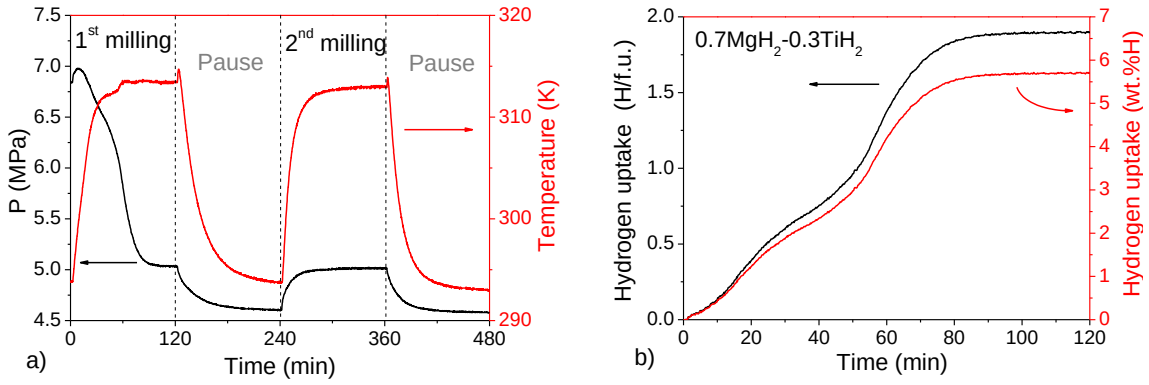

Figure 5.1. a) Time evolution of hydrogen pressure (black line) and vial temperature (red line) during RBM of 70 at.% Mg - 30 at.% Ti mixture. b) Corresponding hydrogen absorption curves during the first milling cycle. The hydrogen to metal atomic ratio is shown on the left axis (black line) and the H-mass uptake is given on the right axis (red line).

The final hydrogen to metal atomic ratio is generally around 1.9 H/f.u. instead of 2.0 H/f.u., owing to the occurrence of a minor amount of MgO. The mass hydrogen uptake depends on the Mg to Ti ratio, as Ti molar mass is almost twice the one of Mg. Thus, the highest storage mass-capacities are obtained for the lowest Ti-contents.

1.2 Ti content *vs.* absorption kinetics

Different (1-x)Mg-xTi compositions have been prepared by RBM under deuterium gas to allow neutron diffraction analyses. The corresponding absorption curves are displayed in Figure 5.2a. The faster absorption kinetics observed for the Ti-containing samples as compared to the pure Mg sample is striking. While absorption is completed in less than 90 min in presence of Ti, almost 240 min are needed to deuterate Mg alone. Besides, the derivative plots of the absorption curves (Figure 5.2b) clearly show the occurrence of two absorption peaks for the Mg-Ti mixtures, corresponding to two absorption stages. It was demonstrated in a previous work [1] that TiD_2 was formed in a first absorption stage during the first minutes of ball milling. The second peak is then attributed to the formation of MgD_2. This last one is significantly accelerated thanks to the abrasive properties of TiD_2 which improve the efficiency of the milling process. In addition, some catalytic properties of this phase are also expected to enhance the kinetics of hydrogenation. It was previously reported that this phase acts as a gateway for H(D) uptake in the Mg phase [1; 3]. Finally, it is worth noting that the influence of

the Mg to Ti ratio on the absorption kinetics is rather limited. The maximum absorption rate during MgD_2 formation is shifted from 28 min to 39 min for x = 0.5 and x = 0.1, respectively. In contrast, the maximum absorption rate of pure Mg occurs at 153 min.

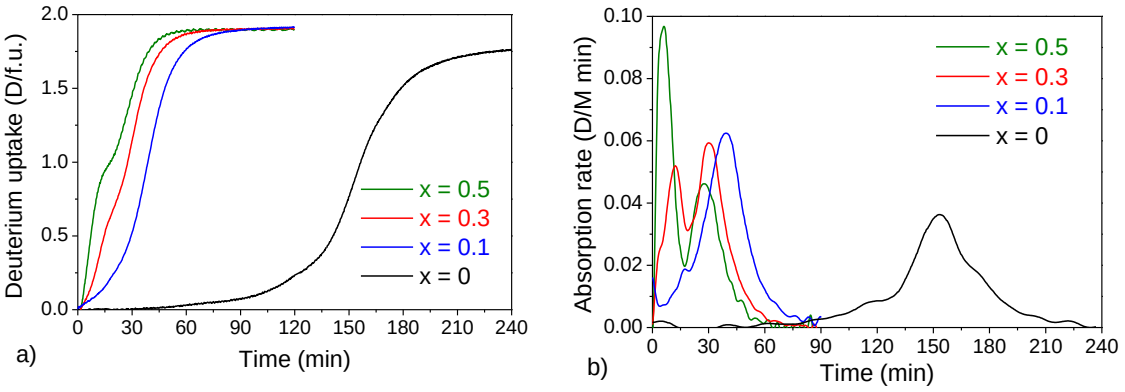

Figure 5.2. a) *In situ* absorption curves during RBM under deuterium gas of (1-x)Mg-xTi powder mixtures (x = 0, 0.1, 0.3 and 0.5). b) Corresponding time-derivative plots.

These results show that Ti significantly improves the kinetics of absorption of Mg during RBM synthesis. This faster kinetics is attributed to the highly abrasive properties and the catalytic effect of TiD_2 which is formed during the first stage of milling.

1.3 Isotopic effect: hydrogen *vs.* deuterium

Besides the Ti content, the isotope of the reactive gas was found to have a remarkable effect on the kinetics of absorption during RBM. Figure 5.3 compares the hydrogen and deuterium absorption rate during RBM of pure Mg and 0.9Mg-0.1Ti mixture. For the x = 0 sample (Figure 5.3a), the formation of MgD_2 is significantly slower than that of MgH_2. In contrast, the Mg-Ti mixture exhibits similar absorption behaviour during RBM under hydrogen or under deuterium (Figure 5.3b). The interpretation of such different behaviour with or without Ti relies on the mechanism controlling absorption during the milling process. Indeed, the nature of the isotope is expected to particularly affect the diffusion coefficient of the interstitial atoms, which according to classical rate theory [5], is slower for D than for H atoms. Therefore, it can be inferred that without Ti, absorption during RBM is controlled by the diffusion of H(D) through $MgH(D)_2$ phase. On the other hand, absorption in Mg-Ti mixtures must

be governed by a mechanism independent of the gas isotope. In fact, the abrasive properties of Ti improve the efficiency of the milling process by rapidly reducing the particle size and creating numerous oxide-free surfaces available for nucleation of the hydride. In consequence, the H(D) diffusion path is strongly reduced and a large amount of hydride nuclei are formed on the surface of the small Mg particles. Therefore, in presence of Ti, the rate limiting step of absorption during RBM depends on the efficiency of the milling process in forming nanosized particles, which is immediately followed by the formation of new $MgH(D)_2$ nuclei. This controlling step does not depend on the isotope nature. In addition, a catalytic effect of the $TiH(D)_2$ phase, which is formed during the first minutes of milling, cannot be discarded.

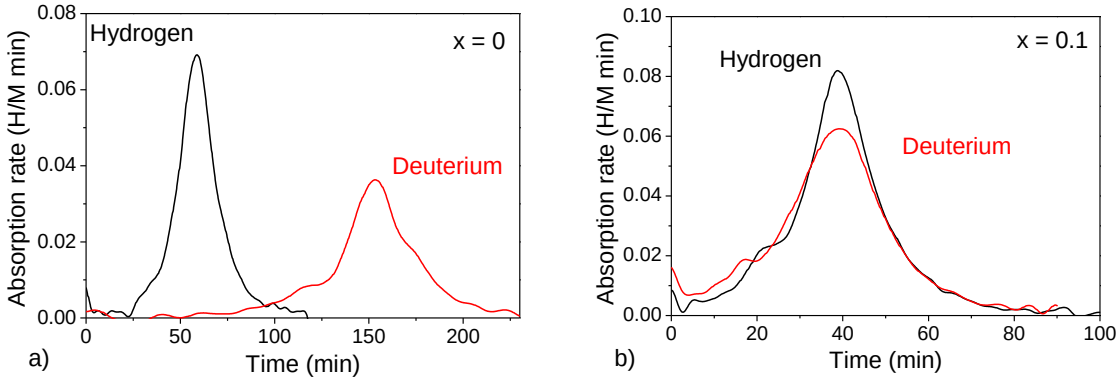

Figure 5.3. Time-derivative plots of the absorption curves obtained during RBM under hydrogen (black line) and deuterium gas (red line) for a) pure Mg and b) 0.9Mg-0.1Ti mixture.

In summary, the isotopic effect observed during *in situ* absorption highlights the different mechanisms that occur during milling of pure Mg and Mg-Ti mixtures. While the absorption in pure Mg is controlled by H(D)-diffusion, the presence of Ti enhances the milling efficiency which allows for fast and abundant nucleation of the hydride and shorter H(D)-diffusion paths.

2 Structural properties of as-milled and desorbed materials

2.1 X-ray and neutron diffraction analysis

Neutron diffraction is an ideal technique for providing deep structural information on deuterated materials. The structural properties of nanocomposites prepared by RBM

have been determined by means of high resolution NPD and XRPD joint analysis. The crystal structure of deuterated (1-x)MgD_2-xTiD_2 nanocomposites ($0 \leq x \leq 0.5$) have been analyzed in the as-milled and desorbed states. Information on Ti and Mg solubility are obtained as well as the influence of Ti content on nanocomposites microstructure.

2.1.1 Structural properties of as-milled deuterated nanocomposites

Deuterated samples previously synthesized by RBM at different Ti concentrations have been measured at room temperature by XRPD and NPD. Corresponding diffraction patterns and peak identification are plotted in Figure 5.4. The Ti-free sample (x = 0) is composed of the rutile type β-MgD_2, (S.G. *P42/mnm*) and the high pressure γ-MgD_2 (S.G. *Pbcn*) phases. The Ti-containing nanocomposites (x = 0.1, 0.3 and 0.5) consist of a mixture of β-, γ-MgD_2 phases and the distorted fluorite type ε-TiD_2 (S.G. *I4/mmm*) phase.

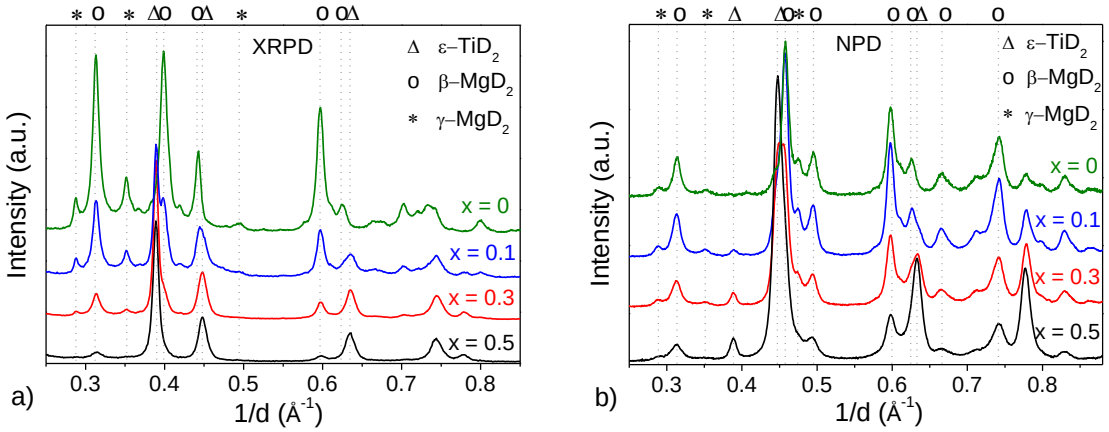

Figure 5.4. a) X-ray and b) neutron diffraction patterns of deuterated (1-x)MgD_2-xTiD_2 nanocomposites for x = 0, 0.1, 0.3 and 0.5.

Crystal data for the detected phases in each sample were determined by Rietveld joint XRPD-NPD analysis. For instance, the graphical output for Rietveld analysis of x = 0.3 is shown in Figure 5.5 and the corresponding crystal data results are gathered in Table 5.1. For each phase, lattice parameters, atomic positions and occupancy factors (chemical composition), and crystallite size underwent joint refinement for both diffraction patterns. The possible solubility of Mg in TiD_2 as well as that of Ti in MgD_2 has been checked by refining the occupancy factor of metal atoms within the crystal

structure of deuterated phases, *i.e.* by allowing for partial replacement of Ti by Mg atoms, and *vice versa*, in the crystal structures of TiD_2 and β-MgD_2 phases, respectively. The γ-MgD_2 relative phase amount was too low to reliably refine its cell parameters and possible Ti substitution. The values displayed in Table 5.1 for the γ-phase correspond to those refined for the x = 0 sample. Anisotropic thermal displacement factors (β^{ij}) were considered for the β-phase, as already pointed out in Ref. [6]. Relative phase amounts were determined from NPD measurements since the neutron beam probes the bulk of the sample while X-ray analysis is reduced to some μm of the sample thickness. Main refinement results obtained for different Ti contents are gathered in Table 5.2.

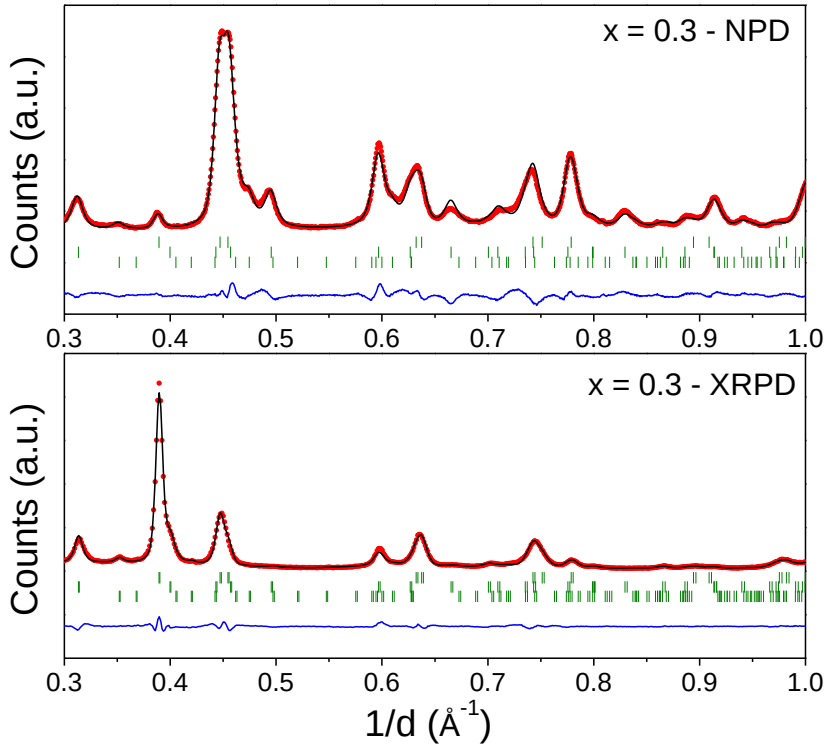

Figure 5.5. NPD and XRPD Rietveld joint analysis of $0.7MgD_2$-$0.3TiD_2$ sample. Continuous line shows the calculated diffraction patterns, vertical bars correspond to the Bragg positions for ε-TiD_2, β-MgD_2 and γ-MgD_2 from top to bottom. The difference between experimental and calculated patterns is given below.

Table 5.1. Results of Rietveld joint analysis for $0.7MgD_2$-$0.3TiD_2$ sample.

Phase/S.G.	Atom	site	*x*	*y*	*z*	*B* (Å^2) / β^{ij} (×10^4)			SOF
ε-TiD_2/ *I4/mmm*	Ti	2*a*	0	0	0	0.6(1)			0.98(1)
	Mg	2*a*							0.02(1)
	D	4*c*	0	1/2	1/4	1.3(1)			1*
a = 3.1630(2) Å, *c* = 4.4010(5) Å; phase amount: 42(1) wt.%.									
β-MgD_2/ $P4_2/mnm$	Mg	2*a*	0	0	0	β^{11}=β^{22}=84(11)	β^{33}=94(33)	β^{12}=134(18)	0.93(1)
	Ti	2*a*							0.07(1)
	D	4*f*	0.3015(4)	*x*	0	β^{11}=β^{22}=367(11)	β^{33}=755(33)	β^{12}=-135(12)	1*
a = 4.5138(4) Å, *b* = 3.0060(4) Å; phase amount: 48(1) wt.%.									
γ-MgD_2/ *Pbcn*	Mg	4*c*	0	0.364*	1/4	0.5*			1*
	D	8*d*	0.249*	0.128*	0.0827*	1.4*			1*
a = 4.515 Å*, *b* = 5.422 Å*, *c* = 4.936 Å*; phase amount: 11(1) wt.%.									

	R_{wp}	R_p	$R_{b\varepsilon}$	$R_{b\beta}$	$R_{b\gamma}$
NPD	3.67	2.74	2.1	5.6	5.4
XRPD	6.86	5.27	1.7	4.3	8.9

Number of fitted parameters: 27
* Not refined

Table 5.2. Results from XRPD and NPD Rietveld joint analysis of deuterated samples (x = 0, 0.1, 0.3 and 0.5).

Sample	Phase	S.G.	Phase amount (wt.%)	Cell parameters (Å)			Cell volume (Å^3)	Crystallite size (nm)	Atomic substitution (at.%)
				a	*b*	*c*			
x = 0	β-MgD_2	$P4_2/mnm$	78(3)	4.510(1)	-	3.014(1)	61.31(1)	7(1)	0*
	γ-MgD_2	*Pbcn*	22(2)	4.515(2)	5.422(2)	4.936(2)	120.83(6)	9(1)	0*
x = 0.1	ε-TiD_2	*I4/mmm*	14(1)	3.160(1)	-	4.397(2)	43.89(2)	15(3)	0*
	β-MgD_2	$P4_2/mnm$	69(2)	4.514(1)	-	3.006(1)	61.25(1)	9(1)	7(1)
	γ-MgD_2	*Pbcn*	17(1)	4.515*	5.422*	4.936*	120.83*	9(1)	0*
x = 0.3	ε-TiD_2	*I4/mmm*	42(1)	3.163(1)	-	4.400(1)	44.02(1)	13(1)	2(1)
	β-MgD_2	$P4_2/mnm$	48(1)	4.513(1)	-	3.006(1)	61.22(2)	7(1)	7(2)
	γ-MgD_2	*Pbcn*	11(1)	4.515*	5.422*	4.936*	120.83*	7(1)	0*
x = 0.5	ε-TiD_2	*I4/mmm*	67(1)	3.168(1)	-	4.415(1)	44.31(1)	10(2)	8(1)
	β-MgD_2	$P4_2/mnm$	26(1)	4.514(1)	-	3.004(1)	61.21(2)	5(1)	4(2)
	γ-MgD_2	*Pbcn*	7(1)	4.515*	5.422*	4.936*	120.83*	5(1)	0*

* Not refined

Figure 5.6 shows the refined phase amounts of MgD_2 and TiD_2 phases as a function of Ti-molar fraction, x, in the RBM reactants. As expected, the TiD_2 phase amount increases with Ti-content. Moreover, this increase is close to the theoretical phase

content that is calculated assuming no solubility of Mg in TiD_2 nor Ti in MgD_2 phases. This result anticipates that the solubility of metal atoms should be low (see last column of Table 5.2). The average relative ratio of the γ-MgD_2 phase amount as compared to the total MgD_2 is of 20 ± 3 wt.%, which is slightly lower than previous results based on XRPD data (27 ± 3 wt.%) [1].

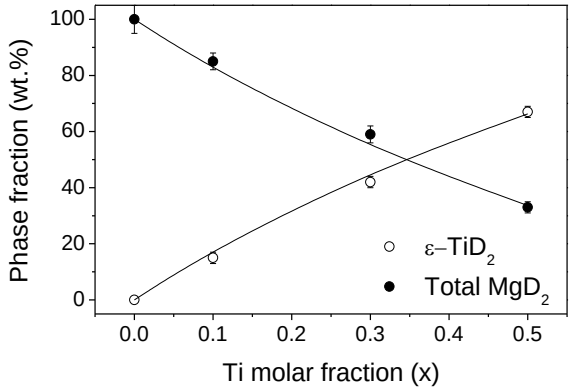

Figure 5.6. Refined phase content (TiD_2 and (β+γ)-MgD_2) in the as-milled (1-x)MgD_2-xTiD_2 samples. Continuous lines display the theoretical phase content for a MgD_2-TiD_2 composite assuming no solubility of Mg in TiD_2 nor Ti in MgD_2 phases.

Figure 5.7 shows the dependence of the relative unit-cell volume of β-MgD_2 and ε-TiD_2 phases with the Ti-molar fraction used for sample synthesis. The relative unit-cell volume is established by comparison to that of the pure phases obtained by RBM of the metallic elements (from ref. [1] for TiD_2 and this work for MgD_2). The TiD_2 cell volume gradually increases when the Ti-molar fraction raises. This phenomenon concurs with the increase of Mg substitution in the TiD_2 phase determined from the refinement of atomic occupancy (Table 5.2). At the highest Ti-molar fraction used in this work (*i.e.* x = 0.5), Mg solubility in TiD_2 phase reaches ~ 8 at.% Mg and the relative cell volume increases by more than 1 %. This fact can be explained by the larger metallic radius of Mg as compared to Ti (r_{Mg} = 1.60 Å, r_{Ti} = 1.47 Å). Regarding Ti substitution in β-MgD_2, site occupancy refinement yields ~ 7 at.% Ti (for x = 0.1 and 0.3) but, strikingly, the relative cell volume of the β-MgD_2 phase only decreases slightly with the Ti-molar fraction.

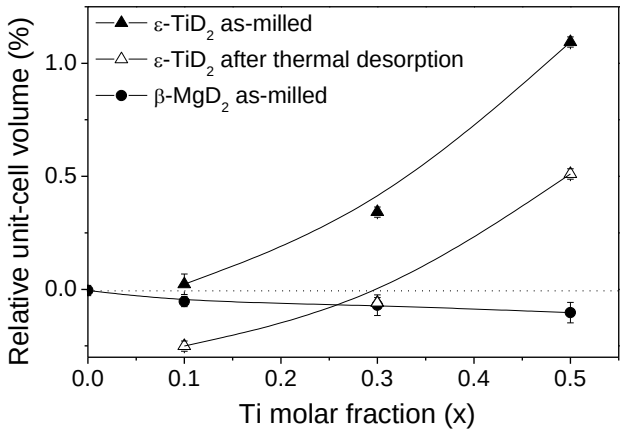

Figure 5.7. Relative unit-cell volume variation as a function of the Ti-molar fraction for ε-TiD_2 (in as-milled and desorbed samples) and β-MgD_2 (in as-milled samples). The unit-cell volumes of the MgD_2 sample (x = 0) synthesized in this work and TiH_2 synthesized by RBM under hydrogen gas [1] are used as references.

Crystallite sizes (Table 5.2) and microstrains of the different phases have been calculated from the width of the Lorentzian and Gaussian components respectively, of the "Thompson-Cox-Hastings pseudo-Voigt" profile shape function after considering instrumental resolution. All as-milled samples exhibit nanocrystalline phases, with TiD_2 crystallites slightly larger than β-MgD_2 ones (13 ± 3 nm and 7 ± 2 nm, respectively). With increasing Ti-molar fraction, smaller crystallite sizes are obtained. This is attributed to the abrasive character of titanium deuteride, which favours nanostructuration of the MgD_2 phase. However, for Ti-free synthesis, mechanical energy induced by RBM is high enough to nanosize MgD_2 as well. Microstrains in the β-MgD_2 phase increased from 0.4 % for the x = 0 sample to 0.6 % for the x = 0.5 sample while the TiD_2 phase showed values from 0.6 to 0.8 % for x = 0.1 and x = 0.5, respectively. This result shows that the abrasive properties of titanium deuteride increase as well the deformation and the amount of defects in the crystal lattices.

2.1.2 Structural properties of thermally desorbed samples

RBM samples were desorbed by heating up to 530 K under a deuterium back-pressure of 0.06 MPa. The amount of desorbed deuterium was measured as 1.5, 1.2 and 0.9 D/f.u. for x = 0.1, 0.3 and 0.5 samples, respectively. Under these measurement conditions, only deuterium from the MgD_2 phase should desorb appreciably, since TiD_2

is reported to have equilibrium pressure far below 0.06 MPa at 530 K [7]. Therefore, the expected deuterium desorption corresponds to the D-content stored in the MgD_2 phase, *i.e.* 1.8, 1.4 and 1 D/f.u., respectively. However, we observe that desorption is not fully completed, in particular for low Ti-molar fractions: only 83, 86 and 90 % of the deuterium amount stored in the MgD_2 phase are desorbed for x = 0.1, 0.3 and 0.5, respectively. Two phenomena may explain this discrepancy:

i) the ocurrence of minor Mg oxidation, making a minor fraction of this phase inactive for hydrogen desorption and

ii) the persistence of non-desorbed MgD_2 phase due to slow kinetics of MgD_2 decomposition, particularly at low Ti-molar fractions.

The second option seems to be more significant as no MgO was observed on diffraction data.

The thermally desorbed samples were analyzed by XRPD and NPD. The measured diffractogramms are displayed in Figure 5.8 and the main results of Rietveld joint analysis are gathered in Table 5.3. Partial replacement of Ti by Mg atoms in the TiD_2 phase is still observed for x = 0.3 and 0.5 samples. This indicates that Mg does not segregate out of the TiD_2 phase below 530 K. This fact is supported by the evolution of relative unit-cell volume of the ε-TiD_2 phase represented in Figure 5.7. The unit-cell volume of this phase increases with the Ti-molar fraction for both as-synthesised and desorbed samples, though it is clearly shifted to lower values for the latter ones.

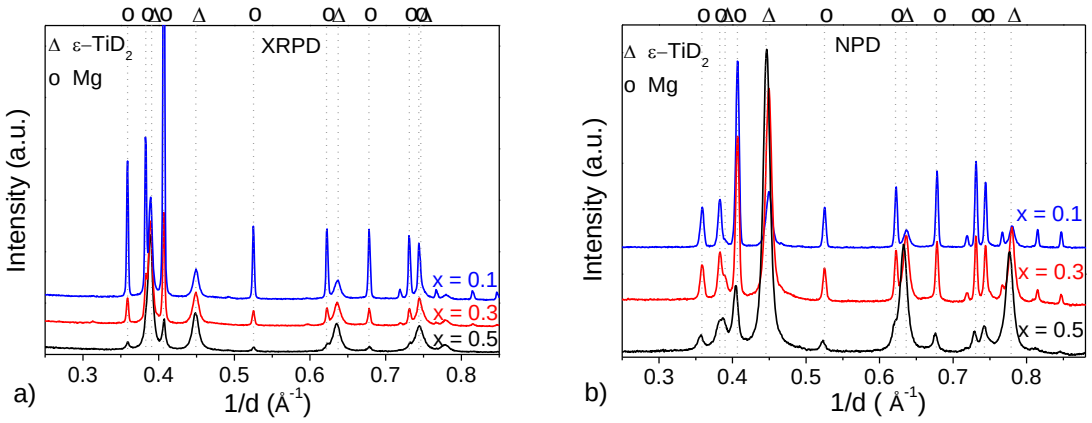

Figure 5.8. a) X-ray and b) neutron powder diffraction patterns of thermally desorbed (1-x)Mg-xTiD_2 nanocomposites for x = 0.1, 0.3 and 0.5.

Table 5.3. Main results from XRPD and NPD Rietveld joint analysis of thermally desorbed samples.

Desorbed samples	Phase	S.G.	Phase amount (wt.%)	Cell parameters (Å)		Cell volume (Å^3)	Crystallite size (nm)	Atomic substitution (at.%)
				a	*c*			
$x = 0.1$	ε-TiD_2	*I4/mmm*	19(1)	3.150(1)	4.413(1)	43.76(1)	16(1)	0
	Mg	*P6$_3$/mmc*	81(1)	3.210(1)	5.213(1)	46.52(1)	95(5)	-
$x = 0.3$	ε-TiD_2	*I4/mmm*	49(1)	3.151(1)	4.417(1)	43.84(1)	13(1)	6(1)
	Mg	*P6$_3$/mmc*	51(1)	3.211(1)	5.214(1)	46.55(1)	29(2)	-
$x = 0.5$	ε-TiD_2	*I4/mmm*	71(1)	3.156(1)	4.426(1)	44.09(1)	10(1)	8(1)
	Mg	*P6$_3$/mmc*	29(1)	3.212(1)	5.220(1)	46.65(1)	10(1)	-

Another major result of the structural analysis concerns changes in crystallite size upon deuterium desorption. Figure 5.9 shows the crystallite size of β-MgD_2, Mg and TiD_2 phases for as-milled and thermally desorbed samples with the different Ti-molar fractions. The crystallite size of TiD_2 does not change during thermal desorption. In contrast, the Mg phase exhibits grain growth during desorption as compared to the as-milled β-MgD_2 phase. It should be noted, however, that grain growth decreases with Ti-content. More information on these effects will be given in next sections concerning *in situ* NPD studies.

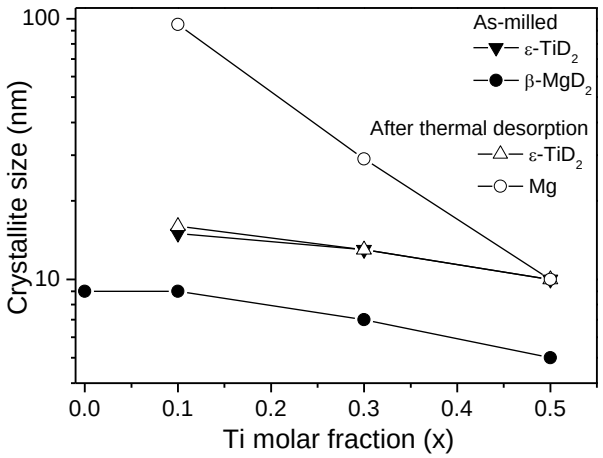

Figure 5.9. Comparison of crystallite size in as-milled (full symbols) and thermally desorbed samples (empty symbols) as a function of Ti content.

2.2 Nanocomposite microstructure

TEM has been used to characterize the microstructure of as-milled RBM samples. Figure 5.10 shows the microstructure of x = 0.3 sample. In bright field, TiD_2 inclusions appear as dark areas, which are easily detected in dark field as white spots. TiD_2 inclusions are homogeneously distributed inside of MgD_2 agglomerates. The measured average size for TiD_2 inclusions is 9 ± 3 nm, with a size distribution ranging from 2 to 16 nm. The size of TiD_2 inclusions matches the crystal size of the TiD_2 phase. This suggests that TiD_2 inclusions are essentially single crystals.

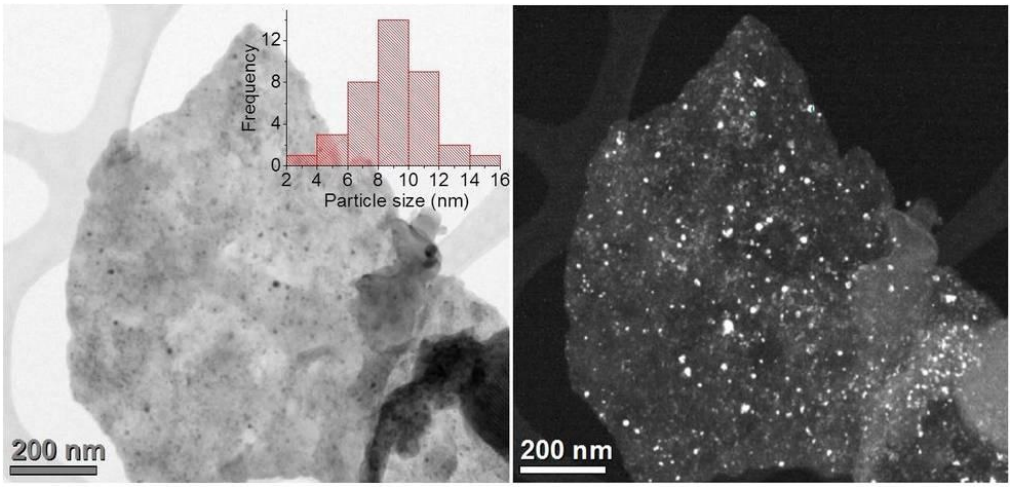

Figure 5.10. Bright field (left) and dark field (right) TEM images of as-milled $0.7MgD_2$-$0.3TiD_2$ sample. Small spots correspond to the TiD_2 phase. The inset in bright field image shows the size distribution of TiD_2 inclusions.

3 Sorption properties

In this section, the sorption properties of the x = 0.3 nanocomposite sample are compared to those of the pure MgH_2 obtained by RBM (x = 0) to understand the role played by TiH_2 on the Mg/MgH_2 system.

3.1 Kinetic properties

The outstanding kinetic properties of the x = 0.3 sample as compared to pure Mg have been previously demonstrated during isothermal absorption and desorption experiments [1]. The Ti-containing material exhibited much faster sorption rates than RBM MgH_2. We here determine the activation energy involved during H-desorption

from as-milled compounds by TDS measurements at several heating rates. The obtained desorption spectra are displayed in Figure 5.11. In both samples, desorption events consist of two overlapped peaks that are better resolved at slow heating rate. This peculiar shape has already been observed in ball milled MgH_2 and was attributed to the presence of the metastable γ-MgH_2 phase which induces partial desorption from the β-phase [8; 9]. However, this interpretation is in contradiction with further results of *in situ* TD on deuterated x = 0 sample where we observe a γ to β transformation prior to D-desorption, as later discussed in section 4.2. Thus, this bimodal peak shape may be better explained by two different desorption steps occurring successively. The low temperature peak is attributed to the fast nucleation and growth of the Mg phase until forming a Mg shell around a MgH_2 core. Owing to the small particle size in both samples, this stage produces an important fraction of Mg. The subsequent high temperature shoulder corresponds to the growth of the Mg phase limited by the MgH_2/Mg interface displacement.

The temperature of the peak onset gives information on the nucleation step. We observe that it occurs at similar temperature (~ 550 K) for both compositions in spite the position of the main peak differs. For the Ti-free sample, the slight H-desorption that occurs between 500 and 600 K may be related to MgH_2/$Mg(OH)_2$ interface reactions leading to low temperature H-desorption [10]. $Mg(OH)_2$ is formed by reaction of MgH_2 with unavoidable moisture present during storage, but its presence is hardly detectable as its main diffraction peak coincides with the (200) reflection of MgH_2. In presence of TiH_2, this step is merged within the main desorption peak that is clearly shifted to lower temperature. Indeed, Mg nucleation is favoured by defects such as abundant MgH_2/TiH_2 interface regions and therefore occurs at lower temperature.

Next, we observe that the activation energies, determined according to the Kissinger method described in section 3.2 of Chapter 2, considerably differ from pure MgH_2 to the composite sample. While RBM MgH_2 possesses an activation energy of 94(12) kJ/molH_2, its value is only of 62(15) kJ/molH_2 for the 0.7MgH_2-0.3TiH_2 sample. The first value is lower than those reported for ball milled MgH_2, which typically reaches 120 kJ/molH_2 [11]. This discrepancy can be attributed to the higher amount of defects achieved by RBM than by conventional milling, as suggested by the smaller crystallite size of RBM MgH_2 (7 nm, Table 5.2) as compared to BM MgH_2 (12 nm,

[11]). Indeed, the numerous defects provide a high number of nucleation sites for the Mg phase and thus reduces the activation energy for desorption. Regarding the value for the nanocomposite sample, it agrees with reported activation energies for MgH_2 catalysed with TM or TM oxides [12–14]. It was suggested that the homogeneous distribution of the catalyst nanoparticles at the surface and grain boundaries of MgH_2 provides a large amount of additional Mg nucleation sites. These results clearly evidence the catalytic properties of TiH_2 nanoparticles that act as Mg nucleation centres and lower the energy barrier necessary to desorb hydrogen from MgH_2.

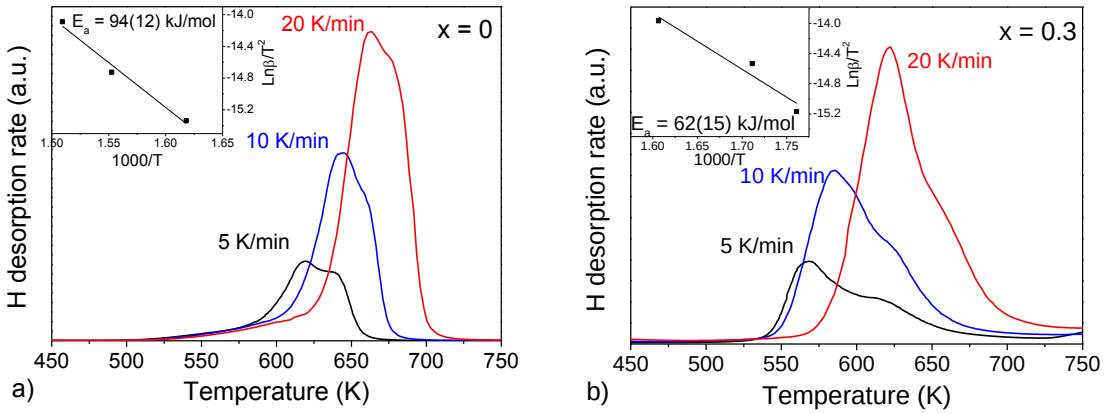

Figure 5.11. TDS spectra of RBM a) MgH_2 and b) $0.7MgH_2$-$0.3TiH_2$ samples obtained during heating at different rates (5, 10 and 20 K/min). The insets display the Kissinger plots used to determine the activation energies of desorption.

3.2 Cycling properties

The stability of the reversible hydrogen uptake of the x = 0.3 sample has been previously confirmed over 32 cycles during isothermal experiments at 573 K [1]. On the contrary, the storage capacity of the x = 0 sample decreased significantly during the first 14 cycles. To obtain further information on the samples evolution during cycling, HP-DSC has been performed under 0.2 MPa of hydrogen pressure during heating and cooling at 5 K/min. Figure 5.12 displays the peak shape evolution on cycling of x = 0 and x = 0.3 samples.

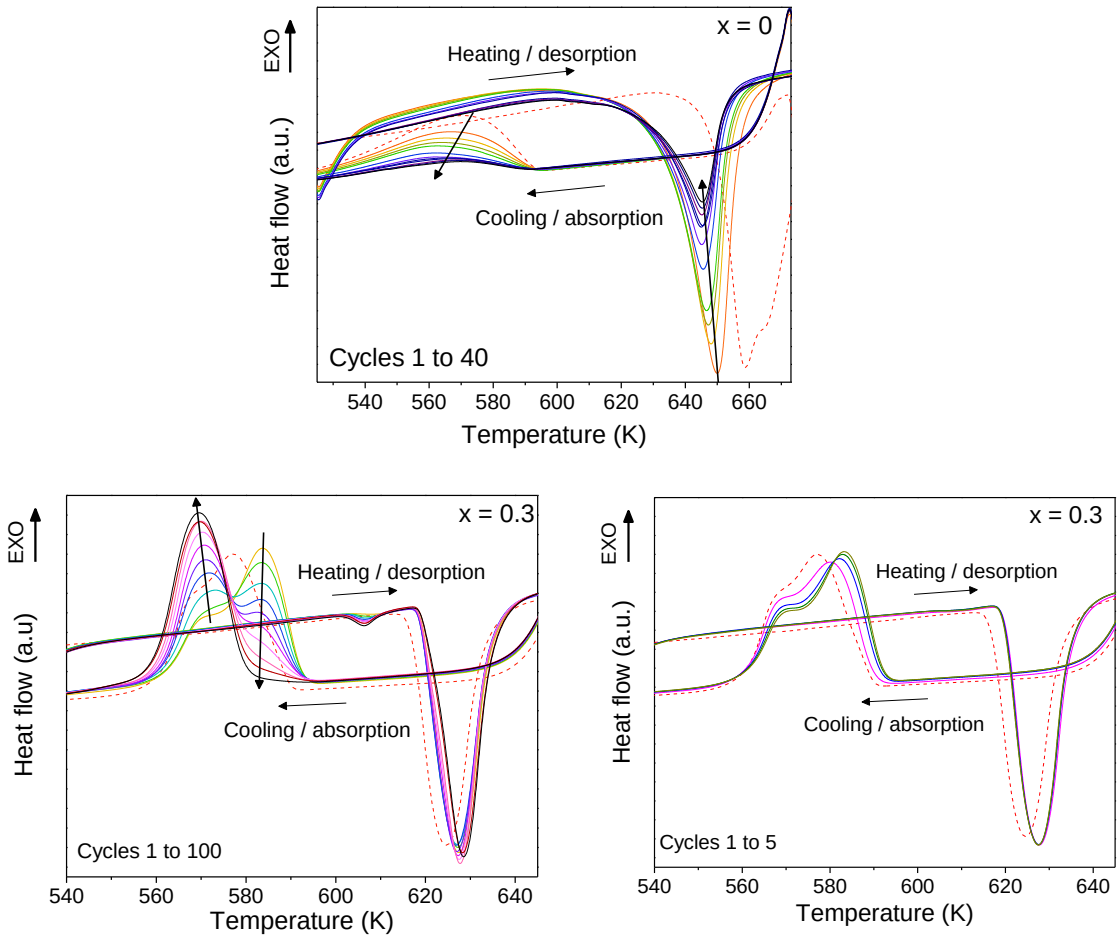

Figure 5.12. Evolution with cycling of x = 0 (top) and x = 0.3 (bottom) samples during HP-DSC under 0.4 MPa of hydrogen pressure at a heating rate of 5 K/min. For x = 0, the 5 first cycles are represented and then every 5 cycles up to cycle 40 (the same sample has been cycled up to 60 times but the ill-defined spectra are not shown). For x = 0.3, data are represented every 10 cycles and cycles 1 to 5 are detailed on the right. Long arrows indicate the direction of cycle evolution for the different peaks. The dashed line corresponds to the first desorption-absorption cycle.

In both cases, a single endothermic desorption peak is observed around 650 K for x = 0 and at 627 K for x = 0.3. The x = 0 sample exhibits a broad peak shape with an ill-defined onset at relatively low temperature (~600 K), probably related to the previously mentioned $MgH_2/Mg(OH)_2$ interface reactions [10]. In contrast, the desorption peak onset of the x = 0.3 sample is sharp and located at 620 K. Though, we can observe the occurrence of a very small peak at 600 K which intensity gradually increases on

cycling. As for x = 0, it is possible to attribute this peak to $MgH_2/Mg(OH)_2$ interactions that become more important as the amount of hydroxide increases with cycling.

It is also worth mentioning that the behaviour of the first cycle significantly differs. In the case of the x = 0 sample, the first desorption is probably hampered because of surface passivation effect that may occur during sample storage inside the glove box. For the x = 0.3 sample, both desorption and absorption peaks are shifted to lower temperatures, suggesting a slight thermodynamic destabilization. This effect may be due to Ti solution in the MgH_2 phase which segregates during the first cycles. Further experiments – *e.g.* longer milling time to increase Ti solution in MgH_2 – are necessary to shed light on this behaviour.

In the next cycles, the area and shape of the desorption peak is almost constant over 100 cycles for the x = 0.3 sample, whereas it progressively and strongly decreases on 40 cycles for the x = 0 sample. These different behaviours are illustrated in Figure 5.13 with the evolution of the relative desorption peak area with cycling, considering that the amount of heat absorbed by the system is directly proportional to the amount of desorbed hydrogen. While the Ti-containing sample barely loses 8 % of its initial capacity after 100 cycles, the amount of desorbed hydrogen is reduced by almost 60 % after 40 cycles in the pure Mg sample. This result shows that an important fraction of the Mg becomes inactive during cycling. In fact, this is confirmed by the XRPD patterns of the cycled samples (Figure 5.14) where we observe that only 10 wt.% of MgH_2 is formed during the 60^{th} absorption of the pure Mg sample. About 85 wt.% of Mg remains neither hydrided, nor oxidized. This clearly demonstrates that the reversible capacity loss in the pure Mg sample is due to progressive slowing down of hydrogen absorption rate on cycling. The origin of this can be twofold: the formation of a MgO shell at the Mg surface or the growth of crystallite size. In contrast, the composite sample is totally hydrided after the 100^{th} absorption, except a small fraction of Mg that is oxidized because of impurities in the HP-DSC system. However, this oxidation has no significant effect on kinetics when the TiH_2 phase is present. Indeed, the Mg/TiH_2 interface provides an oxide free area where hydrogen can reach Mg phase after fast diffusion through the protecting TiH_2. This demonstrates that the TiH_2 phase acts as a gateway for hydrogen transfer to Mg.

In addition, the crystallite size between both samples differs significantly. The MgH_2 crystallites reach 1200 nm in the x = 0 sample while they remain around 600 nm in the Ti-containing compound after 60 and 100 cycles, respectively. This important coarsening is certainly favoured by the high temperatures reached during cycling (670 K and 650 K for x = 0 and x = 0.3, respectively). However, this phenomenon is limited by the presence of TiH_2. The large crystallite size is probably also limiting the absorption kinetics in the case of pure Mg, which is hampered by H-diffusion through the MgH_2 shell, but does not seem to affect the composite sample. Once again, we demonstrate the outstanding catalytic properties of TiH_2 on the reversibility of the Mg/MgH_2 system, even in presence of MgO.

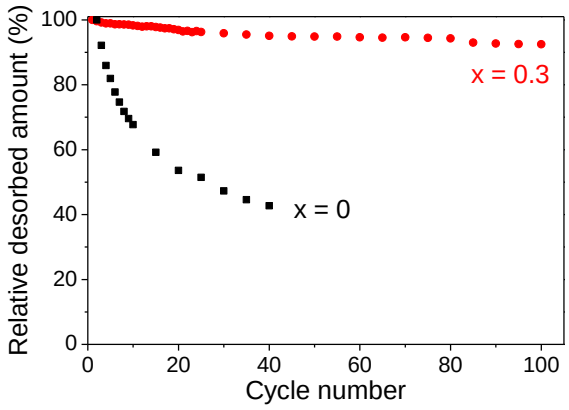

Figure 5.13. Evolution of the relative desorption peak area during HP-DSC cycling of x = 0.3 and x = 0 samples.

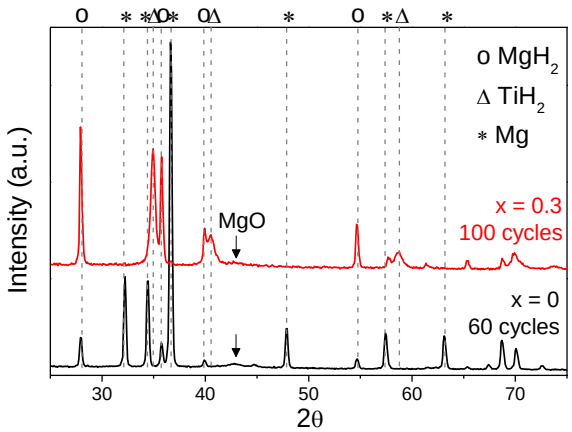

Sample	Phase	Phase amount (wt.%)	Crystallite size (nm)
x = 0.3	ε-TiH_2	39(1)	530(50)
	β-MgH_2	58(1)	580(30)
	MgO	3(1)	-
x = 0	β-MgH_2	10(1)	1200(700)
	Mg	85(1)	1600(100)
	MgO	5(1)	-

Figure 5.14. XRPD patterns of the x = 0 and x = 0.3 samples after 60 and 100 cycles respectively (right) and the main results of the corresponding Rietveld refinements (left).

Let's focus now on the HP-DSC exothermic absorption peaks shown in Figure 5.12. For pure Mg, a unique broad (span of temperature > 60 K) and ill-defined peak is observed. It rapidly decreases in intensity on cycling. Absorption in the nanocomposite sample starts at the same temperature (T_{onset} = 590 K), but occurs in a narrower span of temperature (~40 K). This behaviour shows the fast absorption kinetics of the nanocomposite sample as compared to pure Mg. The Ti-containing material exhibits a complex behaviour with two peaks of absorption which relative intensities vary with cycling. During the first cycles, the main peak occurs at 583 K and a secondary peak appears at 569 K. Throughout cycling, the first peak decreases in intensity until complete disappearing while the second one grows at the expense of the first one. The different peak shape and evolution between absorption and desorption reflects different sorption mechanisms. Indeed, it has been widely demonstrated that absorption is controlled by H-diffusion through the MgH_2 phase while desorption is generally governed by the MgH_2/Mg interface displacement [15]. In the case of the MgH_2-TiH_2 nanocomposite, the almost constant position and shape of the desorption peak, even after crystal growth through 100 cycles, seems to indicate that the desorption rate that is controlled by interface displacement hardly changes on cycling at these temperatures (620-640 K), resulting only in a very small shift of the desorption peak to higher temperature.

In contrast, the absorption mechanism seems to occur in two steps which relative importance probably depends on the crystallite size. This two-stage regime has already been evidenced during isothermal absorption curves on the same material [1]. The absorption mechanism in presence of TiH_2 catalyst can be described according to two successive stages. The first one consists in the abundant nucleation of the MgH_2 phase, favoured by the TiH_2 nanoparticles at Mg/TiH_2 interfaces. When the TiH_2 inclusions are small and numerous, the amount of MgH_2 formed during this step is large, giving rise to the first absorption peak at 583 K. As Mg and TiH_2 phases grow on cycling, the number of TiH_2 inclusions decreases and the Mg surface available for MgH_2 nucleation is reduced. Therefore, the number of nuclei formed during the first absorption step decreases and the first peak shrinks. The second absorption step depends on the diffusion of H atoms through the layer of MgH_2 formed during the first stage. This step

is fast and almost insignificant when Mg and TiH_2 particles are small but becomes more important as they grow, thus explaining the increase of the second peak at 569 K.

Even if the absorption is shifted to lower temperature with cycling owing to crystal growth of both phases, complete absorption of the Mg phase is always achieved in a narrow temperature range (590 to 560 K) thanks to the catalytic effect of TiH_2. This demonstrates the striking robustness of MgH_2-TiH_2 composites even after prolonged cycling and concomitant grain growth.

3.3 *In situ* neutron diffraction investigation

In situ NPD experiments were conducted to better understand the role of the TiD_2 phase on the sorption properties of (1-x)MgD_2-xTiD_2 nanocomposites. The x = 0.3 sample was chosen as representative of the Ti containing materials as it provides fast absorption kinetics and the significant amount of the TiD_2 phase yields a strong enough NPD signal. Ti-free sample (x = 0) was used as a reference. Both samples were first thermally desorbed (*in situ* TD) on heating from 298 to 600 K under dynamic vacuum (residual pressure ~ 1 Pa). The deuterium desorption rate was determined from changes in the residual pressure. Next, PCI on deuterium absorption and desorption (*in situ* PCI) were performed at 548 K between 0.01 and 1 MPa. Typical equilibrium times were 50 minutes for x = 0.3 compound and 90 minutes for x = 0. An additional absorption process was monitored at room temperature (RT) under a deuterium pressure of 0.8 MPa.

3.3.1 *In situ* TD experiments

Neutron diffraction acquisitions and simultaneous TD curves are displayed in Figure 5.15. For both samples, the TD signal exhibits a single desorption peak matching with the phase transformation of β- and γ-MgD_2 phases into Mg observed on the 2D diffraction plot. It is worth noting that the TD peak of the TiD_2-MgD_2 composite is located about 30 K lower than for the pure MgD_2 sample. In addition, the width of the TD peak is narrower for the x = 0.3 sample. It extends from 450 to 600 K in pure MgD_2, whereas it occurs from 425 to 550 K in presence of TiD_2. These facts reveal much faster desorption kinetics for the Ti-containing sample.

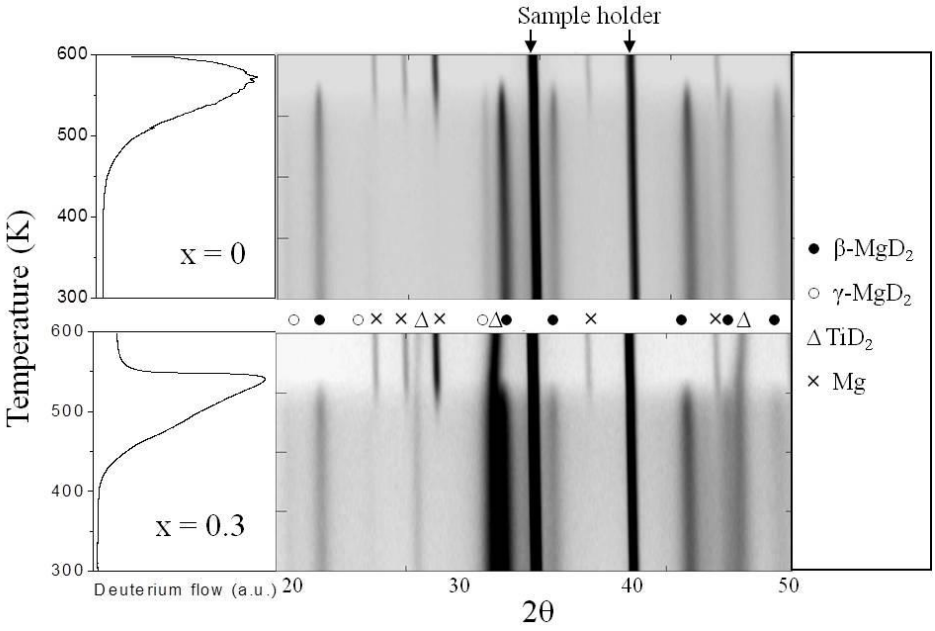

Figure 5.15. Thermal desorption curves and corresponding 2D diffraction pattern projections (λ = 1.287 Å) for x = 0 and x = 0.3 samples.

The analysis of these neutron diffraction patterns allows quantifying the phase amounts during *in situ* TD. Figure 5.16 displays the evolution of phase distribution upon deuterium desorption as determined by Rietveld refinements. For the Ti-free MgD_2 sample (Figure 5.16 top), the amount of γ-MgD_2 gradually decreases with temperature with a simultaneous increase of the β-MgD_2 phase. No significant formation of Mg occurs below 500 K, whereas most of the γ-MgD_2 phase has disappeared at this temperature. Therefore, it can be concluded that the γ-MgD_2 phase gradually transforms into the β-MgD_2 structure before significant deuterium desorption occurs.

In the case of the Ti-containing material (Figure 5.16 bottom), both β- and γ-MgD_2 phases disappear simultaneously above 475 K, whereas a concomitant increase of the Mg phase occurs. The tetragonally distorted ε-TiD_2 (S.G. *I4/mmm*) phase observed at room temperature transforms into the fluorite type δ-TiD_2 (S.G. *Fm*-3*m*) phase at temperatures over 320 K [16]. The amount of the TiD_2 phase is almost constant during the whole desorption process, confirming that this hydride does not significantly decompose in the studied temperature range. However, its amount slightly increases between 510 and 540 K and then decreases between 540 and 600 K. The increase of the relative weight fraction of TiD_2 between 510 and 540 K is explained by a mass balance

effect: the TiD_2 relative amount increases as a result of deuterium mass loss due to desorption from the MgD_2 phase. Above 540 K (hatched area in Figure 5.16), the decline of the TiD_2 amount matches a concomitant increase of the Mg content since all traces of MgD_2 phases have disappeared at these temperatures. However, some deuterium desorption (dashed line) is still detected.

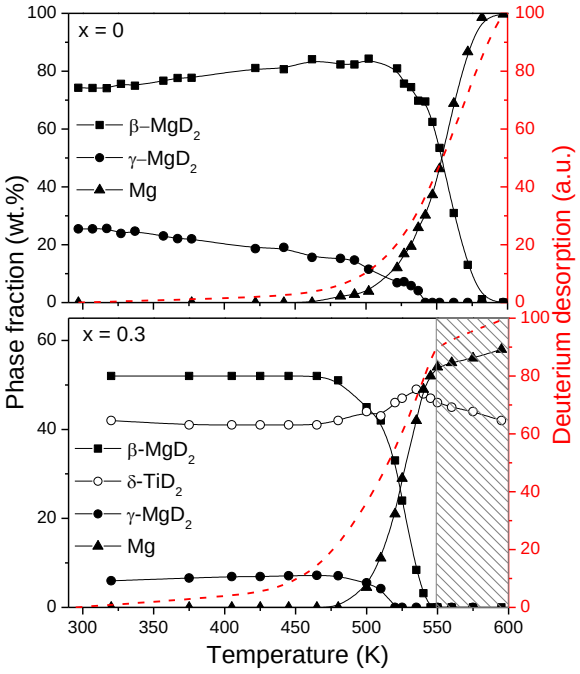

Figure 5.16. Evolution of the phase amounts with temperature during *in situ* TD experiments (heating rate: 0.5 K/min) for x = 0 and 0.3 samples. Dashed lines show desorbed fraction of deuterium. Hatched area for x = 0.3 sample indicates the temperature region where MgD_2 phases are no longer detected. For the sake of clarity, error bars are not represented in the graph.

The evolution of the unit-cell volume of the TiD_2 phase during *in-situ* TD of the TiD_2-MgD_2 composite is shown in Figure 5.17. Up to 510 K, it increases due to thermal expansion. Then, during the MgD_2 to Mg transformation (510 to 540 K), the unit-cell volume drops by ~ 0.2 $Å^3$ and seems to stabilize. However, above 540 K (hatched area in Figure 5.17), it undergoes a continuous and further decrease. The origin of the latter decrease can be two-fold. First, it may indicate Mg segregation out of TiD_2 phase since the metallic radius of Mg is larger than it is for Ti. The segregation probably occurs in the form of MgD_2 leading to a slight raise of the Mg amount due to simultaneous MgD_2

decomposition above 550 K (Figure 5.16). In addition, TiD_2 may partially desorb deuterium at high temperature, causing an additional cell volume reduction. Unfortunately, the quality of *in situ* diffraction data does not allow for a reliable refinement of partial substitution of Mg atoms in Ti sites, nor of D atom occupancy, in order to quantify the individual contribution of these two effects.

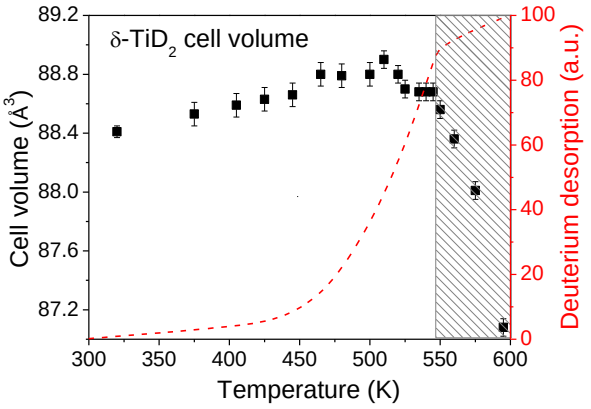

Figure 5.17. Cell volume evolution of the δ-TiD_2 phase during *in situ* TD of x = 0.3 sample. Dashed lines show desorbed fraction of deuterium. Hatched area indicates the temperature region where MgD_2 phases are no longer detected.

The evolution of the crystallite size of β-MgD_2 and Mg phases during *in situ* TD experiments on both samples is displayed in Figure 5.18. For the Ti-free sample, the Mg phase exhibits severe grain coarsening after desorption of MgD_2. The size of Mg crystallites reaches 90 ± 20 nm after desorption (*i.e.* above 560 K), which is much larger than the crystallite size of β-MgD_2 (22 ± 3 nm) before deuterium desorption (*i.e.* at 525 K). On the other hand, for the Ti-containing sample, the presence of the TiD_2 phase limits grain coarsening of Mg crystallites. The crystallite size of the Mg phase only attains 30 ± 5 nm after deuterium desorption. As for the TiD_2 phase, its crystallite size remains constant (13 ± 3 nm) all over the desorption process.

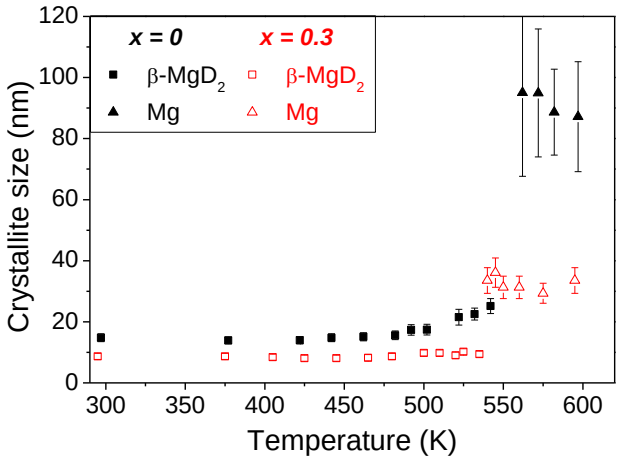

Figure 5.18. Evolution of the crystallite size of β-MgD_2 and Mg phases during *in situ* TD of x = 0 and x = 0.3 samples.

3.3.2 PCI

PCI curves on absorption and desorption have been measured in neutron beam at 548 K. The results are displayed in Figure 5.19 with reversible D-content evaluated from manometric measurements.

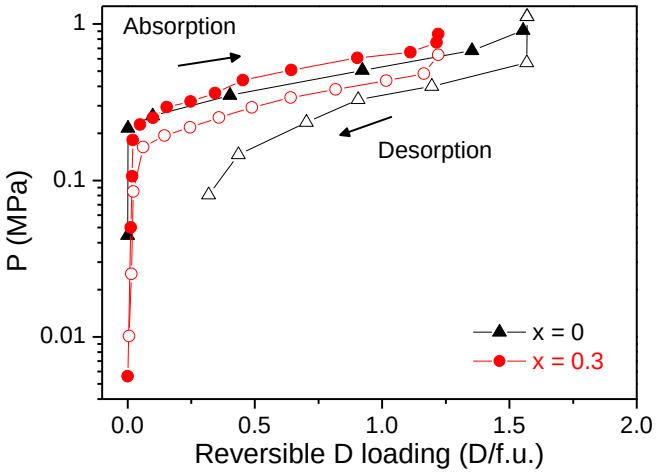

Figure 5.19. PCI absorption (full symbols) and desorption (empty symbols) curves at 548 K of x = 0 and 0.3 samples.

The Ti-containing sample absorbs reversibly 1.2 D/f.u. due to reversible deuterium loading in the magnesium phase. The equilibrium pressure at half-plateau is about 0.5 MPa on absorption and 0.3 MPa on desorption. For the Ti-free sample, 1.6 D/f.u. are

absorbed, but only 1.3 D/f.u. are desorbed. Such irreversible behaviour is attributed to the slow H-sorption kinetics of the Ti-free sample. Full equilibrium could not be reached during the rest time used (90 minutes). Both isotherms exhibit sloping plateaus. This fact is attributed to unavoidable temperature gradients along the sample-holder used for *in situ* measurements. Indeed, *ex situ* PCI curves monitored in properly thermalized Sievert's laboratory devices exhibit flat plateaus, as reported in Ref. [1].

Neutron diffraction patterns recorded at each PCI equilibrium point have been refined using the Rietveld method (not shown). The occurrence of the γ-MgD_2 phase is not detected, showing that this phase is metastable and that it is not formed by deuterium absorption from the gas phase. Besides the TiD_2 phase, only the β-MgD_2 phase is observed on deuteration. The amount of the TiD_2 phase during all PCI measurements is almost constant. It varies between 44 and 50 wt.% as result of mass balance variations associated with reversible D-loading in the β-MgD_2 phase. The β-MgD_2 phase amount followed a linear increase with D-content, at the expense of the Mg amount.

Figure 5.20 displays the crystallite size of the different phases during *in situ* PCI measurements. The crystallite size of both Mg and β-MgD_2 phases remains constant but is larger for the Ti-free sample (100 ± 20 nm) than for the Ti-containing one (40 ± 10 nm). TiD_2 does not suffer any crystal growth and remains around 13 ± 3 nm throughout the experiment.

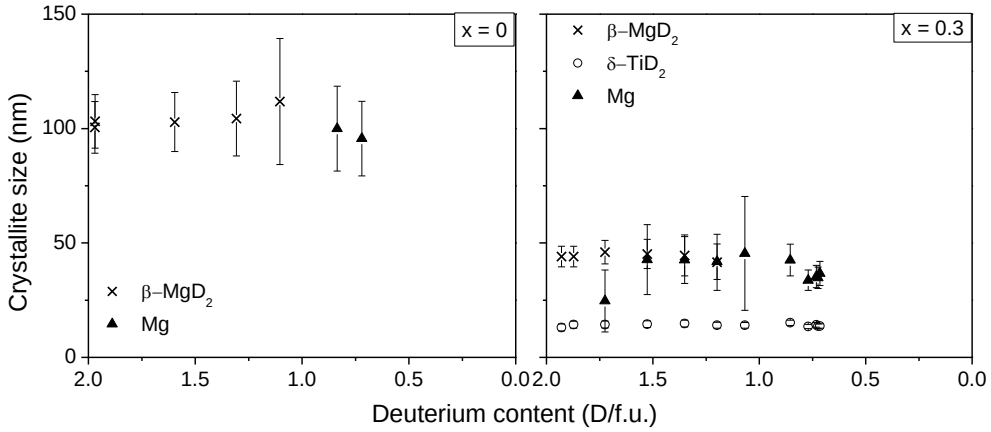

Figure 5.20. Evolution of the crystallite size with deuterium content for x = 0 and x = 0.3 samples during the acquisition of PCI desorption measurements at 548 K.

3.3.3 Absorption at room temperature

Once desorbed, both samples have been exposed to a deuterium pressure of 0.8 MPa at room temperature. For the Ti-free sample, no absorption was detected and no changes were observed for the diffraction patterns. In contrast, the Ti-containing material absorbed about 0.2 D/f.u. after 160 minutes under the same conditions. As represented in Figure 5.21, the β-MgD_2 phase amount raises progressively up to 5.6 wt.% while the Mg quantity decreases. The reaction rate slows down after 100 minutes. This result demonstrates that the intimate mixture of TiD_2 and Mg phases makes deuterium absorption at room temperature and moderate pressure possible. Thus, deuterium absorption likely results from MgD_2 nucleation at Mg/TiD_2 interfaces. However, the progression of the reaction is still probably limited by the slow deuterium diffusion into the growing deuteride phase.

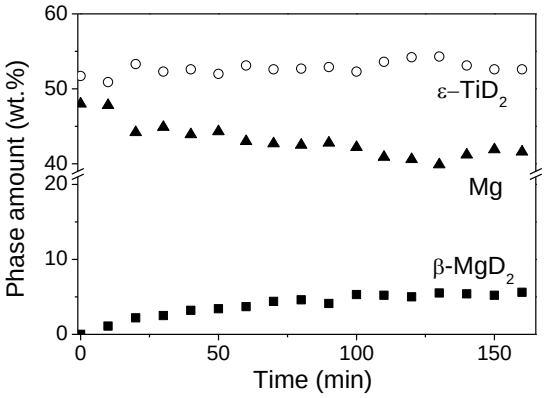

Figure 5.21. Evolution of phase contents during deuterium absorption at RT and 0.8 MPa for the x = 0.3 sample.

4 Discussion

4.1 Metal solubility in milled Mg-Ti-D systems

In spite of their thermodynamic immiscibility, significant solubility of Mg into Ti and *vice versa* can be attained by mechanical milling [17; 18]. Unfortunately, these metastable phases dissociate into MgH_2 and TiH_2 upon hydrogenation at 563 K [17]. However, Asano *et al.* were able to hydrogenate at low temperature (423 K) a $Mg_{50}Ti_{50}$ *bcc* alloy obtained by mechanical milling to form a *fcc* $Mg_{0.42}Ti_{0.58}H_{1.77}$ hydride phase with the fluorite structure of TiH_2 [19]. In complementary experiments, they obtained

closely related hydride phases (*fcc* $Mg_{0.40}Ti_{0.6}H_{1.13}$) by milling of MgH_2 and Ti powders over a long time (200 h) [20]. In contrast, the RBM technique allows for the direct synthesis of MgH_2-TiH_2 nanocomposites in a short milling time, but thus far no evidence of solubility of Mg (respectively Ti) into TiH_2 (respectively MgH_2) by RBM has been reported.

4.1.1 $Ti(Mg)D_2$ solid solution and its thermal stability

In this work, the structural analysis of as-milled samples proves that Mg solid solution in TiD_2 increases with Ti-molar concentration reaching 8 at.% at x = 0.5. The unit-cell volume of the $Ti(Mg)D_2$ phase increases with Mg incorporation into the Ti sub-lattice. Such an increase concurs with the cell expansion reported by Sun and Froes for Mg solubility in Ti [18]. The increase of Mg solubility with the Ti-molar fraction is attributed to the abrasive properties of titanium deuteride which forms during RBM and enhances the milling efficiency in the mixture. This solubility persists after thermal desorption of the β-MgD_2 phase at a moderate temperature of 530 K (Table 5.3), but disappears at temperatures above 540 K as suggested by *in situ* neutron diffraction during TD experiments (Figure 5.16 and Figure 5.17) and discussed below.

Figure 5.22 displays the change in cell volume of the TiD_2 phase at different stages (labelled events 1, 2 and 3, in chronological order) of *in situ* experiments (thermal desorption and PCI isotherms). During the *in situ* TD experiment (event 1), the TiD_2 cell volume drastically decreases between 548 and 600 K (see Figure 5.17). Next, during PCI absorption at 548 K, the cell volume increases again at the early stage of D-absorption (event 2), but does not recover the value observed during the TD experiment at 548 K. One should remark that during the PCI absorption, as D-content increases due to the formation of the MgD_2 phase, the cell volume increases slightly ~ 0.2 $Å^3$. This increase is attributed to interface coupling between TiD_2 and Mg/MgD_2 phases as discussed below (section 4.3). Next, during the PCI desorption, the TiD_2 cell volume decreases reversibly for high D-contents, *i.e.* while MgD_2 transforms into Mg. Finally, at low D-contents (D/f.u. ~ 0.5) the TiD_2 cell volume decreases strongly (event 3). Events 2 and 3 can be explained by reversible partial D-sorption within the TiD_2 phase. This indicates that a sub-stoichiometric $TiD_{2-\eta}$ phase with smaller cell volume is formed at low D-pressure. On the other hand, the cell volume difference observed between the

in situ TD experiment (88.6 $Å^3$) and PCI measurements both at 548 K (88.2 $Å^3$) can only be explained by the irreversible Mg segregation out of the TiD_2 phase. It can be concluded that Mg solubility in the $Ti_{0.92}Mg_{0.08}D_2$ phase is stable on heating up to 548 K. Further heating to 600 K results in Mg segregation as well as partial deuterium desorption from the TiD_2 phase to form a sub-stoichiometric $TiD_{2-\eta}$ phase.

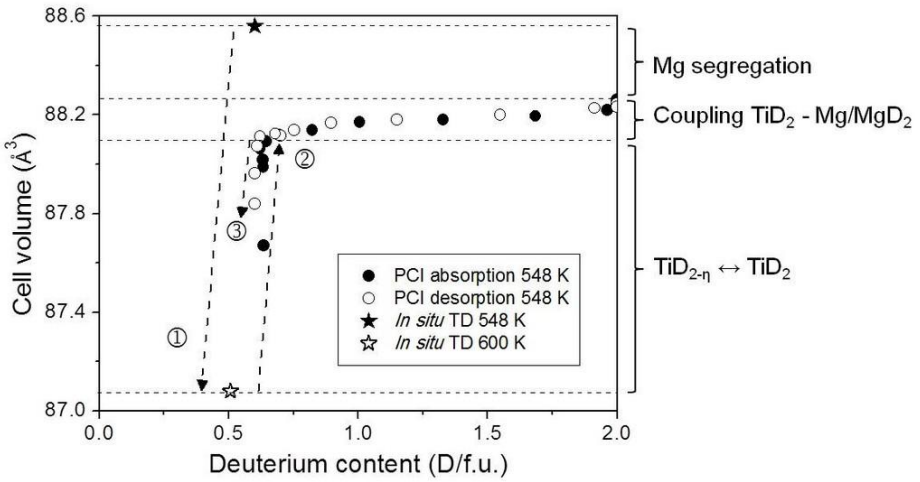

Figure 5.22. Evolution of TiD_2 cell volume during *in situ* TD and PCI measurements as a function of deuterium concentration for x = 0.3 sample. Event 1 corresponds to cell volume decrease between 548 and 600 K during *in situ* TD. Events 2 and 3 correspond to the cell volume variations during partial absorption and desorption of deuterium in TiD_2 phase during PCI experiments at 548 K. The cell volume decrease from 88.6 to 88.2 $Å^3$ is attributed to Mg segregation. Variations in the range 88.1 - 88.3 $Å^3$ result from the interface coupling between the TiD_2 phase and Mg/MgD_2 interfaces. The largest variations between 87.1 and 88.1 $Å^3$ correspond to the reversible formation of a sub-stoichiometric $TiD_{2-\eta}$ phase.

4.1.2 $Mg(Ti)D_2$ solid solution and its thermal stability

Ti solubility in the MgD_2 phase has also been observed up to 7 at.% by site occupancy refinement in as-milled samples (Table 5.2), but this result was poorly supported by the cell-volume variation of the $Mg(Ti)D_2$ phase with the Ti-molar fraction (Figure 5.7). This quasi-constant cell volume behaviour can be attributed to the ionic nature of the Mg-D bonding, in contrast to the metallic bonding of TiD_2. Indeed, the ionic radius of Mg^{2+} (r_{Mg2+} = 0.72 Å) is rather close to that of Ti^{2+} (r_{Ti2+} = 0.86 Å) in the same oxidation state, and even closer to the Ti^{3+} ionic radius (r_{Ti3+} = 0.67 Å).

Therefore, the very small reduction observed in $Mg(Ti)D_2$ lattice (Figure 5.7) seems to point towards the ionic character of Ti-D bonding in the $Mg(Ti)D_2$ solid solution. Theoretical studies on the effect of transition metal solution in MgH_2 cell-volume are not conclusive. While Song *et al.* [21] predict a cell reduction for $Mg(Ti)H_2$ phase, Chen *et al.* [22] report similar volume lattice for MgH_2 with our without Ti doping. Our experimental results support the latter calculations.

Regarding the thermal stability of Ti solubility in the $Mg(Ti)D_2$ phase, Ti segregation should occur below 530 K, *i.e.* the maximum temperature used for *ex situ* thermal desorption. Indeed, the unit-cell volume of the Mg phase in desorbed samples (Table 5.3) did not significantly deviate from the reported value for pure Mg (46.47 $Å^3$ [23]).

4.1.3 Solubility mechanisms

Solubility of 7 at.% Ti in MgD_2 and 8 at.% Mg in TiD_2 is observed in as-milled $(1-x)MgD_2$-$xTiD_2$ nanocomposites at x = 0.1 and 0.5 respectively. It is worth discussing how immiscible Mg and Ti elements may combine with hydrogen to form metastable ternary hydrides. Two possibilities can be considered. The first concerns the formation of nano-domains of one phase into the host hydride. We will refer to these mixed phases as $MgD_2(TiD_2)$ and $TiD_2(MgD_2)$. If the nano-domains are large enough to form a coherent domain (typically > 2 nm), then they will diffract as separate phases though yielding very broad peaks. The other possibility to be considered is atomic random substitution of Mg or Ti atoms, which can be written as $Mg(Ti)D_2$ or $Ti(Mg)D_2$ phases. In this case, the crystal structure of the host hydride remains the same, but its lattice constant is expected to change if the two elements have different atomic radii.

Our experimental results suggest that the second mechanism occurs as the refinement of site occupancies yields significant atomic substitution on Mg and Ti sites. Cell volume increase was observed for the $Ti(Mg)D_2$ phase, in agreement with the larger Mg atomic radius as compared to that of Ti, but the $Mg(Ti)D_2$ lattice remained constant due to the ionic character of MgD_2 bonds.

4.2 Structural properties and reversible deuterium loading in β- and γ-MgD_2 phases

Reversible deuterium loading in all MgD_2-TiD_2 nanocomposites occurs through the reversible MgD_2 to Mg transformation. However, some characteristics of this transformation depend on the presence of the TiD_2 phase. Figure 5.11 and Figure 5.15 show that the deuterium desorption temperature from the MgD_2 phase depends on the Ti-molar fraction. In this context, the evolution of unit-cell parameters of the β-MgD_2 phase during *in situ* TD of Ti-free and $0.7MgD_2$-$0.3TiD_2$ samples are displayed in Figure 5.23. For the Ti-free sample, the cell volume, as well as both *a*- and *c*-lattice parameters, increases continuously on heating due to the thermal expansion of the β-MgD_2 phase (Figure 5.23a). In contrast, for the Ti-containing sample, a cell distortion of the β-MgD_2 phase is observed between 510 and 540 K during *in situ* TD of $0.7MgD_2$-$0.3TiD_2$: the length of the *a*-axis decreases while the *c*-axis remains constant (Figure 5.23b). Interestingly, this deformation only occured in presence of TiD_2. A similar trend is observed during deuterium absorption at room temperature for the Ti-containing sample (Figure 5.23c), with a contraction of the *a*-axis at low D concentration. As solubility of Ti in MgD_2 hardly affects cell volume, this cell distortion cannot be related to Ti segregation. A possible explanation of such effect can rely on the formation of a sub-stoichiometric $MgD_{2-\eta}$ phase favoured by the presence of TiD_2, as recently reported in ref. [6; 24]. This fact suggests structural coupling between both phases as later discussed in section 4.3. The observed deuterium absorption at room temperature may well correspond to the formation of a sub-stoichiometric $MgD_{2-\eta}$ phase at Mg/TiD_2 interfaces.

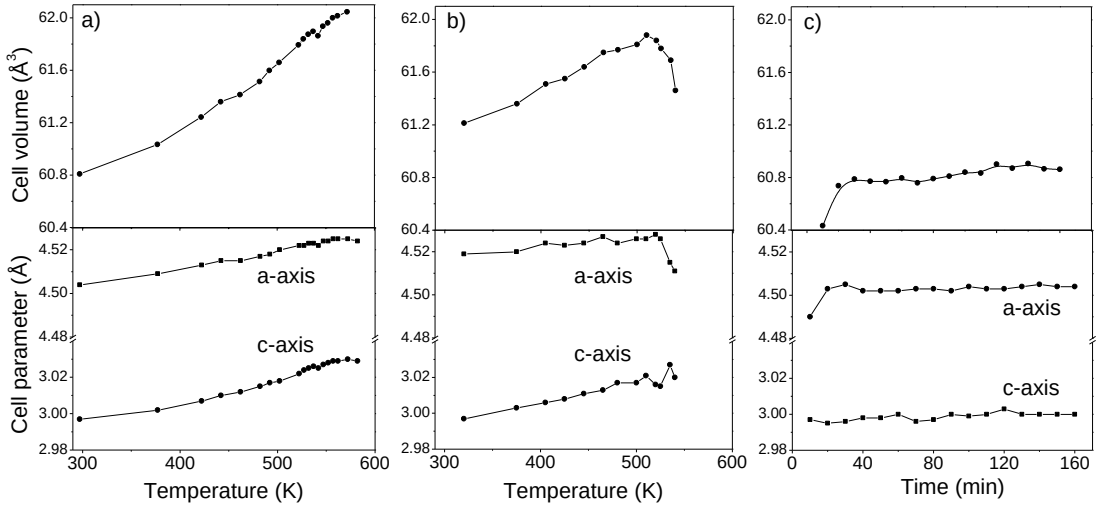

Figure 5.23. Evolution of cell volume (up) and cell parameters (down) of the β-MgD_2 phase during a) *in situ* TD of x = 0, b) *in situ* TD of x = 0.3 samples and c) absorption at RT of x = 0.3 sample.

Sub-stoichiometric $MgH_{2-\eta}$ has already been reported in the case of catalysed MgH_2. Schimmel *et al.* observed the occurence of hydrogen depleted $MgH_{2-\eta}$ during the early stage of hydriding of Mg catalysed with Nb or V [6]. However, contrary to our observations, they report a stretching of the *a*-axis and a contraction of the *c*-axis as a signature of $MgH_{2-\eta}$ formation. More signs of the existence of this phase were given later by Borgschulte *et al.* on MgH_2 ball milled with transition metal oxide catalysts [24]. Both studies suggested that the H vacancies generated in such destabilized phase would increase H diffusion and enhance sorption kinetics. This assumption is consistent with the fast kinetics observed in MgD_2-TiD_2 nanocomposites.

The behaviour of the γ-MgD_2 phase during thermal desorption experiments also merits attention. Two different behaviours are reported in the literature. Some authors report that the γ-phase decomposes into Mg + H_2 at a lower temperature than the β phase [8] while others claim a γ- to β-MgH_2 phase transformation before hydrogen desorption [25]. The *in situ* neutron diffraction analysis performed in this work allows us to state that, for a pure Mg sample, γ-MgD_2 progressively transforms into β-MgD_2 from temperatures as low as 330 K, *i.e.* before desorption occurs. To this respect, Figure 5.24a clearly shows the decrease of the γ/β-MgD_2 phase ratio with temperature. The γ-MgD_2 phase fully disappears at ~ 540 K. Deuterium is then gradually desorbed, leading

to the formation of the *hcp*-Mg phase (dashed curves in Figure 5.24). For the $0.7MgD_2$-$0.3TiD_2$ sample, in spite of the lower γ-phase amount and the consequently larger error, a different trend is observed (Figure 5.24b). Both γ- and β-MgD_2 phases decompose simultaneously from 480 K. The persistence of the γ-MgD_2 phase at higher temperature shows the higher stability of this phase in the composite sample. Taking into account that the β-MgD_2 phase admits Ti solid solution, we can speculate that Ti solubility also takes place in the γ-phase, although it could not be refined, and may be responsible for the stabilization of the γ-MgD_2 phase. This result opens a new route to the possible stabilization of this metastable phase.

However, it is likely that γ-MgD_2 does not contribute significantly to lowering the desorption temperature of MgD_2, as this phase is irreversible (*i.e.* does not form during rehydrogenation of Mg) and does not participate in the following hydrogenation cycles.

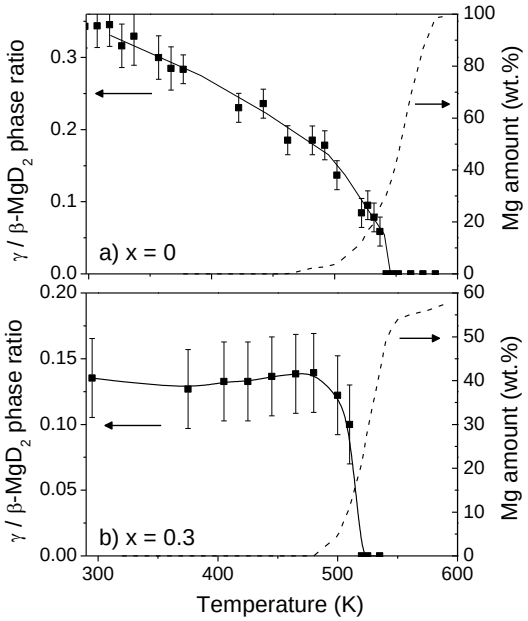

Figure 5.24. γ to β phase ratio during *in situ* TD of a) pure MgD_2 and b) $0.7MgD_2$-$0.3TiD_2$ samples. Dashed curves represent the amount of Mg phase.

4.3 Interface coupling between TiD_2 and Mg/MgD_2 phases

An intimate and homogeneous mixture of MgD_2 and TiD_2 phases at the nanometric scale is obtained by RBM of Mg and Ti powders under deuterium atmosphere. The TEM images presented in Figure 5.10 show the homogeneous distribution of TiD_2

nano-crystallites into MgD_2 agglomerates. Therefore, interface interactions between both hydrides can be expected. Through first principle density functional theory calculations, S. Hao and D.S. Sholl demonstrated that the formation of epitaxial contact between $TiH_2(111)/Mg(0001)$, and $TiH_2(111)/MgH_2(110)$ interfaces are energetically favourable [26]. Experimental evidence of coherent coupling between TiH_2 and Mg phases has also been reported in Mg-Ti-H thin films [27] and mechanically alloyed powders [28].

Our experimental results also support the existence of coupling between TiD_2 and Mg/MgD_2 phases. As shown in Figure 5.7, the cell volume of TiD_2 phase shrinks when the MgD_2 phase transforms into the Mg one after *ex-situ* thermal desorption. A similar shrinkage is observed during *in-situ* TD experiments (Figure 5.17) within the temperature range 510-540 K, *i.e.* when MgD_2 transforms into Mg. Finally, reversible changes of TiD_2 cell volume are detected during reversible D-loading of Mg during PCI isotherms (Figure 5.22). In all cases, the unit-cell volume of TiD_2 expands by ~ 0.2 $Å^3$ during the formation of MgD_2 and reversibly contracts when the Mg phase is formed. Such induced volume changes in the TiD_2 phase during reversible loading of Mg clearly demonstrate the occurrence of epitaxial relationships at TiD_2-Mg/MgD_2 interfaces. It is very likely that this coupling favours H mobility at interfaces and ensures a fast hydrogen transfer between TiH_2 and Mg phases.

According to this mechanism, it is essential to achieve the smallest particle size of both phases in order to have the highest boundary density between the TiH_2 and Mg/MgH_2 phases.

4.4 TiD_2 inclusions as grain growth inhibitors of the Mg phase

One of the most relevant outcomes of this investigation is the effect of the TiD_2 phase on the limited grain growth of the Mg phase during deuterium desorption and reversible loading. The crystallite size of the Mg phase strongly depends on the Ti-molar fraction (Figure 5.9): the smallest crystallites are obtained for the highest Ti content. This phenomenon can be explained by the effect of inclusions on the grain boundary mobility that was first considered by Zener [29]. It was demonstrated that crystal grain growth in the presence of randomly distributed second phase particles reaches a limiting size. Such a limit is determined by the size of inclusions and its

concentration in the solid. In the case of spherical inclusions, the Zener relationship can be expressed as follows:

$$G_{lim} = \frac{2}{3} \times \frac{D}{f} \quad \textbf{(5.1)}$$

where G_{lim} is the limiting grain size, D is the diameter of the inclusion and f is the volume fraction of inclusions in the solid.

Using the Zener relationship, Figure 5.25 shows G_{lim} of Mg phase for TiD_2 inclusions with a particle size of 10, 13 or 16 nm (*i.e.* those reported for different Ti-molar fractions in Table 5.3). The experimental Mg crystallite size after deuterium desorption for the different Ti-contents (Table 5.3) follows the same trend as the Zener relationship, although they have not reached G_{lim}. The Zener relationship currently overestimates the limiting crystallite size as shown for model systems such as α-Fe [30].

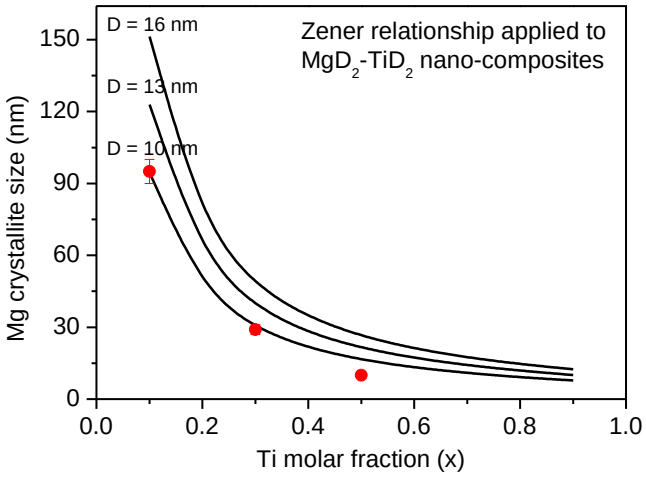

Figure 5.25. Limiting grain size of Mg crystallites as a function of Ti-molar fraction according to Zener relationship (continuous lines) for TiD_2 inclusions of 10, 13 and 16 nm. Full symbols correspond to experimental values of Mg crystallite size after *ex situ* desorption experiments.

These results clearly show the grain refiner role played by the TiD_2 phase on the Mg one during desorption experiments. Furthermore, *in situ* TD and PCI measurements for x = 0.3 sample confirmed that crystallite size remains stable on cycling at moderate temperature (548 K). This is a key fact to ensuring fast kinetics in this system during reversible H-sorption by maintaining short diffusion paths within the Mg phase. For the Ti-containing sample, the crystallite size of the Mg phase after TD is 30 ± 5 nm, while

in pure Mg it coarsens up to 90 ± 20 nm. Very close values are observed after subsequent PCI measurement (35 ± 5 nm and 100 ± 20 nm for x = 0.3 and x = 0 compositions, respectively). According to the Zener relationship, the limiting Mg size will be maintained as long as TiD_2 inclusions do not undergo coalescence. However, in HP-DSC experiments, such small crystallite size was not maintained after 100 cycles at higher temperatures (650 K) where both TiH_2 and MgH_2 suffered important grain growth (530 and 580 nm, respectively). Nevertheless, this growth was significantly limited by the presence of TiH_2 as compared to the pure Mg sample. This process opens a new route to limit grain coarsening in hydrogen storage materials that need to be operated or treated at high temperatures.

4.5 Kinetic mechanisms during reversible H-loading

At the light of the structural characteristics and sorption properties gathered along this study, the following mechanisms can be proposed for reversible hydrogen absorption and desorption in MgH_2-TiH_2 nanocomposites.

Both absorption and desorption are governed by a nucleation and growth mechanism. Figure 5.26 illustrates the absorption and desorption nucleation step at the TiH_2-Mg/MgH_2 interfaces. Nucleation occurs mainly at this interface because TiH_2 acts as a gateway for hydrogen gas which is dissociated and transferred to the Mg phase where MgH_2 nucleates. This is supported by the large diffusion coefficient of H in TiH_2 [31]. In addition, it is proposed that fast H-absorption is possible in nanocomposites because the MgO barrier is bypassed through the TiH_2 phase.

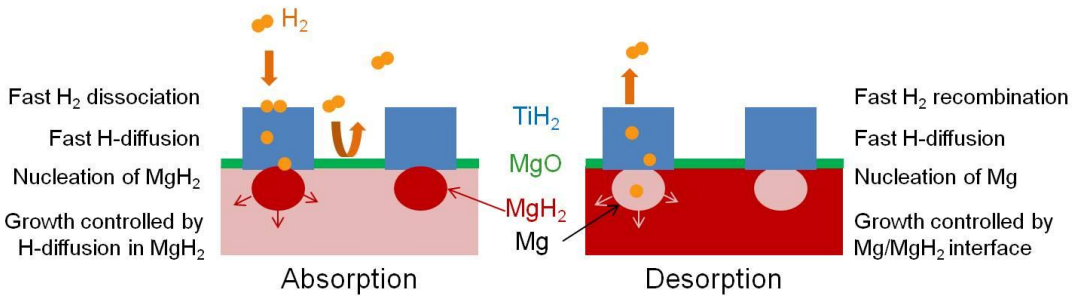

Figure 5.26. Schematic representation of hydrogen absorption and desorption mechanisms in MgH_2-TiH_2 nanocomposites.

As illustrated in Figure 5.27 for absorption, the amount of hydride phase associated to the nucleation step is more important when the number of interfaces is high, *i.e.* when the crystallites of both phases are small. In consequence, the growth of the MgH_2 phase would not be a limiting step if the density of nuclei is elevated, as observed in the smallest particles configuration of Figure 5.27. In the case of larger particles, the MgH_2 phase growth is limited by H-diffusion through the MgH_2 phase.

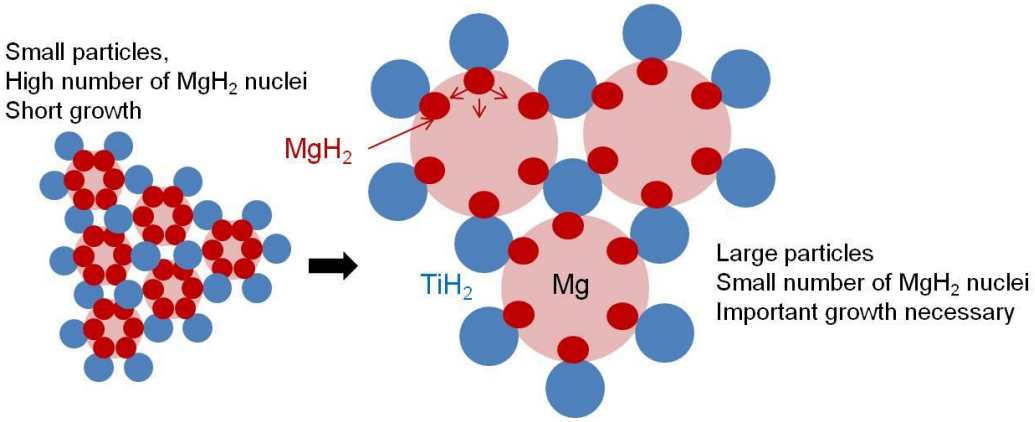

Figure 5.27. Illustration of the crystallite size effect on the absorption kinetics in MgH_2-TiH_2 nanocomposites.

Finally, TDS experiments revealed that the desorption process is accelerated thanks to the abundant and fast nucleation of the Mg phase at the TiH_2/MgH_2 interfaces. This results in a reduced activation energy (62(15) $kJ/molH_2$ for the desorption of the $0.7MgH_2$-$0.3TiH_2$ sample). The subsequent growth of the Mg phase is governed by the Mg/MgH_2 interface displacement.

5 Conclusion

$MgH(D)_2$-$TiH(D)_2$ nanocomposites have been synthesized by RBM which allows for fast nanosizing and simultaneous hydriding of the material at room temperature. The presence of Ti during RBM enhances the absorption kinetics by increasing the $MgH(D)_2$ nucleation rate and reducing the H(D)-diffusion path length. The catalytic effect of the TiH_2 phase has been also evidenced during desorption by means of TDS experiments. The activation energy necessary for desorption of the $0.7MgH_2$-$0.3TiH_2$ nanocomposite is significantly lower (62(15) $kJ/molH_2$) than for the Ti-free sample

(94(12) kJ/molH_2). Besides, this catalytic effect was proved to be maintained over at least 100 cycles by means of HP-DSC experiment. A deep structural characterization of these compounds has been accomplished by XRPD, NPD and TEM methods in order to shed light on the outstanding H-sorption kinetics of this system. In this respect, the main results can be summarized as follows:

- Mg solubility in TiD_2 up to 8 at.% Mg and Ti solubility in β-MgD_2 up to 7 at.% Ti have been evidenced in as-milled samples. Such metal solubilities are metastable on heating: Mg segregates out of Ti(Mg)D_2 between 550 and 600 K, whereas Ti segregates out of Mg(Ti)D_2 below 530 K, *i.e.* during deuterium desorption from this phase. As a consequence, Ti solubility in the MgD_2 phase does not play any significant kinetic role during the reversible deuterium loading of the Mg/MgD_2 system.

- The metastable γ-MgD_2 phase is formed during RBM synthesis. For the Ti-free sample, it irreversibly transforms into its polymorph β-MgD_2 before decomposition of the deuteride (T < 540 K). For Ti-containing nanocomposites, both γ- and β-MgD_2 desorb simultaneously. Nevertheless, the γ-MgD_2 phase is not formed during the deuteration of desorbed samples and therefore does not contribute to the fast reaction kinetics on cycling.

- In MgD_2-TiD_2 nanocomposites, TiD_2 inclusions with typical sizes of 10 nm are homogeneously distributed within the MgD_2 matrix. Their size remains constant on cycling at moderate temperature. Coupling at the interface between TiD_2 inclusions and the Mg/MgD_2 matrix are evidenced by TiD_2 cell-volume variations induced by reversible D-loading in the Mg phase. This coupling is expected to enhance deuterium mobility within the nanocomposite components.

- The occurrence of sub-stoichiometric deuterides $MgD_{2-\eta}$ and $TiD_{2-\eta}$ has been identified at low D contents in the nanocomposite. Both defective phases may enhance deuterium diffusion within each phase. The Mg/TiH_2 interface coupling and the formation of $MgD_{2-\eta}$ may explain deuterium absorption of MgD_2-TiD_2 nanocomposites at room temperature and the lower activation energy for H-desorption of these compounds.

- TiD_2 inclusions act as effective inhibitors for the crystal growth of Mg and MgD_2 phases during reversible deuterium loading. Limited grain growth is explained by the Zener pinning model. This phenomenon holds during H-cycling at

moderate temperature which demonstrates the key role of the TiD_2 phase for attaining fast H-kinetics and stability on cycling.

Although the TiD_2 phase does not modify Mg/MgH_2 thermodynamics, it provides outstanding H-sorption kinetics, making MgH_2-TiH_2 nanocomposites able to absorb a significant amount of hydrogen, even at room temperature. These kinetic properties are attributed to the limited grain growth of Mg and MgH_2 phases, the interface coupling between TiH_2 and Mg/MgH_2 phases and the fast H-diffusion through sub-stoichiometric $MgH_{2-\eta}$ and $TiH_{2-\eta}$ phases.

References

1. Cuevas F, Korablov D, Latroche M. Synthesis, Structural and Hydrogenation Properties of Mg-rich MgH_2-TiH_2 Nanocomposites Prepared by Reactive Ball Milling under Hydrogen Gas. *Phys. Chem. Chem. Phys.* 2012; **14** (**3**): 1200.
2. Shao H, Felderhoff M, Schüth F. Hydrogen Storage Properties of Nanostructured MgH_2/TiH_2 Composite Prepared by Ball Milling under High Hydrogen Pressure. *Int. J. Hydrogen Energy* 2011; **36** (**17**): 10828–10833.
3. Lu J, Choi YJ, Fang ZZ, Sohn HY, Ronnebro E. Hydrogen Storage Properties of Nanosized MgH_2-$0.1TiH_2$ Prepared by Ultrahigh-Energy-High-Pressure Milling. *J. Amer. Chem. Soc.* 2009; **131** (**43**): 15843–15852.
4. Zhang J, Cuevas F, Zaïdi W, Bonnet J-P, Aymard L, Bobet J-L, et al. Highlighting of a Single Reaction Path during Reactive Ball Milling of Mg and TM by Quantitative H_2 Gas Sorption Analysis to Form Ternary Complex Hydrides (TM = Fe, Co, Ni). *J. Phys. Chem. C* 2011; **115** (**11**): 4971–4979.
5. Völkl J, Alefeld G. Diffusion of hydrogen in metals. In: Alefeld PDG, Völkl DJ (eds). *Hydrogen in Metals I*. Springer Berlin Heidelberg; 1978. pp. 321–348.
6. Schimmel HG, Huot J, Chapon LC, Tichelaar FD, Mulder FM. Hydrogen Cycling of Niobium and Vanadium Catalyzed Nanostructured Magnesium. *J. Amer. Chem. Soc.* 2005; **127** (**41**): 14348–14354.
7. Arita M, Shimizu K, Ichinose Y. Thermodynamics of the Ti-H System. *Metall. Mater. Trans. A* 1982; **13** (**8**): 1329–1336.
8. Gennari FC, Castro FJ, Urretavizcaya G. Hydrogen Desorption Behavior from Magnesium Hydrides Synthesized by Reactive Mechanical Alloying. *J. Alloys Compd.* 2001; **321** (**1**): 46–53.
9. Varin RA, Czujko T, Chiu C, Wronski Z. Particle size effects on the desorption properties of nanostructured magnesium dihydride (MgH_2) synthesized by controlled reactive mechanical milling (CRMM). *J. Alloys Compd.* 2006; **424** (**1-2**): 356–364.
10. Leardini F, Ares JR, Bodega J, Fernandez JF, Ferrer IJ, Sanchez C. Reaction pathways for hydrogen desorption from magnesium hydride/hydroxide composites: bulk and interface effects. *Phys. Chem. Chem. Phys.* 2010; **12**: 572–577.
11. Huot J, Liang G, Boily S, Van Neste A, Schulz R. Structural Study and Hydrogen Sorption Kinetics of Ball-Milled Magnesium Hydride. *J. Alloys Compd.* 1999; **293-295**: 495–500.
12. Barkhordarian G, Klassen T, Bormann R. Kinetic investigation of the effect of milling time on the hydrogen sorption reaction of magnesium catalyzed with different Nb_2O_5 contents. *J. Alloys Compd.* 2006; **407** (**1–2**): 249–255.
13. Huot J, Pelletier JF, Lurio LB, Sutton M, Schulz R. Investigation of dehydrogenation mechanism of MgH_2-Nb nanocomposites. *J. Alloys Compd.* 2003; **348** (**1-2**): 319–324.

14. Liang G, Huot J, Boily S, Schulz R. Hydrogen desorption kinetics of a mechanically milled MgH_2-5at.%V nanocomposite. *J. Alloys Compd.* 2000; **305** (**1-2**): 239–245.
15. Aguey-Zinsou K-F, Ares-Fernandez J-R. Hydrogen in magnesium: new perspectives toward functional stores. *Energy Environ. Sci.* 2010; **3** (**5**): 526–543.
16. Fernández JF, Cuevas F, Algueró M, Sánchez C. Influence of the Preparation Conditions of Titanium Hydride and Deuteride $TiH_x(D_x)$ ($X \approx 2.00$) on the Specific Heat Around the δ-ε Transition. *J. Alloys Compd.* 1995; **231** (**1–2**): 78–84.
17. Liang G, Schulz R. Synthesis of Mg-Ti Alloy by Mechanical Alloying. *J. Mater. Sci.* 2003; **38** (**6**): 1179–1184.
18. Sun F, Froes FH (Sam). Synthesis and Characterization of Mechanical-Alloyed Ti-xMg Alloys. *J. Alloys Compd.* 2002; **340**: 220–225.
19. Asano K, Enoki H, Akiba E. Synthesis of Mg-Ti FCC Hydrides from Mg-Ti BCC Alloys. *J. Alloys Compd.* 2009; **478** (**1-2**): 117–120.
20. Asano K, Akiba E. Direct Synthesis of Mg-Ti-H FCC Hydrides from MgH_2 and Ti by Means of Ball Milling. *J. Alloys Compd.* 2009; **481** (**1-2**): L8–L11.
21. Song Y, Guo ZX, Yang R. Influence of selected alloying elements on the stability of magnesium dihydride for hydrogen storage applications: A first-principles investigation. *Phys. Rev. B* 2004; **69** (**9**): 094205.
22. Chen D, Wang YM, Chen L, Liu S, Ma CX, Wang LB. Alloying Effects of Transition Metals on Chemical Bonding in Magnesium Hydride MgH_2. *Acta Mater.* 2004; **52** (**2**): 521–528.
23. Becerra A, Pekguleryuz M. Effects of Lithium, Indium, and Zinc on the Lattice Parameters of Magnesium. *J. Mater. Res.* 2008; **23** (**12**): 3379–3386.
24. Borgschulte A, Bösenberg U, Barkhordarian G, Dornheim M, Bormann R. Enhanced Hydrogen Sorption Kinetics of Magnesium by Destabilized $MgH_{2-\delta}$. *Catal. Today* 2007; **120** (**3–4**): 262–269.
25. Pelletier JF, Huot J, Sutton M, Schulz R, Sandy AR, Lurio LB, et al. Hydrogen Desorption Mechanism in MgH_2-Nb Nanocomposites. *Phys. Rev. B* 2001; **63** (**5**): 052103.
26. Hao S, Sholl DS. Effect of TiH_2-Induced Strain on Thermodynamics of Hydrogen Release from MgH_2. *J. Phys. Chem. C* 2012; **116** (**2**): 2045–2050.
27. Borsa DM, Gremaud R, Baldi A, Schreuders H, Rector JH, Kooi B, et al. Structural, Optical, and Electrical Properties of $Mg_yTi_{1-y}H_x$ Thin Films. *Phys. Rev. B* 2007; **75** (**20**): 205408.
28. Srinivasan S, Magusin PCMM, Kalisvaart WP, Notten PHL, Cuevas F, Latroche M, et al. Nanostructures of $Mg_{0.65}Ti_{0.35}D_x$ Studied with X-ray Diffraction, Neutron Diffraction, and Magic-Angle-Spinning ^2H NMR Spectroscopy. *Phys. Rev. B* 2010; **81** (**5**): 054107.
29. Rahaman MN. Grain Growth and Microstructural Control (Chap. 9). In: *Ceramic processing and sintering*. New York: M. Dekker; 1995.
30. Couturier G, Doherty R, Maurice C, Fortunier R. 3D Finite Element Simulation of the Inhibition of Normal Grain Growth by Particles. *Acta Mater.* 2005; **53** (**4**): 977–989.
31. Kaess U, Majer G, Stoll M, Peterson DT, Barnes RG. Hydrogen and deuterium diffusion in titanium dihydrides/dideuterides. *J. Alloys Compd.* 1997; **259** (**1–2**): 74–82.

Chapter 6.

Final remarks and conclusions

OUTLINE

This final chapter aims to address a comprehensive discussion of the main results achieved throughout this PhD Thesis. Different strategies have been implemented through different Mg-based materials to improve the hydrogen sorption properties of pure Mg. On one hand, the thermodynamic properties have been tackled by alloying Mg with several transition metals. On the other hand, the kinetic properties were enhanced by the use of catalysts. In addition, nanostructuration of the material was found to play a role on both kinetic and thermodynamic properties. It is now essential to consider the relevance of these strategies to correctly orientate future investigations.

1 Thermodynamic modifications

Destabilizing metal hydrides is one of the main conditions required to allow working at reasonable temperatures and pressures. However, attaining the target of $-45 < \Delta H < -35$ kJ/molH_2 with $\Delta S = -130$ J/ K.molH_2 while maintaining satisfactory hydrogen gravimetric density is a real challenge for on-board hydrogen storage applications. In this PhD thesis, new steps toward this objective have been accomplished, opening potential routes for further investigation.

1.1 By formation of stable alloys

Different TMs have been associated to Mg by different synthesis processes. In a first approach, stable alloys based on the Mg_6Pd ρ-phase were formed by conventional melting techniques. The interest of this strategy is to change the global enthalpy of the hydriding reaction by bringing into play intermetallic phases instead of pure Mg. Thus, if the formation enthalpy of the initial reactants is lower than it is for the final intermetallic products (*i.e.* in the hydrided state), then the global enthalpy of reaction will be reduced as compared to the formation enthalpy of MgH_2. In the simple case of non-substituted Mg_6Pd, the global reaction thermodynamics can be illustrated by comparison of the energy levels in Figure 6.1. It appears that the difference of formation enthalpies between initial Mg_6Pd and final MgPd is fundamental to decrease the net enthalpy of reaction. However, only little enthalpy reduction ($\Delta_r H = -69.8$ kJ/molH_2) is achieved because this difference is rather small for these compounds ($\Delta_f H(Mg_6Pd) = -173.7$ kJ/mol$_{compound}$ and $\Delta_f H(MgPd) = -150$ kJ/mol$_{compound}$).

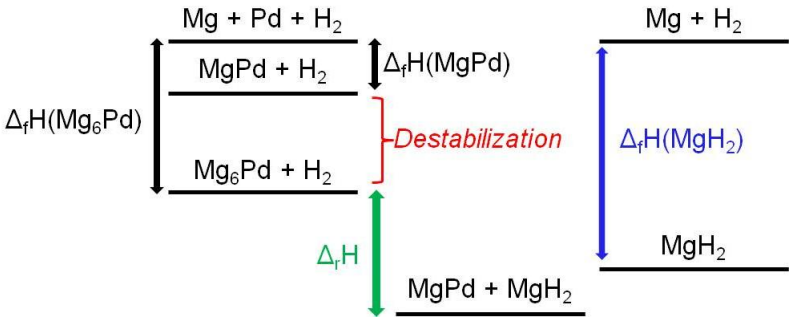

Figure 6.1. Schematic representation of the thermodynamic states during hydrogenation of the Mg_6Pd compound. Δ_rH is the enthalpy change corresponding to the global hydriding reaction ($Mg_6Pd + 5\ H_2 \leftrightarrow 5\ MgH_2 + MgPd$). Δ_rH is smaller than $\Delta_fH(MgH_2)$ because Mg_6Pd is more stable than MgPd.

In clear, it is necessary to start from a stable Mg-rich phase that decomposes into MgH_2 and a Mg-poor phase with much smaller formation enthalpy than the initial one. The interest of the Mg_6Pd phase resides in its high Mg content that provides a high storage capacity. We have seen along Chapter 3 that Pd can be substituted by several TMs, leading to Mg-rich pseudo-binary phases with different hydrogenation properties. For example, the case of Ag substitution is characterized by a significant enthalpy reduction at high H-content while, unfortunately, a strong entropy decrease is also observed. More accurately, a significantly reduced entropy variation was also measured for the Ni-substituted compound on the high pressure plateau of absorption. While enthalpy of hydrogenation is generally presented as the unique thermodynamic parameter that governs hydride stability, we show here that entropy also has a primordial importance. Thus, the needed equilibrium temperature of a system working at atmospheric pressure is a more relevant parameter to evaluate the effective destabilization of a hydrided compound. This equilibrium temperature is represented in Figure 6.2 for the different $Mg_6Pd_{1-x}TM_x$ compounds as a function of hydrogen content. Hence, non-hydrided compounds need high temperature, *i.e.* the same as pure Mg, to initiate H-absorption. In the H-content range corresponding to the high plateau pressure, the operating temperature is significantly lower. For instance the Ni-substituted compound can reversibly store about 2 wt.% H at 510 K and atmospheric pressure. Although this capacity is relatively low, it is available at about 40 K lower than pure

Mg. This result is encouraging on the potential of Mg-based alloys to form less stable hydrides.

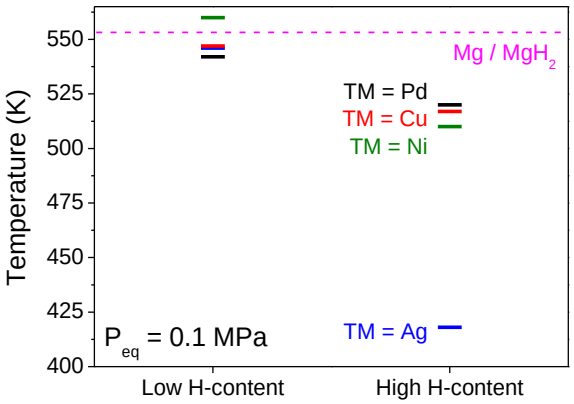

Figure 6.2. Equilibrium absorption temperatures at atmospheric pressure (P = 0.1 MPa) as a function of hydrogen content in $Mg_6Pd_{1-x}TM_x$ compounds, as calculated from ΔH and ΔS values determined by PCI measurements between 590 and 650 K.

The field of binary Mg-TM alloys is already well studied and no relevant candidate stands out. However, investigation of ternary systems rich in Mg opens a wide range of possibilities. For example, the Mg-Co phase diagram [1] possesses only one intermetallic phase ($MgCo_2$) but the Pd-Co system exhibits complete miscibility in the liquid and solid states [2]. Therefore, a $Mg_6Pd_{1-x}Co_x$ pseudo-binary phase with large homogeneity range may exist. In addition, the formation enthalpy of the $MgCo_2$ phase (ΔH_f = -19 $kJ/mol_{compound}$ [3]) is much lower than the one of MgPd (ΔH_f = -150 $kJ/mol_{compound}$) and may result in a reduction of enthalpy of the hydrogenation reaction if this phase is present in the final products, though the formation of the complex hydride Mg_2CoH_5 cannot be ruled out. However, *ab initio* calculations are necessary to determine the formation enthalpy of the $Mg_6Pd_{1-x}Co_x$ pseudo-binary phase.

1.2 By formation of metastable phases

Another approach to tailor the thermodynamics of the Mg-H system is the addition of an immiscible element, such as Ti, to form metastable hydride phases. This was achieved by the technique of RBM with the formation of $Mg(Ti)H_2$ and $Ti(Mg)H_2$ phases. Ti solubility in MgH_2 was limited to 7 at.% in the best case and was not maintained after desorption at 530 K. In consequence, no thermodynamic change was

observed during PCI measurements, as the metastable $Mg(Ti)H_2$ phase was no longer engaged. However, some hints of thermodynamic destabilization did appear during the first desorption-absorption cycle of HP-DSC. This result encourages deepening this aspect of the MgH_2-TiH_2 nanocomposites properties, for instance by increasing Ti solubility in MgH_2 through longer milling times. Besides, low temperature hydrogenation experiments must be carried out to preserve the metastable phase on cycling. As presented in Chapter 1, the formation of Mg-Ti based metastable alloys strongly depends on the synthesis method (ball milling with different parameters, vapour deposition on thin films, *etc*.), thus opening many routes of investigation on metastable phases in the Mg-Ti-H system.

1.3 By nanostructuration

We already know from theoretical calculations [4; 5] that the enthalpy of formation of metal hydrides can be reduced by decreasing the particle size up to a nanometric scale. We have experimentally demonstrated in this PhD Thesis that hydrided nanoparticles ranging from 4 to 10 nm are less stable than the equivalent bulk hydride. This destabilization is helped by the porous scaffold which limits the particle growth during cycling. The technique of nanoconfinement for Mg-based alloys is quite new and opens promising lines of investigation. For instance, it is possible to confine other Mg-based compounds with interesting properties for hydrogen storage, such as stable binary phases (*e.g.* Mg_2Ni [6] or Mg_2Cu [7]), pseudo-binary phases (*e.g.* $Mg_6Pd_{1-x}Ni_x$) or even metastable phases (*e.g.* Mg-Ti or Mg-Nb).

2 Kinetic modifications

Improving the sorption kinetics in a metal-hydride system is somehow easier than its thermodynamic destabilization. However, maintaining high kinetic performance over cycling is more challenging. Indeed, one of the main issues of Mg-based materials is that they undergo coarsening during hydrogen cycling that usually occurs at rather high temperature. Along this Thesis, kinetic issues have been addressed through two main axes: catalyst addition and nanostructuration.

2.1 By metal addition

2.1.1 TM alloying

Catalytic properties for hydrogen dissociation/recombination have been reported for instance for Pd [8], Ni [9] or Mg_2Cu [10]. Therefore, we can expect that the $Mg_6Pd_{1-x}TM_x$ compounds will possess better kinetic properties than pure Mg. This seems to be the case though different properties are found, depending on the composition of the alloy and the pathways involved during (de)hydrogenation reactions.

For all compositions, the absorption reaction paths are similar: hydrogen pressure induces disproportionation of the pseudo-binary phase into MgH_2 (and Mg_2NiH_4 in the case of TM = Ni) and Pd-containing intermetallic phases. Analyses of the isothermal absorption curves show that they are all controlled by the diffusion of metal atoms that allows disproportionation. In consequence, faster kinetics are achieved for more mobile metallic atoms in the ρ-phase and finer microstructures. Apparently, Ni substitution is more suitable for better absorption kinetics.

As for desorption, kinetics are controlled by the MgH_2/Mg interface displacement. Thus, no significant improvement is achieved when the only hydride in presence is MgH_2 as the growth velocity of the Mg phase is constant. However, Mg nucleation was strikingly accelerated in presence of finely structured Mg_2NiH_4 resulting in a much lower activation energy (68 kJ/molH_2).

In summary, from a kinetic point of view, Ni seems to be a better choice to substitute Pd atoms in the Mg_6Pd phase. On the other hand, it is necessary to perform cycling experiment to check the ability of this compound to preserve its microstructure and its phase composition. As a general rule, the kinetic properties of Mg-based alloys strongly depend on the catalytic properties of the present phases as well as the microstructure of the material.

2.1.2 TM inclusions (TiH_2)

The kinetics of the MgH_2-TiH_2 nanocomposites are certainly the fastest achieved in this PhD Thesis. Indeed, activation energy of desorption is remarkably low (62 kJ/molH_2) and absorption occurs in less than one minute at 573 K and P_{H2} = 0.8 MPa [11]. Besides, the storage capacity only loses 8 % of its initial capacity after

100 cycles between 523 and 650 K during HP-DSC experiments, being probably due to impurities in the gas phase.

In this case, the phase responsible of the kinetic improvement is not alloyed to Mg, but in close contact by means of coupled interfaces. One of the roles of inclusions is to provide a gateway for hydrogen. The gas molecules are dissociated (recombined) on TiH_2 surface, they diffuse through this phase towards (from) Mg, and MgH_2 (Mg) nucleates at the interface.

This mechanism is demonstrated to be highly efficient and has to be considered for developing efficient hydrogen storage materials.

2.2 By nanostructuration

The effect of nanostructuration on the H-sorption kinetics is obviously related to the shorter diffusion path (of H or TMs) and to the high surface density for hydrogen chemisorption. One efficient method to obtain nanosized materials following a top-down approach is mechanical milling, which, in the case of Mg, is more effective in presence of an abrasive component. RBM was shown to be an excellent technique to rapidly obtain nanostructured hydrides. The main issue related to nanostructuration is that it is hardly preserved on cycling. To this purpose, two methods have been implemented in this thesis to limit the material coarsening during cycling.

The first one applies to MgH_2-TiH_2 nanocomposites. It consists in blocking the grain growth of the Mg/MgH_2 phase by pinning the grain boundary movement by TiH_2 inclusions. This method was proved to be particularly efficient as long as the temperature was not too high. Thus, at high temperature (> 548 K), TiH_2 inclusions start to coalesce and the pinning effect is reduced. However, sorption properties of these nanocomposites are still sufficient at 548 K where the Mg crystallite size was maintained around 30 nm with 30 at.% Ti. This process is highly interesting to overcome coarsening issues in hydrogen storage materials and could be extended to many types of compounds.

The second method used to limit coarsening is the nanoconfinement of the active material. Here, nanostructuration is achieved thanks to a bottom-up approach. In this method, a nanoporous carbon scaffold is used to hinder the material coalescence on cycling. The cycling results are encouraging as the absorption kinetics was maintained

over at least 10 cycles. Though, these materials are more sensitive to air oxidation, which can result in a progressive loss in hydrogen storage capacity.

2.3 Comparative desorption properties

Finally, a comparison of thermal desorption spectra of $Mg_6Pd_{1-x}TM_x$ alloys, $0.7MgH_2$-$0.3TiH_2$ and MgH_2 obtained by RBM, and commercial MgH_2 is displayed in Figure 6.3a. As can be better appreciated on the integrated plots (Figure 6.3b), the hydrided $Mg_6Pd_{0.25}Ni_{0.75}$ compound has the lowest onset of desorption. This is explained by the reduced thermodynamic stability of the Mg_2NiH_4 phase as compared to MgH_2. Besides, the peak corresponding to the desorption from the MgH_2 phase in this sample occurs at lower temperature than RBM MgH_2. This result shows that the catalytic properties of the Mg_2NiH_4 phase reported in section 5.2.2 of Chapter 3 are more powerful than nanostructuration of pure MgH_2 by RBM. Thus, substituting Pd by Ni in the Mg_6Pd phase results in very interesting desorption kinetics, with an activation energy almost as low as for MgH_2-TiH_2 nanocomposites. As for this last one, most of its hydrogen is desorbed at lower temperature than for all the other materials, though the desorption rate is slower owing to the reduced temperature. Regarding the $Mg_6Pd_{1-x}TM_x$ compounds with TM = Pd, Ag and Cu, their kinetics of desorption are very similar to those of commercial MgH_2.

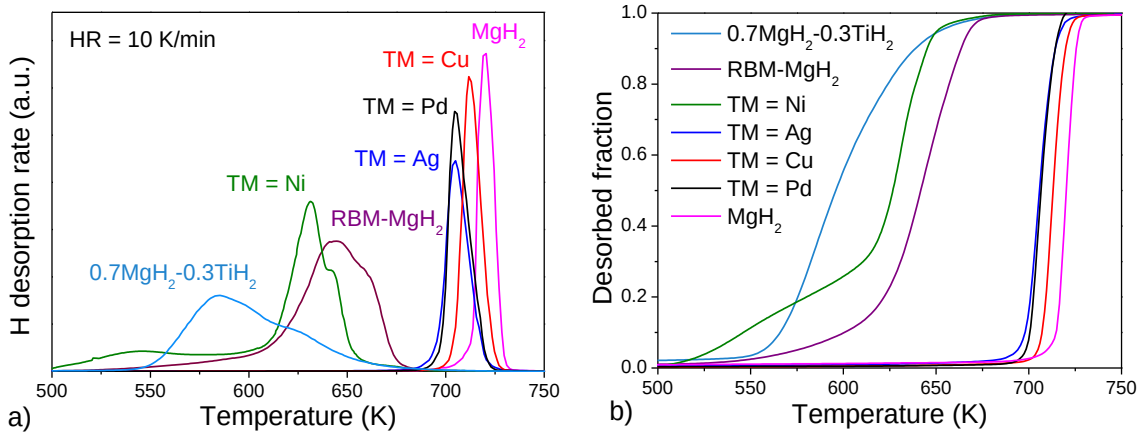

Figure 6.3. a) Comparison of the TDS spectra of $Mg_6Pd_{1-x}TM_x$ compounds (TM = Pd, Ag, Cu, Ni), $(1-x)MgH_2$-$xTiH_2$ nanocomposites (x = 0 and 0.3) and commercial MgH_2 powder at a heating rate of 10 K/min. b) Integrated plots of the TDS spectra.

Finally, we have to mention that Mg_6Pd@C hybrid sample could not be measured in the same TDS apparatus, because of its high air-sensitivity. However, TDS measured under secondary vacuum (Chapter 4, section 3.1.2) seems to indicate a desorption peak situated between those of MgH_2-TiH_2 nanocomposites and $Mg_6Pd_{0.25}Ni_{0.75}$ compound.

3 Advances and bottlenecks of Mg-rich materials for hydrogen storage

As suggested by the increasing research activity on Mg-based materials for hydrogen storage during the last fifty years, Mg element remains of major interest to develop efficient storage materials. Indeed, considerable progresses have been achieved to improve its sorption properties thanks to theoretical studies and experimental investigations. For instance, the stability of alloy phases and their thermodynamic properties of hydrogenation can be predicted from first principles or semi-empirical calculations [12–15]. These are powerful predictive techniques that should be implemented for systematic investigation of Mg-based ternary systems.

From a technical point of view, nanostructuration is one of the essential characters that should be considered for future hydrogen storage materials, as it confers to the system fast kinetics. The use of additives and ball milling techniques are now mature to be implemented at large scales. On the other hand, nanoconfinement methods are very promising but require further adjustments such as reducing the high air-sensitivity of the hybrid materials and increasing their gravimetric storage capacity.

Certainly, the main impediment to Mg-based hydrogen storage materials for potential on-board applications resides in their thermodynamic stability and relatively low gravimetric capacity. Indeed, DOE's targets require a gravimetric capacity for the whole storage system of 5.5 wt.% H [16], *i.e.* including tank material, heat exchanger and other components. However, Mg-based materials can be reasonably employed for stationary hydrogen tanks, thus providing a safe and compact storage. In such applications, the difficulties encountered to reduce the stability of the hydrided materials can possibly be overcome by coupling the storage system to a residual heat source from one of the many generated by industries (metalworking industry, cement manufacturing, glass melting, *etc.*). In a near future, hydrogen will definitely be part of the energy

landscape and Mg-based materials are real potential storage candidates to make this energy carrier viable.

4 Conclusions

This PhD Thesis has been devoted to the investigation of three families of Mg-rich materials for hydrogen storage. The main achievements can be summarized as follows:

- The thermodynamics of the Mg/MgH_2 system have been modified by alloying Mg with TMs to form new Mg-rich phases. Pseudo-binary $Mg_6Pd_{1-x}TM_x$ (TM = Pd, Ag, Cu and Ni) alloys have been synthesized to the TM solubility limit by conventional melting techniques.
- The TM solubility limit is determined by electronic effects, being higher when TM chemical properties approach to those of Pd. Thus, Ni solubility reaches 9 at.% while it does not exceed 3.9 at.% for Cu. Ag exhibits a solubility of 7.2 at.%. The crystallographic model developed by Samson for the Mg_6Pd phase [17] is suitable for all the TM substitutions. Cu and Ni site occupancy was then determined by XRPD Rietveld refinements. Owing to steric effect, TMs preferentially occupy Pd sites with low CN.
- For all $Mg_6Pd_{1-x}TM_x$ compounds, absorption PCI curves occur according to two plateau pressures. The low plateau pressure does not show any notable destabilization as compared to MgH_2. However, the enthalpy corresponding to the high plateau pressure is significantly less negative, in particular for the Ag-containing compound. Though, this enthalpy decrease was found to be correlated to a reduced entropy of reaction, attributed to a disorder increase in the solid products of hydrogenation. Calculated thermodynamic values are in good agreement with experimental values for TM = Pd and Ni, encouraging further *ab initio* studies.
- The detailed hydrogenation pathways have been determined for all the $Mg_6Pd_{1-x}TM_x$ pseudo-binary compounds as illustrated in Figures 3.18, 3.32 and 3.43.
- The kinetic mechanism governing absorption in these compounds is the diffusion of TM atoms and therefore depends on their mobility and the microstructure of the alloy. Desorption is controlled by the MgH_2/Mg interface displacement, but nucleation of the Mg phase was found to be significantly accelerated in presence of the

finely structured Mg_2NiH_4 phase. Thus, the activation energy for desorption from the Ni-containing compound was reduced to 68 kJ/molH_2.

- Innovative melt-infiltration technique has been used to confine Mg_6Pd nanoparticles into the pores of an activated carbon. Alloyed nanoparticles as small as 4 nm have been achieved.

- This hybrid Mg_6Pd@C material exhibits strongly accelerated kinetics as compared to the bulk alloy. This fast kinetics is maintained during at least 10 cycles thanks to the porous scaffold that limits particles coarsening. In addition, PCI and HP-DSC measurements compared to bulk Mg_6Pd point toward a thermodynamic destabilization of the hydrided compound.

- MgH_2-TiH_2 nanocomposites with outstanding kinetic properties have been synthesized by RBM. As-milled samples are composed of β- and γ-MgH_2 polymorphs and ε-TiH_2 fluorite phase. Solubility of 7 at.% Ti and 8 at.% Mg in β-MgH_2 and ε-TiH_2 phases has been evidenced by neutron diffraction analysis. It is observed during thermodesorption of as-milled compounds that the γ-MgH_2 phase is stabilized by the presence of Ti.

- The growth of the Mg phase is limited thanks to the pinning effect of the TiH_2 particles. The maximum grain size reached by the Mg phase is properly modeled through the Zener relationship, as a function of the concentration and dimension of TiH_2 inclusions.

- Besides, TiH_2 phase acts as a catalyst for hydrogen sorption in Mg through an intimate coupling at the (Mg-MgH_2)/TiH_2 interface that allows for fast Mg and MgH_2 nucleation. The mobility of hydrogen is also facilitated by the formation of sub-stoichiometric $MgH_{2-\eta}$ and $TiH_{2-\eta}$ phases. The introduction of TiH_2 inclusions in nanosized MgH_2 is highly efficient to improve kinetics and cycling properties.

- The material containing 30 at.% Ti is able to rapidly absorb and desorb hydrogen during at least 100 cycles. These enhanced kinetic properties are related to the fast and abundant nucleation of the Mg-MgH_2 phases thanks to the high density of interfaces with TiH_2 inclusions, thus bypassing the unavoidable MgO layer. During absorption, the growth of the MgH_2 phase is controlled by the diffusion of H through the MgH_2 shell, while on desorption Mg growth depends on the MgH_2/Mg interface displacement.

Finally, a comparative overview on the hydrogenation properties of the investigated compounds is presented in Table 6.1.

Table 6.1. Summary of the main hydrogenation properties of the Mg-based materials investigated in this Thesis. The equilibrium temperature at atmospheric pressure corresponds to the high pressure plateau for all the $Mg_6Pd_{1-x}TM_x$ compounds. Qualitative assessment is given for kinetics and cyclability from – (bad) to +++ (very good). /-symbol stands for not determined property.

Material	T (K) for P_{eq} = 0.1 MPa	Kinetics	Cyclability	Reversible H-capacity (wt.% H)
Mg_6Pd	520	–	/	4.3
$Mg_6Pd_{0.5}Ag_{0.5}$	418	–	/	4.4
$Mg_6Pd_{0.7}Cu_{0.3}$	517	–	/	4.3
$Mg_6Pd_{0.25}Ni_{0.75}$	510	++	/	5.6
Mg_6Pd@C	/	++	+	<1
$0.7MgH_2$-$0.3TiH_2$	553	+++	+++	4.3
RBM-MgH_2	553	+	–	7.6
MgH_2	553	–	–	7.6

Two types of materials stand out in this Thesis: the $Mg_6Pd_{0.25}Ni_{0.75}$ alloy and the MgH_2-TiH_2 nanocomposites. The first one offers a good compromise between improved thermodynamics, good kinetic properties and a rather high storage capacity. Its robustness on cycling still has to be tested. The second one is remarkable for its extremely fast kinetics and stability over cycling. Besides, its reversible storage capacity could be improved by optimizing the Mg to Ti ratio. Regarding the other investigated compounds, they provide a deep comprehension of hydrogenation mechanisms and potential pathways for hydride destabilization.

References

1. Nayeb-Hashemi AA, Clark JB. The Co-Mg (Cobalt-Magnesium) system. *Bull. Alloy Phase Diagr.* 1987; **8** (**4**): 352–355.
2. Ghosh G, Kantner C, Olson GB. Thermodynamic modeling of the Pd-X (X=Ag, Co, Fe, Ni) systems. *J. Phase Equilib.* 1999; **20** (**3**): 295–308.
3. Widom M, Mihalkovic M. Alloy database. *http://alloy.phys.cmu.edu/* 2011;
4. Bérubé V, Chen G, Dresselhaus MS. Impact of nanostructuring on the enthalpy of formation of metal hydrides. *Int. J. Hydrogen Energy* 2008; **33** (**15**): 4122–4131.
5. Wagemans RWP, van Lenthe JH, de Jongh PE, van Dillen AJ, de Jong KP. Hydrogen Storage in Magnesium Clusters: Quantum Chemical Study. *J. Am. Chem. Soc.* 2005; **127** (**47**): 16675–16680.

6. Bogerd R, Adelhelm P, Meeldijk JH, de Jong KP, de Jongh PE. The structural characterization and H_2 sorption properties of carbon-supported $Mg_{1-x}Ni_x$ nanocrystallites. *Nanotechnology* 2009; **20** (**20**): 204019.
7. Au YS, Ponthieu M, Zwienen R van, Zlotea C, Cuevas F, Jong K de, et al. Synthesis of Mg_2Cu nanoparticles on carbon supports with enhanced hydrogen sorption kinetics. *J. Mater. Chem. A* 2013; **1** (**34**): 9983–9991.
8. Adams BD, Chen A. The role of palladium in a hydrogen economy. *Mater. Today* 2011; **14** (**6**): 282–289.
9. Pozzo M, Alfè D. Hydrogen Dissociation and Diffusion on Transition Metal (= Ti, Zr, V, Fe, Ru, Co, Rh, Ni, Pd, Cu, Ag)-doped Mg(0001) Surfaces. *Int. J. Hydrogen Energy* 2009; **34** (**4**): 1922–1930.
10. Karty A, Grunzweig-Genossar J, Rudman PS. Hydriding and dehydriding kinetics of Mg in a Mg/Mg_2Cu eutectic alloy: Pressure sweep method. *J. Appl. Phys.* 1979; **50** (**11**): 7200–7209.
11. Cuevas F, Korablov D, Latroche M. Synthesis, Structural and Hydrogenation Properties of Mg-rich MgH_2-TiH_2 Nanocomposites Prepared by Reactive Ball Milling under Hydrogen Gas. *Phys. Chem. Chem. Phys.* 2012; **14** (**3**): 1200.
12. Fernandez JF, Widom M, Cuevas F, Ares JR, Bodega J, Leardini F, et al. First-principles phase stability calculations and estimation of finite temperature effects on pseudo-binary $Mg_6(Pd_xNi_{1-x})$ compounds. *Intermetallics* 2011; **19** (**4**): 502–510.
13. Andreasen A. *Predicting formation enthalpies of metal hydrides*. Risoe National Laboratory; 2004.
14. Joubert J-M, Thiébaut S. Thermodynamic assessment of the Pd–H–D–T system. *J. Nucl. Mater.* 2009; **395** (**1–3**): 79–88.
15. Joubert J-M, Crivello J-C. Stability of erbium hydrides studied by DFT calculations. *Int. J. Hydrog. Energy* 2012; **37** (**5**): 4246–4253.
16. U.S. Departement of Energy. Targets for Onboard Hydrogen Storage Systems for Light-Duty Vehicles. 2009;
17. Samson S. Complex Cubic A_6B Compounds. II. The crystal structure of Mg_6Pd. *Acta Cryst.* 1972; **B28**: 936.